2-D Data Analysis in High-Pressure Powder Diffraction

Scott A. Belmonte

A thesis submitted in fulfilment of the requirements
for the degree of Doctor of Philosophy
to the
Department of Physics and Astronomy
University of Edinburgh
1998



Declaration

This thesis has been composed by myself and it has not been submitted in any previous application for a degree. The work reported within was executed by me, unless otherwise stated.

January 1998

Acknowledgements

Firstly, I would like to thank my supervisor, Richard Nelmes, for his guidance, patience and support at all stages of my Ph. D. studies. I would also like to thank Stuart Pawley for introducing me to Richard and suggesting that a Ph. D. in high-pressure physics would be fruitful.

Special thanks go to my colleagues and friends who have made the last three years very enjoyable: Malcolm McMahon; John Loveday; Bill Marshall; Hengda Liu; Dave Allan, who has been a veritable smorgasbord of fun and laughter during long beamtimes; and John B. Parise for introducing me to the phrase 'squeeze the bejeezus'.

I would like to thank all the staff at The University of Edinburgh with whom I've had the pleasure of meeting. I would especially like to thank Ronny Proc from the Department of Physics & Astronomy Mechanical Workshop for his excellent workmanship and good advice throughout the upgrade of the beamline equipment.

I would also like to thank all my friends and colleagues at SRS Daresbury for making me feel very welcome when I first arrived and for making my stay at Daresbury a happy one.

And finally, and most importantly, I am most grateful to all my family for their love and support at all times.

Abstract

In high-pressure powder diffraction, microstructural effects in the samples (such as preferred orientation and anisotropic stress) can be a great hindrance to accurate structure determination and can sometimes make structure determination impossible. However, it has been found that there is a wealth of information available about sample microstructure from the 2-d angle-dispersive powder patterns collected by an image-plate detector.

This thesis presents the development of the experimental techniques required to study microstructure in powder samples at high pressure through the use of 2-d data. A description is given of the upgrade and installation of new experimental apparatus constructed to permit routine investigation of microstructure in samples under pressure. The experimental techniques have been applied to the modelling of preferred orientation in powders at high pressure. A demonstration of the qualitative information about preferred orientation in powders available from a 2-d detector is given. Details are presented of a quantitative model applied to image-plate data based on preferred orientation corrections commonly used in Rietveld refinement programs. It is shown that this quantitative model is not completely adequate for describing the extremely strong preferred orientation often found in powder samples at high-pressure and a new more general model based on a commonly used model of texture used by the texture analysis community is presented and shown to work well.

The structural pressure dependence of the cinnabar phase of HgS is presented.

Strong preferred orientation can be induced in HgS at high pressure, it is shown that, by using the preferred orientation modelling techniques presented in this thesis, it has been possible to de-correlate the effect of preferred orientation from the refined structural parameters.

Finally, a brief qualitative description is given of the manifestation of other micro-structural effect in 2-d data. And the possibilities for developing a quantitative analysis of these effects are discussed.

Contents

Acknowledgements ii

Abstract iii

1 Introduction 1

1.1 High-Pressure Structural Studies 1

1.2 Thesis Outline 8

2 High-Pressure Powder Diffraction Techniques Using an Image-Plate on Synchrotron Sources 10

2.1 Introduction 10

2.2 Powder Diffraction Techniques 11

2.3 Solving Structures at High Pressure: Criteria for Accurate Structure Determination 13

2.4 Experimental Set-up and Procedures: Data Collection 13

2.4.1 Pressure Cells and Pressure Cell Techniques 14

2.4.2 Pressure Measurement 20

2.4.3 Image-Plate Set-up on Station 9.1 22

2.4.4 Sample Alignment 25

2.4.5 Image-Plate Detector 26

2.5 Experimental Set-up and Procedures: Data Analysis 29

2.5.1 2-d Powder Pattern Integration 29

2.5.2 Data Calibration 31

2.5.3 Structure Solution and Refinement 32

3 Experimental Methods for 2-D Analysis **35**

3.1 Introduction 35

3.2 Criteria for High Quality 2-D Data Collection 36

3.3 Development of Experimental Set-up: Data Collection 37

3.3.1 High-Precision Rotation Stage 41

3.3.2 Pressure Cell Holders 44

3.3.3 Alignment Microscope Modification 46

3.3.4 Beamstop and Shielding 48

3.3.5 Image-Plate Holder 53

3.3.6 Alignment Procedure 55

3.4 Development of Experimental Set-up: Data Preparation 57

3.4.1 Extension to Platypus: Sector Output 57

3.4.2 Absorption Correction for Inclined Samples 60

4 Preferred Orientation Modelling by 2-D Analysis **70**

4.1 Introduction 70

4.2 Preferred Orientation and Texture 71

4.3 Preferred Orientation Modelling 74

4.3.1 Simple Analytic Model 75

4.3.2 Symmetrised Spherical Harmonic Model 97

4.3.3 Pressure Induced PO in HgS 103

4.3.4 2-D Rietveld Refinement 105

5 Application of Preferred Orientation Modelling in High-Pressure Structural Studies **111**

5.1 Introduction 111

5.2 The Cinnabar Structure 112

5.3 Structural Pressure Dependence of HgS to 11 GPa. 114

5.4 Conclusions 125

6 Other Microstructural Effects in 2-D **126**

6.1 Introduction 126

6.2 Texture 126

6.3 Anisotropic Stress and Strain 131

7 Conclusions **135**

References **140**

Published Work **145**

Chapter 1

Introduction

1.1 High-Pressure Structural Studies

Of the two thermodynamic variables—pressure and temperature—pressure has the most dramatic effect on the structure of materials. Readily accessible experimental pressures can reduce interatomic distances by as much as 10–20%. In contrast, changing the temperature of a sample from its melting point to 0K will only decrease interatomic distances by a few percent. Strong reductions in interatomic distances bring about a wide variety of changes in physical properties and structure. As band gaps are reduced, many insulators and semiconductors become metals. Hydrogen is believed to be metallic at very high pressures. Structural transitions can be accompanied by electronic transitions as outer valence electrons are pushed into electron shells closer to the nucleus. Changes in the nature of chemical bonding at high pressure open up the possibility of making novel forms of materials that cannot be made at ambient pressure. One of fastest growing areas of research, where accurately known structures and transitions have become essential, is computational simulation. Much of the current computational research is related to, and depends on, pressure research. Accurate

ab initio modelling of structures needs well-known atomic potentials. Information about the structures and dynamics of materials at high pressure greatly aids the calculation of accurate potentials. Computational calculations are now being used to investigate the nature of materials under conditions far beyond those that can be reached by experiment. These investigations rely heavily on accurate structural information at ever higher pressures.

The two main aims in high-pressure structural studies are (i) to reach higher pressures than in the past to extend our knowledge into previously unexplored areas, and (ii) to determine structures accurately at all pressures. Single-crystal and neutron techniques generally give the most accurate results. In the single-crystal techniques, all reflections are separated in space, whereas many reflections are overlapped in powder techniques, which makes intensity assignment less accurate when using powder techniques. Neutron techniques do not suffer from the form factor effect of x-ray techniques where the scattered intensity falls off rapidly with increasing scattering angle and, therefore, the intensities at higher angle (smaller d-spacing) can be determined with greater accuracy by neutron techniques than by x-ray techniques. But single crystals of many materials tend to shatter at high pressure after passing through a phase transition and the low flux of neutron sources necessitates the use of large sample volumes limiting the maximum pressure attainable (around 20–25 GPa). Consequently, most of the mainstream high-pressure work has been carried out using x-ray powder diffraction techniques.

Much of the past effort in the field of high-pressure crystallography has been directed towards fulfilling (i) above. With the advent of the diamond-anvil cell (DAC) in the 1960s, it became possible to take small samples to pressures well above 10 GPa. In 1972, the highest pressures reached were around 40 GPa (Jayaraman (1972)), and by 1978 this limit had increased to 100 GPa (or 1 Mbar) (Mao *et al.* (1978)). However, to reach such pressures requires extremely small

sample volumes, which results in a very weak signal. This limitation was overcome by the use of synchrotron radiation sources. The DAC was first used with synchrotron radiation in 1977 (Buras *et al.* (1977)) using energy-dispersive techniques. Energy-dispersive x-ray powder diffraction (EDX) takes advantage of the high intensity of the full white beam from synchrotron sources to overcome the problem of small sample sizes. However, EDX techniques suffer from known limitations such as poor resolution, unreliable peak intensities due to insufficient powder averaging and contaminant peaks from fluorescence. Consequently, in most cases, the structures of high-pressure phases can only be determined very approximately using EDX.

In the late 1980s, Japanese scientists at the Photon Factory developed the use of the 2-d image-plate as a detector for high-pressure angle-dispersive x-ray powder diffraction (ADX) (Shimomura *et al.* (1992)). ADX has intrinsic advantages in resolution and lack of fluorescent scatter over EDX but, because ADX is a monochromatic technique, it does not take advantage of the full white beam of the synchrotron. However, this advantage is recouped by using an area detector, which captures a much greater part of the total diffracted intensity than a conventional 1-d angle-dispersive detector. This, combined with the sensitivity of the image-plate, meant that sufficient signal could be captured to make ADX a feasible technique for high-pressure studies. Also, because more of the diffraction pattern is intercepted, much improvement is achieved in the signal-to-noise ratio and powder averaging, leading to more accurate peak intensities. However, the Japanese used pressure cells with slot apertures so that only a strip through the diffraction pattern could be recorded and they did not use the data to carry out full structural refinements.

In 1991, the image-plate techniques pioneered by the Japanese were implemented by members of the Condensed Matter Physics Group of The University of Edinburgh on Station 9.1 at SRS Daresbury, where the techniques were substantially developed (Nelmes *et al.* (1992), Nelmes and McMahon (1994)). Beryllium

backed diamond-anvil cells with their full conical apertures allowed complete 2-d powder patterns to be recorded. Sophisticated data analysis software was developed to integrate the 2-d images into 1-d powder patterns, which could then be used in Rietveld structure refinement packages. The data were of sufficient quality to enable accurate structure refinements to be carried out up to the pressure limits of the pressure cells. Over the following 2–3 years, studies of group IV, III-V, and II-VI semiconductors showed that much of the previously accepted structural systematics in these systems were incorrect (Nelmes *et al.* (1995a), Nelmes *et al.* (1995b), McMahon and Nelmes (1995)).

The initial reason for using the image-plate as a detector was that, by capturing a large part of the diffracted intensity simultaneously, the image-plate affords great gains in sensitivity and data quality over other types of detector. But it became apparent that the sensitivity of the image-plate revealed problems of great importance caused by the effects of high-pressure on a powder sample. Diffraction peak positions and intensities can be changed by microstructural effects in the sample (i.e. deviations from an ideal powder) as well as by crystal structure changes. When the crystal structure is unknown, the correct positions and intensities are unknown, so the presence of microstructure would limit the accuracy of structure determination or could even make it impossible to solve the structure. This means that, if the crystal structure of a sample at high pressure is to be determined accurately, it is essential to detect the presence of microstructure and, if possible, to model it separately from structure solution and refinement.

Microstructure in a powder is caused when the powder deviates from being ideal. In an ideal powder, the crystallites in the sample are assumed to be small (of the order of 1 μm) and to be randomly oriented. Also, in high-pressure experiments, the crystallites of an ideal powder are expected to be under uniform (hydrostatic) stress. A long known effect in powders is preferred orientation or texture, which affects relative peak intensities. For example, if the crystallites are plate-like, then the normals to the plates might all tend to align along the same direction.

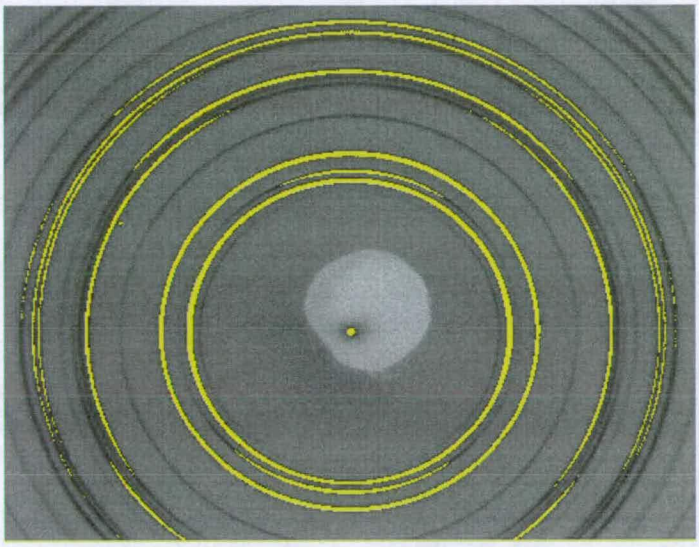


Figure 1.1. A contrast enhanced 2-d powder pattern of HgS. Preferred orientation in the sample reveals itself as intensity variations around the powder rings.

This can happen quite strongly in pressure cells where such plates align along the axis of the cell coincident with the direction of the sample compression. Although preferred orientation has been recognised as a problem for a long time, little effort has gone into accounting for it properly. Indeed, preferred orientation has often been used as an excuse when the observed intensities failed to agree with the intensities predicted by a proposed structural model.

Other microstructural effects, which can be induced quite strongly in samples at high pressure, cause peak displacements such that no unit-cell can be found that correctly predicts the position of all the diffraction peaks in a pattern. These effects were largely unrecognised until recently, simply because they only become apparent when full structure fitting is attempted. They are an even greater problem for high-pressure structural studies than preferred orientation because they stop structure solution at the first hurdle—determining the unit cell. The origin of these anisotropic peak displacements is unknown at present but it is likely to be a combination of anisotropic strains (either due to the elastic properties of the sample or defects such stacking faults) and non-uniform stress in the sample which is often present at high pressures.

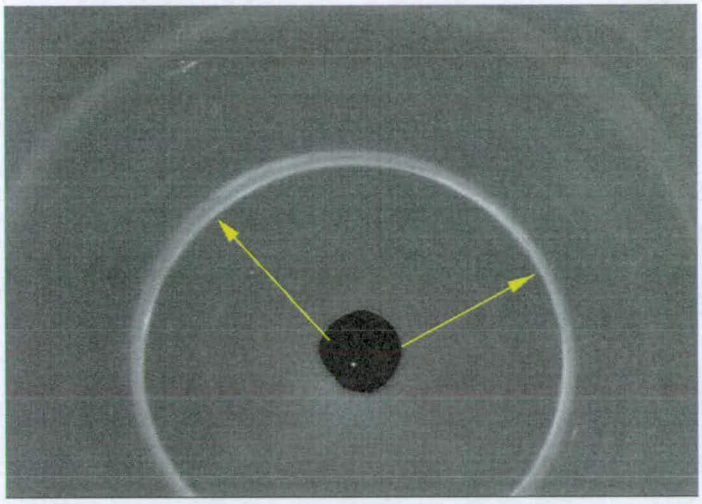


Figure 1.2. 2-d powder pattern of CsBr at 52.5 GPa. The arrows highlight the change in splitting as a function of azimuth.

As well as highlighting the problems caused by microstructure, the 2-d nature of the image-plate also provides a means by which to tackle them. There is potentially a much greater amount of information available in a 2-d powder pattern than in a 1-d pattern. For example, in a 1-d pattern, preferred orientation manifests itself as changes in relative intensities but in a 2-d image this effect can be manifested as changes in intensity around the powder rings (see Fig. 1.1). Similarly, anisotropic strain effects can show up as deviations in scattering angle, 2θ, around the rings (see Fig. 1.2). It is these variations that contain the information required to characterise the sample's microstructure. The effects of microstructure on a powder pattern depend on properties of the sample such as elasticity and crystallite morphology and not on the details of the crystal structure. So by developing models that describe the effects of microstructure on a 2-d powder pattern it is possible to fit the intensity and position variations separately from structural refinement without any knowledge of atomic arrangement. The refined microstructure parameters can then be fixed in full structural refinements thus de-correlating the atomic parameters from the microstructure parameters.

Considerable progress had been made by 1994 in measuring and modelling simple well-behaved preferred orientation in powder samples at high pressure (Wright

(1994)), but general quantitative fitting of the intensity variations in the powder rings of a 2-d image had not been fully achieved. The microstructural effects observed in many samples have cylindrical symmetry about the axis of the pressure cell. Thus, when the incident beam is along the axis of the cell—as is normally the case—no variations are observed around the powder rings. In this case, the cell has to be inclined in order to bring out the variations around the rings caused by microstructure. The experimental equipment and techniques needed to be substantially upgraded if sample inclinations were to become a routine part of the experimental method.

The general aim was to be able to extract microstructural information from 2-d data routinely and for microstructural modelling to become a standard part of the experimental method. This thesis presents a contribution towards achieving this aim. The work consisted of the development of new experimental equipment and the upgrade of existing equipment so that sample inclinations could be carried out routinely. The main image-processing software has been modified to include 2-d data analysis routines to enable azimuthal data to be extracted easily from the image-plate data. Completely new texture refinement software has been written to allow the intensity variations around many powder rings to be fitted simultaneously. A more general model of texture has been adapted for use with image-plate data which has led to considerable improvements in fitting and is able to model more complex textures than simple well-behaved preferred orientation. The first quasi-2-d refinement from image-plate data has been carried out.

The new texture model has been applied to a high-pressure structural study of the cinnabar phase in HgS in which very strong preferred orientation is induced reproducibly by pressure. The success of the texture modelling is demonstrated by the good agreement between the variable atomic coordinates determined as a function of pressure both when severe preferred orientation is and is not present.

An overview of other 2-d effects, such as more complex PO and texture is given along with suggestions for handling them. And finally, the possible origins of

peak displacements and non-circular powder rings are discussed

1.2 Thesis Outline

This thesis is organised as follows:

Chapter 2 serves as an introduction to the experimental methods for high-pressure powder diffraction using an image-plate detector. Although the author was not involved in implementing any of these methods, the methods described in this chapter are the core to all the work presented in this thesis, and it is necessary to present them here for subsequent chapters to be understood.

Chapter 3 presents the experimental methods for 2-d data analysis. The key criteria for collecting accurate 2-d data are outlined. The development of new equipment, and the upgrade of existing equipment to enable the routine collection of high-quality 2-d data for microstructural analysis, are described. A description is given of the extensions to the image-plate data analysis software for extracting azimuthal information. And a new analytical absorption correction for 2-d data collected from an inclined pressure cell is presented.

Chapter 4 describes one particular aspect of 2-d data analysis—preferred orientation modelling. Two common models of preferred orientation are presented with details of how to apply them to image-plate data. Details are given of the preferred-orientation refinement software written especially for the analysis of image-plate data. The 2-d data analysis techniques are used to study the strong simple preferred orientation induced in HgS at high pressure. And the results of the first structural refinement from 2-d data are presented.

Chapter 5 presents a structural study of the cinnabar phase of HgS. Severe uniaxial preferred orientation is induced in HgS at pressure. It is shown that the structural parameters of HgS can be determined accurately as a function of pressure in the presence of strong preferred orientation.

Chapter 6 serves as an overview of other microstructural effects in 2-d and discusses the possibilities for quantitative modelling of these effects. The handling of more complex preferred orientation is discussed. The possible use of the (hkl)-dependence of microstructural effects for obtaining the indexing of a powder pattern of an unknown phase is presented. And finally, the possible origins of the anisotropic peak displacement and non-circular powder rings are discussed.

Chapter 7 concludes the thesis, summarising the achievements to date and discusses possible future developments in 2-d data analysis in high-pressure structural studies.

Chapter 2

High-Pressure Powder Diffraction Techniques Using an Image-Plate on Synchrotron Sources

2.1 Introduction

This chapter provides a description of the image-plate set-up and techniques at SRS Daresbury for carrying out high-pressure structural studies. The set-up was implemented by members of the Condensed Matter Physics Group of The University of Edinburgh and, although the author was not involved in the development of the beamline equipment or techniques, it is necessary to detail them here because they provide the foundation for the development work presented in this thesis and comprise a large part of the experimental procedure used to collect the data for this thesis.

2.2 Powder Diffraction Techniques

All diffraction techniques are based on simple principles first used by Bragg in 1913. When a beam of particles (for example, neutrons or x-ray photons) strikes a crystalline material, the particles are diffracted from the planes of atoms in the crystal—defined by the Miller indices h, k and l—according to Bragg's Law

$$\lambda = 2d_{hkl} \sin \theta_{hkl} \tag{2.1}$$

where λ is the wavelength of the incident radiation, d_{hkl} is the spacing between a given set of (hkl) planes and θ_{hkl} is half the angle between the incident beam and the beam diffracted from that set of (hkl) planes. The intensity of the diffracted beam depends on the arrangement of atoms within the layers from which the incident beam is being diffracted. There are two experimental variables in this equation—λ and θ_{hkl}. The two powder diffraction techniques arise from which variable is held constant during the experiment. In energy-dispersive x-ray diffraction (EDX) θ_{hkl} is held constant and the diffracted data are collected as a function of wavelength λ, which is related to energy. In angle-dispersive x-ray diffraction (ADX) λ is held constant and the diffraction data are collected as a function of the angle, θ_{hkl}.

An ideal powder sample comprises many small ($\sim$1 μm across) randomly oriented crystallites. For any set of planes, (hkl), with spacing d_{hkl}, there are many crystallites oriented such that their (hkl) planes make the Bragg angle, θ_{hkl}, with the incident beam. Since these crystallites have all orientations about the incident beam, the diffracted intensity forms a cone with half-angle $2\theta_{hkl}$ about the incident beam. For each set of (hkl)-planes there is a cone with half-angle $2\theta_{hkl}$. When these diffraction cones are intercepted by a flat area detector—such as film or an image-plate—perpendicular to the incident beam, a pattern of smooth, sharp, concentric powder rings is recorded.

If the crystallites in the incident beam are large or limited in number, the powder rings will no longer be smooth. Some parts of the powder rings will have little intensity; other parts might have strong intensity if there is a large crystallite oriented such that it causes diffraction to that part of the ring. When this happens the data set is said to have 'poor powder averaging'. If the crystallites are very much smaller than 1 μm the diffraction peaks, or reflections, will be diffraction broadened. It is possible for the crystallites to be much smaller in a particular crystallographic direction causing (hkl)-dependent broadening. In an ideal powder there is an equal proportion of crystallites contributing to every reflection. But, if the powder has preferred orientation, the number of crystallites contributing to each reflection will be different, affecting the relative intensities of the reflections.

In high-pressure powder diffraction, the crystallites should, ideally, be under isotropic stress. However, in practice, there is often a stress gradient over the sample. Stress causes strain in the crystallites which displaces the diffraction peaks. When the beam intercepts crystallites with a range of strains the resulting diffraction pattern is broadened. The sample may have anisotropic elastic properties causing anisotropic strain even if the sample is under isotropic stress. The leads to (hkl)-dependent peak displacements. Another source of strain comes from defects in the crystal lattice such as stacking faults. These, too, cause (hkl)-dependent peak displacements.

All deviations from an ideal powder need to be taken into account if structures are to be determined accurately by powder diffraction techniques. This is especially true for high-pressure powder diffraction because the effects outlined above can be extremely pronounced.

2.3 Solving Structures at High Pressure: Criteria for Accurate Structure Determination

Before carrying out any experiment, it is important to establish the criteria necessary for successful completion of the experiment. The following factors are the most important for structure determination of powders samples at high pressure.

(a) As much of the diffraction pattern should be collected as possible.

(b) The diffraction pattern should be as free from contamination as possible and the background should be low and smoothly varying.

(c) The powder should comprise small randomly oriented crystallites such that the Bragg peaks are sharp and free from preferred orientation for reliable intensities. The stress on the powder should also be uniform, if possible. But, as noted above, this is often not possible. In this case, deviations from an ideal powder should be modelled.

(d) Absorption by the sample and environment (such as the pressure cell and gasket) should be taken into account. Along with other experimental conditions affecting the diffracted intensity such as incident beam polarisation.

With these criteria in mind, the techniques for high-pressure powder diffraction using an image-plate detector will be discussed in the rest of this chapter.

2.4 Experimental Set-up and Procedures: Data Collection

This section describes the equipment developed by members of the Condensed Matter Physics Group of The University of Edinburgh at SRS Daresbury for the collection of image-plate data for structural studies of materials at high pressure.

Firstly, the various types of diamond-anvil pressure cells used by the group are described, along with a description of sample loading procedures, pressure transmitting media and methods for pressure measurement. The image-plate set-up on Station 9.1 is presented and a description of the sample alignment procedure is given. Finally, a description of the image-plate detector system is given, including a description of how the image-plate works and is read. Section 2.5 presents details of the data analysis procedures used to process the data after they have been collected.

2.4.1 Pressure Cells and Pressure Cell Techniques

The diamond-anvil cell (DAC) was first conceived in 1959 by two independent groups. Jamieson *et al.* (1959) used a DAC for a high-pressure x-ray powder diffraction study, while Weir *et al.* (1959) used a DAC for infrared absorption measurements. Since 1959, the DAC has been developed for powder (Piermarini and Weir (1962)) and single-crystal x-ray diffraction (Block *et al.* (1965), Weir *et al.* (1965)). The introduction of the metal gasket technique (Van Valkenburg (1965)) and pressure transmitting media (Piermarini *et al.* (1973)) increased high-pressure limit and the range over which the sample was under hydrostatic pressure (i.e. uniform stress). These developments turned the DAC into an excellent tool for quantitative high-pressure studies.

The principle behind the DAC is very simple. The sample is contained in a hole drilled in a metal gasket that is situated between two flat parallel diamond faces (or culets). The pressure is then applied when a force pushes the two diamonds together. Although there are many different types of DAC, the schematic diagram shown in Figure 2.1 shows the main components of all types of cell. The main differences between the types are the mechanism by which the pressure generating force is applied to the diamonds, and the method by which the diamond culets are aligned and supported. Jayaraman (1983) describes many of types of DAC available, as well as presenting many results in high-pressure studies.

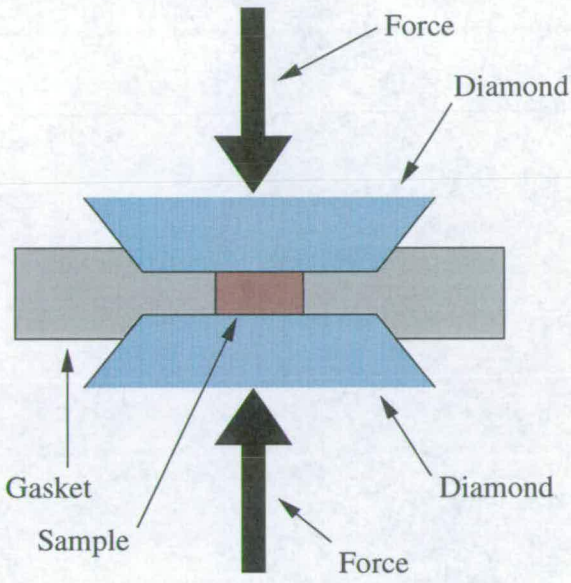


Figure 2.1. The main components of a diamond-anvil cell.

Three types of full conical-aperture diamond-anvil cells have been used to carry out the experiments used to collect data for this thesis: Merrill-Bassett pressure cells (Merrill and Bassett, (1974)), a cell designed by Mao and Bell (1980), and the DXR series of pressure cells designed by Adams (1992).

The Merrill-Bassett (M-B) cells were originally developed for single-crystal work, but their compact design and wide angular access for x-rays makes them useful for angle-dispersive powder diffraction at a synchrotron source. Figure 2.2 shows an exploded view of the M-B DAC taken from Merrill and Bassett (1974). The diamond anvils are mounted on beryllium backing discs. The backing discs need to be strong, and transparent to x-rays if the diffracted beams are to exit the cell. Beryllium satisfies both these criteria. However there are disadvantages when using beryllium, these being that beryllium is hard to machine and the oxide of beryllium is highly toxic. The Be discs have a 0.8 mm diameter hole drilled through them to enable optical alignment of the cell by viewing the sample through the diamond. The backing discs are encased in a steel body and pressure is applied by tightening the three Allen screws to drive the two halves of the cell together. The two halves of the cell are kept in alignment by three guide pins.

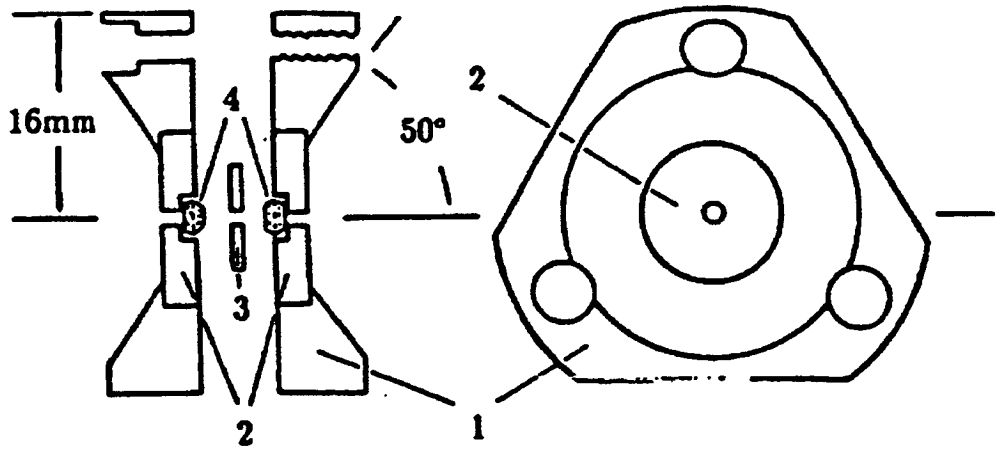


Figure 2.2. Schematic diagram of a Merrill-Bassett diamond-anvil pressure cell. (1) Steel body. (2) Beryllium discs. (3) Gasket. (4) Diamond anvils. (After Merrill and Bassett (1974).)

The M-B cells have the capability for aligning the diamond culets translationally but there is no way to adjust the culets so that they are parallel. One of the Be discs is held in place by three grub screws; using these screws it is possible to translate one of the diamonds with respect to the other.

Figure 2.3 shows an exploded view of the cell design by Mao and Bell (1980). It is basically an enlarged version of a Merrill-Bassett cell and was originally designed for the cryogenic loading of gases. The two halves of the cell are circular and one half is guided down over the other by four guide pins. The pressure is applied by tightening two pairs of left- and right-handed Allen screws. The use of oppositely threaded screws helps to keep the diamonds well aligned during the application of pressure, which increases the upper pressure limit. As with the M-B cell, one of the diamonds can be translated by using three grub screws; there is no provision for parallel alignment of the diamond culets.

The DXR cells designed by Adams (1992) employ a piston-cylinder arrangement. Figure 2.4 shows a DXR-4 cell. Again the diamonds are mounted on beryllium

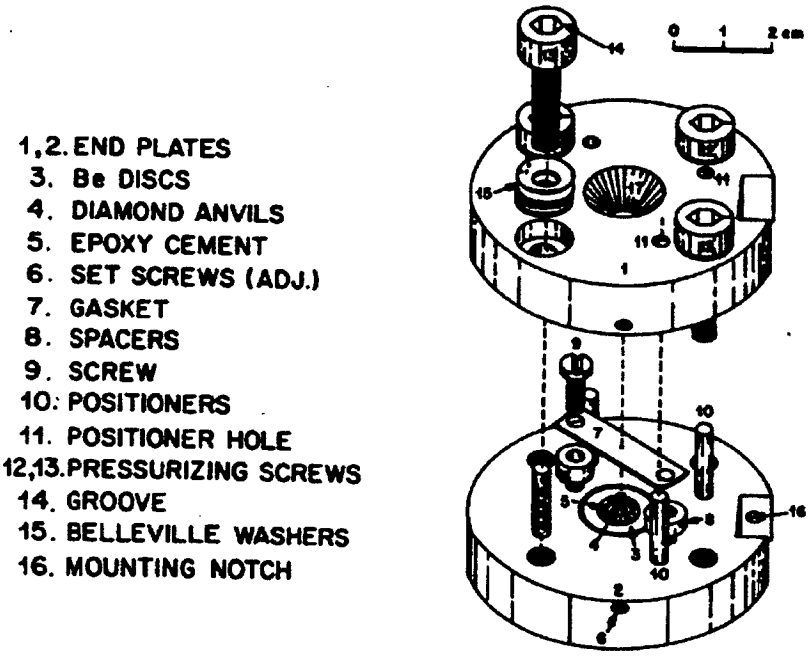


Figure 2.3. An exploded view of the DAC of Mao and Bell (1980). (From Jayaraman (1983).)

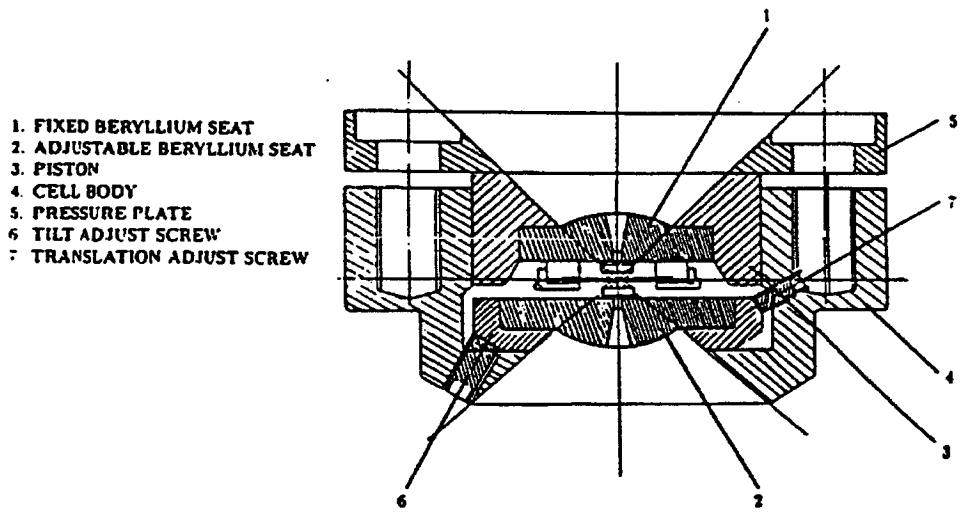


Figure 2.4. A diagram of a DXR-4 DAC. (Adams (1992)).

discs. One disc is seated in the piston and the other in the cell body. The piston and body are precisely machined from high-quality steel such that the piston fits tightly in the body. The tight fit of the piston means that the diamonds remain well aligned while pressure is applied. The pressure is applied by two oppositely threaded screws which push a steel plate down onto the piston which, in turn, pushes the piston into the cell bringing the diamonds together. It is possible to adjust the centring and tilt of the diamond culets in the DXR cells. The DXR-4 has both adjustments on the same diamond, but later versions (DXR-5 and DXR-6) have translational and tilt adjustments on different diamonds, which allows the diamonds to be aligned much more easily and with greater accuracy.

The maximum pressure attainable by these cells depends on many factors. The main factor is the diameter of the diamond culets; for a given force, the pressure applied to the sample is greater the smaller the culet size. A range of culets sizes have been used in the cells described above: 600 μm, 400 μm, 300 μm, and 200 μm in diameter. Other factors affecting maximum pressure are the robustness of the cell body in which the Be discs are contained and the opening angle of the conical apertures in the cell body. The basic principles are that higher pressures can be reached using a tougher body and a smaller opening angle.

The M-B is the smallest cell and has the widest opening angle in the cell housing of all the cell, having a 45° half-angle cone opening allowing up to 45° 2θ of diffraction to leave to cell. The Mao-Bell cell and DXR cells have an opening angle of 40°. The M-B cells with 600 μm culets diamonds are limited to a top pressure of ~15–18 GPa, but with 400 μm culet diamonds pressures of ~25 GPa can be reached. Although the pressure range of these cells is modest, they are useful because they allow finer control over changes in sample pressure than the other cells. The Mao-Bell cell with 400 μm diamonds can reach ~35 GPa. This increase in top pressure, over an M-B cell with the same size of diamonds, is mainly due to a stronger cell body and more stable diamond alignment during changes in pressure. 300 μm and 200 μm culet diamonds are usually used in the

DXR cells. The maximum pressure of the DXR-4 cell is lower than the more advanced DXR-5 and DXR-6 cells. With 300 μm diamonds, the top pressure of a DXR-4 cell is $\sim$40 GPa. The DXR-5's performance is very similar to the DXR-6's. These cells will routinely reach a top pressure of $\sim$50 GPa with 300 μm diamonds and $\sim$80 GPa with 200 μm diamonds. Recently, a pattern of Ge in a DXR-5 at 90 GPa has been collected and the data has been used in structure refinement. This is a remarkable achievement considering that it was generally believed, initially, that it would be impossible to take Be-backed cells above $\sim$20 GPa.

The first stage when loading a pressure cell is preparing the gasket. Many different types of metal are used as gasket material. Inconel is a popular material, which is a 72:16:8 alloy of Ni:Cr:Fe; and various types of steel are often used as gasket material. Spain and Dunstan (1989) go into great detail about gasketing techniques as well as other DAC techniques. 250 μm thick foil tungsten is used as a gasket material in all the experiments presented in this thesis because it is hard (which helps to contain samples at high pressures) and its high absorption helps to shield any extraneous scattering that may occur between the x-ray source and the cell. The tungsten foil is placed between the diamond culets of the pressure cell by lightly holding it in position on one of the diamonds, by using Blu-Tack to fix the gasket to the cell body, while the cell is closed. Pressure is applied to the gasket, which draws the diamonds together to create an indent in the tungsten. The foil is then removed from the cell and a hole, typically 50–150 μm in diameter, is spark-eroded in the centre of the indent. Indenting the gasket work-hardens it, and spark-erosion tends to anneal the edge of the hole, which stops cracks forming which can cause the gasket hole to fail at high pressure.

The gasket is replaced on the first diamond and, using a fine needle, the hole is filled with the sample. The cell is closed and the diamonds are lightly pressed together by hand to pack the sample into the hole and to clean up any residual powder around the edge of the hole, which sticks to the second diamond. The cell

is opened up and the residual sample on the second diamond is cleaned off using methanol. At this point, the sample is normally run to collect an ambient pressure powder pattern which is then used to calibrate all subsequent data collected using that cell. (Section 2.5.2 gives details of the calibration procedure.) After the ambient pressure calibration run, if any, the cell is opened up again and the second diamond face is covered in a thin film of Vaseline and a single-crystal ruby sphere ($\sim$10 μm in diameter) is placed in the centre of the diamond culet for pressure measurement purposes (detailed in Section 2.4.2). The indent in the gasket is then filled with a 4:1 mixture of methanol:ethanol as the pressure transmitting medium. The cell is quickly closed and pressure applied immediately, before the methanol:ethanol evaporates. The pressure transmitting medium is included to try to ensure hydrostatic conditions in the sample. The hydrostatic limits of several organic pressure transmitting media were determined by Piermarini *et al.* (1973). A methanol:ethanol 4:1 mixture freezes at 10.4 GPa but is soft enough for quasi-hydrostatic conditions to prevail until $\sim$20 GPa. Above 20 GPa, conditions in the sample become steadily less hydrostatic. Several condensed gases have been investigated (e.g. He) as pressure transmitting media (Mao *et al.* (1982), Liebenberg (1979)) but these have the disadvantage of requiring special loading apparatus and techniques.

2.4.2 Pressure Measurement

The direct determination of pressure requires the measurement of force over area but this is not possible above $\sim$2 GPa because of the problems of estimating accurately frictional and other forces that need to be taken into account in devices capable of reaching higher pressures. A common method of pressure calibration is the use of a reference material whose equation of state is well known—the equation of state of NaCl, for example, has been calculated from first principles by Decker *et al.* (1972). The reference material is mixed with the sample and, from the shift of the diffraction peaks with pressure, the unit cell volume of

the reference material can be calculated and converted into pressure using the equation of state. The disadvantage of this method is that the powder diffraction pattern of the sample is contaminated by the powder pattern of the reference material. This can reduce the accuracy of any subsequent Rietveld refinement fit to the sample's profile.

The ruby fluorescence method for measuring pressure was introduced by in 1972 by Forman *et al.* (1972). This method causes very little contamination of the diffraction pattern—occasionally the single crystal of ruby may be oriented such that it diffracts but even in this case the contamination is limited to a small spot of intensity. When the light from a He-Cd laser is focused on a chip of ruby (Cr^{3+}-doped Al_2O_3), the R lines of the ruby (ruby lines) fluoresce. The ruby lines are quite intense, and the doublet R_1 and R_2 have wavelengths of 6927 Å and 6942 Å, respectively, at ambient pressure. Forman *et al.* (1972) showed that the R lines shift linearly with pressure over the range of 0.1–2.2 GPa by using the well-known freezing points and phase transitions of several materials as fixed points. In 1975, Piermarini and Block (1975) linked the shift of the ruby lines to the equation of state of NaCl and showed the shift to be linear up to 29 GPa. Pressure could be calculated from the equation $P = A(\Delta\lambda)$, where P is the pressure in GPa, $\Delta\lambda$ is the shift in wavelength of the R_2 line from its ambient pressure value of 6942 Å and the constant of proportionallity, A, is given as 0.2740 GPa.Å^{-1}. Mao *et al.* (1978) observed a slight non-linearity in the shift of the ruby line which becomes noticeable above 30 GPa. They proposed:

$$P = 380.8[(\Delta\lambda/694.2 + 1)^5 - 1] \tag{2.2}$$

where P is in GPa and $\Delta\lambda$ is the shift in nanometers of the R_2 line from its ambient pressure value. Figure 2.5 shows a comparison of the linear ruby calibration scale of Piermarini and Block (1975) (dashed line) and the Mao *et al.* (1978) scale (solid line), with the scale used at Daresbury shown with squares.

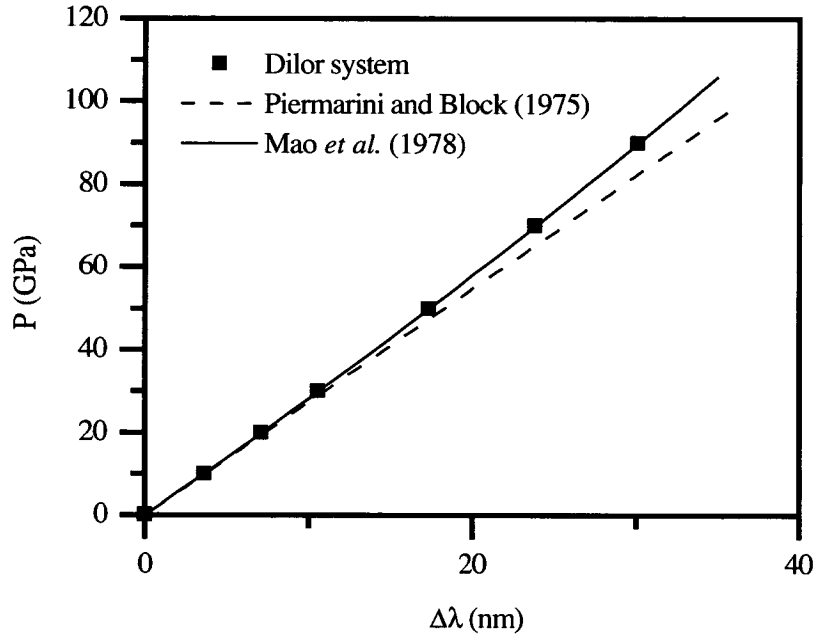


Figure 2.5. The ruby calibration scales of Piermarini and Block (1975) (dashed line), Dilor software at Daresbury (squares) and Mao *et al.* (1978) (solid line).

The ruby fluorescence set-up at Daresbury is manufactured by Dilor and comprises a He-Cd laser, to excite the ruby fluorescence, and a spectrometer to measure the wavelength of the fluorescence. The laser light travels through a fibre optic cable and is focused onto the sample containing a ruby sphere, by using a microscope with a camera attachment to view the sample and laser spot. The fluorescence travels back down the same path as the laser light until it is deflected by a beam-splitter into the spectrometer. A grating in the spectrometer disperses the fluorescence onto a light-sensitive diode array, and the collected spectrum is displayed on a PC where the wavelength of the R_2 line is measured. The wavelength is converted to pressure using equation 2.2 above.

2.4.3 Image-Plate Set-up on Station 9.1

The implementation for the image-plate set-up for high-pressure powder diffraction on Station 9.1 at SRS Daresbury by the Edinburgh group follows closely the design of the Japanese image-plate set-up (Shimomura *et al.* (1992)). The

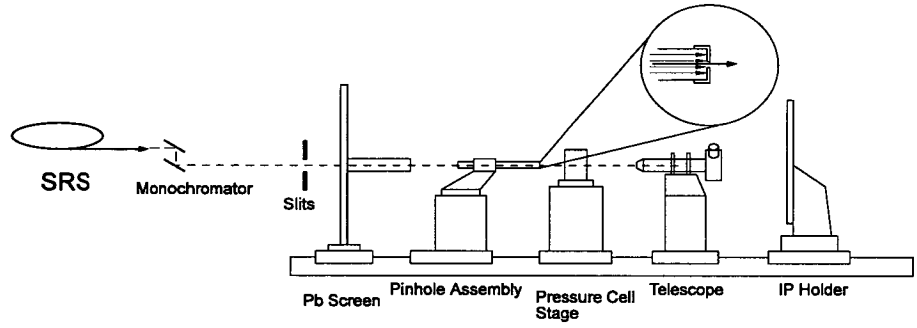


Figure 2.6. A schematic diagram of the beamline set-up on Station 9.1 at SRS Daresbury developed before the upgrades described in Chapter 3.

set-up was substantially developed by using full-conical aperture DACs and full image-plate data integration software (Piltz *et al.* (1992)).

Figure 2.6 shows a schematic diagram of beamline set-up on Station 9.1 at SRS Daresbury as implemented prior to the upgrades detailed in Chapter 3. Station 9.1 is situated approximately 15 m from a 5 T superconducting 'wiggler' magnet. The Si(111) double-bounce channel-cut monochromator selects the wavelength of the incident x-rays; there is a small but significant amount of $\frac{\lambda}{3}$ diffraction from the (333) planes of the monochromator. The x-ray beam passes through a pair of tungsten carbide slits which reduce the beam dimensions to 0.5×0.5 mm^2. The beam is enclosed in lead shielding until it is collimated to a circular beam of 50–100 μm diameter by a platinum pinhole. Platinum is used because of its absorption properties. For wavelengths shorter than 0.4745 Å, the platinum K absorption edge at 0.1582 Å provides enhanced attenuation of the $\frac{\lambda}{3}$ component of the incident beam. At longer wavelengths, the $\frac{\lambda}{3}$ component of the beam would pass through the platinum without being collimated and strike the gasket; the tungsten gasket scatters strongly enough for the image to be contaminated significantly by a $\frac{\lambda}{3}$ tungsten powder pattern.

A key part of the set-up is the alignment laser. It has be shown by Allan (1993) that it is essential to align the pressure cells and microscope parallel to the x-ray beam for accurate sample alignment (see Section 2.4.4); the laser is used to align these components parallel to the beam. The laser is aligned coincident with the x-ray beam before the pinhole assembly has been placed on the optical bench. Two pieces of x-ray sensitive paper are used to align the laser: one piece is held in place over the end of the tube on the lead shielding, and the other is positioned close to the laser. The pieces of paper are then exposed to the x-ray beam, which leaves a black mark on the paper. A hole is carefully pierced through the mark on the paper closest to the laser using a fine needle. This allows the laser beam to pass through the paper when it is aligned to the hole. The laser alignment is adjusted such that the laser beam passes through the hole and is centred on the mark on the paper attached to the lead shielding. Once this is achieved, the laser beam is coincident with the x-ray beam.

After the laser has been aligned, the pinhole assembly is clamped to the optical bench. The pinhole assembly is motorised so it can be moved vertically and horizontally across the beam under remote control. At the beginning of a run, the beam intensity is optimised by scanning the pinhole across the beam and maximising the signal from an ion chamber placed in the microscope position (see Fig. 2.6) to collect the collimated beam. After the intensity of the beam has been optimised, the ion chamber is removed, and the rest of the experimental equipment is installed on the beamline. Next, the alignment microscope is aligned so that its optical axis is parallel to the x-ray beam. The eyepiece and objective lenses are removed and a mirror attachment is screwed into the objective end of the microscope body. The microscope is adjusted until the laser spot, reflected from the mirror, coincides with the exit aperture of the laser; the optical axis of the microscope is now parallel to the x-ray beam. The mirror attachment is then removed and the objective and eyepiece lenses are re-attached. At this point, the set-up is ready to use.

2.4.4 Sample Alignment

This section describes the techniques for accurately aligning a pressure cell to the x-ray beam. Typical samples sizes are around 50–150 μm in diameter. Since the beam is normally 50–100 μm in diameter, sample alignment has to be very accurate if the gasket is not to be illuminated by the incident beam causing contamination of the powder pattern. The alignment techniques are based on the optical alignment method originally devised by the Japanese group at the Photon Factory (Shimomura *et al.* (1992)). However, the Japanese group tolerated contamination of the pattern by scattering from the gasket, so the techniques were developed considerably by the Edinburgh group to allow samples to be aligned routinely to the incident beam without the beam illuminating the gasket.

Allan (1993) showed that the main source of error in sample alignment was related to the high refractive index of diamond. If the optical axis of the microscope is not parallel to the incident beam and the back face of the diamond through which the sample is viewed is not perpendicular to the optical axis of the microscope, then the apparent position of the sample is significantly shifted from its actual position. The alignment of the microscope is described in Section 2.4.3 above. The pressure cell is aligned by 'shimming' the pressure cell holder until the back face of the diamond through which the sample is viewed reflects the alignment laser beam back on itself, in a similar way to the microscope alignment. The shimming procedure consists of adding suitably sized pieces of masking tape to the edges of the base of the pressure cell holder, thus changing the orientation of the holder when it is located on the sample stage, until the reflected laser beam is coincident with the incident laser beam. Each pressure cell has its own customised mount so the shimming procedure need only be carried out once for each cell at the beginning of the experimental run.

The sample is aligned to the x-ray beam as follows. The pressure cell is placed on the sample mount and the microscope is focused on the sample through the diamond. The cell is removed and replaced with a mount for a piece of x-ray

sensitive paper. The position of the paper along the incident beam direction is adjusted by a micrometer on the paper mount until the surface of the paper is in focus when viewed with the microscope. The paper is then exposed to the x-ray beam for approximately one minute, which leaves a small mark about the size of the beam on the paper. The microscope is moved vertically and horizontally perpendicular to the beam direction until the microscope's crosshair is aligned to the centre of the mark. The paper holder is replaced by the pressure cell on the sample stage and the sample stage is moved until the centre of sample coincides with the crosshair. A typical alignment takes 6–10 minutes, and centres the sample to within ± 1 μm from the centre of the beam. This allows a sample 100 μm across to be centred on a beam 75 μm in diameter without the beam striking the gasket. The telescope is removed during exposure.

2.4.5 Image-Plate Detector

The image-plate detector overcame the limitation of small sample sizes in high-pressure powder diffraction by enabling enough signal to be captured for accurate structural studies to be possible with a monochromatic beam. The image-plate (IP) has many properties which make it a particularly suitable detector for diamond-anvil cell work. The active component of the IP is the phosphor material BaFBr:Eu^{2+}, which is protected by a layer of plastic and is bonded to a flat aluminium plate. The image-plates normally used to carry out the experiments detailed in this thesis have dimensions of 20 cm $\times$ 25 cm (so-called A4 plates), but 35 cm $\times$ 43 cm (A3) plates can also be used. The x-ray photons incident on the phosphor create excited electron states, which emit visible light when stimulated by a He-Ne laser. The IP is highly sensitive to the short wavelengths (< 0.7 Å) necessary to penetrate pressure cells; at this wavelength, the image-plates can detect less than 10 photons per pixel (approximately 0.1 x 0.1 mm^2). Image-plates have a large dynamic range of $\sim 10^5$, which is about three orders of magnitude greater than film, and the low intrinsic noise of the IP is about 300

times smaller than the chemical fog of film. Also, the easy digital readout makes sophisticated data analysis possible.

During exposure, the IP is enclosed in a light-tight cassette on a holder approximately 300 mm from the sample. At this distance, an A4 plate on the set-up on Station 9.1 at SRS can capture up to 30° 2θ of diffraction. The cassette has a lead beamstop that absorbs the intense λ component of the incident beam that passes through the sample. The beamstop is partially transparent to the much weaker but higher energy $\frac{\lambda}{3}$ component of the beam, which allows the centre of the powder pattern to be marked by a beam spot. This beam spot is useful for subsequent data analysis (see Section 2.5.1). After the exposure, the IP is taken out of its cassette and quickly inserted into a carriage in a Molecular Dynamics 400A Phosphor Imager, which reads the plate. A He-Ne laser is rastered across the IP while a wire attached to a stepper motor pulls the IP in its carriage perpendicular to the laser raster direction. The photoluminescence is captured by a fibre-optic light guide which collects the light onto a photomultiplier tube where the intensity is converted into a voltage and then a digital signal. The size of a full image from an A4 plate is 2816 × 2052 pixels; the pixel dimensions are approximately 88 μm × 87 μm. The size of the resulting computer file is approximately 11 Mbytes.

During the read process, intensity and spatial distortions are introduced into the data. These distortions have to be calibrated before any subsequent data analysis. The intensity distortions come from two sources: the non-uniform sensitivity of the reader optics along the laser raster direction, and the non-linear intensity response of the reader (i.e. the recorded intensity does not vary linearly with incident intensity). The non-uniform sensitivity is calibrated by exposing a strip of the IP (along the laser raster direction) to uniform incident intensity provided by C^{14}-doped polythene strip. The IP is read in the normal manner and the data are integrated along the exposed strip in the direction perpendicular to the laser scan direction to produce a graph of intensity variation across the strip in the

laser raster direction. This graph is used to normalise IP data read subsequently. The non-linear intensity response is calibrated by exposing the IP to varying, but known, amounts of radiation. This allows the measured intensities to be calibrated. Both these intensity distortions are calibrated periodically by Molecular Dynamics engineers.

The other type of distortion introduced by the reader is spatial distortion. The distortion in the laser raster direction arises from the read method. The fixed laser is rastered across the plate by a motorised mirror mechanism that reflects the laser beam onto the IP. Because the origin of the reflected laser beam is fixed and the IP is flat the distance the beam has to travel from source to plate varies as the beam is rastered across the plate—the distance is greater when the beam is at the end of its raster than in the middle. This causes a change in the laser spot size as the beam is rastered across the plate. Also, the constant angular velocity of the mirror maps to a variable linear velocity of the beam across the plate. Both these effects cause the real size and separation of the pixels to vary across the plate. The spatial distortion in the direction perpendicular to the raster direction arises from the uneven step of the wire pulley mechanism that draws the IP over the laser. The distortion in the laser raster direction is largely reproducible. In the direction perpendicular to the laser raster, the distortion is smaller but much less reproducible (Svensson *et al.* (1993)).

No position information is stored in the image file from the reader, only the intensity of each pixel is recorded. And since the spacing between the pixels is non-uniform, the pixel positions need to be calibrated. This is carried out by placing a grid of holes in a nickel sheet over the IP and exposing the grid to a source of parallel x-rays that cover an area at least as large as the IP (Stanton *et al.* (1992)). The holes in the nickel have an accurately known spacing (2 mm) and diameter (200 μm). As long as the energy of the incident x-ray beam is not too high, the x-ray beam will be absorbed by the nickel and pass through the holes leaving and image of uniformly spaced spots on the plate. The IP is read

and, because of the spatial distortion, the grid spots are not uniformly spaced. The coordinates (measured in pixels) of the centre of each spot are measured by calculating the centre of mass of the spot. Since the actual spacing in mm between the measured pixel positions of the grid spots is known, a spline function can be fitted to the measured grid. Using this spline function, the distance, in mm from an arbitrary origin, of any pixel can be calculated. Since all subsequent data analysis only relies on knowing the distance between pixels in the image, it is not necessary to know absolute pixel position.

2.5 Experimental Set-up and Procedures: Data Analysis

Section 2.4 detailed the main techniques for collecting image-plate (IP) data for high-pressure powder diffraction, this section describes the techniques used to analyse the data once it has been collected. The program used to integrate the IP data into a 1-d intensity vs. pixel plot is described first. This is followed by a description of the method for converting the intensity vs. pixel plot into intensity vs. 2θ data which can be used in conventional Rietveld refinement packages. And finally, the various programs used to solve and refine structures from powder data are described.

2.5.1 2-d Powder Pattern Integration

This section describes the operation of the image-plate integration software, called 'Platypus' (Piltz *et al.* (1992)), which was specially written for the image-plate project. A prominent feature of 'Platypus' is its 'X Window System' based graphical-user-interface (GUI), which allows the raw image-plate (IP) data and integrated 1-d patterns to be displayed and manipulated easily. The GUI provides

a user-friendly and intuitive interface for image-plate processing. All the functions for integrating the IP data are accessible from pull-down menus. The main function of 'Platypus' is to produce a 1-d powder pattern from the 2-d image after applying corrections for spatial distortion, IP tilt and incident beam polarisation.

The first step in this process is the determination of the IP tilt. Generally, the IP is not perpendicular to the incident beam. This results in the circular Debye-Scherrer rings being recorded as ellipses on the IP. If no correction for tilt is applied, the diffraction peaks in the integrated pattern will be broad or even split. The method for tilt correction is as follows. Firstly, the image is 'sectored' into 60 azimuthal sectors about the centre of the pattern. The centre of the pattern is usually obtained by fitting the incident beam spot. If there is no beam spot or the centre of the pattern is not on the plate, the pattern centre can be refined, along with the plate tilt. The sectoring effectively produces 60 1-d powder patterns. However, if the IP is not perpendicular to the incident beam, the peaks in the 60 powder patterns will not all line-up. A routine called 'sharpen' adjusts the tilt parameters (and centre parameters, if required), which changes the effective radial position of the data points in each sector, until the all the sectors line-up.

The whole image is then 'rebinned', using the calculated tilt values (and fitted or refined centre values), into the final 1-d pattern. For each pixel in the image an effective radius from the centre of the pattern is calculated—taking into account plate tilts and spatial distortion—and the intensity of the pixel is added to the appropriate bin. Normally the pixel will overlap two bins so the intensity is partitioned and assigned to the appropriate bin. For example, the intensity (I) of a pixel at radius r that lies between the radial bins r_1 and r_2 such that $r_1 < r < r_2$ is partitioned thus: $(r - r_1) \times I$ is added to r_1 and $(1 - (r - r_1)) \times I$ is added to r_2. An array of corrections to the intensity (for taking into account incident beam polarisation) is also collated and the array of rebinned intensity is divided by the array of rebinned corrections at the end of the rebin procedure. To increase the

speed of the processing, full calculations of pixel radius and intensity correction are carried out on every 16th pixel and the radius and intensity corrections of the intervening pixels are calculate by quadratic interpolation between the values of every 16th pixel.

2.5.2 Data Calibration

The 1-d profile output from Platypus is in the form of intensity vs. radius, in pixels, from the centre of the pattern. Before any subsequent data analysis can be carried out, the data need to be converted to the conventional intensity vs. 2θ format. For each pressure cell, the powder pattern from a sample with known lattice parameters is used to calibrate the data obtained from that pressure cell. The calibrant sample should have a relatively simple powder pattern with well separated diffraction peaks out to 25°–30° 2θ. Usually, the ambient-pressure pattern of the material being studied is used to calibrate the data collected during the rest of the experiment.

From the known lattice parameters of the calibrant and the known wavelength, the 2θ values of the observed diffraction peaks can be calculated. A polynomial function is fitted to the measured pixel positions of the observed reflections and this function is used to convert pixels to 2θ. From basic geometry, it would be expected that the fitting function should be linear in $\tan\theta$ from the equation: $p = D\tan\theta$, where p is the radius in pixels and D is the sample-to-plate distance, but the spatial-distortion and plate-tilt corrections in Platypus cause slight but critical deviations from this form.

Most Rietveld refinement programs require that the data are equally spaced in 2θ, but simply converting from pixels to 2θ using a polynomial function produces unequal 2θ steps. The final step of the data conversion is the interpolation of the powder pattern into equally spaced 2θ steps. Prior to the work presented in this thesis, all of the steps outlined above were carried out separately on

two different computers. A single program has been written by the author that gathers together all these steps and produces output suitable for a variety of Rietveld packages.

2.5.3 Structure Solution and Refinement

The first stage of structure solution is the determination of the unit cell. This procedure consists of finding a unit cell and indexing (i.e. (hkl) values) that predicts the observed 2θ of all the diffraction peaks in the pattern. This can sometimes be achieved by picking a unit cell that is related in some way to the unit cell of a known adjacent phase or phases. Indexing programs such as DICVOL (Boultif and Louer (1991)) or TREOR (Werner *et al.* (1985)) are also used. These programs find possible unit cells and indexings by a computational trial-and-error method. Such programs require a list of accurately measured 2θ values of as many diffraction peaks in the powder pattern as possible. Indexing programs are very sensitive to inaccuracies in measured 2θ; if one or more of the measured peak positions deviates from the correct 2θ value by as little as $0.05°$, the indexing programs will fail to find the correct solution. And in high pressure patterns, the peaks are often broad or overlapped making indexing by these programs precarious. After a unit cell has been found, an inspection of the indexing is carried out to find any systematic absences that can narrow down the possible space groups.

The next stage of structure solution is to find approximate atomic coordinates that can be used as starting values for structural refinement. This is achieved by trial-and-error or by inferring an approximate structure from correlations in the relative intensities of different reflections. Once an approximate trial structure has been found, the least-squares method of Rietveld (1969) is used to refine the exact atomic structure. Rietveld introduced a method for whole-pattern fitting for use in neutron powder-diffraction studies. This method has been extended to x-ray powder diffraction as well (Young *et al.* (1977)).

The Rietveld method can be summarised as follows. A powder pattern is calculated from a model based on the trial structural parameters (lattice parameters and atomic coordinates), parameters defining peak shape and other experimental parameters, such as the effects of incident beam polarisation, background, preferred orientation etc. The parameters are adjusted (refined) using a least-squares method until the difference between the calculated pattern and the observed pattern is minimised. The least-squares method is a general method for obtaining the best-fit parameters of a model to a set of data. A modelling function is defined that is a function of one independent variable (either 2θ or d-spacing in Rietveld refinement) and many dependent variables (the refineable parameters of the model). The function used in Rietveld refinement calculates the intensity of a point at a given value of 2θ or d-spacing from the parameters of the model—some typical parameters are listed above. The least-squares method attempts to find a set of parameters that minimises the equation:

$$\chi^2 = \sum_i w_i (y_i - y_{ci})^2 \tag{2.3}$$

where y_i is the observed intensity at point i and y_{ci} is the calculated intensity. w_i is a statistical weight often set equal to $1/y_i$, which is valid if counting statistics hold. There are a variety of other numbers that can be calculated from χ^2 that are used to assess the quality of the fit, two of which are given below:

$$R_{wp} = \sqrt{\frac{\chi^2}{\sum_i w_i y_i^2}} \tag{2.4}$$

$$S = \sqrt{\frac{\chi^2}{(N-P)}} \tag{2.5}$$

R_{wp} is the weighted residual and given a number that independent of the scaling of the input data. S is the goodness-of-fit and takes into account the number of data points (N) and the number of refined parameters (P) to give an idea of

how well the model describes the data and whether the number of parameters refined is justified by the input data. The ideal value for S is 1. If $S \gg 1$ then the model is not a good description of the data. If $S < 1$ then there are too many parameters being refined than are justified by the data. The least-squares function in Rietveld refinement is generally non-linear so the best-fit parameters have to be found by an iterative method whereby a trial set of parameters is tested at each iteration to try to minimise χ^2. The main problem with this method is that it is possible to find a set of parameters where χ^2 is locally minimised and not at its true global minimum, and it is not possible to tell whether χ^2 is in a local minimum or not.

The Rietveld method had been widely adopted and has proven to be very accurate. A distinct advantage is gained over other whole-pattern fitting techniques by refining structural parameters directly; other techniques refine integrated intensities without reference to a full structural model and use this information in separate single-crystal refinement programs. This limits the accuracy of these methods. But, as with all least-squares techniques, the starting values in Rietveld refinement need to be quite close to the correct values for the method to work. Also, the model needs to describe accurately the experimental conditions if any of the refined parameters are to be meaningful. A common problem for accurate high-pressure powder diffraction studies is that the model used in Rietveld refinement programs does not adequately describe the actual conditions prevalent in many powders at high pressure.

Chapter 3

Experimental Methods for 2-D Analysis

3.1 Introduction

The previous chapter described the experimental set-up and procedures that form the foundation of all the subsequent developments for 2-d data analysis. This chapter details the development of the experimental equipment and procedures for 2-d data analysis. The author implemented or was involved closely with all these developments. The key experimental technique in 2-d data analysis is the ability to incline the sample at different angles to the incident beam for investigating the orientational properties of sample microstructure. Thus, the main part of the equipment upgrade has been the installation of a high-precision rotation stage. The rotation stage set-up is described along with ancillary developments that were implemented to aid data collection for inclined samples. These developments include new cell holders, modifications to the alignment microscope, a new beamstop and shielding, and a new image-plate holder.

The procedure for aligning samples that are to be inclined is described, followed by a description of how the image-plate data is prepared for subsequent 2-d data

analysis (i.e. how information about intensity and position around the powder rings is extracted and details of the absorption correction for inclined samples is given).

3.2 Criteria for High Quality 2-D Data Collection

All of the criteria set out in Section 2.3 above apply to 2-d data collection. They are re-iterated here for completeness along with the other criteria applicable only to data collection for accurate 2-d analysis.

(a) The sample must be accurately aligned to a rotation axis if it is to be inclined without the beam hitting the gasket surrounding the sample. With the sample being $\sim$100 μm across and the typical beam diameter being 75 μm, strict requirements are necessary from the equipment, these requirements are detailed in Section 3.3.1.

(b) The background should be low and, more importantly, isotropic about the incident beam. Accurate analysis of intensity variations around the powder rings of on a 2-d could be adversely affected by the presence of a varying background around the beam.

(c) Ideally, the image-plate should be perpendicular to the incident beam. This criterion is not especially important for PO or texture studies since only intensity information is important for these studies, but it is very important when studying non-circular powder rings caused by sample microstructure. To decorrelate the effect of plate tilt from the effects of sample microstructure which cause non-circular powder rings requires accurate knowledge of the tilt of the image-plate to the incident beam. The best way to know the plate tilts is by accurately orienting the plate perpendicular to the incident beam.

(d) Absorption from the sample, cell and gasket must be taken into account and the data corrected accordingly. When a cell is inclined, the absorption as a function of azimuth about the beam is not uniform because the lengths through various parts of the cell and sample that the diffracted beam must pass depend on both the polar and azimuthal angles that the diffracted beam makes with the incident beam. This causes variations of intensity around the powder rings that are independent of the sample.

(e) Synchrotron radiation is naturally highly plane polarised. The polarisation causes intensity variation round the powder rings so a correction must be applied to the data to model these variations.

(f) The intensity and position of the IP data should be well calibrated. A good position calibration is very important when analysing non-circular rings. Distortions of the powder rings caused by poor spatial calibration of the IP data will adversely affect any analysis of non-circular rings.

With these criteria set out, the aim was to develop the experimental equipment and methods that would fulfil them.

3.3 Development of Experimental Set-up: Data Collection

Figure 3.1 shows a schematic diagram of the upgraded beamline equipment. All of the major features of the old set-up have been retained, so all of the procedures detailed in Chapter 2 are still applicable to the new set-up. The aim of the new set-up is to allow samples to be inclined as a routine part of the experiment. This not only means that inclined samples can be aligned without the beam hitting the gasket, but also that many samples can be inclined many times over the course of an experiment with minimum effort.

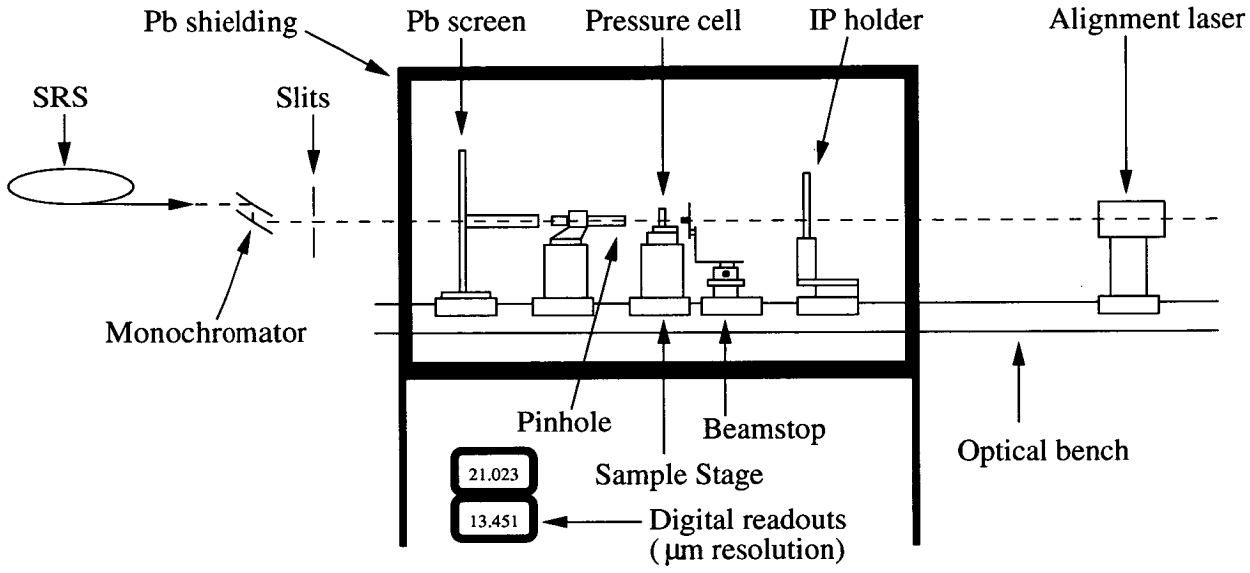


Figure 3.1. Schematic diagram of the upgraded beamline equipment.

Figure 3.2 shows a schematic diagram of (a) a non-inclined DAC and (b) a DAC inclined at 30° to the beam. The inset shows a close-up of the sample in the gasket between the two diamonds of the cell. In the non-inclined setting, the alignment tolerance is $\pm\frac{1}{2}(d_S - d_B)$, where d_S is the diameter of the sample and d_B is the diameter of the beam. However, when the sample is inclined, the opening through which the beam has to pass is foreshortened in the horizontal plane. By simple geometry (see Figure 3.3a), it can be shown that the maximum beam diameter, D, that can pass through a gasket hole of diameter d_S and thickness t inclined at ω degrees to the beam, if the beam is perfectly aligned with the centre of the sample, is given by

$$D = d_S \cos\omega - t \sin\omega \tag{3.1}$$

The tolerance is now given by $\pm r$, where $r = \frac{1}{2}(d_B - D)$. For example, inclining a typical sample (~100 μm diameter, ~20 μm thickness) by 30° gives a maximum beam diameter of ~77 μm. This gives a tolerance of $r = \pm 1$ μm when using the normal 75 μm beam. Samples can be aligned to a beam with an accuracy much greater than ± 1 μm but inclined samples must also be aligned to a rotation axis.

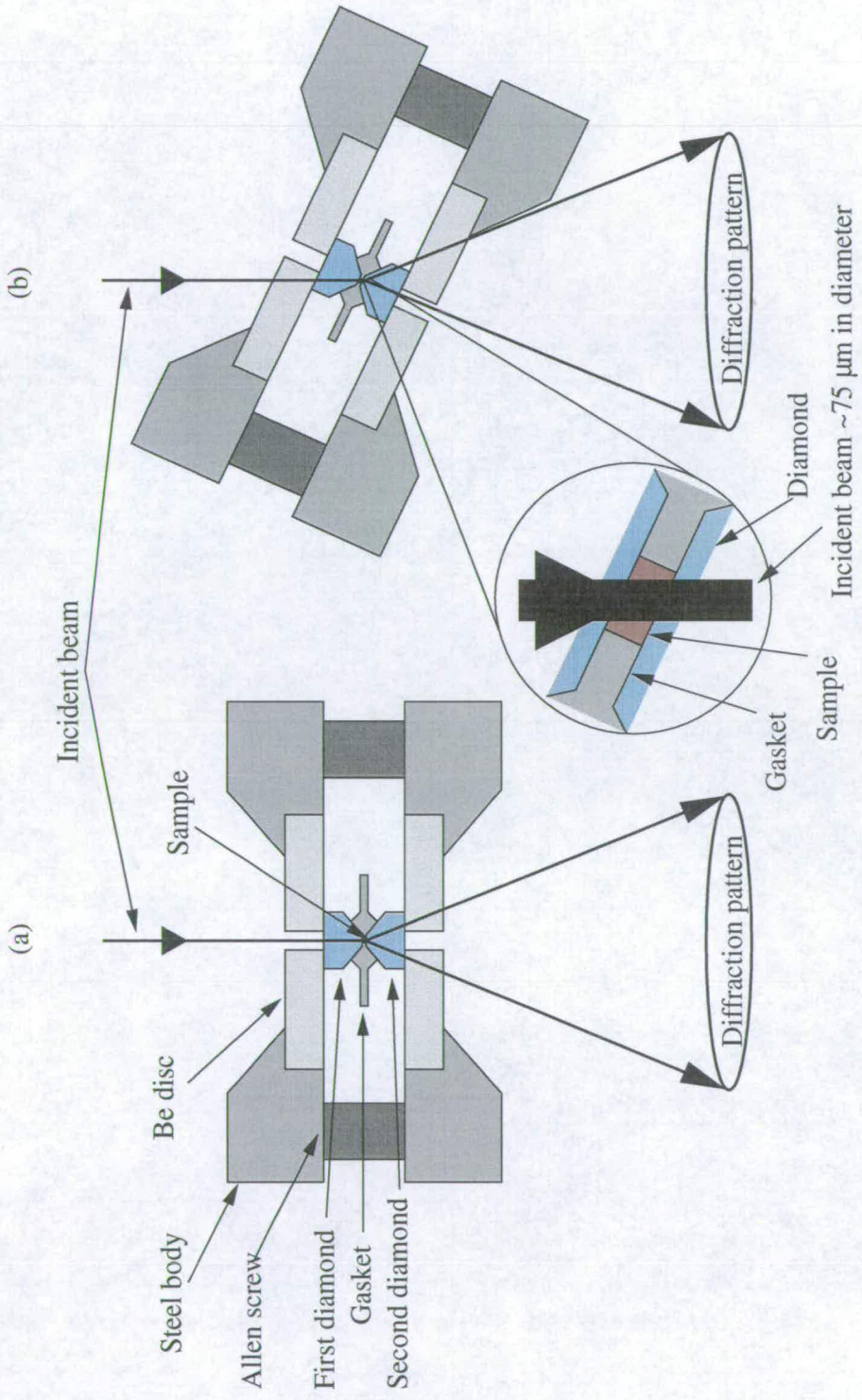


Figure 3.2. A schematic diagram of (a) a DAC in the normal setting, and (b) a DAC inclined to the beam with inset showing a close-up of the sample in the gasket. (Viewed from above.)

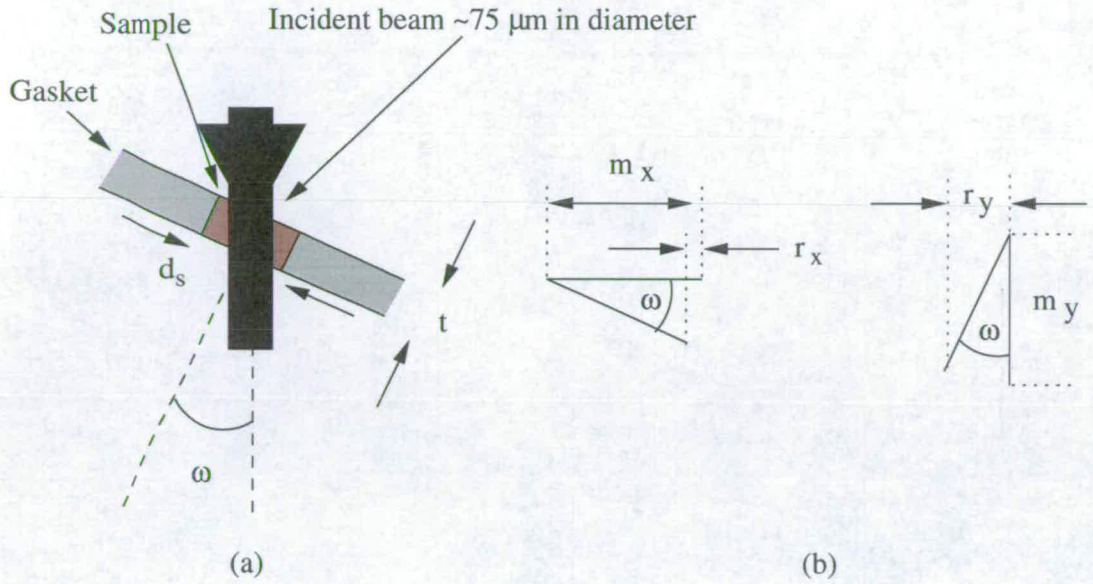


Figure 3.3. (a) Diagram illustrating the factors relevant to the alignment tolerance of aligning an inclined sample to the beam. (b) Diagrams illustrating the factors relevant to the alignment tolerances of aligning a sample to a rotation axis.

The sample centre will move in the horizontal plane when it is rotated if it is not aligned exactly with the rotation axis. The rotation axis alignment is most sensitive to misalignments in the incident beam direction and least sensitive to misalignments perpendicular to the beam direction. Figure 3.3b shows how the alignment tolerances from aligning a sample to a rotation axis are calculated. If the sample is misaligned by m_y along the beam and the sample is then inclined by ω to the incident beam, the sample will move r_y across the beam where r_y is given by:

$$r_y = m_y \cos(90 - \omega) \tag{3.2}$$

The equivalent equation for a sample that is misaligned perpendicular to the beam by m_x is:

$$r_x = m_x(1 - \cos\omega) \tag{3.3}$$

For example, the maximum misalignment along to beam that can be tolerate before the sample will move more that 1 μm across the beam when inclined at 30° to the beam is:

$$m_y = 1/\cos(90 - 30) = 2\mu\text{m} \tag{3.4}$$

The equivalent calculation for the across-beam misalignment gives:

$$m_y = 1/(1 - \cos 30) \sim 7.46\mu\text{m} \tag{3.5}$$

3.3.1 High-Precision Rotation Stage

Figure 3.4 shows the new sample stage which includes the high-precision rotation stage. There are basically three functions incorporated in the stage: the ability to position the rotation axis such that it intersects the incident x-ray beam; the ability to align samples onto the rotation axis; and the ability to incline samples. Working from the bottom up, the global z-stage comes first. Each cell, when mounted on the sample stage, is at a slightly different height than the other cells. The z-stage adjusts the height of the whole sample stage set-up to allow these height variations to be accommodated. It is essential that the direction of the z-stage motion is as parallel to the rotation axis as possible. If it is not parallel then, when the height is changed, the rotation axis will no longer intersect the beam. The z-stage motion has been measured to be parallel to the axis of rotation to within 1 part in 128, i.e. the rotation axis moves 1 μm across the beam for every 128 μm change in height. The pressure cell holders described in Section 3.3.2 have been designed to minimise the height variations between the cell so the maximum z-stage movement necessary to accommodate of the cells is $\sim$100μm.

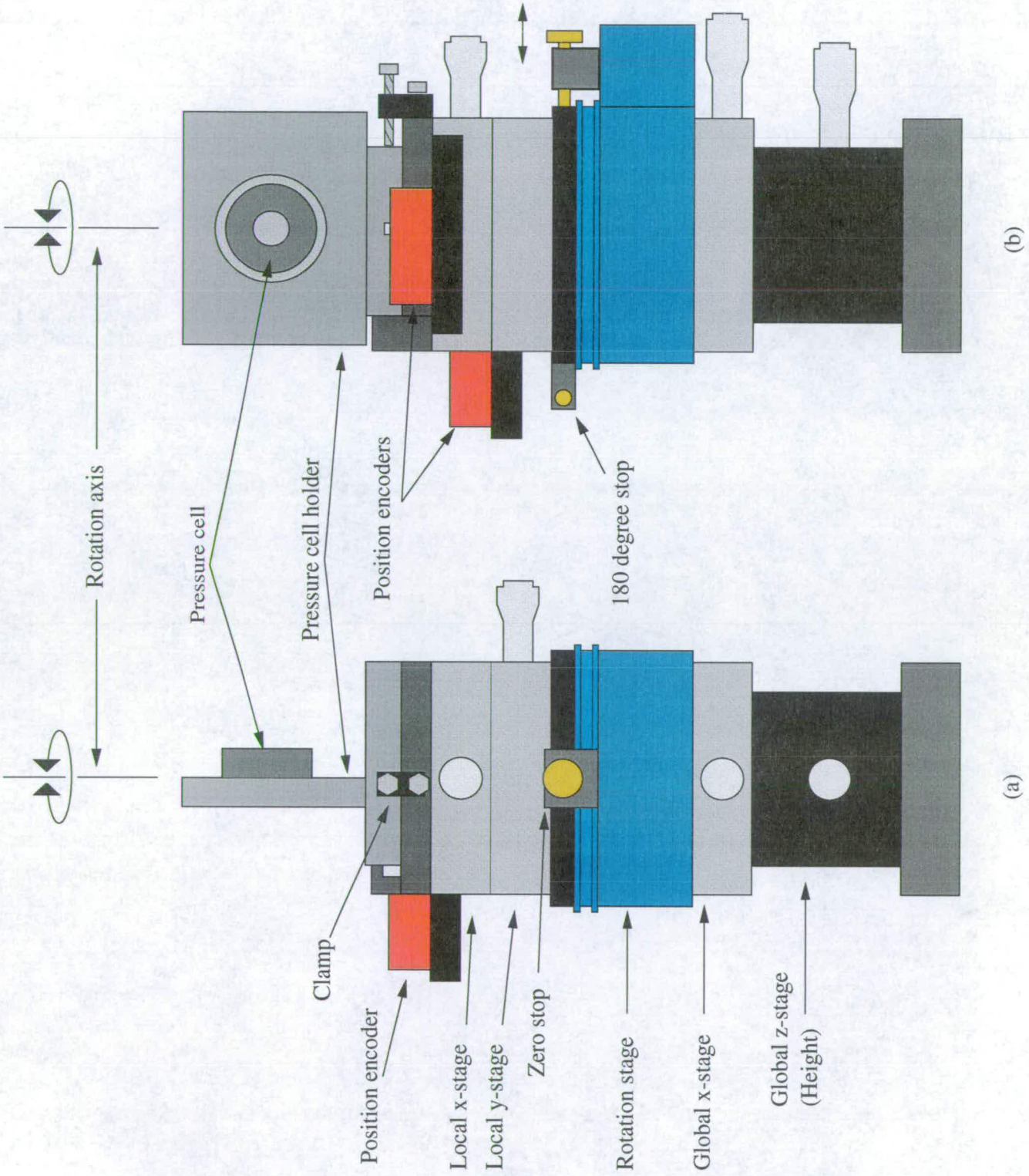


Figure 3.4. A schematic diagram of the new sample stage which incorporates a high-precision rotation stage. (a) Side view (incident beam travels from left to right). (b) Back view (looking away from the synchrotron toward the image-plate).

The global x-stage moves the whole set-up across the beam to enable the rotation stage axis to be moved such that it intersects the beam. This adjustment is normally carried out once at the start of the experimental run. First, a sample is aligned to the rotation axis (the alignment procedure is described in Section 3.3.6). The sample is removed and a piece of x-ray sensitive paper is mounted of the sample stage and moved until it is in focus when viewed through the microscope (as described in Section 2.4.4 on page 26). The paper is exposed to the beam and the microscope is centred on the beam mark. The sample is replaced on the sample stage and the global x-stage is moved until the sample is centred on the microscope's crosshair. The rotation axis now intersects the beam since rotation axis passes through the centre of the sample. It is crucial that the sample is replaced exactly on the rotation axis after it has been removed. The design of the top-plate and the cell holders ensures that this is possible.

The rotation stage is model RTN120 from Newport Ltd. and was specially selected to have the least wobble from a number of different stages of the same model. The rotation stage allows a sample to be inclined to the beam at any angle about a vertical axis. It is also possible to motorise the stage and, although this has not yet been done, it is expected that the stage will be motorised in the future to enable samples to be oscillated by $\pm 5^{\circ}$ during an exposure to enhance powder averaging. An adapter plate sits between the rotation stage and the local y-stage, this plate has a hole drilled in it into which a pin locates to define the zero degree position. The pin can be easily removed to allow the rotation stage to move freely.

The local x- and y-stages are used to position the sample on the rotation axis. The positions of these stages are encoded by RGH22X encoders from Renishaw PLC. The encoders use an optical method to measure changes in position with 1 μm resolution. Infrared light is scattered from a gold-plated steel scale that has a 'saw-tooth' profile with a pitch of 20 μm. The resulting interference pattern is detected by a diode array. The interference pattern changes as the encoder moves

over the scale; these changes are converted into actual changes in position. This position is displayed on a digital readout. An absolute zero position is defined by a magnet attached near to one end of the scale; when a sensor in the encoder head passes over the magnet, the zero position is set. The global z-stage will also be encoded in the future.

The position encoding is used when aligning a sample to the rotation axis—the alignment procedure is detailed in Section 3.3.6. The encoding also allows the position of each sample to be recorded, after it has been aligned, so that the sample can be replaced on the rotation axis without having to carry out the full alignment procedure again for that sample. This is only feasible if the samples can be placed on the stage in exactly the same position every time they are mounted. The next section describes the design of the universal DAC holders built to fulfil this criterion.

3.3.2 Pressure Cell Holders

Figure 3.5 shows a diagram of the new pressure cell holders. There are many different types of DAC, of varying shapes and sizes, so the holders have been designed the accommodate these differences. Each cell has its own collar that fits into a universal mount. The cells are loaded before they are inserted into their collars. Once a DAC had been inserted into its collar it is not removed until it is reloaded. The collar, however, must be removed from its holder to allow pressure to be measured, so the mount has three ball bearings onto which the indents in the collar kinematically locate. The two spring loaded brass clamps, when rotated by 90°, hold the collar firmly in place. This ensures that the cell always relocates to the same position in the holder.

There are 36 indents on the rear face of the collar which allow the cell to be kinematically located in different orientations—10° apart—about the cell axis. This extra degree-of-freedom, combined with the ability to incline the sample on

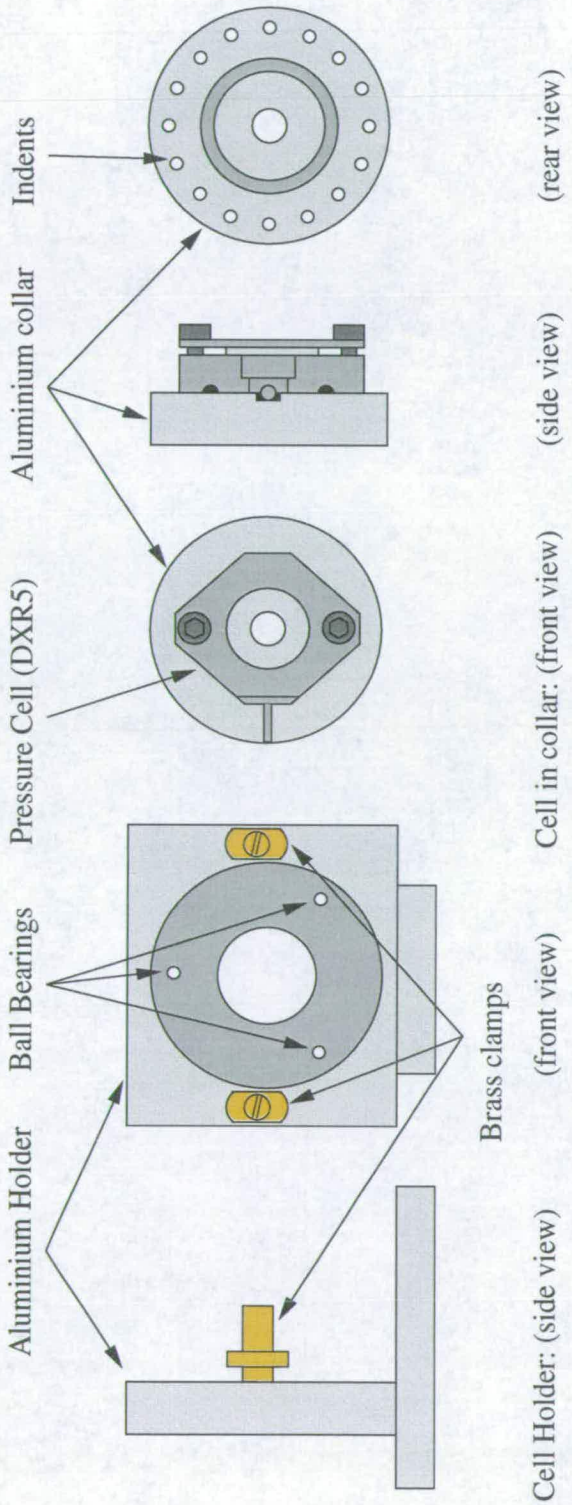


Figure 3.5. Schematic diagram of the new pressure cell holder and collar.

the sample stage, permits the sample to be oriented in any direction with respect to the incident beam—of course, only certain orientations of the sample allow x-rays to enter and exit the pressure cell. However, the sample moves when the collar is rotated in its holder because it is not possible to align the sample to the centre of rotation, thus, every time the cell is rotated in its holder, the sample must be realigned to the rotation axis of the sample stage.

3.3.3 Alignment Microscope Modification

Figure 3.6 is a schematic diagram of the alignment microscope. View (a) shows the microscope viewed perpendicular to the beam and (b) shows the microscope viewed along the beam towards the IP holder (see Fig. 3.1). View (c) shows the microscope viewed along the beam when it is tilted, the tilt feature is described below and is one of two modifications to the alignment microscope that have been carried out to aid the sample alignment procedure. The first of these modifications is the installation of position encoders on the x- and y-stages of the microscope. The encoders are the same model as those on the sample stage and are a key part of the alignment procedure described in Section 3.3.6. The microscope position can only be read with a precision of ± 5 μm or less with the translation stage micrometers. This precision is not sufficiently high for the sample to be aligned accurately to within 1 μm. The encoders allow the position of the microscope across and along the beam to be measured with 1 μm resolution.

The second modification is the addition of a hinge that allows the microscope to be tilted out of the line of the beam, as shown in Fig 3.6. The objective lens of the microscope is approximately 3 cm from the cell when the sample is in focus. Part of the alignment procedure requires that the cell be rotated by 180° about the vertical axis of the rotation stage so the microscope has to be moved away from the cell for it to be rotated. Before the hinge was installed, the y-stage was used to translate the microscope away from the cell by 15 cm to allow the cell

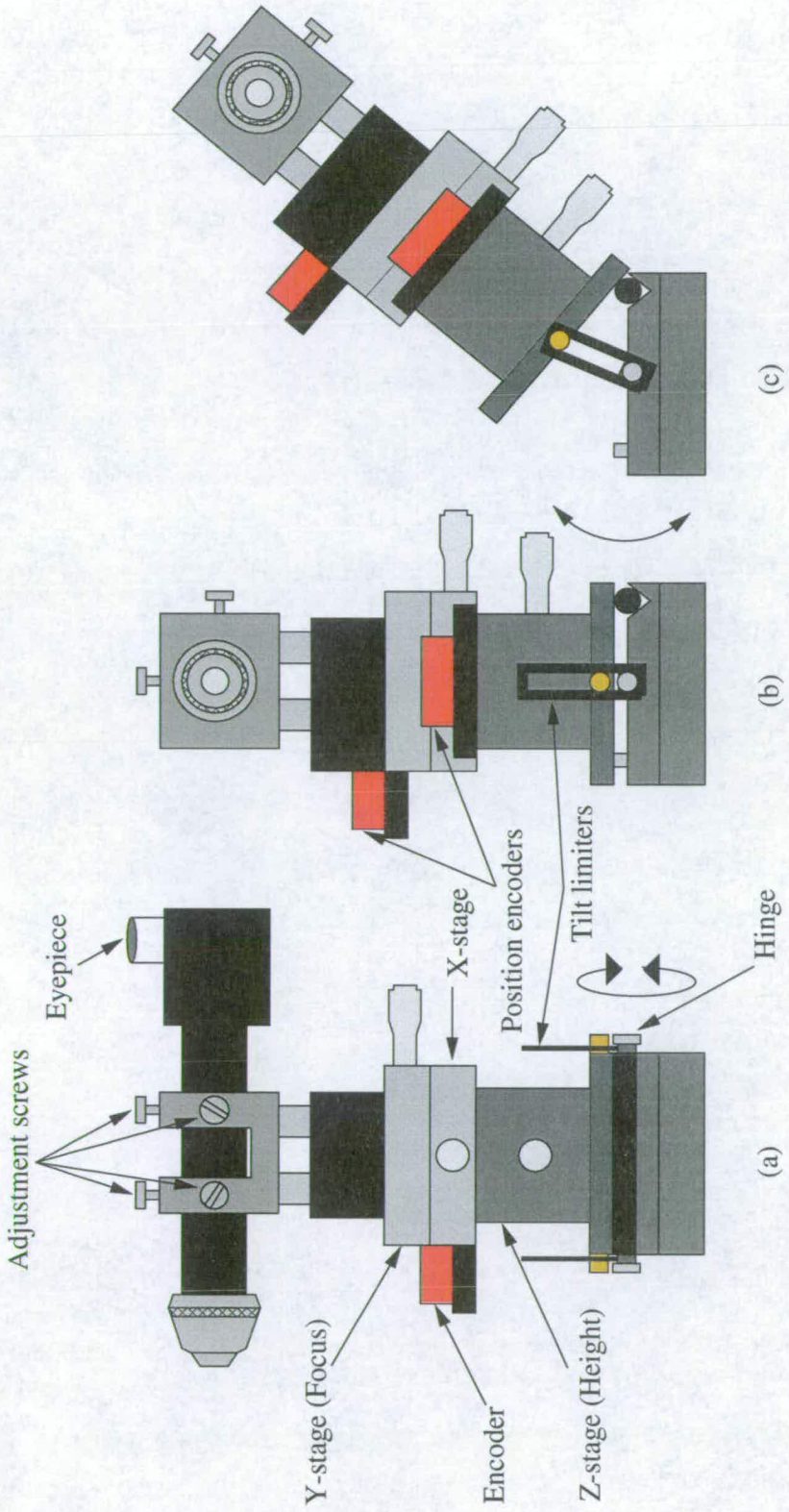


Figure 3.6. Schematic diagram of the alignment microscope. (a) Side view (incident beam travels from left to right). (b) Front view (looking towards image-plate). (c) shows the front view of the microscope when it is tilted.

to be rotated. Once the cell had been rotated, the microscope had to be moved back, using the y-micrometer, until the sample was in focus again. As this had to be carried out several times during a typical alignment, a considerable amount of time was taken up just by this translation. The hinge allows the microscope to be tilted away from the pressure cell. The cell can then be rotated without it hitting the microscope, after which, the microscope can be tilted back into its original position. The hinge is made up of a hardened steel rod in a 'vee'-groove and is designed so that the microscope goes back to less than 1 μm of the position it was in before being tilted. This tilt capability shortens the total alignment time from $\sim$40 minutes to $\sim$20 minutes.

3.3.4 Beamstop and Shielding

The image-plate is sensitive to x-rays over a wide range of wavelengths so it not only detects x-rays scattered from the sample but also any stray (fluorescent) scatter from around the experimental hutch. This fluorescence is caused when x-rays from the monochromator vessel scatter from the floor of the hutch and other components in the hutch. The fluorescence will cause a high background to be recorded by the image-plate unless the image-plate is shielded from it. Prior to the equipment upgrade described in this chapter, the shielding consisted of a sheet of lead-lined rubber which was draped over a frame which enclosed the experimental set-up. This shielded the image-plate from background radiation that entered the enclosure from the top and from the sides. But the image-plate was not completely shielded from radiation that entered the enclosure from below. As part of the equipment upgrade, a new lead-lined enclosure was built that completely encloses the experimental set-up. Each side of the enclosure is a removable panel of lead-lined aluminium. The front panel consists of two halves that are removed during sample alignment. The background level has been much reduced with the installation of the new shielding. The greatest benefit, however, is that the background is now isotropic about the beam—prior

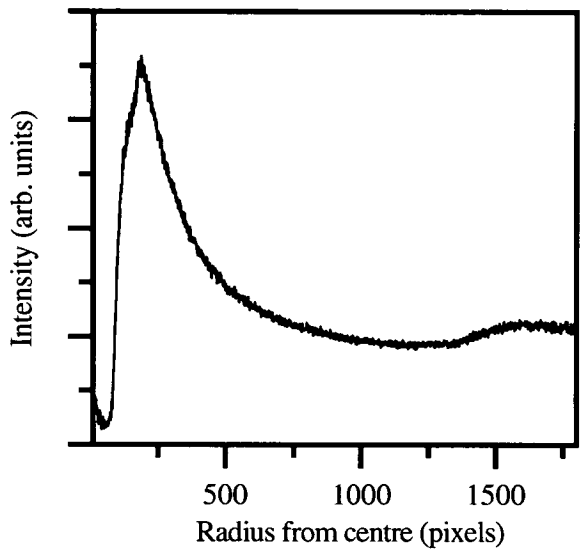


Figure 3.7. Contribution to the background from air scatter.

to the new shielding being installed, the 2-d images revealed 'hot-spots' where the background was 2–3 times higher than the average over the rest of the plate. This resulted in a generally higher background in the 1-d integrations that caused little problem during subsequent 1-d data analysis. In 2-d data analysis, it is preferable to have an isotropic background so any observed intensity variations can be attributed to the sample and cell conditions only.

There are other sources of background that originate from within the enclosure: Compton scattering by the diamond anvils of the pressure cell, and air scatter caused by the incident beam as it passes through the air between the cell and the image-plate. Tests were carried out to determine the magnitude of these sources of background. A gasket was indented, drilled and mounted on a sheet of lead with a hole drilled through it. The empty hole in the gasket was aligned such that the beam passed through it and an exposure was taken. The resulting image was integrated to give the 1-d plot shown in Figure 3.7. This plot shows the background caused by air scatter alone between the sample position and the image-plate. Next, the empty gasket was placed into a DAC and the cell was

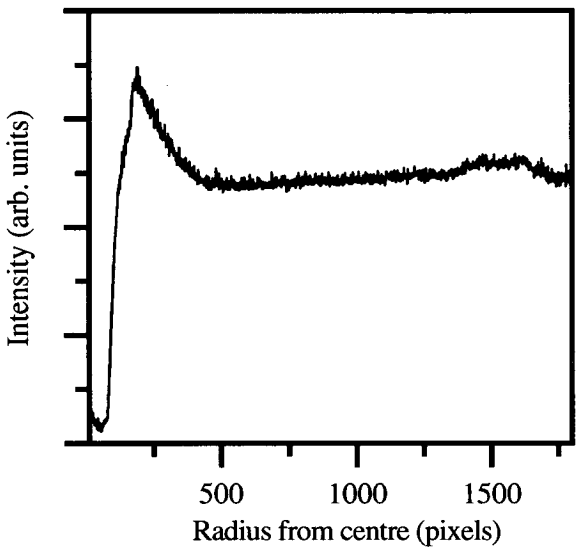


Figure 3.8. Contribution to the background from Compton scattering and air scatter.

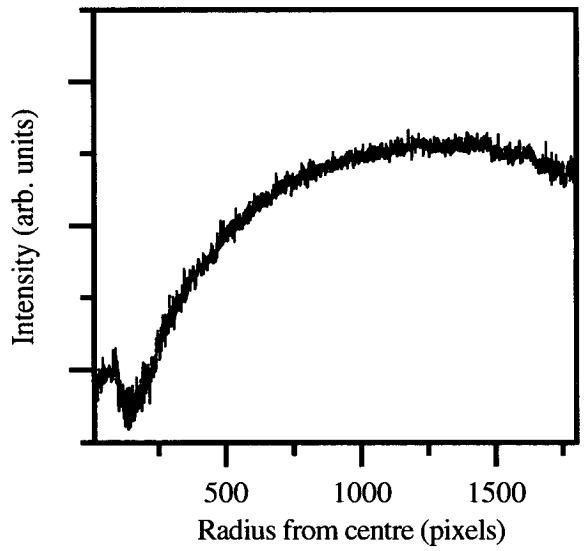


Figure 3.9. Contribution to the background from Compton scattering alone.

aligned to the beam. The integration of the image is shown in Figure 3.8. The background now shows a contribution from Compton scattering as well as air scatter. By subtracting the intensity data shown in Fig. 3.7 from the data shown in Fig. 3.8 the contribution from Compton scattering alone can be plotted. This is shown in Figure 3.9.

Compton scattering from the diamonds is unavoidable but air scatter can be significantly reduced if the straight-through beam is captured close to the pressure cell; the beamstop (shown in Figure 3.10) is designed to do this. A lead cup mounted on a sheet of mylar absorbs the the beam after it has passed through the sample. The beamstop is mounted on the same clamp that the alignment microscope is mounted on during sample alignment. The along-beam position of the lead cup is adjustable. The cup is normally placed as close to the cell as possible without the components of the pressure cell, sample stage or beamstop touching. The lead cup is approximately 6 cm from the sample during normal running. In this position, the lead cup obscures approximately 2° 2θ of the diffraction pattern. This is not usually a problem for the type of samples normally studied at high-pressure, which have relatively small unit cells, as the lowest angle diffraction peak normally occurs at $2\theta > 3°$ at the wavelengths used in high-pressure diffraction experiments ($\sim$0.45 Å).

The mylar, on which the lead cup is mounted, is attached to an aluminium frame, the area of which is large enough to allow up to 45° 2θ of diffraction pattern to pass through without the pattern being obscured by the frame when the beamstop is in place during normal running. The across-beam position and height of the lead cup are adjusted by specially constructed screw mechanisms. The beamstop is aligned to the beam by adjusting its position until the alignment laser beam strikes the rear face of the lead cup.

Figure 3.11 shows the effect of the beamstop on the background: (a) is a pattern from FeS at 7.7 GPa run for 8 hours without the beamstop in place—note high the sloping background at low angles; (b) is a different FeS sample—but the

EX BIBL UNIV. EDINBURGEN

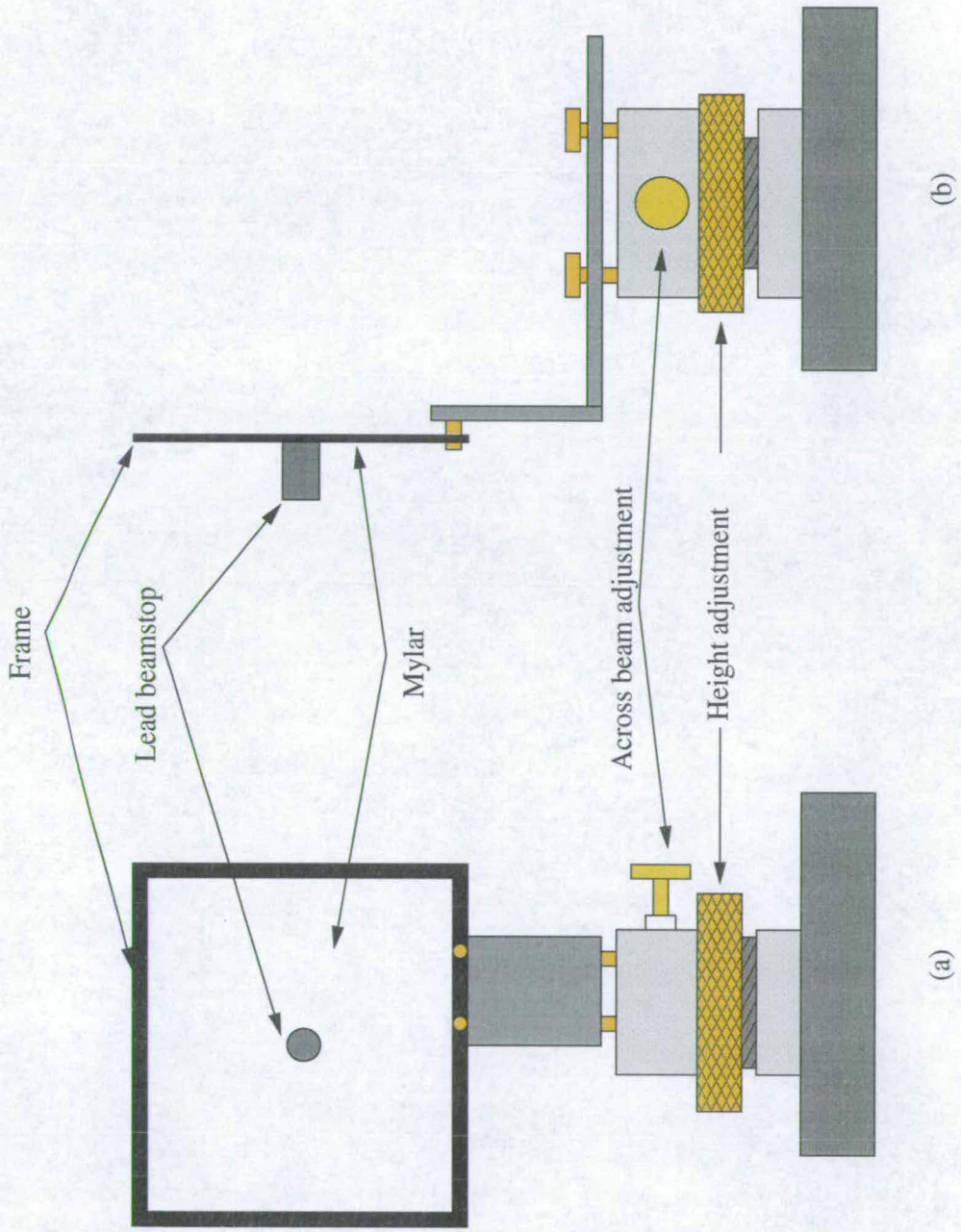


Figure 3.10. Schematic diagram of the new beamstop. (a) Front view (looking towards image-plate). (b) Side view (incident beam travels from left to right).

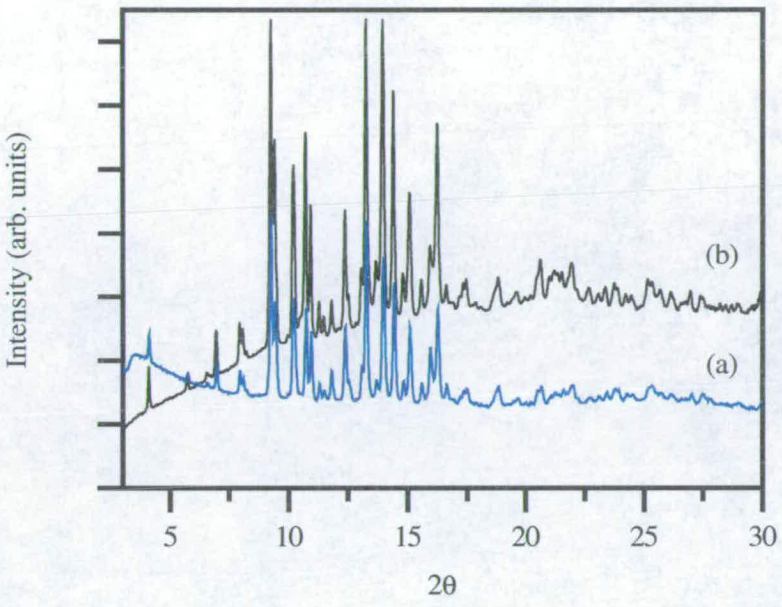


Figure 3.11. (a) FeS at 7.7 GPa without beamstop, (b) FeS at 7.6 GPa with beamstop.

same structure and similar sample volume—at 7.6 GPa run for 6 hours with the beamstop in place—the low angle background is significantly reduced.

3.3.5 Image-Plate Holder

The image-plate (IP) holder and cassette have been modified as part of the equipment upgrade. The old IP holder had adjustments that allowed the plate tilts to be changed but there was no way of ensuring that the IP was perpendicular to the incident beam. It was accepted that the IP would be slightly tilted with respect to the beam and, as described, the image-processing software incorporates a tilt determination algorithm so that a correction for plate tilts could be included in the final rebinned data. This algorithm assumes that the powder rings are circular, but as has been found over the past few years, microstructural stress effects can cause the rings to be non-circular (independent of IP tilts). The new image-plate holder and cassette have been designed so that the IP can be aligned perpendicular to the beam thus removing any uncertainty as to the origin

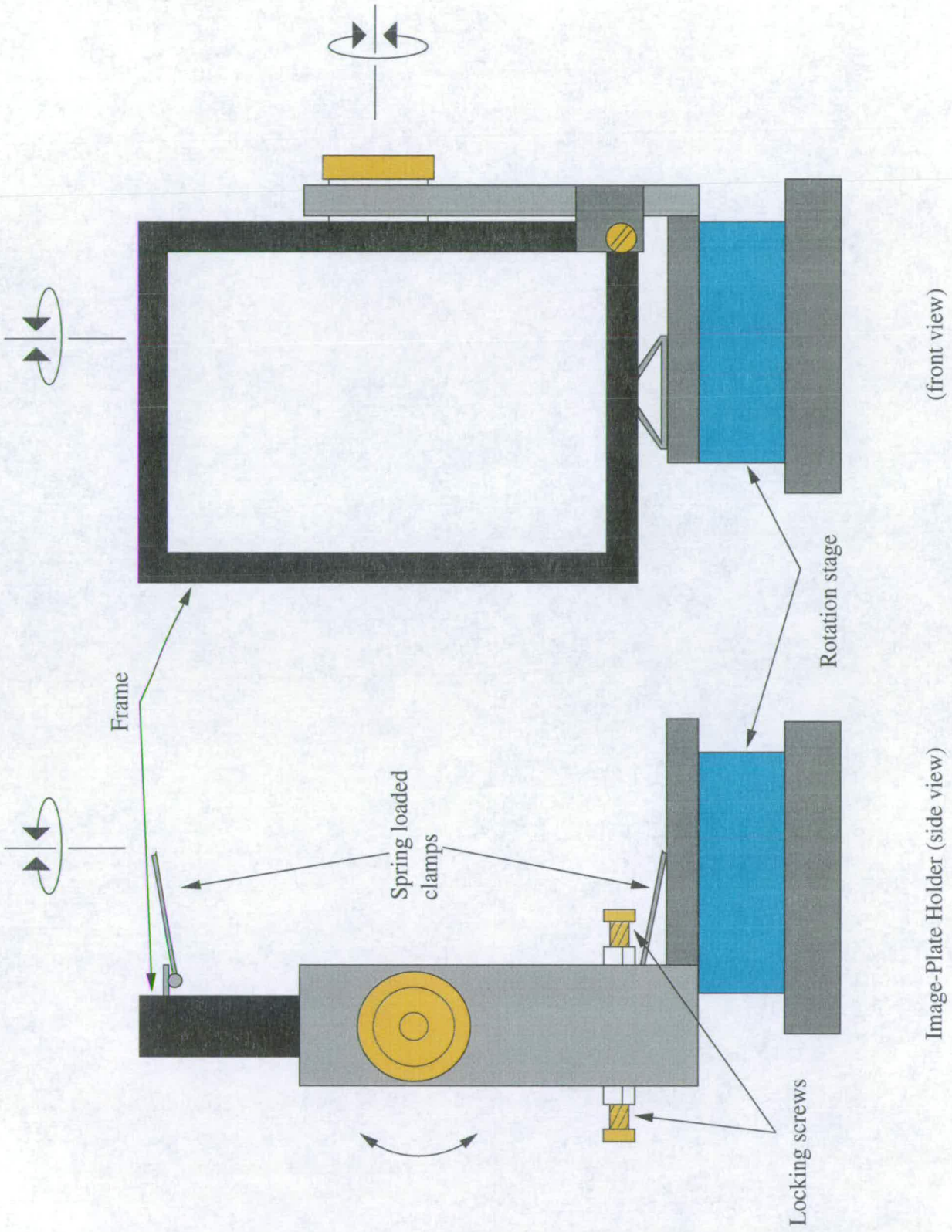


Figure 3.12. Schematic diagram of the new image-plate holder. The clamps hold the image-plate cassette into the frame of the holder. The image-plate cassette is not shown.

of any deviation from circular powder rings.

The new IP holder (see Figure 3.12) is based on a 'picture-frame' design. This allows the alignment laser beam to pass through the holder when the IP (in its cassette) is not in place—the old IP holder had to be tilted out of the way of the laser beam when the laser was being used. The IP cassette is inserted from behind the holder. A lip around the edge of the IP cassette presses against a raised edge around the inside of the frame stopping the cassette from passing through the holder. The cassette is held in place against the frame of the holder by two spring-loaded clamps. The IP slides into the cassette from the top and is pressed against the inside front edge of cassette by spring-loaded strips of steel. A metal cover fits over the top of the cassette to make it light-tight. The cassette is constructed from anodised aluminium except the front face which is a black plastic sheet. The diffraction pattern can pass through the plastic (with little absorption) but visible light cannot. There is a hole in the back face of the cassette where the alignment laser can reflect from the back surface of the IP. The IP is perpendicular to the x-ray beam when the laser beam reflects back onto itself.

3.3.6 Alignment Procedure

This section describes the procedure for aligning samples to the rotation axis of the sample stage. As stated, the aim is to be able to align a sample to the rotation axis to within 1 μm and, after the initial alignment, to be able to replace the sample on the rotation axis without re-aligning it.

The alignment procedure consists of measuring the across-beam position and focus position of the sample in two orientations (0° and ~180° inclinations). As with the normal alignment procedure, care has to be taken that the refractive properties of the diamonds do not interfere with the position measurements. The

back face of the second diamond (see Fig. 3.2) is aligned such that it is perpendicular to the optical axis of the microscope but the first and second diamonds are not necessarily parallel so the exact position of the $\sim$180° inclination has to be adjustable. (This is especially true for the Merrill-Bassett and Mao-Bell type of pressure cells which do not have culet tilt alignment capabilities.) The '180 degree' stop on the sample stage can be adjusted to stop the sample anywhere over the range 180°$\pm$3°. The stop is adjusted so that the reflection of the alignment laser beam from the back face of the first diamond lies on a vertical line that passes through the exit aperture of the laser. Normally, the reflection does not fall exactly on the exit aperture, but as long as the reflection is in the vertical plane, measurements of the across-beam position of the sample will not be affected by the refractive index of the diamond.

Once the '180°' position has been set, the sample is aligned to the rotation axis of the sample stage by an iterative procedure. The microscope crosshairs are centred and focused on the sample and the positions of the x- and y-stages of the microscope are read from the digital read-out and noted. The sample is rotated to the '180°' position and again the microscope is focused and centred (in the across-beam direction) on the sample and the positions noted. An average of the noted positions is taken and the microscope is driven to the average positions. The sample is moved, by adjusting the local x- and y-stages on the sample stage, until it comes into focus and is centred. This procedure is repeated until there is no change in position of the sample between the 0° and 180° settings of the sample. The sample is now aligned to the rotation axis. The positions of the local x- and y-stages are noted so that the cell can be replaced onto the rotation axis by driving the local stages to the noted positions rather than having to carry out the complete alignment procedure again.

3.4 Development of Experimental Set-up: Data Preparation

This section describes how the azimuthal data are extracted from the collected image-plate data and details are given of a new absorption correction for inclined samples.

3.4.1 Extension to Platypus: Sector Output

The last stage before data analysis is carried out is the extraction of azimuthal data from the 2-d image. When Platypus was originally written there was no concept of 2-d data analysis and therefore no facilities were included in the software for the analysis of intensity and position variations around the powder rings. To extract this information, the paint-out option of Platypus was used to exclude all parts of the image apart from one sector. The image was integrated as normal, but only the pixels that had not been excluded from the processing were rebinned and thus a 1-d plot of the sector was obtained. This process had to be laboriously carried out for each sector of the image. The Platypus source code has been extended to include a facility for sectoring the 2-d image into an arbitrary number of sectors between 1–60 and outputting the data into a separate rebin file for each sector. Figure 3.13 shows a screen-shot of Platypus (re-named EDIPUS—**Ed**inburgh **I**mage-**P**late **U**ser **S**oftware—after the upgrade). Small ruby reflections have been removed from the processing by using the red paint-out feature. The menu item '2-D Analysis' has been added as part of the upgrade and includes the functions for sectoring the image. The 'Plot' window shows five sectors from the image shown in the main window.

The process of sectoring the image is generally the same as the rebin procedure described in Section 2.5.1 except that instead of rebinning the data into one plot, each pixel is assigned a sector—determined by calculating the angle of the pixel

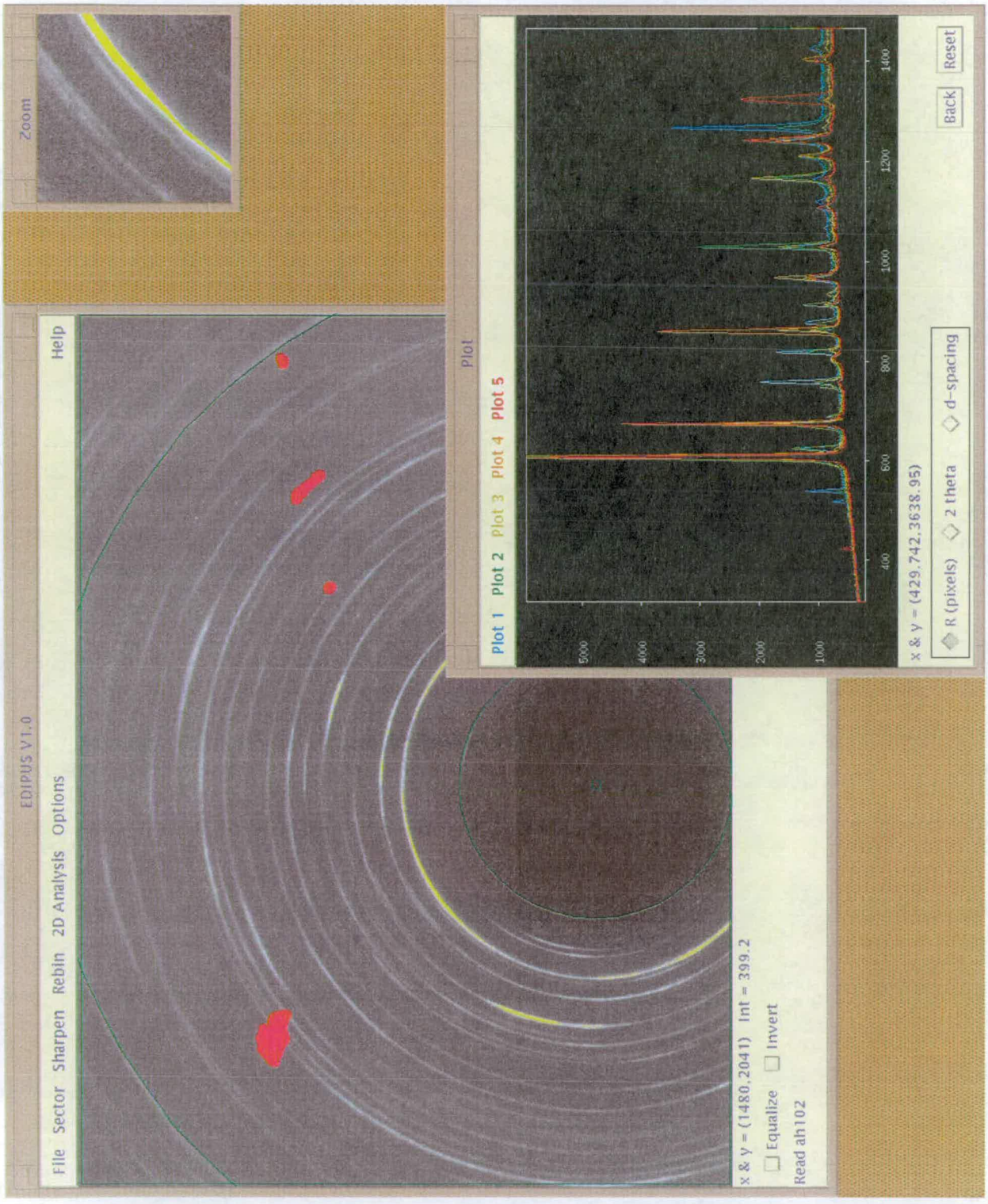


Figure 3.13. Screen-shot of the upgraded version of Platypus—EDIPUS—which now includes functions for 2-d data analysis. The image on the main screen is Ba at 13.3 GPa.

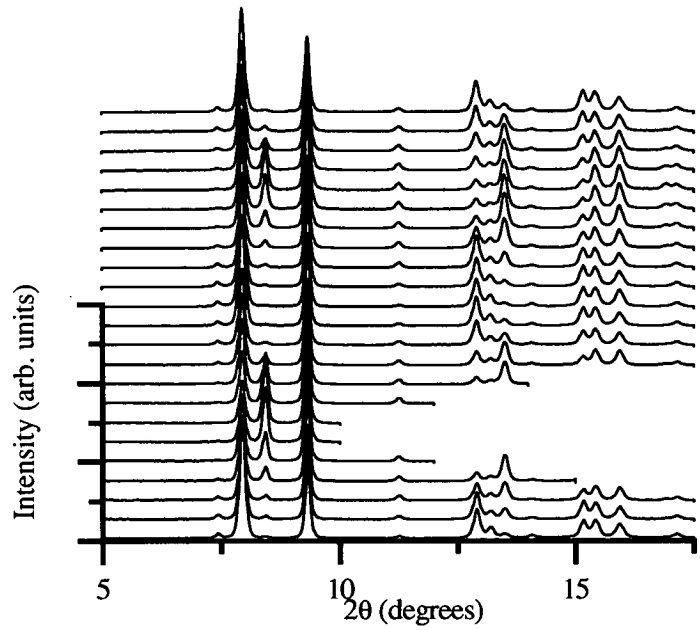


Figure 3.14. Multiplot of sectors around the rings of the image shown in Fig. 1.1.

around the incident beam—and the intensity is rebinned into the appropriate plot. The sectored data has all the corrections for plate tilts, beam polarisation and spatial distortion that are applied to the normal rebin data.

The output is in the form of many rebin files—one for each sector. Figure 3.14 is a multiplot of 24 sectors extracted from the image shown in Figure 1.1. The intensity and position variations around any given powder ring can be extracted by using peak fitting software to fit the peak of interest in the sector rebin files. By fitting the corresponding peak in all sector rebins, information about the position and intensity of the powder rings can be extracted as a function of angle around the incident beam. The sector rebin files can also be calibrated and converted into intensity vs. 2θ plots. These plots can be used as the input data for a simultaneous refinement of all the sectors.

3.4.2 Absorption Correction for Inclined Samples

Both the incident and diffracted beams are partially absorbed as they pass though the sample and components of the cell. The amount of absorption depends on the path of the beams through the sample and cell. In the normal configuration (i.e. non-inclined setting), there is cylindrical symmetry about the incident beam direction. In this case, the amount of absorption suffered by the incident and diffracted intensity depends only on the diffraction angle, θ, and not on the azimuthal angle, γ, about the incident beam. When the cell is in an inclined position, however, the cylindrical symmetry is broken and the path of the beams through the sample and cell depends on θ and γ. The γ dependence introduces intensity variations around the powder rings that are due to absorption, so any analysis of intensity around the rings has to take into account absorption.

There are two ways to correct for absorption: (i) measure the absorption of the cell by recording the intensity of a beam after it has passed through an empty cell in a variety of orientations; (ii) calculate the absorption if the geometry of the cell is known. Each method has advantages and disadvantages. The absorption measurement has to be carried out for every type of cell and if any component of the cell changes (for example, the thickness and diameter of the gasket hole), a new absorption measurement has to be carried out. Also, the absorption of the sample is not properly accounted for in this method. Calculation of the absorption requires accurate knowledge of the size and shape of the sample and each component of the cell. However, the geometry of each cell can be parameterised with relative ease and this computational method is more flexible to changes in sample and cell geometry. It is this method of absorption correction that is detailed here.

The diffraction intensity, I_{hkl}, for a given reflection (hkl) measured at a given point on the powder ring can be expressed by the equation:

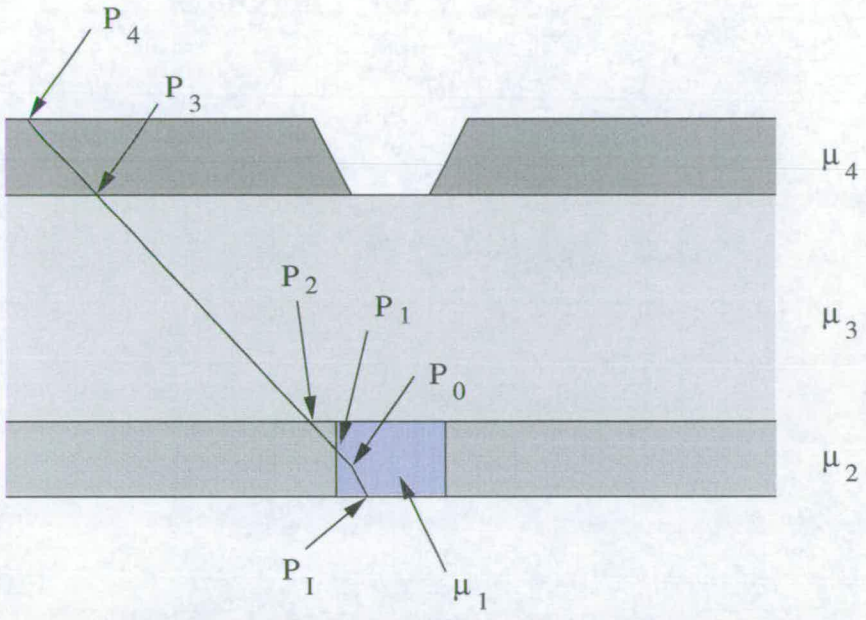


Figure 3.15. The path of an arbitrary beam through the sample and cell.

$$I_{hkl} = I_0 \left|F_{hkl}\right|^2 \lambda^3 V L_p P A + B \tag{3.6}$$

where I_0 is the intensity of the incident beam, F_{hkl} is the structure factor of reflection (hkl), λ is the incident beam wavelength, V is the sample volume illuminated by the incident beam, L_p is the Lorentz-polarisation factor applicable to the given experimental geometry, P is a preferred orientation correction, A is the absorption correction and B is the background count.

The general form for the absorption factor is $e^{-\mu l}$ where μ is the absorption coefficient of the material through which a beam of length l passes. There are four different materials through which the incident and diffracted beams can pass in a pressure cell: sample, gasket, diamond and the backing disc on which the diamonds are mounted. Figure 3.15 shows the path of an arbitrary beam as it passes through components of a typical cell. The incident beam impinges on the sample at an angle ω, the angle of inclination of the cell. The beam passes through the sample in a straight line from point P_I to point P_0. If the distance between P_I and P_0 is denoted by l_I, the incident beam intensity is diminished

by $e^{-\mu_1 l_I}$, where μ_1 is the absorption coefficient of the sample. The diffracted beam travels through the sample from P_0 to P_1 (distance l_D); through the gasket (absorption coefficient μ_2) from P_1 to P_2 (distance l_2); through the diamond (absorption coefficient μ_3) from P_2 to P_3 (distance l_3); and through the backing disc (absorption coefficient μ_4) from P_3 to P_4 (distance l_4). The diffracted beam intensity is, thus, attenuated by $e^{-\mu_1 l_D} e^{-\mu_2 l_2} e^{-\mu_3 l_3} e^{-\mu_4 l_4}$. Combining the incident and diffracted beam absorption, the absorption factor is:

$$A = e^{-(\mu_1(l_I + l_D) + \mu_2 l_2 + \mu_3 l_3 + \mu_4 l_4)} \tag{3.7}$$

or, letting $l_1 = l_I + l_D$,

$$A = e^{-(\mu_1 l_1 + \mu_2 l_2 + \mu_3 l_3 + \mu_4 l_4)} \tag{3.8}$$

The beam in this case has no cross-section but, in practice, the incident beam has a diameter. However, the beam can be thought of as an infinite number of parallel rays with zero cross-section, so the absorption correction becomes the average of the absorption of all the rays that cause diffraction in the direction of interest. For computational purposes, only the absorption of a subset of rays is calculated and averaged. Each ray is defined by the incident beam angle, ω, the diffraction angle, θ and γ, and the point within the sample where the diffraction occurs, (x_0, y_0, z_0). A subset of rays can be obtained by picking a grid of n points, $\{x_0[i], y_0[i], z_0[i]\}$, which lie within the diffracting volume. So the absorption factor becomes,

$$A = \frac{1}{n} \sum_{i=1}^{n} e^{-(\mu_1 l_1[i] + \mu_2 l_2[i] + \mu_3 l_3[i] + \mu_4 l_4[i])} \tag{3.9}$$

The calculated value of A is more accurate the closer n is to infinity. Of course, there is a trade-off between accuracy and computational time. Tests on the

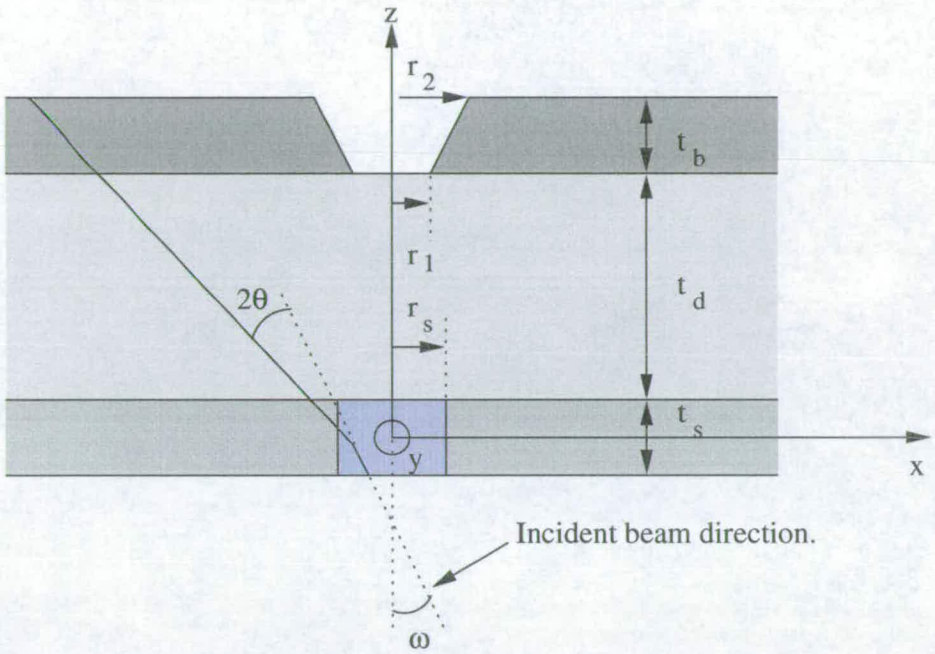


Figure 3.16. The definition of the sample coordinate system. The frame is centred on the centre of the cylindrical sample (thickness t_s, radius r_s) with x and z in the horizontal plane and z along the cylindrical axis of symmetry of the sample. The sample is inclined to the incident beam (radius r_b) by an angle ω about a vertical axis that is coincident with the y-axis of the coordinate system (out of page).

program written to calculate the absorption correction detailed here have shown that the calculated absorption from a grid of 1000 points is equal to the absorption calculated from a grid of 1 million points to four decimal places.

The task, then, is to calculate $l_1[i]$, $l_2[i]$, $l_3[i]$ and $l_4[i]$ for the chosen set of points in the diffracting volume. By defining the diffracting volume by a set of parametric equations, a grid of points can be chosen by taking discrete values of the parameters. Working in the sample coordinate frame shown in Figure 3.16. The projection of a circular beam onto an inclined plane is an ellipse given by the parametric equations:

$$\left.\begin{aligned} x_0 &= x_c + \frac{s}{\cos\omega}\cos t \\ y_0 &= y_c + s.\sin t \\ z_0 &= z_c \end{aligned}\right\} \begin{aligned} &0 \le t < 2\pi \\ &0 \le s < r_b \end{aligned} \qquad (3.10)$$

where s and t parameterise the elliptical area illuminated by a beam of radius r_b on a plane inclined at an angle ω to the beam, and (x_c, y_c, z_c) is the centre of the ellipse. The total volume illuminated by the beam can be thought of as comprising an infinite number of ellipses, as defined in Equation 3.10, whose centres lie on the line within the sample defined by the beam centre in the sample frame. The beam centre can be parameterised as follows:

$$x_c = \frac{ut_s \tan\omega}{2}, \quad y_c = 0, \quad z_c = \frac{ut_s}{2} \tag{3.11}$$

where t_s is the sample thickness and u parameterises the part of the line within the sample, $(-1 \leq u \leq 1)$.

Combining equation 3.10 and equation 3.11, the complete parametric equation describing the diffracting volume is:

$$\left.\begin{array}{rcl} x_0 &=& \dfrac{ut_s \tan\omega}{2} + \dfrac{s.\cos t}{\cos\omega} \\ y_0 &=& s.\sin t \\ z_0 &=& \dfrac{ut_s}{2} \end{array}\right\} \quad \begin{array}{l} 0 \leq s \leq r_b \\ 0 \leq t < 2\pi \\ -1 \leq u \leq 1 \end{array} \tag{3.12}$$

A grid of points that belong to the diffracting volume can be collated by picking discrete values of the parameters s, t and u in the ranges given above. Of these points, only points that satisfy $x_0^2 + y_0^2 \leq r_s^2$ lie within the sample.

An incident beam enters the sample and diffracts from a point in the sample at point (x_0, y_0, z_0). The diffracted beams form a cone about the incident beam vector with half angle 2θ (the diffraction cone). The diffraction cone can be described by defining a new coordinate system (x', y', z')—(the beam frame). The z'-axis is coincident with the incident beam direction, the y'-axis is parallel the y-axis of the sample frame and the x'-axis is orthogonal to y' and z'. In the beam frame, the diffracting cone is described by:

$$\begin{aligned} x'_d &= \sin 2\theta \sin\gamma \\ y'_d &= \sin 2\theta \cos\gamma \\ z'_d &= \cos 2\theta \end{aligned} \tag{3.13}$$

where θ is the diffraction angle and γ is the azimuthal angle around the powder ring. Rotating the beam frame by ω about y' it is possible to find the representation of the diffraction cone in the sample frame, thus:

$$\begin{bmatrix} x_d \\ y_d \\ z_d \end{bmatrix} = \begin{bmatrix} \cos\omega & 0 & \sin\omega \\ 0 & 1 & 0 \\ -\sin\omega & 0 & \cos\omega \end{bmatrix} \begin{bmatrix} x'_d \\ y'_d \\ z'_d \end{bmatrix} \tag{3.14}$$

$$\Rightarrow \begin{aligned} x_d &= \cos\omega \sin 2\theta \sin\gamma + \sin\omega \cos 2\theta \\ y_d &= \sin 2\theta \cos\gamma \\ z_d &= -\sin\omega \sin 2\theta \sin\gamma + \cos\omega \cos 2\theta \end{aligned} \tag{3.15}$$

The path, in the sample frame, of the diffracted beam through the sample and cell from the point (x_0, y_0, z_0) to point $(2\theta, \gamma)$ on the image-plate is given by the parametric equations:

$$\left.\begin{aligned} x &= x_0 + v x_d \\ y &= y_0 + v y_d \\ z &= z_0 + v z_d \end{aligned}\right\} 0 \leq v < \infty \tag{3.16}$$

Figure 3.15 shows the various components of the cell. Six parameters describe these components: sample thickness t_s, sample radius r_s, diamond thickness t_d, backing disc thickness t_b and the two radii, r_1 and r_2, that describe the conical aperture in the backing disc through which the sample is viewed during alignment. It is possible to calculate the path-lengths $l_1 = l_I + l_D$, l_2, l_3 and l_4 using these parameters combined with equation 3.16. The expression for l_I is relatively simple, for a point (x_0, y_0, z_0):

$$l_I = \frac{t_s + 2z_0}{2\cos\omega} \tag{3.17}$$

To calculate the other path-lengths it is necessary to calculate coordinates of the diffracted beam at the points $P_1(x_1, y_1, z_1)$, $P_2(x_2, y_2, z_2)$, $P_3(x_3, y_3, z_3)$ and $P_4(x_4, y_4, z_4)$ (see Fig. 3.15). This can be done by computing the value of the parameter v in equation 3.16 at each of these points. All the components of the sample and cell are planes parallel to the xy-plane of the sample frame and pass through the z-axis at a point determined by the thickness of the various components. The value of z where the beam enters the diamond is $z_2 = t_s/2$. The value of z where the beam enters the backing disc is $z_3 = t_s/2 + t_d$. And, similarly, the value of z where the beam exits is $z_4 = t_s/2 + t_d + t_b$. v can be calculated by inserting the relevant value of z into equation 3.16, for example, the coordinates of P_2 can be determined by calculating v_2 and setting $v = v_2$ in equation 3.16:

$$v_2 = \frac{z_2 - z_0}{z_d} \tag{3.18}$$

Similarly, the coordinates of P_3 and P_4 can be found by setting $v = v_3$ and $v = v_4$, respectively. If $x_2^2 + y_2^2 \leq r_s^2$, then P_2 lies on the surface of the sample and the diffracted beam does not pass through the gasket, so $P_1 = P_2$, otherwise, the beam does pass through the gasket, $P_1 \neq P_2$, and the coordinates of P_1 need to be computed by finding the value of v where the beam enters the gasket. The beam enters the gasket when $x_1^2 + y_1^2 = r_s^2$. Therefore, from equation 3.16:

$$(x_d^2 + y_d^2)v_1^2 + 2(x_0x_d + y_0y_d)v_1 + (x_0^2 + y_0^2 - r_s^2) = 0 \tag{3.19}$$

v_1 is the largest root of the quadratic equation 3.19, i.e.:

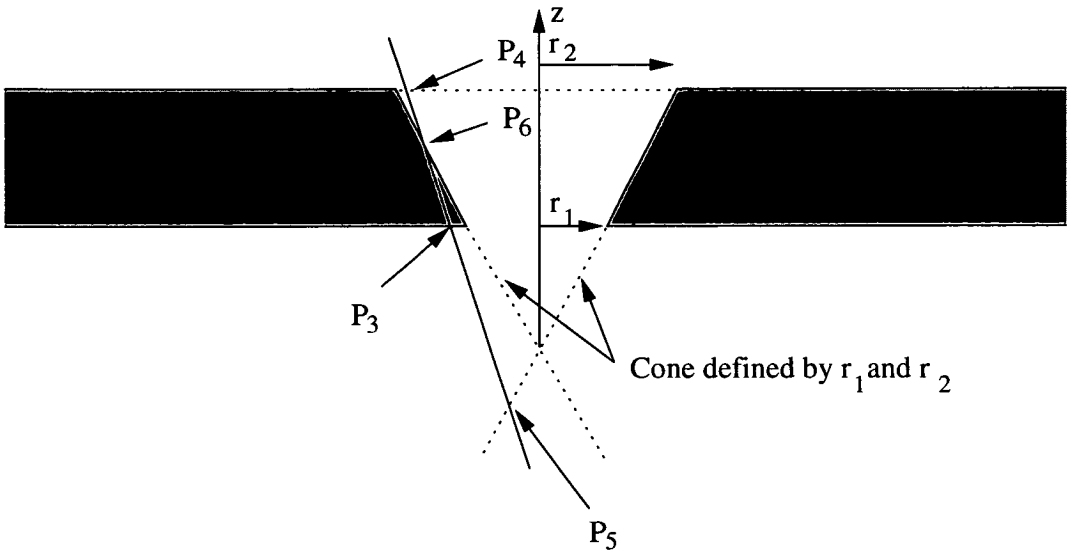


Figure 3.17. A close-up of the conical aperture in the backing disc of the pressure cell.

$$v_1 = \frac{-b + \sqrt{(b^2 - 4ac)}}{2a} \tag{3.20}$$

where $a = (x_d^2 + y_d^2)$, $b = 2(x_0 x_d + y_0 y_d)$ and $c = (x_0^2 + y_0^2 - r_s^2)$.

Once the coordinates of all the points P_0, P_1, P_2, P_3 and P_4 have been computed, the path-lengths can be obtained by calculating the distance between the relevant points. For example,

$$l_D = \sqrt{[(x_1 - x_0)^2 + (y_1 - y_0)^2 + (z_1 - z_0)^2]} \tag{3.21}$$

The calculation of l_4 is complicated by the aperture in the backing disc. The aperture is a partial cone defined by two radii, r_1 and r_2. r_1 is the radius of the hole at a distance $t_s/2 + t_d$ (half the sample thickness plus the diamond thickness) from the centre of the sample and r_2 is the radius of the hole situated a further distance t_b (the thickness of the backing disc) from the sample. Figure 3.17 is a diagram of the conical aperture in the sample frame. To calculate l_4, it is necessary to find the values of the parameter v where the diffracted beam cuts

the cone defined by r_1 and r_2. The cone can be defined thus:

$$\begin{aligned}(x^2+y^2) &= (r_1+d(z-e))^2 \\ &= r_1^2+2r_1d(z-e)+d^2(z-e)^2 \\ &= (r_1^2-2r_1de+d^2e^2)+2(r_1d-d^2e)z+d^2z^2\end{aligned} \tag{3.22}$$

where $d=(r_2-r_1)/t_b$ and $e=(t_s+2t_d)/2$.

Substituting x, y and z from equation 3.16 and gathering the terms to get a quadratic equation in v:

$$av^2+bv+c=0 \tag{3.23}$$

where $a=(x_d^2+y_d^2-d^2z_d^2)$, $b=2(x_0x_d+y_0y_d-r_1dz_d+d^2ez_d-d^2z_0z_d)$ and $c=(x_0^2+y_0^2-r_1^2+2r_1de-d^2e^2-2r_1dz_0+2d^2ez_0-d^2z_0)$. The two solutions, $v_{5,6}$, of v are given by:

$$v_{5,6}=\frac{-b\pm\sqrt{(b^2-4ac)}}{2a} \tag{3.24}$$

The diffracted beam cuts the aperture in the backing disc only if $v_3<v_5<v_4$ or $v_3<v_6<v_4$. If neither of these conditions holds and $x_3^2+y_3^2\leq r_1^2$ and $x_4^2+y_4^2\leq r_2^2$ then the beam exits the cell by passing completely through the aperture, so $l_4=0$, otherwise the beam travels through the backing disc material from P_3 to P_4 so $l_4=\sqrt{[(x_4-x_3)^2+(y_4-y_3)^2+(z_4-z_3)^2]}$. There are three other types of path the diffracted beam can follow through the backing disc. If both v_5 and v_6 lie between v_3 and v_4 and $v_5<v_6$, then the beam passes through the backing disc from P_3 to P_5 (or P_6, if $v_6<v_5$), through air from P_5 (or P_6) to P_6 (or P_5) and through the backing disc again from P_6 (or P_5) to P_4. If only one of the parameters—v_5 or v_6—are in the correct range and $x_3^2+y_3^2<r_1^2$ then the beam passes through air from P_3 to P_5 (or P_6, whichever is in the correct range)

and through the backing disc from P_5 (or P_6) to P_4, otherwise the beam travels through the backing disc first then through air. l_4 is thus calculated from the distances between the appropriate points.

The analysis above had been incorporated into a stand alone absorption correction program and is also included in the texture fitting software described in the next chapter. The absorption coefficients (μ_1, μ_2, μ_3 and μ_4), the sample tilt (ω), beam radius (r_b), sample thickness and radius (t_s, r_s), diamond thickness (t_d), backing disc thickness (t_b) and the radii that define the conical aperture in the backing disc (r_1, r_2) are all refineable parameters in the fitting program, although most of the parameters would be fixed at known values in practice.

The treatment given above is quite general with respect to the geometry of the components of the diamond-anvil cells described in Chapter 2. In practice, however, gasket shielding from the highly absorbing tungsten gasket typically used by the Edinburgh group has by far the greatest effect on the absorption suffered by the beam as is passes through the cell; the gasket effectively absorbs all the beam entering it (i.e. $\mu_2 = \infty$ and $\mu_1 = \mu_3 = \mu_4 = 0$). When part of the diffracted beam passes through the gasket it is not necessary to carry out the full ray-tracing calculation and in this case the effect of the absorption in equivalent to reducing the sample size.

Chapter 4

Preferred Orientation Modelling by 2-D Analysis

4.1 Introduction

This chapter describes the application of 2-d analysis techniques to the study of preferred orientation and texture in powder samples. The phenomenon of preferred orientation (PO) is introduced and a description of its effect on high-pressure powder diffraction experiments is given. A model based on a simple analytic function is presented. However, it has been found that this model cannot describe very strong PO often found in powder samples at high pressure. This had led to the application of the symmetrised spherical harmonics model commonly used in texture analysis to image-plate data. This model has been successfully applied to the study of severe PO induced in HgS at high-pressure. The chapter finishes with a demonstration of a quasi-2-d (many sectored) Rietveld refinement. It should be emphasised the much of the work presented here is expected to form the foundation of all future 2-d analysis techniques and is not wholly specific to preferred orientation studies.

4.2 Preferred Orientation and Texture

Preferred orientation (PO) or texture occurs when the crystallites in a powder sample are not randomly oriented, i.e. there is not an equal number of crystallites in every orientation. (The difference in meaning between the terms texture and preferred orientation (PO) is not well defined; but PO can be generally regarded as describing powders with a simple, smoothly varying distribution of crystallite orientations, whereas texture describes powders with a much more complex form of orientation distribution that is not necessarily smoothly varying.) PO affects the relative intensities of the reflections from a sample because the proportion of crystallites contributing to the intensity of a reflection depends on the direction of the diffracted beam. But accurate relative intensities are needed to determine accurately the position of the atoms in the unit cell. It is therefore important to characterise the PO in the sample and if possible quantify its effect on the diffraction intensities. This is done by measuring or modelling the probability distribution of crystallite orientations (orientation distribution) in the sample.

Much work on determining orientation distributions has been carried out in the field of texture analysis. Workers in this field are interested in the influence that texture has on the properties of polycrystalline materials. For instance, texture in metals has been the source of a great deal of study by metallurgists because of the effects of texture on the mechanical and electromagnetic properties of the metal (Barrett and Massalski (1992)). The rolling or extrusion of metal can induce pronounced and varied texture in the metal. For example, introducing texture into materials used to make transformer cores can make it easier to magnetise the core in one direction.

In texture analysis, the orientation distribution is determined by measuring pole figures (often collected on specialised texture diffractometers). Pole figures are obtained by recording the intensity of a reflection as a function of sample orientation; the intensity of a reflection is proportional to the number of crystallites

contributing to the diffracted beam in a given direction. From the pole figures, the probability density that a single crystallite can be found in a given orientation can be deduced. This process is known as pole-figure inversion. The orientation distribution function (ODF) of crystallites is extracted from pole figures by a variety of methods, three of which are mentioned here. All of the methods, however, are based on parameterising the pole figures with respect to the two distinguishable Euler angles. The orientation of a crystallite in a powder sample can be described by three Euler angles which are defined in an arbitrary coordinate system. The coordinate system is often chosen to relate to the diffraction geometry in simple way. In practice, it is only possible to distinguish two of the angles necessary to describe the orientation of a crystallite—the polar and azimuthal angle of the diffracted beam with respect to the incident beam; the different orientations about the normal to a diffraction plane (scattering vector) cannot be distinguished because the intensities from all the crystallites oriented about the scattering vector are diffracted in the same direction an thus fall on the same point on the detector. The range of orientations about the scattering vector of a given reflection can be constrained by information from the pole figures of other reflections if angular relationship between the reflections is known (i.e. if the crystal symmetry is known); but to determine fully the orientation of every crystallite contributing to one point on a pole figure would require the measurement of an infinite number of pole figures.

There are many methods for extracting the ODF of crystallites in a powder. The most common technique used in texture analysis is the harmonic expansion method of Bunge (1982) where the ODF is represented by a series expansion of appropriately chosen spherical harmonics—many of the procedures for ODF determination used in texture analysis are modifications of the harmonics method. The harmonics expansion is known to produce unphysical results in some cases by permitting areas of negative orientation density in predicted pole figures (although this is normally only a problem when fitting very strong textures where

the true ODF has large regions of zero density). The possibly of obtaining unphysical results from the harmonics method has prompted the development of other techniques which ensure that the orientation density is positive for all orientations. The vector method (Ruer and Baro (1977)) partitions the intensity of the measured pole figures on a discrete grid, and relates these grid squares to unmeasured grid squares by symmetry to give a set of linear equations that are solved iteratively to determine the values of the unmeasured grid squares. Since only grid squares that can be related to actual measured intensity are assigned a value and indeterminable squares are fix at zero density, this procedure results in an ODF that does not contain areas of negative density. The method of Williams (1968), Imhof (1982) and Matthies and Vinel (1982) (WIMV) determines the ODF by a product expansion of positive definite functions and thus ensures that the calculated ODF is physically reasonable. These three methods are compared in Matthies, Wenk and Vinel (1988).

The least-squares structure refinement techniques used in conventional powder diffraction studies have many parameters and require considerable computing power for refinements to proceed with reasonable speed. The complex nature of the full texture analysis techniques and the large number of parameters in these models, meant that it was unfeasible to use them as PO models in structure refinement packages until recently. As a consequence, in structure refinement, PO is often modelled by an analytic function of one variable that is easy to compute with one or two parameters (varied during refinement) that describe the shape of the function. By making some assumptions about the nature of the PO in the sample (discussed later), the function is used to describe the orientation distribution of a particular (hkl)-plane. This orientation distribution can be related, by symmetry, to the orientation distribution of other (hkl)-planes contributing to the diffraction pattern. Several functions have been used in structure refinement packages, often with little theoretical justification, and the most common ones are compared in Dollase (1986). Unfortunately, the PO corrections in refinement

packages are often only applicable to one particular diffraction geometry (commonly the Bragg-Brentano geometry of many powder diffractometers) and are not generally applicable to the DAC transmission geometry used in high-pressure powder diffraction with image-plates.

The next section describes the application of two models of PO to 2-d image-plate data. A model based on the simple analytic function model often found in Rietveld refinement packages is presented together with a description of a useful graphical construction developed by Wright (1994) to aid qualitative understanding of simple uniaxial PO. This model is applied to the quantitative study of severe pressure-induce PO in HgS at ambient pressure. As will be demonstrated, the simple analytic function model is not wholly adequate for describing strong PO. This has led to the application of the symmetrised spherical model used in texture analysis to image-plate data.

4.3 Preferred Orientation Modelling

Figure 4.1 shows the coordinate system (the IP frame) used to describe the data collected on the image-plate set-up. The intensity at a given point on the image-plate, $(2\theta, \gamma)$, is the sum of the intensities of the n reflections, (H_i, K_i, L_i), that satisfy the Bragg condition $\lambda = 2d_{HKL} \sin\theta$. Each reflection, (H_i, K_i, L_i), contributing to the diffracted intensity consists of M_i symmetry equivalent reflections, (h_j, k_j, l_j). The total diffracted intensity at $(2\theta, \gamma)$ can be written:

$$I(2\theta,\gamma) = \sum_{i=1}^{n} \frac{I_i}{M_i} \sum_{j}^{M_i} P_j(\mathbf{h}_j, \mathbf{q}) \tag{4.1}$$

where I_i ($= I_0 |F_{hkl}|^2 \lambda^3 V L_p A$, after Equation 3.6) is the intensity of reflection (H_i, K_i, L_i). $\mathbf{h}_j$ is the unit vector parallel to the reciprocal lattice vector defined by the crystal planes, (h_j, k_j, l_j) and the unit cell of the material being studied. $\mathbf{q} = \mathbf{q}(2\theta, \gamma)$ is a unit vector in the sample. $P_j(\mathbf{h}_j, \mathbf{q})$ is the probability density

of finding the reciprocal lattice vector $\mathbf{h}_j$ oriented parallel to $\mathbf{q}$—i.e. $P_j(\mathbf{h}_j, \mathbf{q})$ is proportional to the volume fraction of the crystallites whose reciprocal lattice vector $\mathbf{h}_j$ falls within the solid angle $d\Omega$ about the direction $\mathbf{q}$. For non-textured samples $P_j = 1$.

In texture analysis I_i is known so the orientation distribution $P_j(\mathbf{h}_j, \mathbf{q})$ can be related directly to the measured intensity I. However, in an unknown high-pressure phase, both I_i and P_j are unknown. To determine both I_i and P_j some assumptions must be made about the form of P_j.

4.3.1 Simple Analytic Model

The simple analytic model of preferred orientation (PO) is commonly used in Rietveld refinement programs to correct for PO. The model describes simple preferred orientation in powders arising from the tendency of certain crystalline planes to align with a certain direction in space. In particular, the morphology of the crystallites in the powder is assumed to be rod- or disc-shape (i.e. the crystallites are significantly longer or shorter in one direction). PO in samples with disc-shaped morphology, for example, can develop from the natural tendency of the normals to the disc plane to align nearly parallel.

More generally, it is assumed that there is one set of crystal planes, defined by a reciprocal lattice vector called the preferred orientation direction (POD), which has a tendency to align either parallel to or perpendicular to an axis in space—the preferred orientation axis (POA). These crystal planes will be either parallel to the disc plane of disc-shaped crystallites or perpendicular to the rod axis of rod-shaped crystallites. Two assumptions are included in this type of model: (i) the orientation distribution of the POD is assumed to be axially symmetric about the POA and, (ii) the distribution of crystallites around the POD (defined by a reciprocal lattice vector) is also assumed to be axially symmetric giving rod- or disc-shaped behaviour. Given these assumptions, the orientation distribution

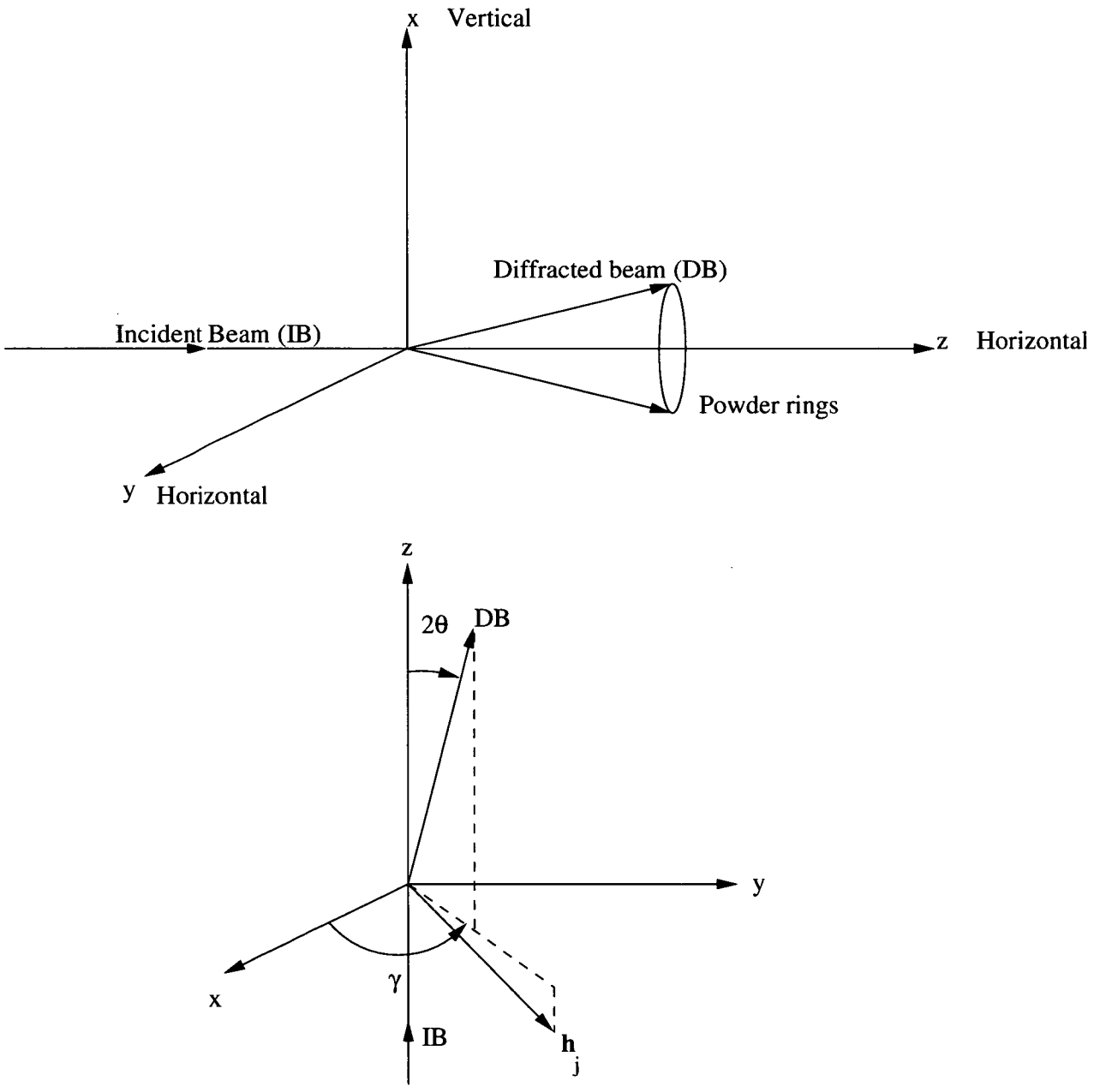


Figure 4.1. The coordinate system used to describe the image-plate data. 2θ is the Bragg angle of the reciprocal lattice vector $\mathbf{h}_j$ and γ is the angle around the powder rings.

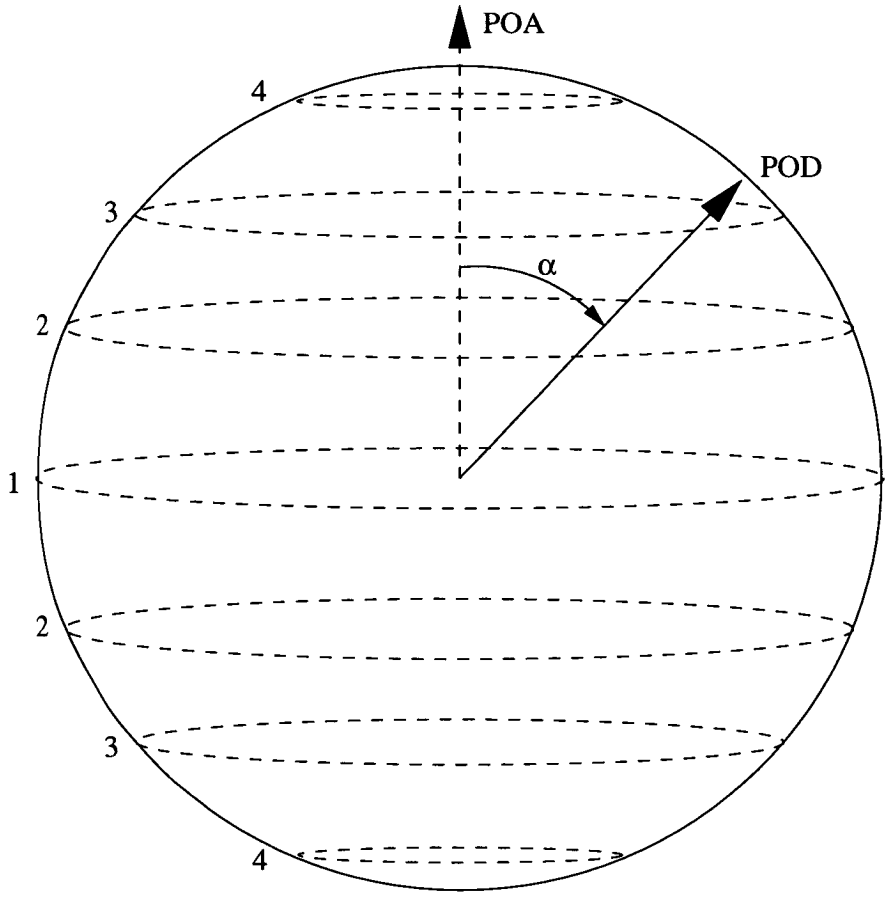


Figure 4.2. The distribution of crystallites in a sample with axially symmetric PO can be represented by contours on a sphere. The values of the contours are given by a simple analytic function of one variable, α, the angle between the preferred orientation axis (POA) and the preferred orientation direction (POD—the reciprocal lattice vector whose ODF is described by the function).

of the POD can be described by a simple function of one variable (the angle between the POD and POA) and one or two parameters that define the 'shape' of the function. The function gives the probability density of finding a single crystallite with its POD oriented at a given angle to the POA.

Qualitative 2-D Analysis of PO

A graphical construction developed by Wright (1994) is particularly useful for visualising preferred orientation of the type described above. Such a distribution can be visualised as contours on a sphere, as shown in Figure 4.2. The values of

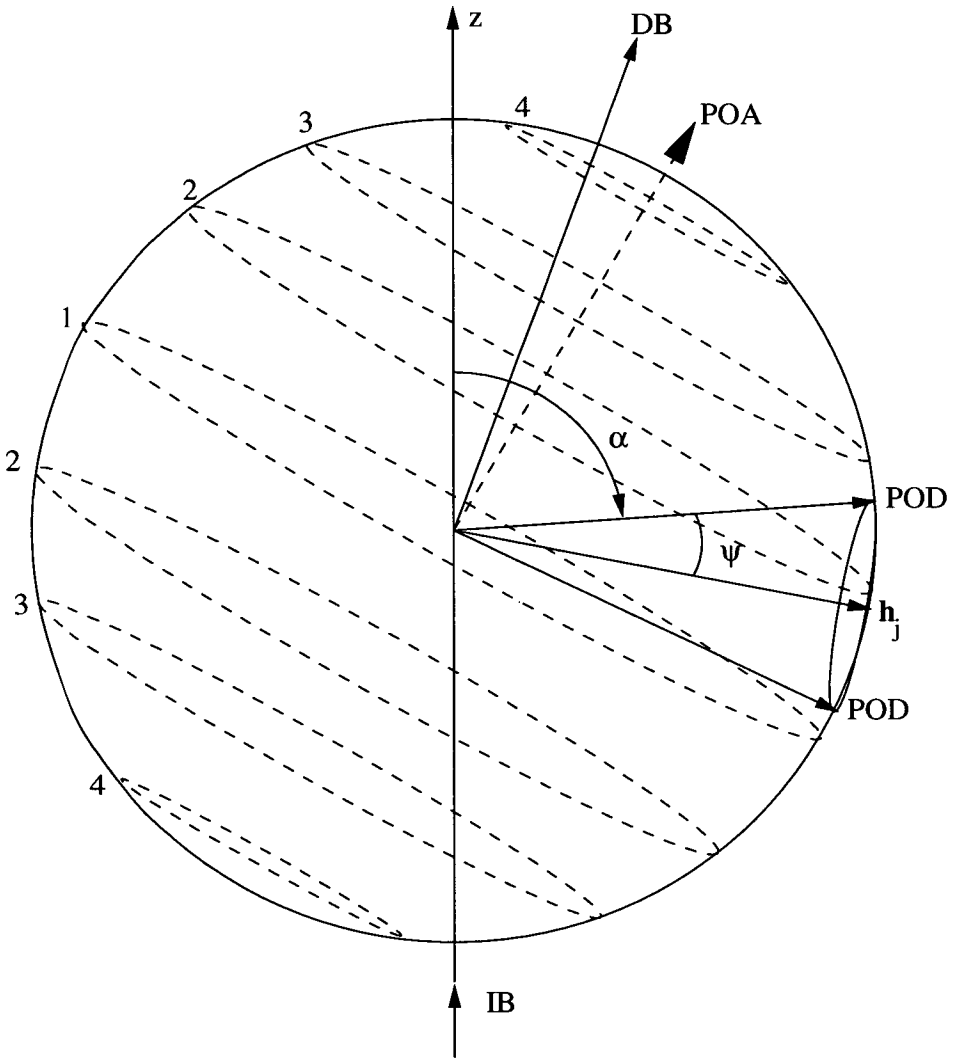


Figure 4.3. For the scattering vector $\mathbf{h}_j$—which makes an angle ψ with the reciprocal lattice vector that defines the POD—all the crystallites with their PODs lying in a cone of half angle ψ around the scattering vector contribute to the intensity of the diffracted beam (DB). The figure represents the general case where the POA is inclined to the incident beam (IB).

the contours are defined by the function describing the orientation distribution of the POD, which is function of the angle α between the POD and the POA. The distribution of the other reciprocal lattice vectors are related to the distribution of the POD by knowing the angle between the reciprocal lattice vector of interest and the POD, which requires knowledge of the crystal symmetry and indexings. For an arbitrary scattering vector, $\mathbf{h}_j$, that makes an angle ψ to the POD, all crystallites with their POD vector lying on a cone of half-angle ψ about the scattering vector satisfy the diffraction condition. Figure 4.3 represents the general case where the POA in inclined to the incident beam (IB). The intensity of the diffracted beam (DB) is proportional to number of crystallites contributing to the diffraction from the scattering vector, $\mathbf{h}_j$, which in turn is proportional to the value of the orientation distribution function of the POD averaged over the cone shown in Fig. 4.3.

Figure 4.4 shows the general case of the beam striking the sample at an angle β to the POA. The diffracted intensity at 0°, 90° and 180° azimuthal angle on a powder ring is represented by the three POD cones shown. The origins of the intensity variations around the powder rings in a 2-d image are revealed in this construction. As can be seen the POD cones at points 1 and 2 are averaged over contours of higher value than the contours over which the POD cone at point 3 are averaged. The intensity at points 1 and 2 will be greater than the intensity a point 3. On closer inspection, the intensity at point 2 can be seen to be higher than the intensity at point 1 since the POD cone at point 2 is averaged over contours with values between ~2.2 and ~3.5; whereas the POD cone at point 1 is averaged over contours with values between ~1.2 and ~2.7.

The POD cones in Fig. 4.4 are the POD cones for a scattering vector that makes a small angle (ψ) to the POD. The POD cone of a scattering vector that makes a large angle to the POD is shown in Figure 4.5. The POD cone at point 2 is averaged over contours with values between ~1 and ~3.8. The POD cone of point 3 (not shown in Figure 4.5 as it lies in the plane of the page) is averaged

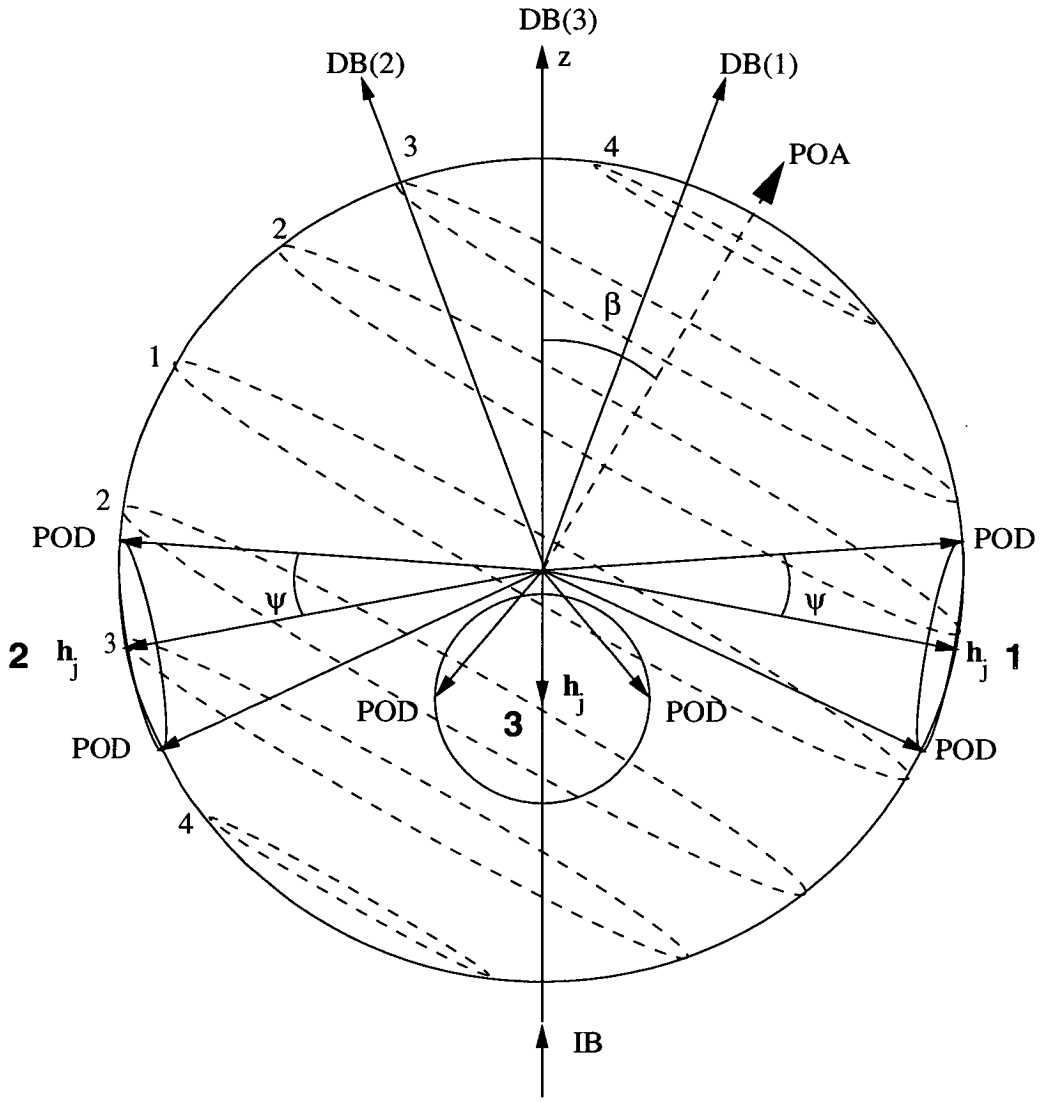


Figure 4.4. The general case of the beam striking a powder sample at angle β to the POA.

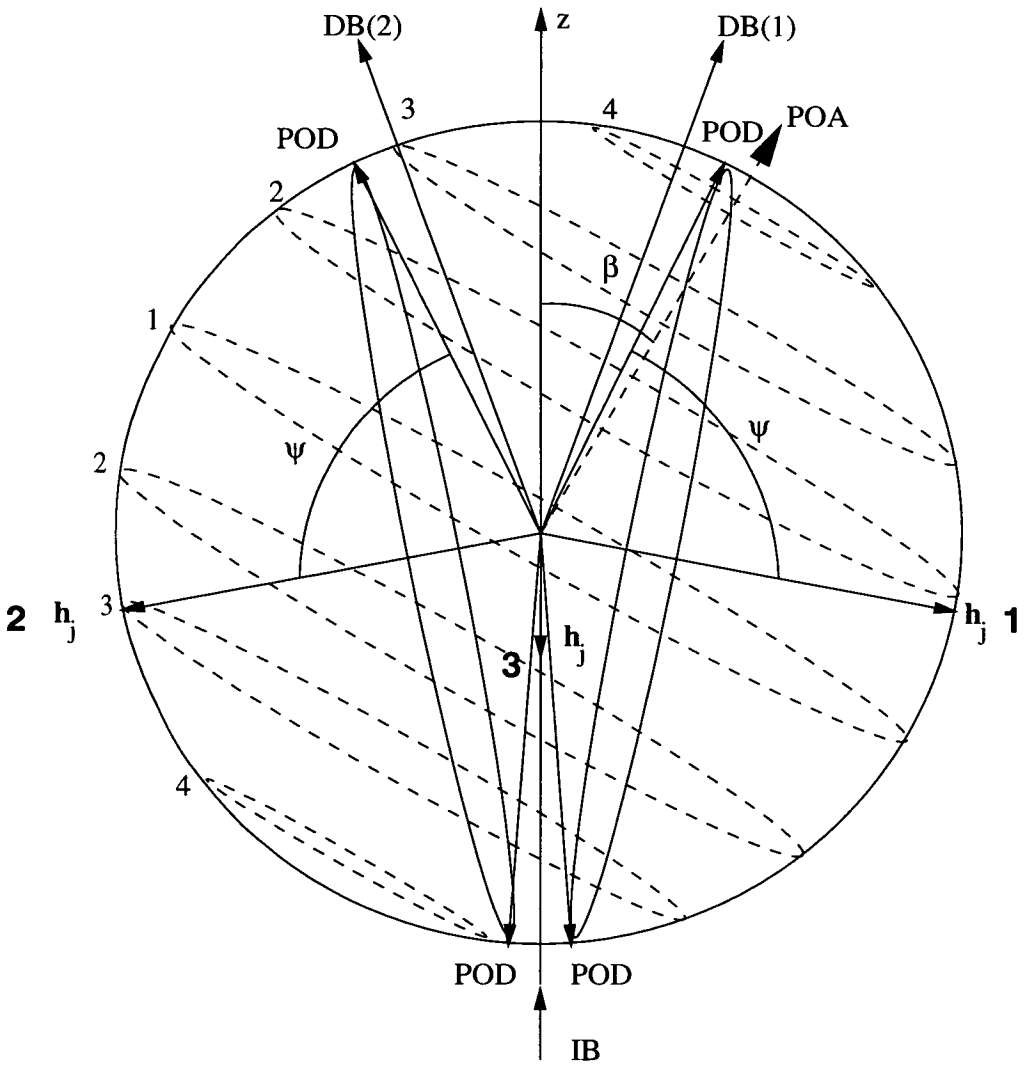


Figure 4.5. The POD cone of a scattering vector that make a large angle with the POD.

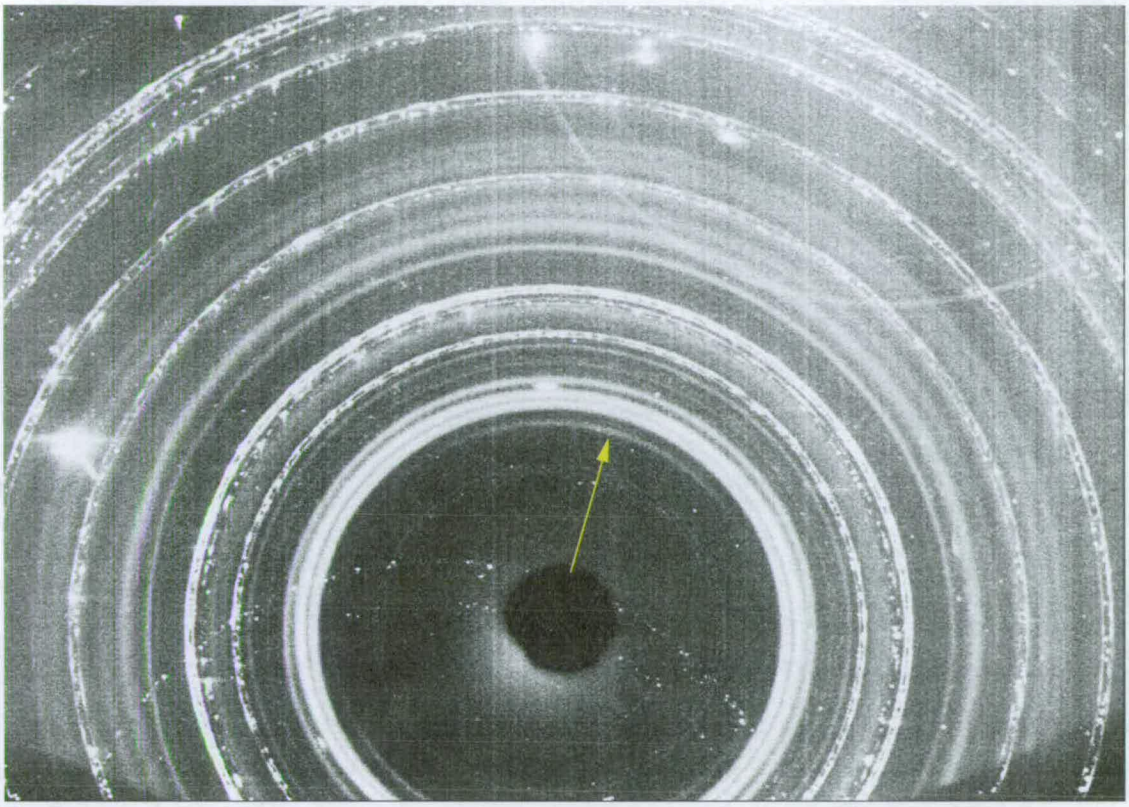


Figure 4.6. A 2-d image of an inclined sample of CsI at 55 GPa, which has strong PO.

over all the contours on the sphere and, thus, has higher average intensity than point 2. The POD cone of point 1 sweeps out nearly all the contours on the sphere so has higher intensity than point 2 but slightly lower intensity than point 3. The points of maximum intensity around the powder ring of the scattering vector shown in Fig. 4.5 occur near the points of minimum intensity around the powder ring of the scattering vector drawn in Fig. 4.4, and vice versa. Thus, the nature of the intensity variations around a powder ring of a sample with PO are determined by the angle the scattering vector makes with the POD, which in turn depends on the indexing of both the POD and the scattering vector and the unit cell parameters.

Even without a full quantitative model of PO, it is still possible to gain a qualitative feel for the PO in the sample with the help of the graphical construction

presented above. Figure 4.6 shows a 2-d image of a sample of CsI at 55 GPa inclined at 30° to the incident beam. The intensity variations around the arrowed ring in Fig. 4.6 reveal immediately the presence of PO in the sample. The image is contaminated with Be powder rings from the Be backing discs of the cell, which, unfortunately, is unavoidable. However, not all of the sample rings are overlapped by Be rings and PO analysis can normally proceed even with the presence of this unwanted contamination. There is some doubt about the published indexing and unit cell for this phase of CsI—Mao *et al.* (1990), have published an orthorhombic structure with spacegroup Pm2m. But, although knowledge of these parameters is necessary to carry out full quantitative analysis of PO, the graphical construction presented above can still useful for qualitative analysis of PO.

By using a PO-sphere diagram, it can be demonstrated that the intensity variation around the arrowed ring is characteristic of the intensity variation expected from a reflection that has low multiplicity and that makes a small angle (ψ) with the POD (and may even be the POD). Figure 4.7 shows the PO-sphere that describes the intensity variation seen around the arrowed ring in Fig. 4.6. The POA is inclined at an angle β to the incident beam. The two scattering vectors that lie in the horizontal plane for this reflection are represented on the diagram. The half-angle of the POD cone is assumed to be close to zero because the most intense parts of the powder ring lie in the horizontal plane so the average of the contours over the POD cone should be highest at these points. This condition is satisfied if the POD cone has a half-angle equal to zero.

It is possible, in this type of PO model, for the POD to have an orientation distribution that has its maximum contour at 90° to the POA and its minimum contour at 0° to the POA—this describes the intuitive distribution of rod-shaped crystallites that all have their cylindrical axis of symmetry lying in the same plane whose normal is coincident with the POA. Such a distribution is shown in Figure 4.8. In this case, the condition that points 1 and 2 are maxima means that

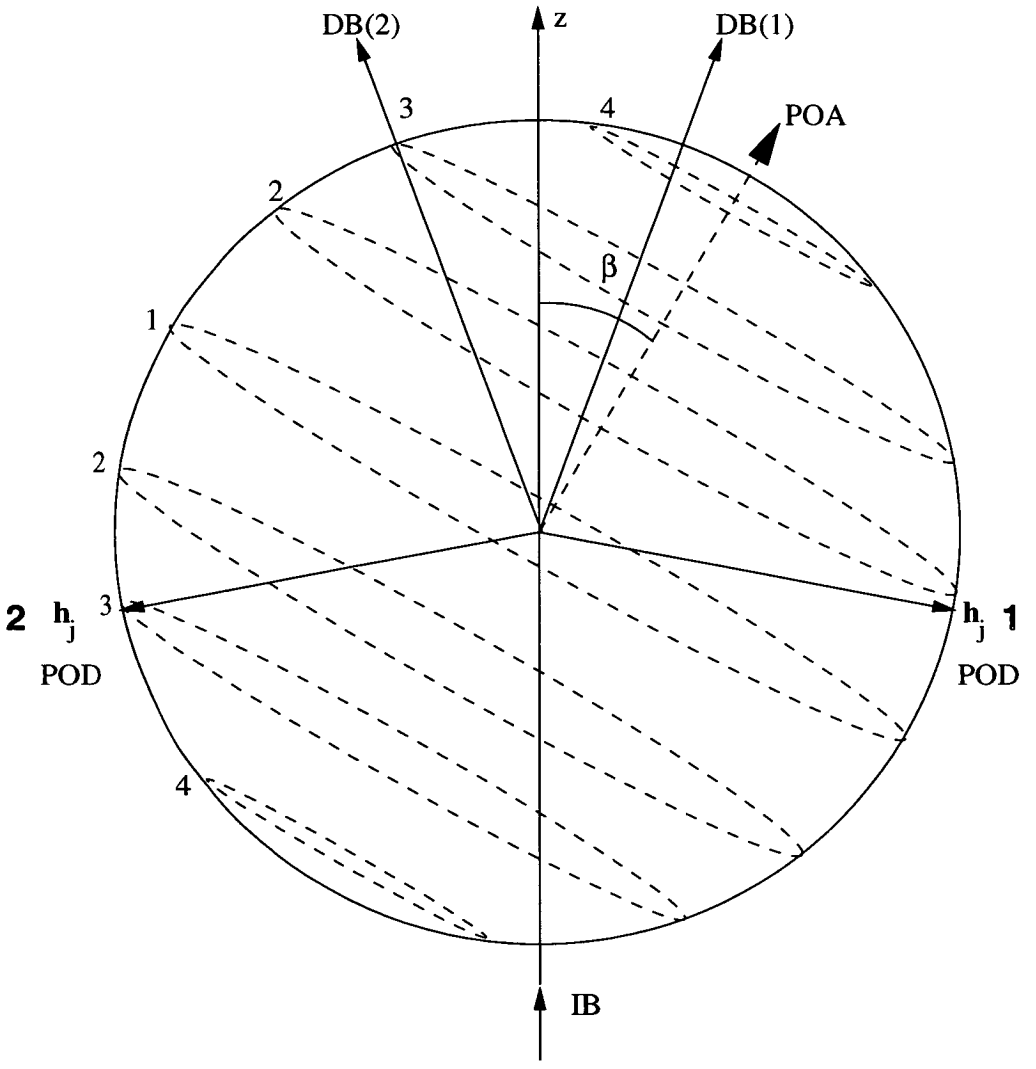


Figure 4.7. The PO sphere representing the diffraction at two points (lying in the horizontal plane) on the arrowed powder ring in Fig. 4.6.

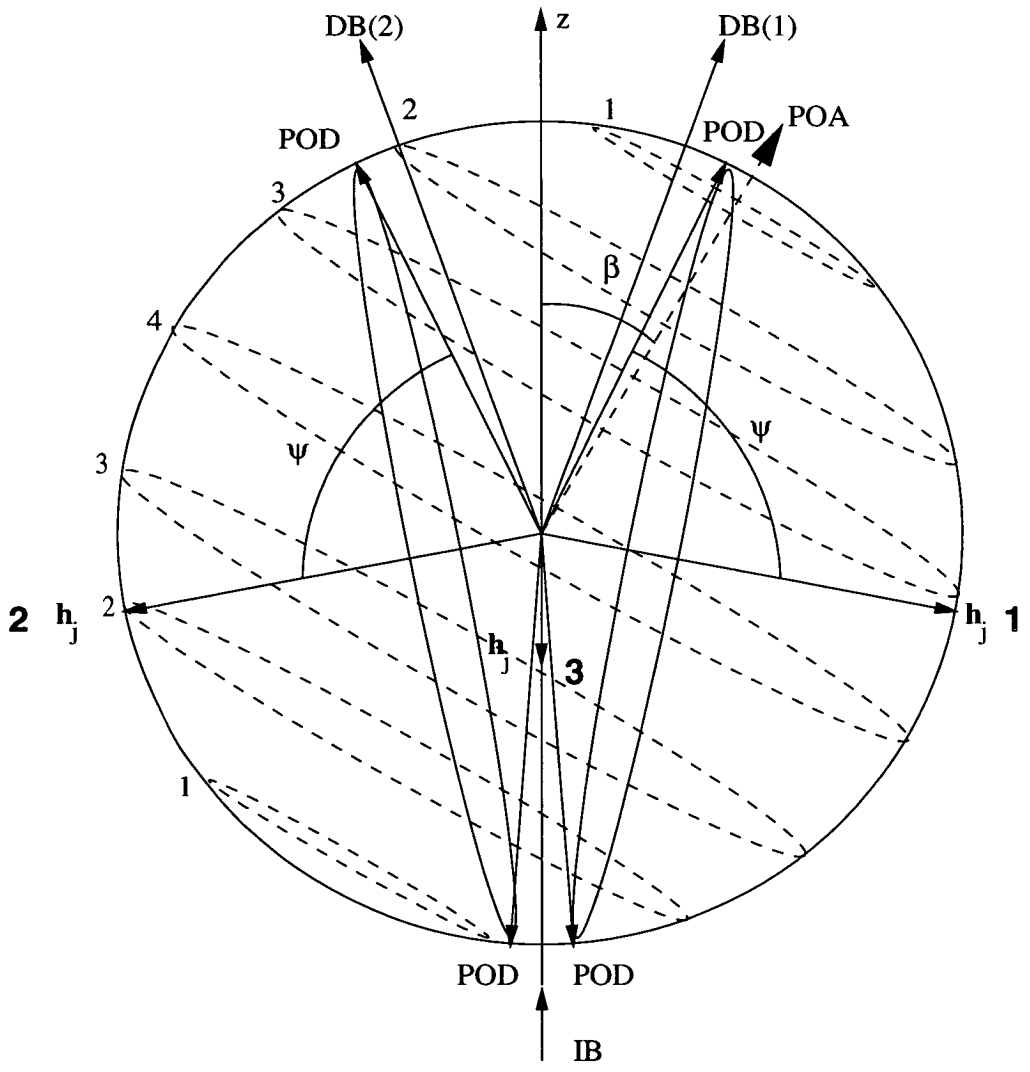


Figure 4.8. The PO sphere representing the distribution of rod-shaped crystallites where the maximum contour lies at 90° to the POA. For points 1 and 2 to have higher intensity than point 3—as required to describe the intensity variations around the arrowed powder ring in Fig. 4.6—the POD cone must have half-angle close to 90°.

the POD cone must have a half-angle close to 90°. When the sample is inclined to the beam (as shown in Fig. 4.8), the POD cone at these points will be averaged over fewer low value contours than the POD cone of the scattering vector at point 3 on Fig. 4.8—90° further round the ring from point 1—thus, points 1 and 2 will have higher average intensity. But even for severe PO, the difference between the maximum and minimum observed intensity around the ring when the POA is inclined at a modest angle to the incident beam (say, 30°) cannot be large enough to describe the range of intensity seen around the arrowed ring in Fig. 4.6. The reason for this is that the lowest intensity point for 90° half-angle POD cones (point 3 in Fig. 4.8) is always averaged over the highest value contours on the PO sphere, so the intensity at this point cannot be significantly lower than the intensity at points 1 and 2, even for extremely strong PO. Consequently, the PO model that best describes the intensity variation observed in this case is the disc-shape crystallite model—where the maximum of the distribution lies along the POA—with the POD cone half-angle close to zero, as shown in Fig. 4.7.

The intensity of the maxima at points 1 and 2 is asymmetric. This arises from the fact that the scattering vectors lie at an angle $90+\theta$ to the incident beam. Thus, as the POA is inclined, the scattering vector at point 2 passes through the minimum contour before passing through higher valued contours, while the scattering vector at point 1 starts to pass through higher valued contours immediately. The sample was inclined at 30° to the incident beam during the collection of the image shown in Fig. 4.6, but the POA need not be coincident with the pressure cell axis. However, inspection of the 2-d image when the sample is not inclined to the beam, shows little intensity variation around the powder rings so the POA must lie almost along the pressure cell axis and the symmetry of the PO in the sample can be assumed to be close to axial about the POA.

The intensity at points 1 and 2 was measured as a function of sample inclination, ω. Figure 4.9 is a plot of these measured intensities with the best-fit polynomial through these points plotted as solid lines. In a sample with axial PO, when

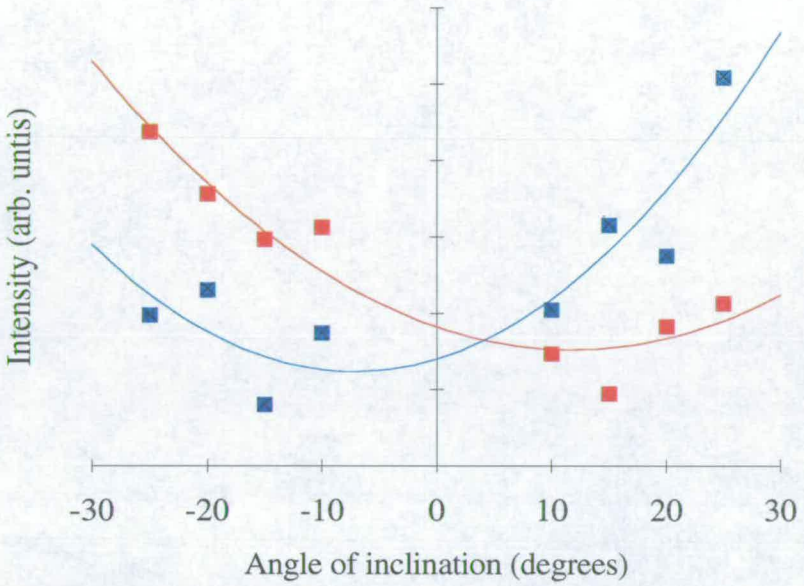


Figure 4.9. A plot of the change in intensity at points 1 and 2 on the image shown in Fig. 4.6 as a function of sample inclination. The solid lines are the best fit polynomials through the measured data.

the POA lies along the incident beam the intensities at points 1 and 2 should be equal. The fits to the data are equal at $\omega \sim 4°$ which is consistent with the fact the POA lies nearly along the pressure cell axis. The data also show a four-fold intensity difference between the lowest and highest intensity values over the measured range $-30° < \omega < +30°$, which implies that the sample has very severe PO.

Useful qualitative information about the PO in a sample can be obtained from the combination of inclined samples and 2-d data. The next step, to take full advantage of 2-d data, is to develop a quantitative model of PO, and fit the intensity variation around the powder rings of a 2-d image.

Quantitative 2-D Analysis of PO

A variety of simple analytic functions have been proposed in the literature to describe the orientation distribution of the POD, in most cases, with little theoretical justification. The functions, as applied in Rietveld refinement packages,

are also often not generally applicable to all experimental geometries—they are commonly limited to Bragg-Brentano geometry where the all the scattering vectors are assumed to be parallel to the POA. Rietveld originally used a Gaussian form for the PO function (Uda (1967) and Rietveld (1969)):

$$P(\alpha) = \exp(-G\alpha^2) \tag{4.2}$$

where α is the angle between the POD and the POA, and G is an adjustable parameter that reflects the strength of preferred orientation in the sample. In practice, this function has been found to have too small a value at high values of α when G is large enough to fit strong PO (Sasa and Uda (1976), Toraya and Marumo (1981)). Sasa and Uda (1976) modified this function to overcome this problem by adding a second adjustable parameter, b:

$$P(\alpha) = b + (1 - b)\exp(-G\alpha^2) \tag{4.3}$$

The addition of parameter, b, effectively describes a powder where only a proportion, $(1 - b)$, of the crystallites in the sample exhibit preferred orientation. Another function, proposed by Will *et al.* (1983), is a non-Gaussian exponential:

$$P(\alpha) = \exp(G(\pi/2 - \alpha)^2) \tag{4.4}$$

This function, however, has a cusp at $\alpha = \pi/2$ (i.e. it has a non-zero derivative at this point) which is a physically unreasonable form for a probability distribution. Čapkova and Valvoda (1974) proposed another pseudo-Gaussian form for P:

$$P(\alpha) = \exp(-G(1 - \cos^n(\alpha)) \tag{4.5}$$

where n is an integer greater than one. For odd n, this function is not symmetric

about $\alpha = \pi/2$, which is a necessary requirement imposed by the symmetry of the problem. However, it can be forced to be symmetric during computation by multiplying $\cos(\alpha)$ by -1 if $cos(\alpha) < 0$.

Dollase (1986) compared the functions above together with a new simple analytical function based on the analysis of March (1932):

$$P(\alpha) = (G^2 \cos^2 \alpha + G^{-1} \sin^2 \alpha)^{-3/2} \tag{4.6}$$

The March model is a theoretical description of the rotation of disc- or rod-shaped crystallites caused by a volume-conserving compression of the sample along one axis. Such a model effectively describes the conditions of compression suffered by a sample at high-pressure in a DAC. Until recently, only Equation 4.6 had a full theoretical justification, but the use of Equation 4.5 as a description of PO has recently been given some theoretical justification by Peschar *et al.* (1995). Equation 4.6 is also normalised so that it has unit integral for all values of the parameter G; a normalisation constant has to be calculated for the other functions for every value of G used with them. $P(\alpha)$ is normalised by dividing by a normalisation constant N, which depends on the value of the parameter G:

$$N = \frac{1}{4\pi} \int_0^{2\pi} \int_0^{\pi} P(\alpha) \sin \alpha \, d\alpha \, d\Theta = \frac{1}{2} \int_0^{\pi} P(\alpha) \sin \alpha \, d\alpha \tag{4.7}$$

Any of the functions above can be used to describe the distribution of the POD. The proportion of crystallites contributing to the intensity at a given point on the 2-d image from a given reflection can be calculated by averaging over the appropriate POD cone. To do this, requires the calculation of the angle α for all points on the cone, which can be obtained from the following equation (Wright (1994) gives the full derivation):

$$\begin{aligned}\cos\alpha &= \sin\beta\cos\phi(-\sin\gamma\sin\psi_j\cos\delta + \sin\theta\cos\gamma\sin\psi_j\sin\delta + \cos\theta\cos\gamma\cos\psi_j) \\ &+ \sin\beta\sin\phi(\cos\gamma\sin\psi_j\cos\delta + \sin\theta\sin\gamma\sin\psi_j\sin\delta + \cos\theta\sin\gamma\cos\psi_j) \\ &+ \cos\beta(\cos\theta\sin\psi_j\sin\delta - \sin\theta\cos\psi_j)\end{aligned} \tag{4.8}$$

where θ is the Bragg angle of reflection j; γ is the angle around the powder ring; (β, ϕ) are the spherical polar coordinates that define the direction of the POA in the IP frame shown in Fig. 4.1; ψ_j is the angle between the scattering vector, $\mathbf{h}_j$, and the reciprocal lattice vector that defines the POD (i.e. half-angle of the POD cone); and δ parameterises the vectors that define the POD cone. Averaging around the POD cone is now equivalent to integrating $P(\alpha)$ with respect to the parameter δ in Equation 4.8:

$$P_j(\mathbf{h}_j, \mathbf{q}) = \frac{1}{2\pi}\int_0^{2\pi} P(\cos\alpha_j)\, d\delta \tag{4.9}$$

The actual function used for $P(\cos\alpha_j)$ can be chosen from any of the equations given above although only the March-Dollase equation (Eqn. 4.6) is based on a physical mechanism. In practice, Equation 4.9 has to be evaluated by numerical integration.

The author has written a program, called 'POFIT', that can fit the model detailed above to the intensity variations around the powder rings caused by PO. The program performs a least-squares refinement of the parameters in the model and can fit the data from many powder rings simultaneously. The ability to fit data from many rings at once is important since the intensity variations from each ring probe a different part of the orientation distribution and, and because of this, a multiple-ring fit places much stricter constraints on the PO model than a single-ring fit. For example, in the model detailed above, if the POA is tilted at, say, 30° to the incident beam, the range of α that is covered, around the entire ring, by a reflection whose scattering vector is coincident with the POD (i.e. the POD cone

has zero half-angle) is $0 \ldots 30+\theta$ degrees. There is no information contained in the intensity variations around this ring about the form of the distribution between $\alpha = 30 + \theta \ldots 90°$ and the assumed form of one of the equations 4.2 to 4.6 has to be used to predict the unknown part of the distribution. For a reflection whose scattering vector makes a large angle, ψ, with the POD, the intensity at each point on the powder ring depends on the integration around the POD cone so, again, only partial information about the orientation distribution can be obtained from the intensity variation around such a ring. But, by combining the information from powder rings with different POD cone angles, a much more accurate determination of the orientation distribution can be made.

POFIT can refine any of the variable parameters in Equation 4.1: the POA direction (β, ϕ); the PO parameter, G; a constant background parameter, B; the intensity of each reflection, I_i; the Bragg angle of each reflection, θ_i; and the POD cone half-angle, ψ_j, for every symmetry equivalent scattering vector contributing to each reflection in the powder ring. Generally, the background is subtracted during the extraction of the intensity around the rings and is set to zero in during refinement. It has also been found that the background parameter is highly correlated with the form of the fitted intensity variations defined by the intensity, I_i, the PO parameter, G, and POA direction, (β, γ). So it is essential to fix the background parameter during refinement. The angles θ_i and ψ_j are normally fixed—although they are refineable—and are calculated from the known lattice parameters, the wavelength of the incident beam and the indexing of reflection i, which consists of j symmetry equivalent reflections.

POFIT has also been designed to allow easy modification of the PO model and, initially, any one of the five equations, 4.2 to 4.6, could be chosen to model the orientation distribution by selecting the appropriate 'switch' in the input parameter file. Subsequent versions of POFIT incorporate the absorption correction of Section 3.4.2 as part of the fitting function as well as a new PO model based on a series expansion of symmetrised spherical harmonics, which will be presented

in Section 4.3.2 below.

Fitting Strong PO in HgS at Ambient Pressure

HgS is the prototype cinnabar structure at ambient pressure. Cinnabar has a hexagonal lattice (a = 4.15 Å, c = 9.50 Å) and is stable over a wide pressure range—ambient pressure to ~22 GPa—where it changes phase to the NaCl-type structure. Very strong PO can be induced in the cinnabar phase of HgS by the application of pressure. The PO is axially symmetric about the pressure cell axis as confirmed by the absence of any intensity variation around the powder rings in the 2-d images collected from non-inclined samples of HgS with strong PO. And, fortuitously, the strong PO induced at high pressure is retained on pressure release to ambient pressure. This allows the sample, in the gasket, to be removed from the pressure cell and used to obtain an image of the inclined sample without the presence of Be scatter which is unavoidable if the inclined sample is enclosed in a pressure cell.

Figure 4.10 shows a 2-d image obtained from such an inclined sample of HgS at ambient pressure with the 1-d integration of the image shown below the 2-d image. The gasket containing the sample was fixed to a lead mount and inclined to the incident beam by 50° (i.e. the cylindrically symmetric axis of the gasket made a 50° angle with the beam). The image shows the large variations in intensity around the powder rings caused by very strong PO in the sample. The sample was loaded, as described in Chapter 2, in a Mao-Bell cell, and pressure was applied in ~3 GPa steps up to 18 GPa. Strong PO can be reproducibly induced in HgS by the application of pressure. The changes in the preferred orientation in the sample start to occur at ~12 GPa and the strength of the PO continuously increases until ~22 GPa where HgS transforms into the NaCl phase.

Figure 4.11 shows the intensity as a function of angle, γ, around the (003), (103) and (110) powder rings of Fig. 4.10 as marked by the arrows labelled A, B and C

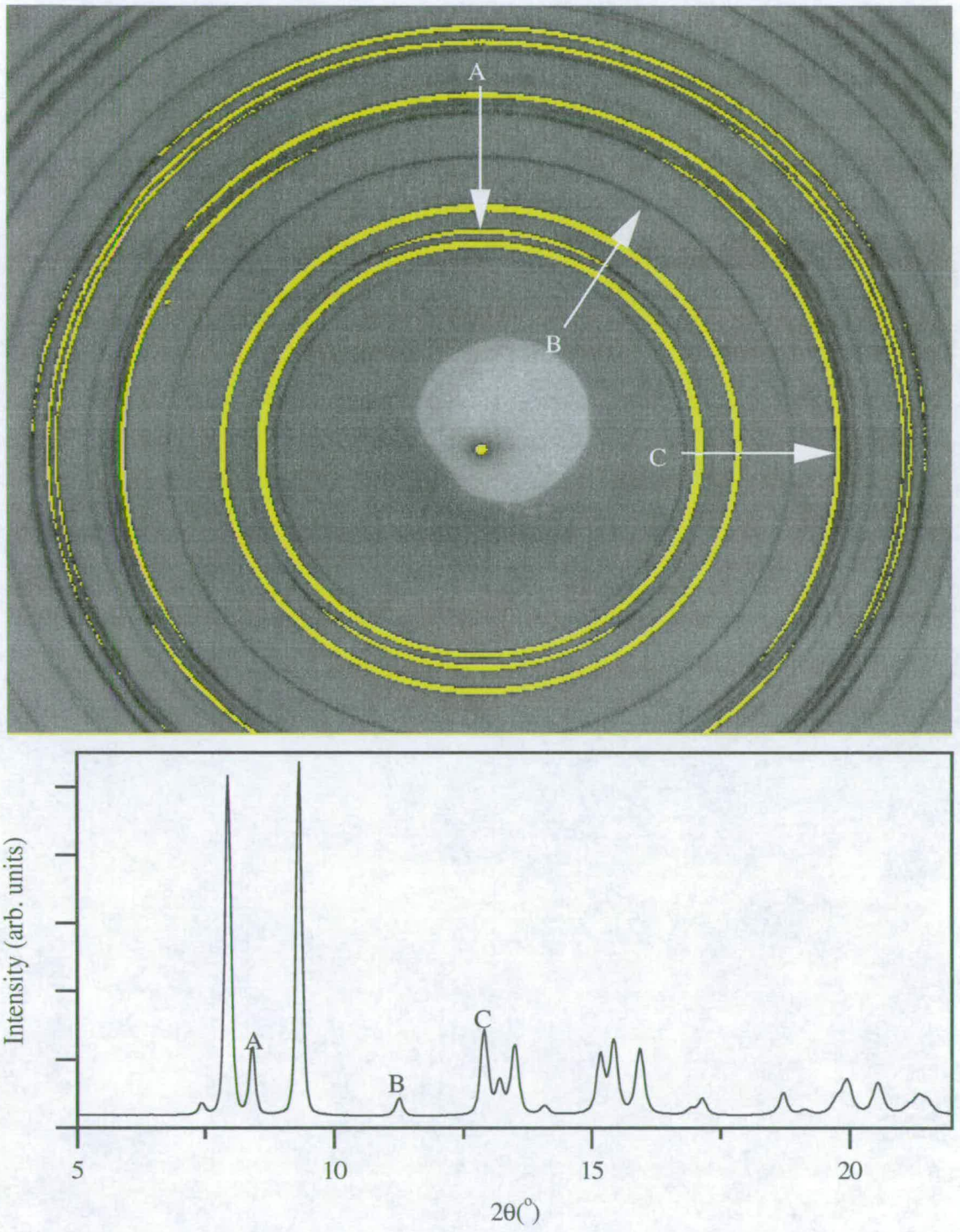


Figure 4.10. A contrast enhanced image from an inclined sample of HgS at ambient pressure mounted in a gasket hole. The yellow colour marks pixel whose intensity is above a certain value while the other pixels are represented by an inverse grey-scale. This method of viewing the image clearly shows the large intensity variations around the powder rings due to PO.

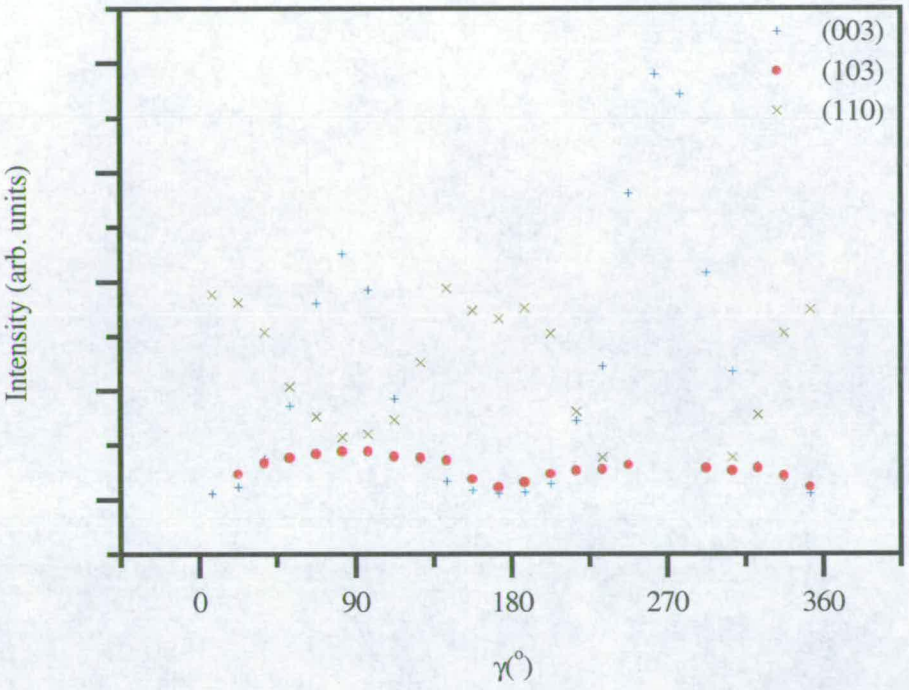


Figure 4.11. The extracted intensity as a function of azimuth around the (003), (103) and (110) powder rings marked by the arrows labelled A, B and C respectively in Fig. 4.10

respectively. The image was sectored into 24 1-d plots as described in Section 3.4.1 in Chapter 3. The intensities were extracted by fitting a pseudo-Voigt peak to the corresponding peak in each of the 24 1-d plots. The intensity variations of the (003) are characteristic of a reflection whose scattering vector makes a small angle, ψ, with the POD—asymmetric maxima 180° apart lying in the plane of inclination—thus the (001) direction was chosen as the POD. With this choice of POD and given the ambient pressure lattice parameters of HgS, the POD cone half-angles, ψ, of the (003), (103) and (110) are 0°, 41.41° and 90°, respectively. Generally, all the symmetry equivalent planes contributing to a given reflection (hkl) do not make the same angle with POD. However, in hexagonal systems, when the POD is coincident with the $(00l)$ reciprocal lattice vector a special case arises where all the symmetry-equivalent planes of a reflection make the same angle with the POD and the distribution of only one member of a symmetry-equivalent set needs to be calculated. Similar special directions exist in the other

Parameter	β fixed	β refined
β	50°	80.11(7)°
ϕ	88.11(4)°	87.02(3)°
G	0.4887(5)	0.5054(4)
χ^2	33485	13437
R_{wp}	0.547	0.347
S	23.62	15.11

Table 4.1. The results of two simultaneous March-Dollase fits to the marked rings in Fig. 4.10. In one fit the polar angle of the POA (β) was fixed at 50°, in the other β was allowed to refine.

crystal systems (except cubic), these are discussed in Čapkova *et al.* (1993).

The March-Dollase function (Equation 4.6) was fitted to the three marked rings simultaneously. Figure 4.12 shows the results of the fit. As can be seen, the March-Dollase function has trouble describing the PO in this sample. Although it accounts for the general variations observed, the March-Dollase function is unable to describe the very strong PO in the sample. Initially, POFIT could only perform single ring fits and the fits obtained this way were good. However, when the parameters obtained from a single ring fit were used to calculate the expected intensity variations around other rings, the agreement was not so good. This highlighted the need to be able to perform simultaneous fits to many rings.

The fit shown in Fig. 4.12 was obtain by refining the reflection intensities, the PO parameter, G, and the azimuthal angle of the POA direction, ϕ. The absence of any intensity variations around the powder rings in the images from the non-inclined sample suggests that the POA lies very near to the samples cylindrical axis of symmetry (i.e. nearly along the incident beam direction in the non-inclined setting), therefore, when the sample is inclined to the beam by 50°, the polar angle of the POA direction, β, must be close to $\beta = 50°$ and was fixed at this value. A better fit could be obtained by refining β as well, but the refined value was physically unreasonable ($\beta = 80.11(7)°$). The full results of the two fits are tabulated in Table 4.1. The PO parameter, G, is small, indicating strong PO

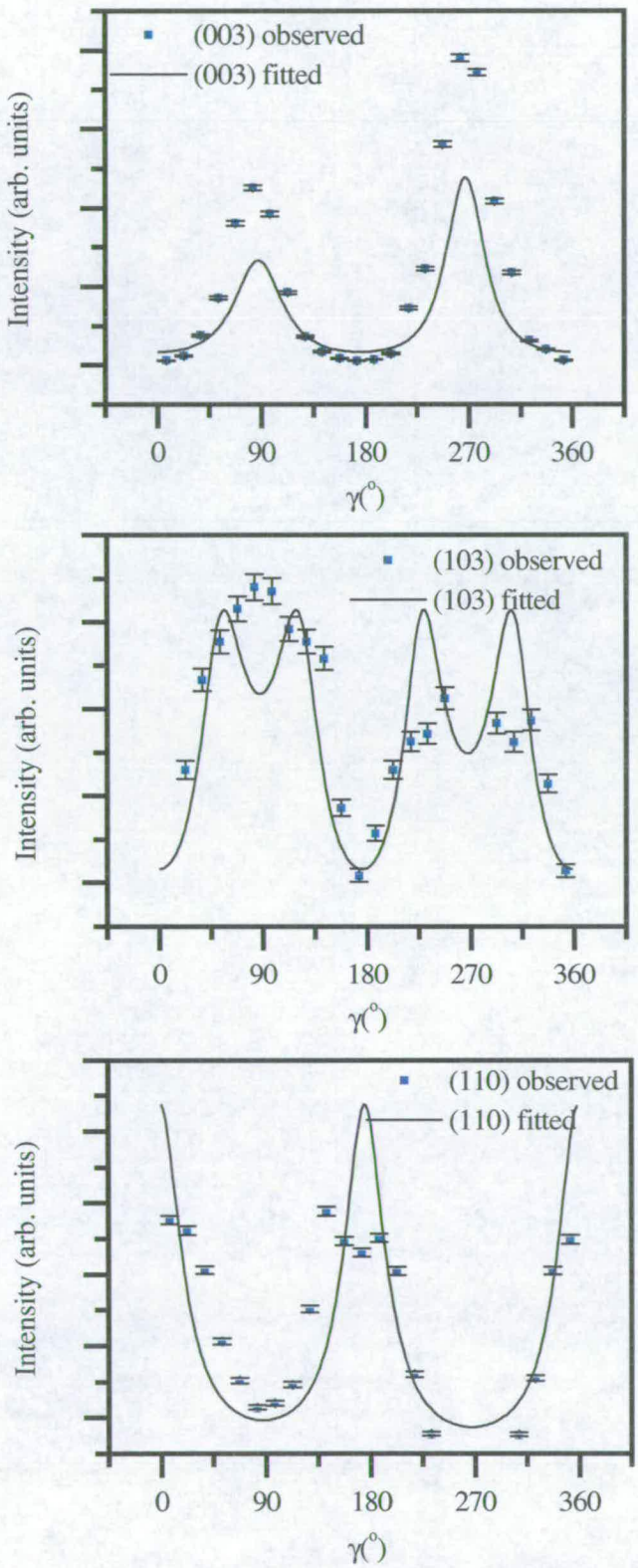


Figure 4.12. A multi-ring fit of the March-Dollase function to the intensity as a function of azimuth around the marked rings in Fig. 4.10.

(for an ideal powder $G = 1$). The tendency for β to refine to a higher value than expected arises from the inability of the chosen orientation distribution function to account for the extreme intensity variations observed; a more pronounced intensity variation can be calculated by increasing the angle between the incident beam and the POA. For a sample where the POA direction cannot be determined experimentally, the polar and azimuthal angle defining the POA direction necessarily become refineable parameters. Unfortunately, as demonstrated, the accuracy of the refined POA direction from a sample with strong PO cannot be guaranteed when fitting with the March-Dollase function.

4.3.2 Symmetrised Spherical Harmonic Model

To try to increase the accuracy of the modelling of strong PO, it was decided that new model of texture should be investigated. The most common model used by the texture analysis community is based on the theory of Bunge (1982) which represents the orientation distribution of crystallites by a series expansion of suitably chosen spherical harmonics:

$$P_j(\mathbf{h}_j, \mathbf{q}) = 1 + \sum_{l=2}^{\infty} 4\pi(2l+1)^{-1} \sum_{m=-l}^{l} \sum_{n=-l}^{l} C_l^{mn} K_l^m(\mathbf{h}_j) K_l'^n(\mathbf{q}) \qquad (4.10)$$

The values of harmonic terms, $K_l^m(\mathbf{h}_j)$ and $K_l'^n(\Psi_q, \Gamma_q)$, depend on the crystal symmetry and sample symmetry, respectively. $K_l^m(\mathbf{h}_j)$ is equal to the real spherical harmonic $Y_l^m(\mathbf{h}_j)$ if Y_l^m is invariant under the symmetry transformations of the crystal system; otherwise $K_l^m(\mathbf{h}_j) = 0$. Similarly, the sample harmonics must be invariant under the symmetry transformations that describe the sample symmetry. Taking the crystal harmonics as an example, the real spherical harmonics can be calculated from normalised associated Legendre polynomials:

$$Y_l^m(\mathbf{h}_j) = Y_l^m(\theta_{h_j}, \phi_{h_j}) = \begin{cases} \sin(m\phi_{h_j}) P_l^m(\cos(\theta_{h_j})) & m < 0 \\ \cos(m\phi_{h_j}) P_l^m(\cos(\theta_{h_j})) & m > 0 \end{cases} \qquad (4.11)$$

where $\mathbf{h}_j = (\theta_{h_j}, \phi_{h_j})$ are the polar coordinates of the h_j reciprocal lattice vector in the crystal system (discussed below):

$$P_l^m(\cos\theta) = P_l^m(x) = \sqrt{\frac{(l+m)!}{(l-m)!}}\sqrt{\frac{2l+1}{2}}\frac{(-1)^{l-m}}{2^l l!}(1-x^2)^{-m/2}\frac{d^{l-m}}{dx^{l-m}}(1-x^2)^l \tag{4.12}$$

For computational purposes, the values of Equation 4.12, for each possible combination of l and m that is to be used, are calculated in terms of $\cos\theta$ and included in a function library that is used by POFIT to evaluate P_l^m, rather than explicitly evaluating Equation 4.12 at run-time. The sample harmonics, $K_l'^n(\Psi_q, \Gamma_q)$ are evaluated in the same way.

The functions given by Equation 4.11 that satisfy the possible combinations of symmetry transformation are given in Popa (1992). There are three symmetry conditions that need to be considered: (i) inversion symmetry in all 11 Laue classes only permits spherical harmonics with l even; (ii) if there exists an n-fold rotation axis, then only spherical harmonics where m is a multiple of n are allowed by symmetry; and (iii) if there is a second order axis perpendicular to the n-fold rotation axis, then it is sufficient to include only spherical harmonics with $m > 0$ in the calculation.

These symmetry conditions impose constraints on the coordinate systems in which $\mathbf{h}_j$ and (Ψ_q, Γ_q) are defined. The z-axis of the coordinate system must be coincident with the n-fold rotation axis and the x-axis must lie along the second order symmetry axis, if one exists. Popa (1992) lists equations for calculating $\mathbf{h}_j = (\theta_{h_j}, \phi_{h_j})$ for the various crystal systems.

The sample coordinate system, in which (Ψ_q, Γ_q) is defined, has its z-axis along the n-fold axis of sample symmetry. In the case of cylindrical sample symmetry this axis in an ∞-fold axis which was called the POA in the simple analytic function description of PO. (Ψ_q, Γ_q) are the polar and azimuthal coordinates of

the scattering vector $\mathbf{h}_j$ in this coordinate system. A similar analysis to that used to derive Equation 4.8 is used to calculate (Ψ_q, Γ_q) for a given scattering vector. The sample frame can be related to the IP-frame shown in Fig. 4.1 by three Euler angles (ϕ, β, χ). The angles ϕ and β are respectively equivalent to the angles ϕ and β used to describe the direction of the POA with respect to the incident beam. The angle χ is redundant in the case of cylindrical sample symmetry as it is equivalent to a rotation of the sample frame about its z-axis (i.e. a rotation about the cylindrical axis of symmetry). But for lower sample symmetry than cylindrical, χ is needed to describe the extra degree of freedom.

The scattering vector is defined by its Bragg angle, θ, and the angle around the powder ring at which the diffraction occurs. These angles can be related to Ψ_q and Γ_q by the Euler angles (ϕ, β, χ) (following Popa (1992) and including the appropriate terms for the image-plate transmission geometry):

$$\cos\Psi_q = cos\beta\cos(90+\theta) - \sin\beta\sin(90+\theta)\sin(\gamma-\phi) \tag{4.13}$$

$$\begin{aligned}\tan\Gamma_q \;=\; & [-\sin(90+\theta)\cos(\gamma-\phi)\sin\chi \\ & +\sin(90+\theta)\sin(\gamma-\phi)\cos\beta\cos\chi \\ & +\cos(90+\theta)\sin\beta\cos\chi] \\ & \div[\sin(90+\theta)\cos(\gamma-\phi)\cos\chi \\ & +\sin(90+\theta)\sin(\gamma-\phi)\cos\beta\sin\chi \\ & +\cos(90+\theta)\sin\beta\sin\chi]\end{aligned} \tag{4.14}$$

POFIT has been modified to include the symmetrised spherical harmonic model. The coefficients C_l^{mn} in Equation 4.10 are the refinable texture parameters. In principle, all orders up to $l = \infty$ should be included, but, in practice, for simple texture, only the first few orders of l are required to describe the ODF to sufficient accuracy. To determine a suitable cut-off value for l, refinements of the model should be carried out for successive values of $l = 2, 4, 6\ldots$ until the highest

Parameter	β refined
β	44.11(8)°
ϕ	88.11(4)°
C_2^{00}	3.192(5)
C_4^{00}	1.995(8)
C_6^{00}	0.435(5)
χ^2	2037
R_{wp}	0.135
S	6.03

Table 4.2. The results of the simultaneous symmetrised harmonics fit to the marked rings in Fig. 4.10.

order coefficient of the fit, C_l^{mn}, refines to an insignificant value such that extra parameters have little effect on the fit.

Figure 4.13 shows the result of a simultaneous fit of the symmetrised harmonics model to the marked powder rings in Fig. 4.10. The sample symmetry was taken to be cylindrical, this permits sample harmonics with $n = 0$ (C_l^{m0}). The crystal symmetry, defined by the space group ($P3_121$) is trigonal (Laue class $\bar{3}m$), this permits crystal harmonics with values of m that are divisible by 3 which are less than the order l—C_2^{00}, C_4^{00}, C_4^{30}, C_6^{00}, C_6^{30}, C_6^{60}, and so on. The order was set to $l = 6$, as terms of order 8 took on small values (< 0.01) and did not improve the fit significantly. The fit is markedly better than the corresponding March-Dollase fit and the POA direction refines to a physically reasonable value, which is important when the POA direction is unknown.

Figure 4.14 shows the results of both the March-Dollase fit and the symmetrised harmonics fit for easy comparison. The symmetrised harmonic model works very well for simple but strong cylindrically symmetric PO and also has the advantage over the simple analytic function model in that it can, in principle, fit textures that have sample symmetries other than cylindrical. An example of such a fit is given in Chapter 6. The use of the symmetrised harmonics model has greatly improved the accuracy of PO modelling using 2-d data from an image-plate.

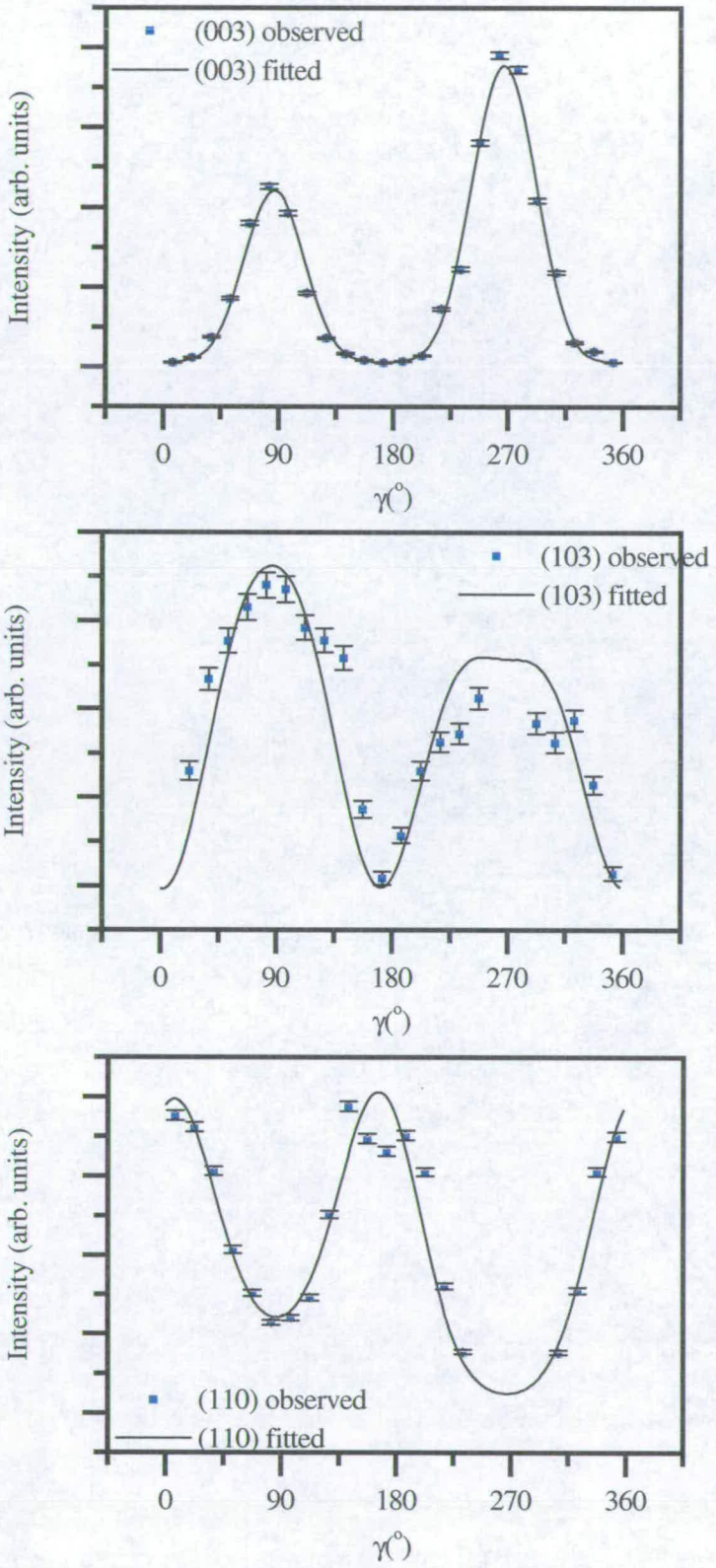


Figure 4.13. A multi-ring fit of the symmetrise harmonics model to the intensity as a function of azimuth around the marked rings in Fig. 4.10.

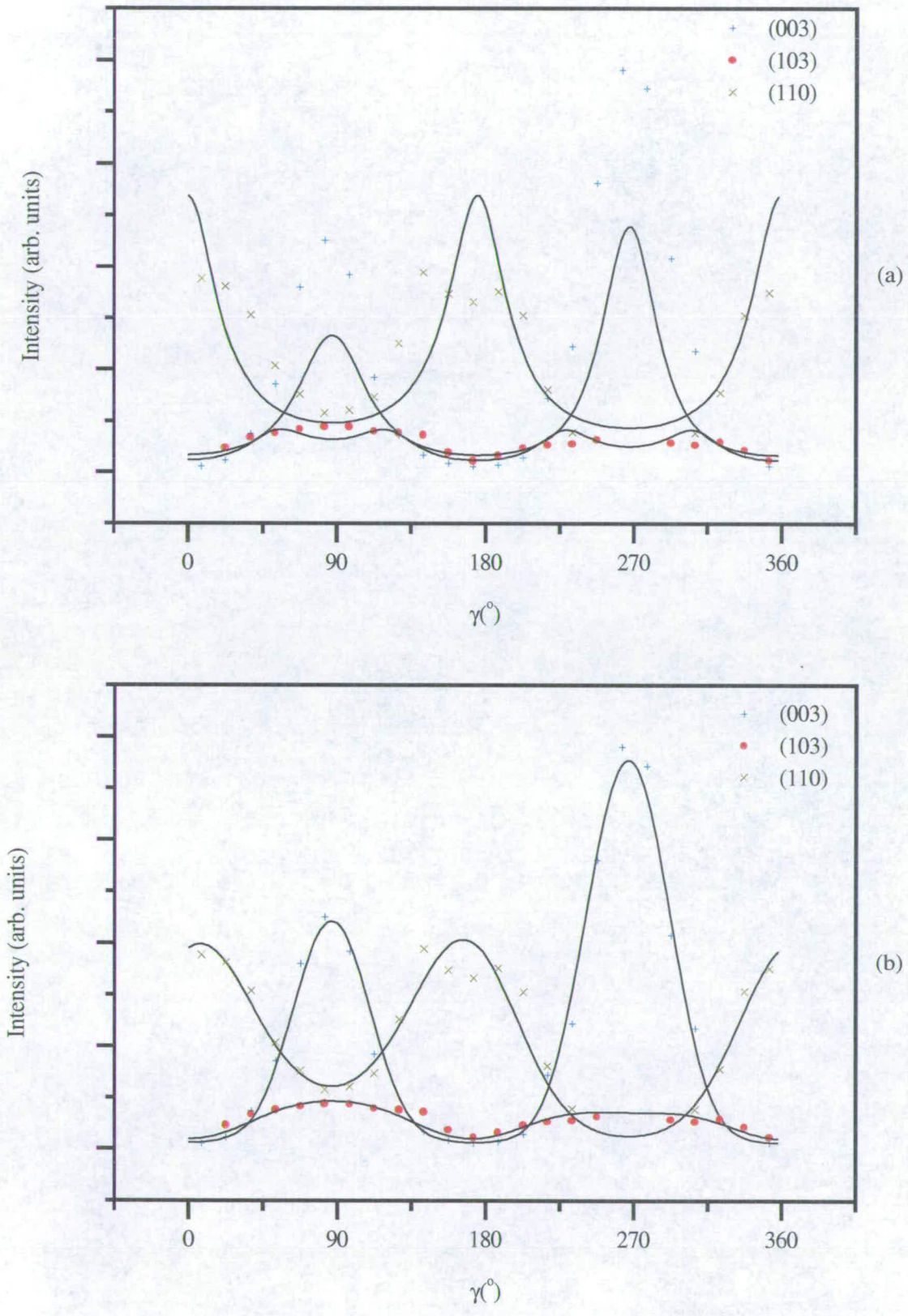


Figure 4.14. The results of (a) the March-Dollase fit and (b) symmetrised harmonics fit shown together for comparison. By using the symmetrised harmonics model the fit is considerable improved.

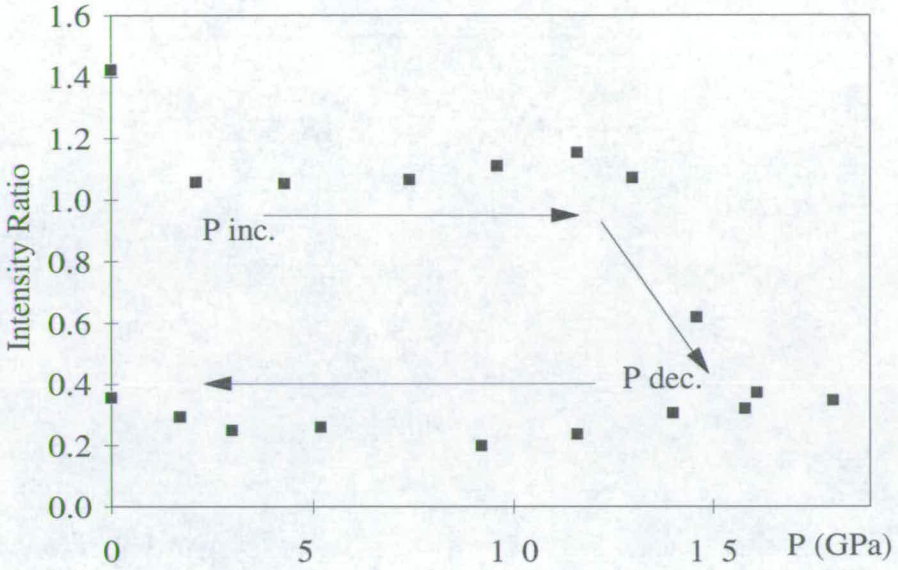


Figure 4.15. The relative intensity of the (104)/(110) reflections in cinnabar HgS as a function of pressure.

4.3.3 Pressure Induced PO in HgS

Cinnabar HgS exhibits a remarkably reproducible microstructural effect on the application of pressure. Figure 4.15 shows the ratio of the intensity of the (104) and (110) reflections in the cinnabar HgS powder pattern on pressure increase and decrease. Initially, on application of pressure, the intensity of the (104) relative to the (110) drops rapidly. This can be understood as an initial settling of the crystallites in the sample. There is little change in the relative intensities on further increase in pressure; a slight increase in the intensity of the (104) relative to the (110) is observed. This change can be attributed to structural changes since the preferred orientation changes little over the pressure range 3–12 GPa. Between 12 GPa and 19 GPa the intensity ratio drops exponentially. It is in this region that the sample develops strong PO. On pressure decrease, the relative intensities change slightly, falling to a minimum at ~9 GPa and then increasing as the pressure is released to ambient pressure. This behaviour has the characteristics of plastic deformation and it is possible that the mechanism generating PO in HgS is related a change in crystallite shape.

Parameter	12 GPa	15 GPa	19 GPa
β	30(3)°	34(2)°	35(1)°
C_2^{00}	2.3(8)	2.7(3)	3.36(5)
C_4^{00}	2.0(5)	2.3(2)	2.37(9)
C_6^{00}	0.4(3)	0.8(1)	0.63(5)

Table 4.3. Analysis of PO in HgS as a function of pressure.

The changes observed in the relative intensities in the pressure range 2–12 GPa are similar on pressure increase and pressure decrease; although the values of the relative intensity on pressure decrease are offset from those observed on pressure increase due to the presence of PO. This indicates that the PO in the sample does not change significantly over this range.

The effect shown in Figure 4.15 is very reproducible and can almost be regarded as a 'preferred orientation transition'. The onset of this 'transition' occurs between 10–12 GPa, which is just above the freezing pressure of the methanol:ethanol pressure transmitting medium (10.4 GPa). Because of this it was expected that the freezing of the medium played a part in the formation of the PO. However, the effect was also observed in experiments where pure water was used as the pressure transmitting medium and where no medium was used. This suggests that the 'PO transition' is caused by the properties of the material.

The techniques presented in Chapters 3 and 4 have used to study the evolution of PO in a sample of HgS over the range 12–19 GPa. The sample was loaded in a Mao-Bell cell (400 μm culet diamonds, 150 μm diameter hole). The cell was aligned to the rotation axis of the rotation stage. At each pressure an exposure was taken when the cell was inclined by 30° to the beam and when the cell was in its standard non-inclined position. The images collected from the sample when it was not inclined to the beam showed little variations in intensity around the powder rings indicating that the PO had cylindrical symmetry. Analysis of the intensity variations around the powder rings observed when the sample was inclined was carried out on the (101) and (003) reflections of the cinnabar powder

pattern. Table 4.3 shows the results of the analysis of PO in the sample at 12, 15 and 19 GPa. The angle between the cylindrical axis of symmetry of the PO and the incident beam (β) refines to sensible values and the strength of the PO steadily increases as pressure increases, as signified by the increasing values of the PO parameters with pressure. The refined PO parameters at 19 GPa are similar to those shown in Table 4.2. The values tabulated in Table 4.2 were refined from a sample of HgS at ambient pressure that had been pre-compressed to 18 GPa. The similarity between the values of the PO parameters obtained from different samples exposed to similar condition is indicative of the reproducibility of the pressure induced PO in HgS.

The phenomenon described above is of significant interest and warrants a full study in future. The analysis described here is the starting point for such a study using the techniques presented in this thesis.

4.3.4 2-D Rietveld Refinement

Normally, it is the 1-d integration of image-plate data that is used as the input data for Rietveld refinement. This poses no problems if the data were collected from an ideal powder. The intensities in the integrated 2-d data will be more precisely determined (because of the averaging) than intensities from a 1-d strip of data, but the intensities will be essentially identical. However, in general, this is not the case for data collected from a non-ideal powder. In the special case of a sample with cylindrically symmetric PO whose POA is coincident with the incident beam, the data collected by the image-plate will show no intensity variations around the rings and the intensities in the integrated data will be the same (to within the standard deviation) as those recorded by a 1-d detector (the equivalent of integrating the 2-d image over a narrow strip through the centre of the powder pattern). But, for a sample whose POA is inclined to the beam or that has texture with a symmetry other than cylindrical, intensity variations will

be observed around the rings, and the intensities in a 1-d integration of such an image will be a complex average of the intensity variations around the rings.

To model the effect of PO on the relative intensities of the 1-d integration of a 2-d image with intensity variations around the rings, requires that the intensity variations predicted by a 2-d model of PO be integrated into 1-d corrections to the calculated 1-d pattern. The method is relatively straight forward if it is assumed that complete rings have been integrated for every peak in the 1-d pattern. But this is not necessarily true since the finite area of the image-plate means that at a certain distance from the centre of the powder pattern the diffraction from certain parts of the powder rings is not recorded by the image-plate. It is certainly possible to include this effect as part of the PO correction calculation. To be able to compute which part of a given powder ring is captured by the image-plate requires information on the dimensions of the image-plate, its orientation in space, and the position of the centre of the 2-d powder pattern on the image-plate. However, this technique for PO correction in Rietveld refinement is very specific to a particular experimental set-up and is perhaps too specialised to be included in any of the generally available refinement packages and too cumbersome to be included in a specialised refinement package.

A better way to deal with this problem would be to use the information available from the full 2-d image and perform a 2-d Rietveld refinement. The GSAS refinement package (Larson and Von Dreele (1985)) has the ability to refine multiple powder patterns simultaneously and, recently, the symmetrised harmonics model for texture correction has been incorporated into the package. It was decided to investigate whether the the multiple powder pattern fit capability of GSAS combined with the new texture correction could fit the data from many sectors of a 2-d image simultaneously. The 24 sectors shown in Fig.3.14 were used as the input data for GSAS. The orientation of each sector with respect to the sample coordinate frame is given by three sample orientation angles (Ω, X, Φ), which are the Euler angles that describe the orientation of the sample frame with respect

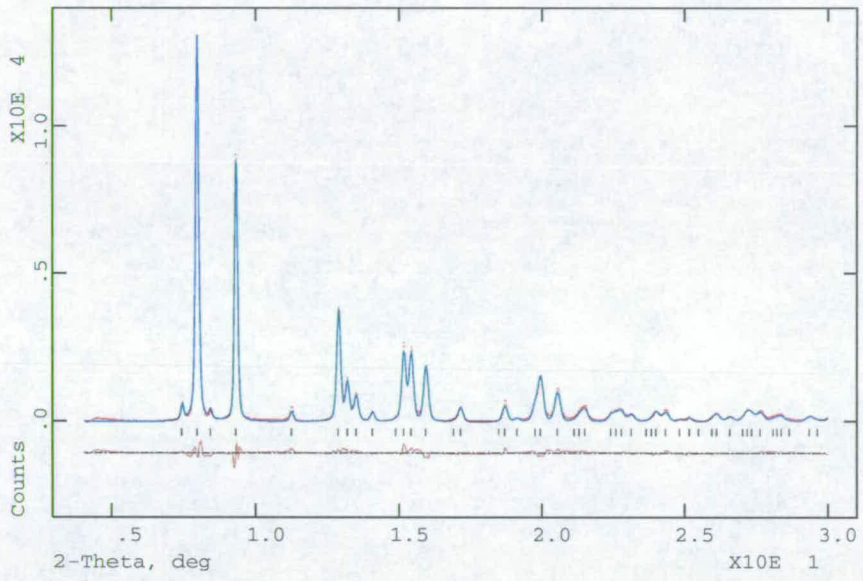
Parameter	Value
a	4.14494(4)Å
c	9.4960(2)Å
u	0.7188(1)
v	0.4929(5)
Ω_s	-33.76(7)°
X_s	-87.30(7)°
C_2^{00}	2.569(63)
C_4^{00}	1.072(96)
C_4^{30}	0.101(86)
C_6^{00}	-0.035(13)
C_6^{30}	-0.757(18)
C_6^{60}	0.226(16)

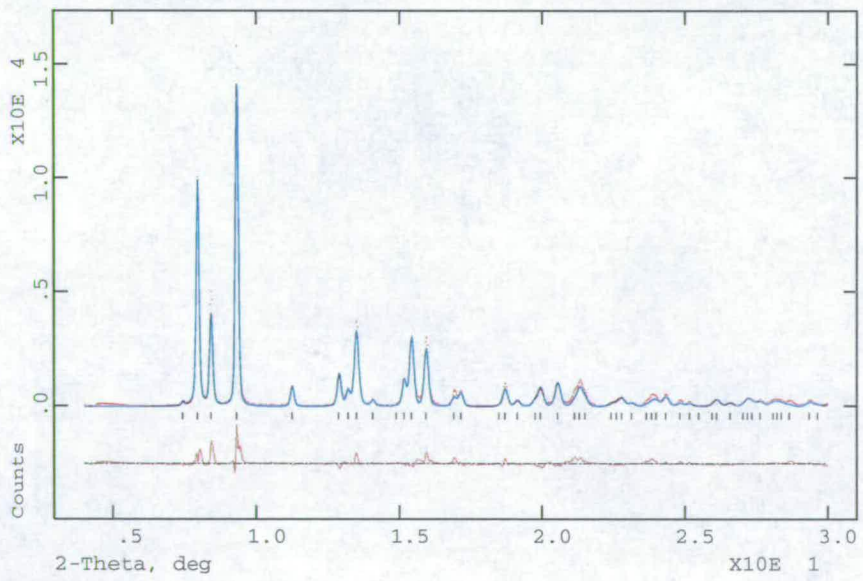
Table 4.4. The results of the simultaneous sector fit to 24 sectors of the image shown in Fig. 4.10.

to an instrument frame defined in GSAS as y-axis coincident with the incident beam, x-axis normal to the diffraction plane and z-axis normal to the xy-plane. For image-plate data Ω and Φ are zero and X is the angle around the powder ring. These angles are fixed for each sector when the data is initially entered. Another set of refineable parameters describes the orientation of the sample frame with respect to the incident beam (Ω_s, X_s, Φ_s). When $\Omega = 0$, $\Phi = 0$, and $\Phi_s = 0$, $\Omega_s = 90 - \beta$ and $X_s = -90 - \phi$, where β and ϕ are from Equation 4.8.

234 parameters were refined: 2 atomic coordinates (u and v)and 2 thermal parameters (one for each atom), 192 background coefficients (8 for each sector), 24 scale factors (one for each sector), 2 lattice parameters (a and c), 8 texture parameters (Ω_s, X_s, 6 C_l^{mn} coefficients), and 4 peak profile parameters. The results of the fit to four sectors at γ = 7.5°, 97.5°, 187.5° and 277.5° are shown in Figure 4.16. The fits, in general, are excellent.

The refined parameters are tabulated in Table 4.4. There are discrepancies between the texture parameters refined by GSAS and those refined by POFIT; although they are generally in agreement. The discrepancies arise from a combination of effects. The powder patterns used in the 2-d refinement have not been


X10E 4
1.0
.5
.0
Counts
.5
1.0
1.5
2.0
2.5
3.0
2-Theta, deg
X10E 1


X10E 4
1.5
1.0
.5
.0
Counts
.5
1.0
1.5
2.0
2.5
3.0
2-Theta, deg
X10E 1

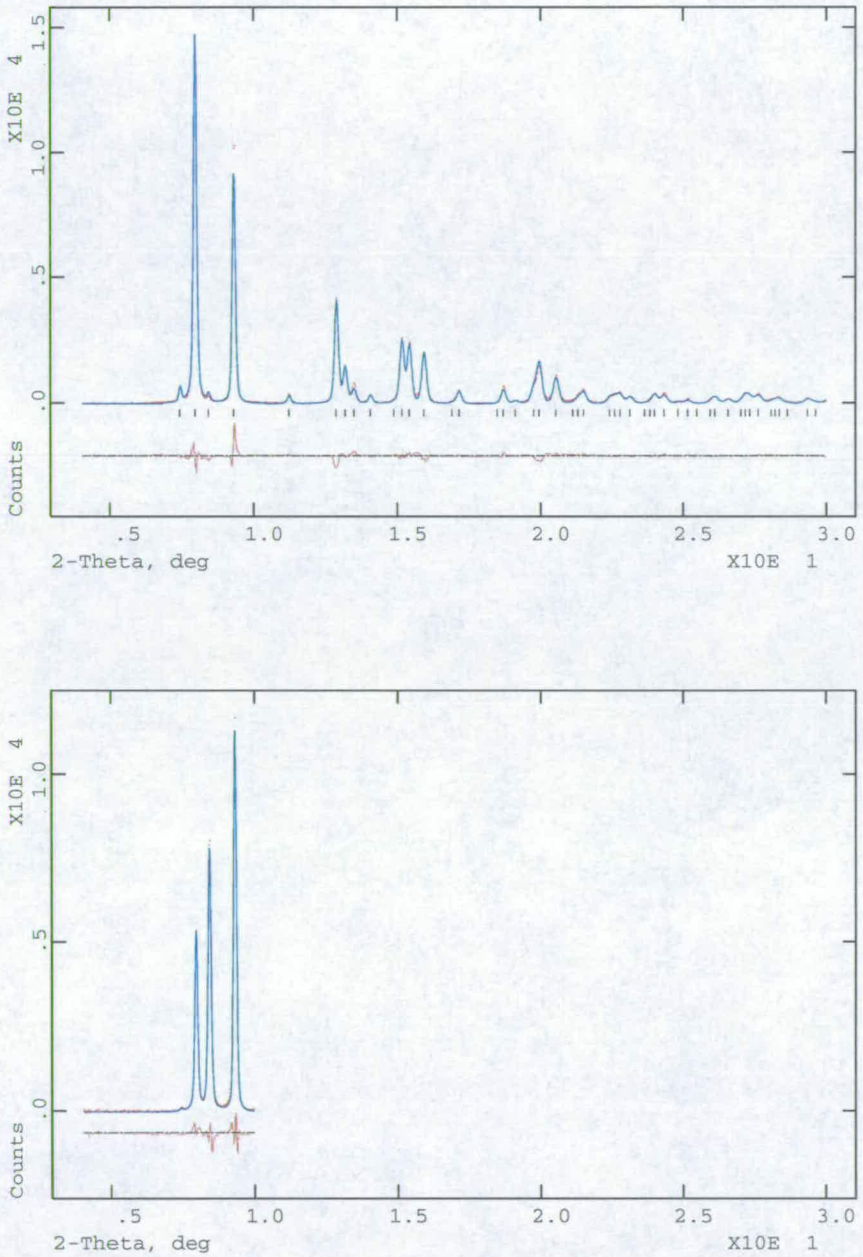


Figure 4.16. The fit to four sectors of a full Rietveld refinement of 24 sector of a 2-d image simultaneously. Due to the fact that the center of the powder pattern is offset from the centre of the plate, the last sector shown above only captures diffraction out to 10° 2θ.

corrected for the effects of the variable sample absorption and gasket shielding which changes as a function of azimuth and 2θ. This effect becomes more pronounced at higher values of 2θ. Also, a common problem with GSAS, is that the peak profile function does not fully describe the peak profiles observed in image-plate data. Normally, such a refinement could only be carried out on data collected from a non-inclined sample since at high pressure the sample would be contained in a pressure cell and the images collected from inclined cell are contaminated by beryllium scatter. The absorption correction is much more simple for non-inclined samples than inclined samples and could be incorporated into the refinement package with relative ease. The peak profile problem also affects the normal 1-d refinements from image-plate data (even with data collected from nearly ideal samples) and warrants further investigation.

This section has presented the first quasi-2-d refinement from image-plate data. 2-d refinements use fully the information available from a 2-d detector and, when the image-plate data exhibit anisotropic effects around the powder rings, this technique offers the possibility for considerably improving the accuracy of structural studies of samples with microstructure. However, due to the beryllium scatter that contaminates the powder pattern when the pressure cells are inclined, it will not normally be feasible to carry out 2-d refinement from data collected from inclined samples. And because the symmetry of sample microstructure is often cylindrical and, thus, variations of intensity or position around the powder rings are only revealed upon sample inclination, methods such as those presented in this chapter need to be used to quantify sample microstructure.

Chapter 5

Application of Preferred Orientation Modelling in High-Pressure Structural Studies

5.1 Introduction

Recent work on the group IV, III-V and II-VI semiconductors (Nelmes and McMahon (1995), Nelmes *et al.* (1995a), Nelmes *et al.* (1995b)) has revealed that, contrary to the previously accepted systematics, where it was believed that these materials pass through various high symmetry structures of increasing coordination on pressure increase, all of the group IV, III-V, and II-VI semiconductors pass through lower symmetry structures with variable atomic coordinates between the higher symmetry phases. The lower symmetry phases obviously play an important part of the phase transition path of these materials at high-pressure and are therefore of interest when trying to understand phase transition mechanisms. Accurate determination of the variable atomic positions in the lower symmetry phases at high-pressure and their evolution as a function of pressure is important for any theoretical description of the phase transition mechanisms at work

between high-pressure phases in the group IV, III-V, and II-VI materials. The presence of texture or preferred orientation in the lower symmetry phases will lead to inaccurate determination of the variable atomic positions in these phases unless such microstructural effects are modelled accurately.

This chapter presents a structural study of the cinnabar phase of HgS to 11 GPa. There is interest in the role of the cinnabar phase as an intermediate phase between the zinc-blende phase, which is often the stable ambient pressure phase of binary II-VI semiconductors, and the NaCl phase that these materials transform into at high pressure. The cinnabar phase in HgS exists until at least 20 GPa but anisotropic strains in the sample make refinement impossible, at present, at pressures above 11 GPa. HgS also develops severe preferred orientation under pressure. Although the major changes in preferred orientation (PO) occur above 11 GPa, and the structural pressure dependence cannot be followed above this pressure, the structure can be followed on pressure decrease below 11 GPa where strong PO is present in the sample. The structure determined on pressure decrease should be the same as the structure determined on pressure increase (as long as no phase transition occurs) despite the presence of severe PO of the sample on pressure decrease. By using the techniques presented in Chapters 3 and 4, it has been possible for the structure of cinnabar HgS to be determined accurately with and without the presence of severe preferred orientation when the PO in the sample is suitably modelled.

5.2 The Cinnabar Structure

HgS has the prototypical cinnabar structure at ambient pressure. Cinnabar has a trigonal lattice (spacegroup $P3_121$) and consists of spirals of alternate Hg and S atoms in the c-axis direction. The spacing in the c-axis direction between the atoms in the spiral is fixed by symmetry at $c/6$. Figure 5.1 shows one of the spirals in the crystal structure of HgS cinnabar at ambient pressure.

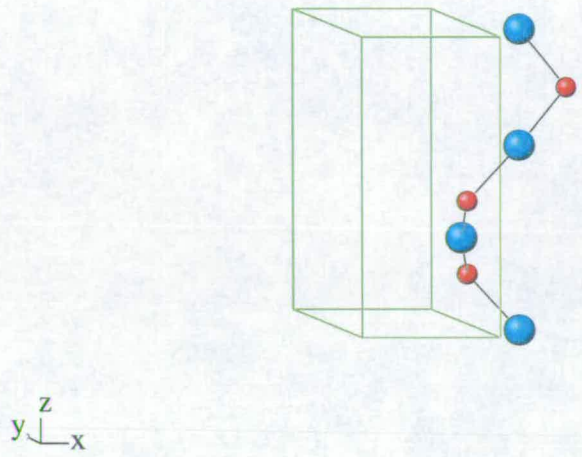


Figure 5.1. The crystal structure of HgS cinnabar viewed as spirals of alternate Hg and S atoms along the c-axis direction.

The cinnabar structure also occurs in the other mercury chalcogenides: metastable at ambient pressure in HgO (Aurivillius and Carlsson (1958)); and at high-pressure in HgSe (Mariano and Warekois (1963), Huang and Ruoff (1983), Huang and Ruoff (1985)), and HgTe (Werner *et al.* (1983), Huang and Ruoff (1985)). Cinnabar was thought to occur only in the mercury chalcogenides but recently cinnabar phases have been found at high-pressure in CdTe (Nelmes *et al.* (1993)) and ZnTe (San-Miguel *et al.* (1993), Kusaba and Weidner (1993), Qadri *et al.* (1993)). And most recently, the first cinnabar phase out of the group II-VI compounds has been observed in the group III-V compound GaAs (McMahon and Nelmes (1997)).

A full structural study of HgS at ambient pressure is presented in Aurivillius (1950) and a similar study of cinnabar HgO was carried out by Aurivillius and Carlsson (1958). A structural study of the cinnabar phase of HgTe was carried out by Wright *et al.* (1993). The pressure dependence of the unit cell parameters in cinnabar HgS and HgTe is detailed in Werner *et al.* (1983), but a

full study of the structural pressure dependence (i.e. following the atomic positions as a function of pressure) was not carried out. Full structural pressure dependence studies have been carried out on HgTe (San-Miguel *et al.* (1995)) and CdTe (McMahon *et al.* (1993)). The next section presents the results of a study of the structural pressure dependence of HgS between ambient pressure and 11 GPa. The structure was determined on pressure increase (in the presence of negligible preferred orientation) and on pressure decrease (in the presence of strong preferred orientation).

5.3 Structural Pressure Dependence of HgS to 11 GPa.

The data were collected using the image-plate set-up and techniques described in this thesis on Station 9.1 at SRS Daresbury. The sample material was 99.5% pure, finely powdered HgS from Aldrich. The data from two samples were collected and the results of the analysis of each sample agree to within the estimated standard deviation. The PO produced in HgS at high-pressure is highly reproducible and both samples exhibited similar PO evolution. Both samples were loaded in the Mao-Bell DAC (400 μm culet diamonds) in a 150 μm hole drilled in a tungsten gasket. The pressure transmitting medium was a 4:1 mixture of methanol:ethanol, and the pressure was measured by the ruby fluorescence technique from a small chip of ruby fixed to the culet of one of the diamond anvils. The wavelength of the incident x-ray beam was 0.4447Å, calibrated from the indium absorption edge at the beginning of the experimental run. The 2-d images were integrated into 1-d plots using Platypus, as described in Section 2.5.1. The results presented here were obtained from the full Rietveld refinement of the integrated profiles using GSAS (Larson and Von Dreele (1985)).

The refined parameters consisted of six background parameters, three peak profile parameters, the a and c lattice parameters and the atomic parameters which

include one variable coordinate, an isotropic thermal parameter for the two atoms in the unit cell and six parameters of the symmetrised harmonics PO model described in Chapter 4. The initial structural parameters were set to the values obtain for the ambient pressure structural study of HgS by Aurivillius (1950). The spacegroup is $P3_121$ with one Hg atom on the 3a site of the spacegroup (u, 0, 1/3) and the S atom at the 3b site (v, 0, 5/6). The starting values of the variable coordinates of Hg and S were u = 0.72 and v = 0.48 (Aurivillius (1950)), respectively, and the initial values of the lattice parameters were set to a = 4.145Å and c = 9.496Å.

At ambient pressure, the lattice parameters refined to a = 4.147(1)Å and c = 9.493(5)Å. The atomic coordinates refined to u = 0.720(5) and v = 0.49(3). The principal source of error in the lattice parameters comes from uncertainty in the calibration that converts pixel values to 2θ, which is effectively an uncertainty in the sample-to-plate distance. There are two principal sources of error in the refined atomic coordinates (u and v): (i) texture or preferred orientation in the sample, and (ii) the relative scattering power of the atoms. The PO in the ambient pressure samples before the application of pressure, was found to be very weak by the methods described in Chapter 4—there was negligible change in relative intensities, or intensity around the powder rings, between inclined and non-inclined samples. The relatively weak scattering power of the sulphur atoms leads to a correspondingly less precise determination of the sulphur positions than the mercury atoms, which scatter strongly. Small changes in the sulphur positions cause insignificant changes in calculated relative intensities, whereas similar changes in the mercury positions will cause significantly larger changes in intensity. The Hg atomic coordinate (u), for all samples, was in excellent agreement with the quoted ambient pressure value of 0.720(3) (Aurivillius (1950)). However, the S atomic coordinate was less well determined (v = 0.49(3), compared with v = 0.48(1) from Aurivillius (1950)). The estimated standard deviations (ESD) given by GSAS are based on the counting statistics only (i.e. $\sigma_i^2 = y_i$, where y_i is the observed intensity of point i). The ESDs do not include estimations of error

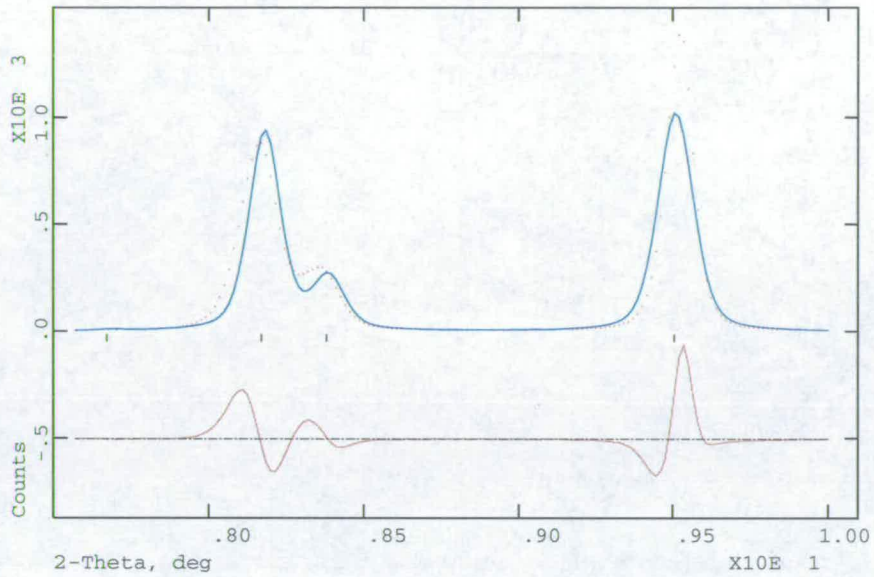


Figure 5.2. The results of the Rietveld refinement of the cinnabar structure at 11.6 GPa. Only the range between 7.6° and 10° 2θ is shown which highlights the misfit of the three most intense peaks in the pattern.

from other sources and, thus, the ESDs given by GSAS underestimate the true standard deviations. Given the scatter on the refined ambient pressure structural parameters, the actual error is estimated to be closer to 10 times the corresponding ESD given by GSAS. The error bars on the graphs of lattice parameters and atomic coordinates have been drawn at 10 times the values given by GSAS.

To determine the pressure dependence of the structural parameters, data were collected at approximately equally spaced intervals on pressure increase from ambient pressure to 18 GPa, and on pressure decrease from 18 GPa to ambient pressure. As stated earlier, is was not possible to refine a structure above ~11 GPa due to anisotropic strains in the sample which made it impossible to find a hexagonal lattice that fitted the observed positions of all the peaks in the pattern. The data begin to misfit the lattice quite abruptly between 9–11 GPa then steadily increase with pressure. The fact that the pressure transmitting medium (4:1 methanol:ethanol) solidifies between 9–11 GPa gives a plausible explanation of the relatively sudden development of lattice misfits. With the solidification of

the pressure transmitting medium, the sample is no longer under truly hydrostatic pressure, that is, there is a directional quality to the applied stress which in turn leads to (hkl) dependent lattice strains. Figure 5.2 shows the results of the refinement at 11.6 GPa. The (101), (003), and (102) reflections are shown. It can be seen that the fitted positions of the (101) and (003) reflections (at 8.2° and 8.4° 2θ, respectively) is are at greater 2θ than the observed positions of these peaks. However, the converse is true of the fit to the (102) (at 9.5° 2θ). By adjusting the lattice parameter any one of the three reflections shown can be fitted but only as the expense of larger misfits to one of both of the other reflections. It should be noted that, despite the lattice misfits, there is no evidence that the lattice is anything other than hexagonal at this pressure.

Figures 5.3a and 5.3b show the a and c lattice parameters as a function of pressure. Figures 5.3c and 5.3d show the c/a ratio and the volume of the unit cell, respectively, against pressure. The black symbols are the data collected on pressure increase and the red symbols are the data collected on pressure decrease. There is good agreement between the data collected on pressure increase and the data collected on pressure decrease in the ambient pressure to 10 GPa range. There is also good agreement with published values (Werner *et al.* (1983)).

The significantly different values for the c lattice parameter at 11.6 GPa arise from the combination of (hkl)-dependent strain and strong preferred orientation. On download, the sample exhibits strong PO such that the (hkl) reflections with $l \gg h, k$ are greatly weakened. This allows the refinement program to shift the calculated position of these weakened peaks without significant detriment to the fit even though the actual misfit to the peak position becomes greater. In turn, this permits the fit to the stronger peaks to be improved (by shifting their position at the cost of a greater misfit in position to weaker peaks) which provides a significant numerical improvement to the overall fit but not necessarily a better fit in the physical sense. Therefore, the results at 11.6 GPa on download are anomalous and should be disregarded.

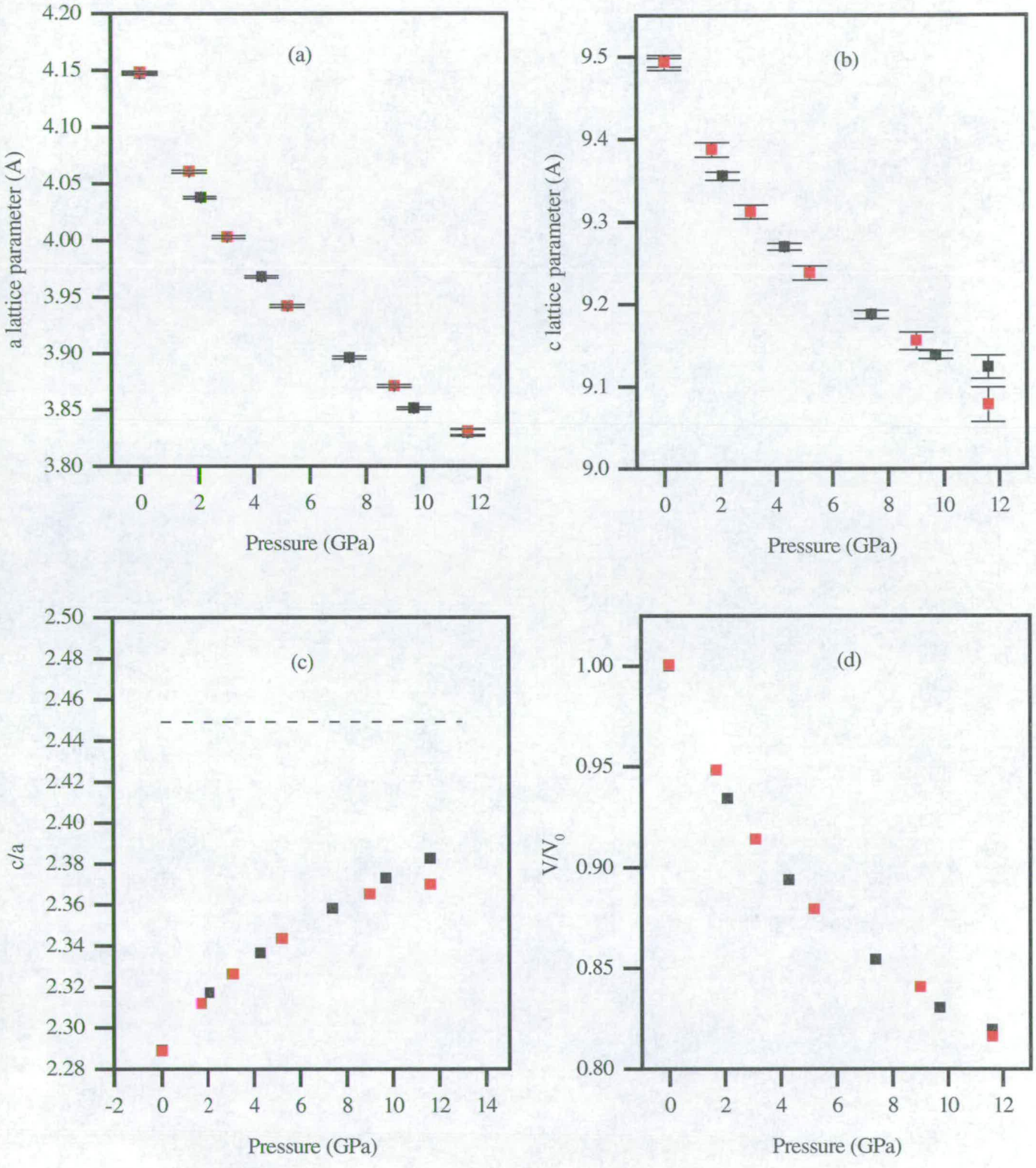


Figure 5.3. (a) The a lattice parameter against pressure. (b) The c lattice parameter against pressure. (c) the c/a ratio against pressure—the dashed line marks the c/a ratio of the NaCl structure. (d) V/V_0 against pressure (V_0 is the ambient pressure unit cell volume.

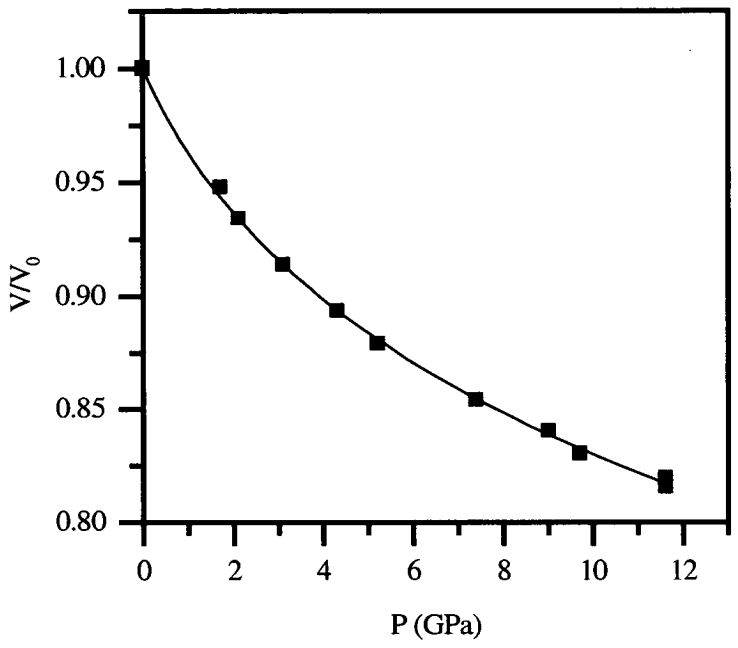


Figure 5.4. A least-squares fit of the Birch equation of state to the P-V data shown in Fig. 5.3d. The values of the fitted parameters are $B_0 = 21.1$ GPa $\pm$ 1.3 GPa, $B_0' = 11.1 \pm 1.0$.

The pressure-volume data shown in Fig. 5.3d were fitted with the Birch equation of state (EOS) (Birch (1952)):

$$P = \frac{3}{2}B_0[(V/V_0)^{-7/3} - (V/V_0)^{-5/3}][1 + \frac{3}{4}(B_0' - 4)((V/V_0)^{-2/3} - 1)] \qquad (5.1)$$

Figure 5.4 shows the results of a least-squares fit of the Birch EOS to the data in Fig. 5.3d. The bulk modulus, B_0, and its pressure derivative, B_0', are 21.1 GPa $\pm$ 1.3 GPa and 11.1 $\pm$ 1.0, respectively. These values are in good agreement with those of Werner *et al.* (1983): $B_0 = 19.4$ GPa $\pm$ 0.5 GPa, $B_0' = 11.1$ (no error stated)—also obtained by fitting the Birch EOS to the pressure-volume data. Comparing these values to the corresponding values for HgTe ($B_0 = 32$ GPa $\pm$ 10 GPA, $B_0' = 5.5 \pm 2$—San-Miguel *et al.* (1995)) and CdTe ($B_0 = 32$ GPa $\pm$ 1 GPa, B_0' unknown—McMahon *et al.* (1993)) it can be seen that cinnabar HgS is much more compressible than cinnabar HgTe and cinnabar CdTe. But the relatively large value for B_0' signifies that the structure stiffens quickly on

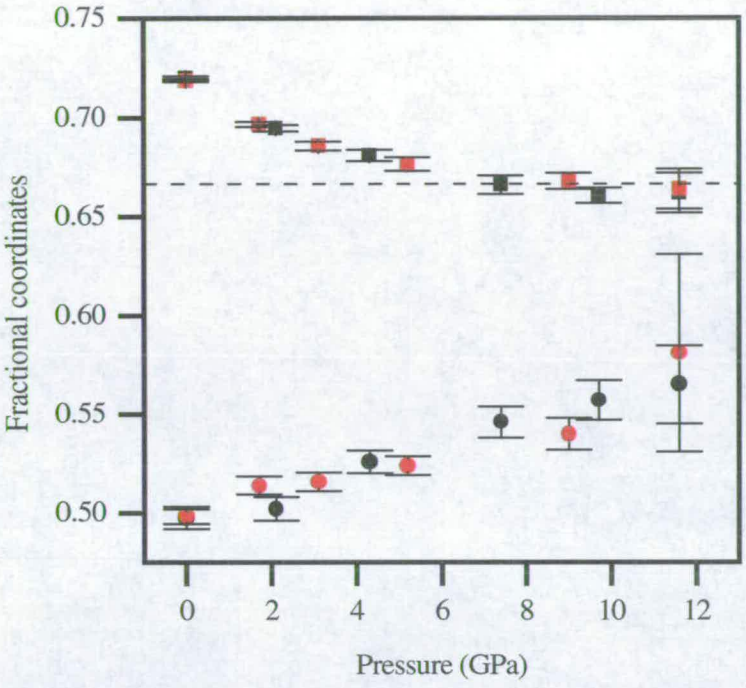


Figure 5.5. The variable atomic coordinate of Hg (squares) and S (circles) against pressure. The fractional coordinates of the Hg and S atoms in the NaCl phase in a hexagonal setting are fixed by symmetry at 2/3 (dashed line).

pressure increase.

The volume change between the cinnabar and NaCl phases of HgTe and CdTe were observed to be rather small at 3±1% and 2.6±0.2%, respectively, compared to the volume change at the zinc-blende → cinnabar transition, which were observed to be 11±2% and 13.4±0.1%, respectively. It is expected that the volume change at the cinnabar → NaCl transition in HgS to be even smaller due to the high compressibility of cinnabar HgS. Unfortunately, due to the problems of anisotropic peak shifts mentioned above, it is not possible to achieve a reasonable fit to the NaCl phase and thus it was not possible to determine the actual value of the volume decrease at the cinnabar → NaCl transition. (The cinnabar → NaCl transition in both HgTe and CdTe occur at relatively low pressures, 8 GPa and 3.8 GPa respectively, and therefore it would be possible to fit the powder patterns collected at all points through the transition.) No similar study of cinnabar HgSe has been carried out at the present time.

Figure 5.5 shows the pressure evolution of the fractional atomic coordinates of the Hg and S atoms in the unit cell. The NaCl structure in the hexagonal representation would have u = v = 2/3. In both HgS and HgO the atomic coordinate of the Hg atom is greater than 2/3 and the atomic coordinate of the S or O atoms lie below this value. This is contrary to the atomic positions measured in the cinnabar phases of HgTe and CdTe where all the variable atomic coordinates have values less than 2/3 (Wright *et al.* (1993)). As the pressure is increased, the value of u decreases while the value of v increases. This has the effect of increasing the radius of the spirals of Hg and S atoms that make up the structure relative to the size of the unit cell. The fractional coordinate of Hg (u) seem to fall below the NaCl value of 2/3 but measurements at higher pressures are required to observe whether the value of u keeps falling as pressure increases. Interesting questions arise about the configuration of the structure at the cinnabar $\rightarrow$ NaCl transition if the Hg atomic coordinate continues to diminish at higher pressures. It is generally expected that the atomic coordinates of cinnabar will tend toward the NaCl value but will not necessarily reach this value before the phase transition. Both atomic coordinates of both cinnabar HgTe (San-Miguel *et al.* (1995)) and cinnabar CdTe (McMahon *et al.* (1993)) are less than 2/3 at ambient pressure and increase towards this value on pressure increase but never reach 2/3 before the phase transition to NaCl occurs. It is possible that the Hg atomic coordinate actually continues to fall below 2/3 as pressure increases and the special value of 2/3 has little relevance to the structural changes that occur between cinnabar and NaCl. It would be interesting to follow the structural behaviour of HgS at pressures higher then $\sim$12 GPa, but hindrances due to sample microstructure need to be overcome prior to further study.

The agreement between the values obtained for the atomic coordinates on pressure increase and those obtained on pressure decrease is excellent, despite the presence of very strong PO in the sample during pressure release. The atomic coordinates of the sulphur atoms are determined less precisely than the mercury coordinates because the sulphur atoms scatter x-rays less strongly than mercury

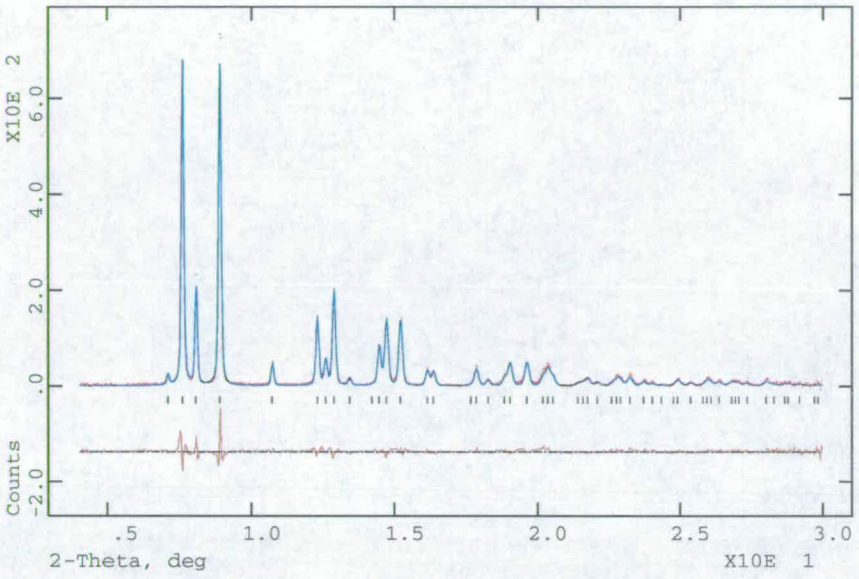


Figure 5.6. Ambient pressure fit of cinnabar HgS with little PO present.

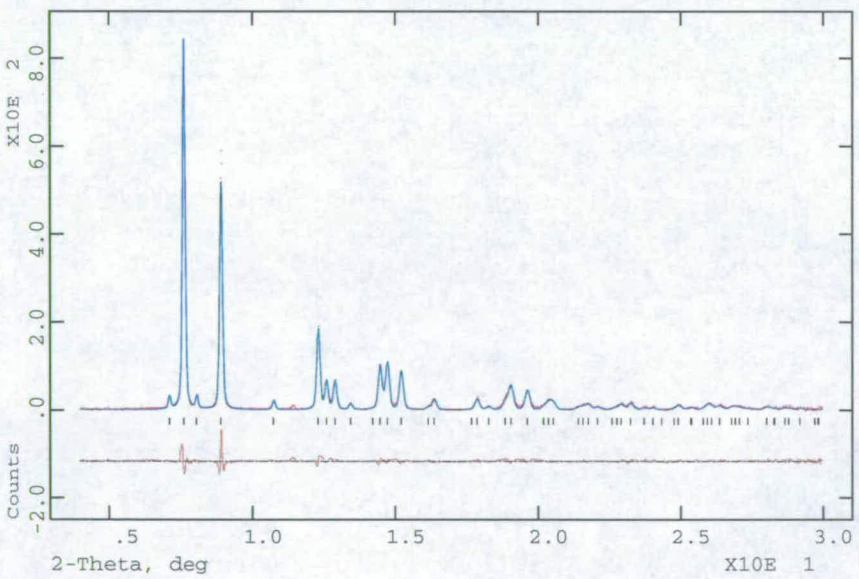


Figure 5.7. Ambient pressure fit of cinnabar. Severe PO is present but, by proper modelling of PO, the refinement essentially give the same structural values as the refinement when no PO is present.

atoms. Again, the large errors on the 11.6 GPa data points are due to the unavoidable lattice misfits. PO modelling has successfully taken account of the severe PO in the sample on pressure decrease. Figures 5.6 and 5.7 show two fits to the ambient pressure data before and after the application of pressure. Both fits are good, and refine to the same structural values within the ESDs.

Figure 5.8 shows the structure of cinnabar viewed along the c-axis at (a) ambient pressure and (b) 9.6 GPa. The six nearest neighbour atoms to one of the Hg atoms are shown (two at a distance a, two at a distance b and two at a distance c). At ambient pressure, a = 2.35Å, b = 3.10Å and c = 3.32Å. At 9.6 GPa, a = 2.43Å, b = 2.73Å and c = 3.04Å. Both the b and the c distances (the distances between the spirals) decrease with pressure at might be expected since the bonds between the spirals are relatively weak compared to the much stronger a-bond. Interestingly, the a distance (the distance between the Hg and S atoms in the spirals) increases in length with pressure. This increase is the cause of the increase in the radius of the Hg–S spirals, which in turn is the cause of the b and c bonds becoming shorter.

In the NaCl phase all three bonds (a, b, and c) must be equal. San-Miguel *et al.* (1995) noted that, in HgTe, the b-bond length is preserved across the cinnabar $\rightarrow$ NaCl transition. The c-bond length decreases with pressure toward the NaCl bond length, and there is a slight shortening of the a-bond length with pressure away from the NaCl bond length. In cinnabar HgS, the b- and the c-bond length both decrease with pressure but the a-bond length increases with pressure. This suggests that the a-, b- and c-bond lengths will be closer to being equal at the cinnabar $\rightarrow$ NaCl transition than the corresponding bonds in HgTe and thus the volume change at the cinnabar $\rightarrow$ NaCl transition in HgS is not as large as the volume change at the same transition in HgTe. This is also backed up by the compressibility measurements, which suggest that the volume change at the cinnabar $\rightarrow$ NaCl transition in HgS may be smaller than the corresponding transition in HgTe. Unfortunately, this cannot be tested at the present time

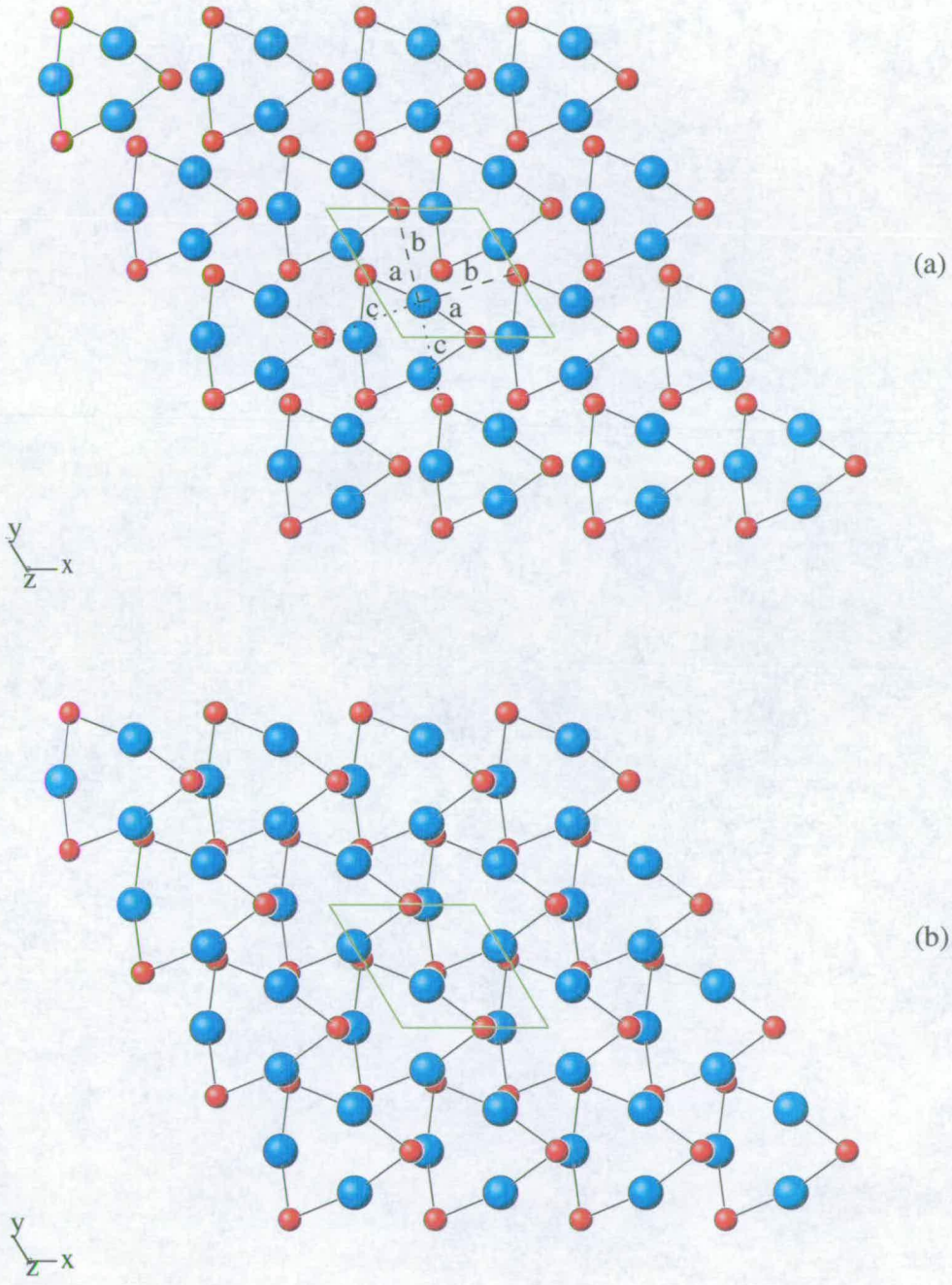


Figure 5.8. (a) the ambient pressure structure of cinnabar viewed along the c-axis. The structure consists of spirals of alternate atoms coming out of the page. (b) the cinnabar structure at 9.6 GPa.

because the data cannot be refined at the transition.

5.4 Conclusions

The structural pressure dependence of the cinnabar phase of HgS has been followed between ambient pressure and 11.7 GPa. The data above 9.6 GPa could not be refined properly due (hkl)-dependent anisotropic peak displacement such that the observed peak position could no longer be described by a hexagonal lattice. However, there was no evidence of major structural changes and it is suspected that such peak displacements arise from microstructural stress effects in the sample, independent of sample structure.

The structural pressure dependence was followed on download where strong uniaxial PO was present in the sample. Modelling of the PO in the sample by the techniques detailed in Chapters 3 and 4 has allowed the structure of cinnabar at pressure to be determined accurately when severe PO is present in the sample. The success of the preferred orientation modelling at high pressure is encouraging and opens the way towards modelling more troublesome microstructural effects in samples at high pressure.

Chapter 6

Other Microstructural Effects in 2-D

6.1 Introduction

This chapter outlines, qualitatively, what is known about other microstructural effects in powder samples at high pressure and how they manifest themselves in 2-d data. The prospects for using 2-d data analysis to develop a quantitative description of these effects are given.

6.2 Texture

Chapter 4 detailed the quantitative modelling of severe uni-axial preferred orientation where the sample symmetry was cylindrical about a certain axis in space (the preferred orientation axis—POA). In this case, when the POA is coincident with the incident beam, no intensity variations around the powder rings due to preferred orientation will be observed. However, many materials exhibit more complex PO or texture where the sample symmetry is not cylindrical. Figure 6.1

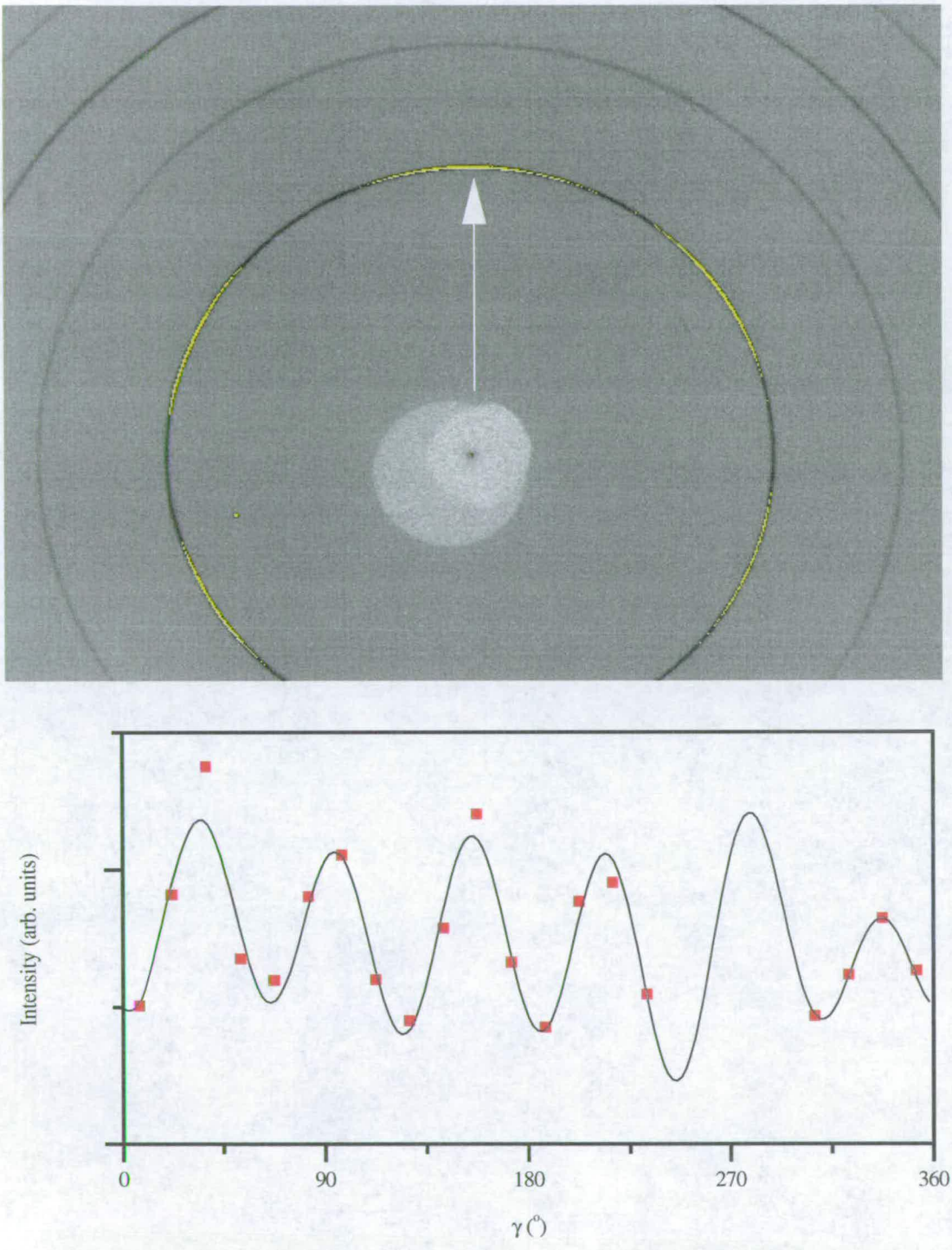


Figure 6.1. (a) Preferred orientation in Sr at 13 GPa. (b) Symmetrised harmonics fit to the intensity variations around the arrowed ring.

β	26(1)°
C_4^{10}	15(4)
C_4^{12}	-19(2)
C_4^{14}	2.8(3)
C_6^{10}	-6(1)
C_6^{12}	3.0(8)
C_6^{14}	-3.4(2)
C_6^{16}	2.5(2)

Table 6.1. The results of a symmetrised harmonics fit to the ring highlighted in Fig. 6.1.

shows the effect of PO in a sample of Sr at 13 GPa. At this pressure, Sr is in its bcc phase. The preferred orientation effects observed in the arrowed ring in Fig. 6.1a are characteristic of the type of texture effects expected in metals with rolling or shear texture—five intensity maxima can be clearly seen with, presumably, a sixth maximum at $\gamma = 270°$.

The symmetrised harmonics model of texture presented in Chapter 4 is general enough to describe textures with non-cylindrical sample symmetries and Fig. 6.1b shows the fit to the intensity variation around the arrowed (111) ring in the 2-d image. The intensity variation, with its six-fold nature, requires that the sample symmetry permits harmonic terms K_{lm} with $m = 6$. The monoclinic symmetry (Laue class $2/m$) was chosen as this is often the symmetry of texture generated by shear mechanisms, one of the major mechanisms of phase transformations. The POA direction and harmonic functions up to order 6 were refined and are given in Table 6.1. The POA direction lies reasonably close to the incident beam, which is expected for samples in diamond-anvil cells. The refined texture parameters are large indicating (as observed) the presence of very strong texture.

Figure 6.2a shows a 2-d image collected from a sample of highly textured Ba at 13.3 GPa. The structure of this phase is completely unknown but the complex pattern (many powder rings) suggests that the unit cell symmetry is low, probably monoclinic. The presence of texture in the sample, however, could provide an

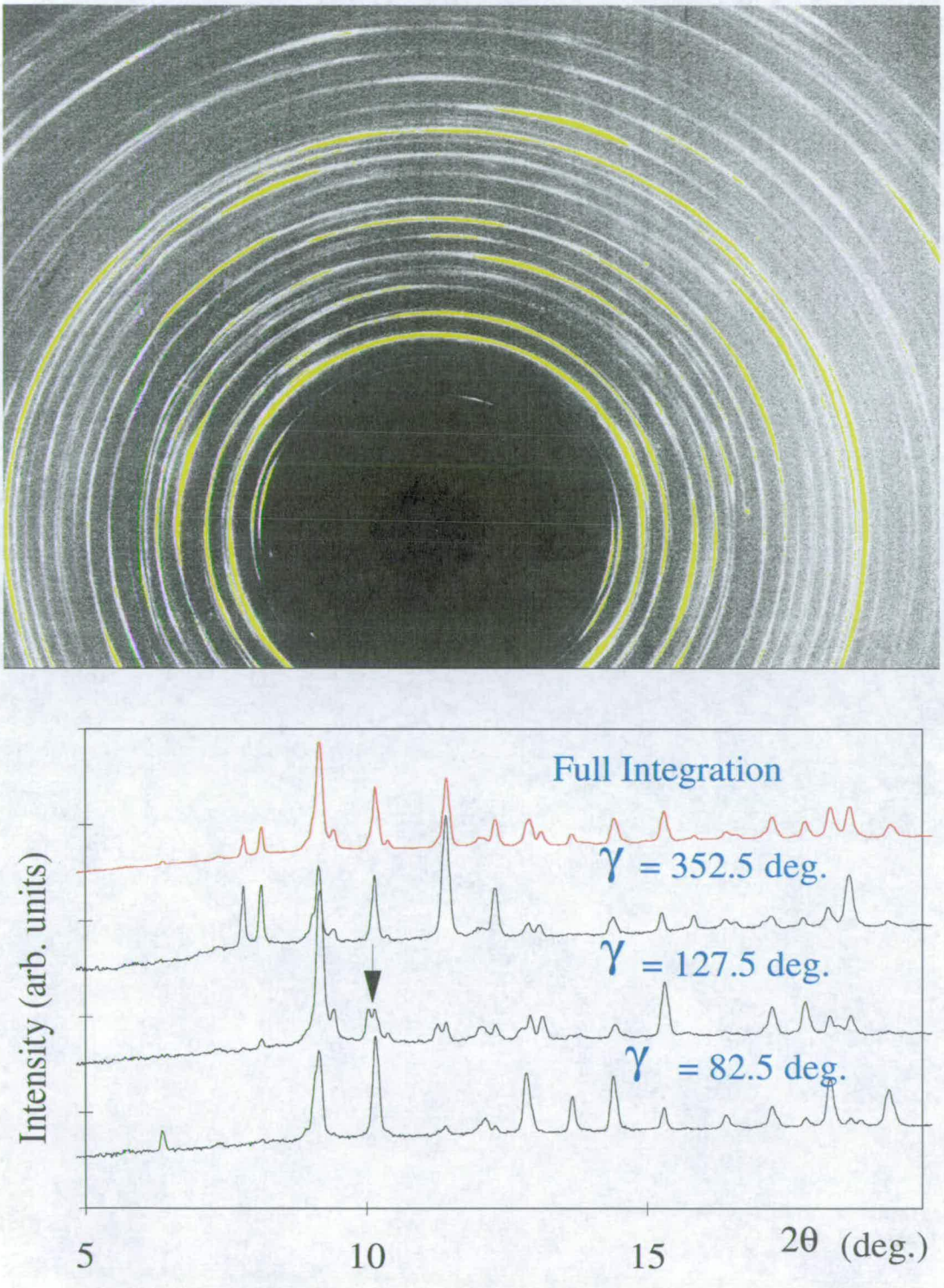


Figure 6.2. (a) Strong texture in Ba at 13.3 GPa. (b) Selected sectors and the complete integration showing the vastly different patterns that can be obtained for one sample.

unexpected aid to structure solution. Fig. 6.2b shows selected sectors from the 2-d image (Fig. 6.2a) along with the full integration. As can be seen, the powder patterns vary greatly between sectors. One particular instance where the texture in the sample might help to index the pattern can be seen in the pattern obtained from the sector at $\gamma = 127.5°$. The arrows highlight a pair of closely spaced peaks that, in this sector, are particularly well resolved compared to the same peaks in other sectors or in the full integration. The peaks are still overlapped in the $\gamma = 127.5°$ sector but, because of texture, the relative intensities are similar (the full integration suggests that under ideal conditions the peak on the right is much more intense that the peak on the left. This makes the determination of the peak positions of this pair of peaks in this sector much more accurate than a similar determination from other sectors (or the full integration) where the peak on the right of the pair is considerably more intense than the peak on the left.

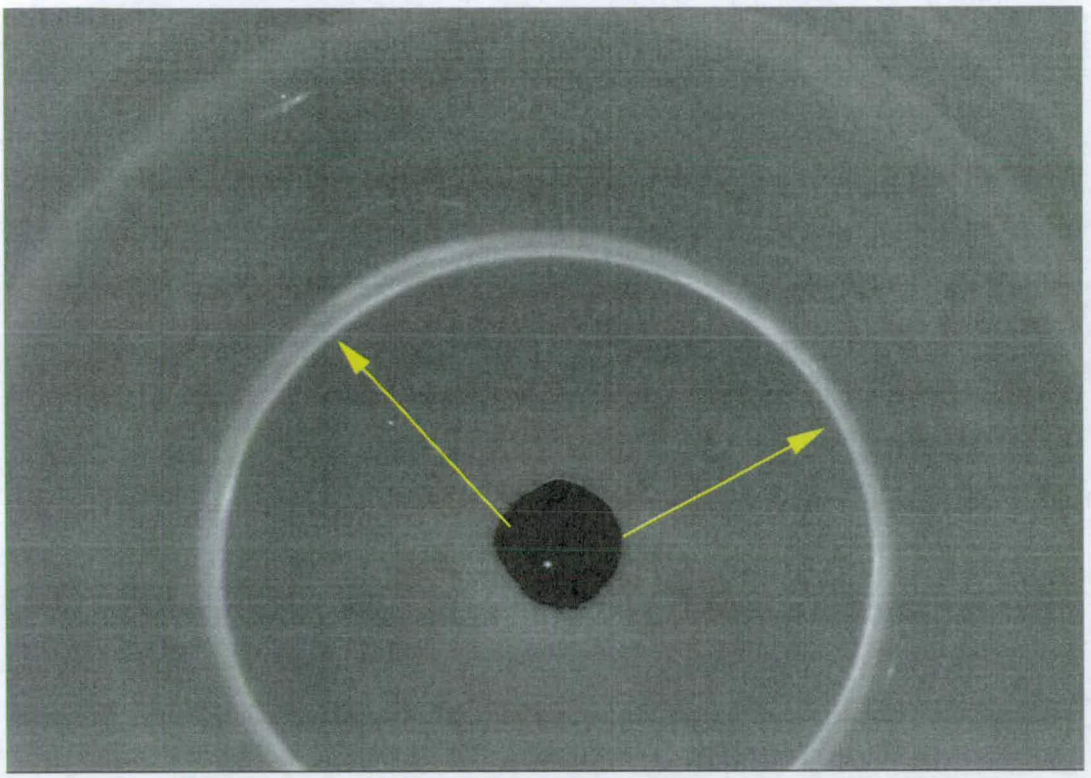
Another instance where texture may help to index a powder pattern comes from the (hkl)-dependence of the intensity variations around the powder rings caused by texture. More precisely, for a fixed POA direction, the variations depend on the polar and azimuthal angles, in the crystal system, of all the scattering vectors that contribute to a powder ring. These angles depend on the indexing of the scattering vectors and the unit cell parameters. The polar and azimuthal angles of the scattering vectors contributing to a given powder rings are normally fixed by the known unit cell and indexing but are potentially refineable parameters in the POFIT program. In the case of unknown unit cell and indexing, these parameters could be refined. This extra angular information, combined with measured 2θ, could be used to narrow down possible indexings. The full practicalities of such a procedure have yet to be assessed, but the best chance of success would come from a sample with pronounced texture (exhibiting large changes in intensity around the powder rings) that has low symmetry (so the number of symmetry-equivalent reflections contributing to a powder ring is low)—the Ba sample, from which Fig. 6.2a was obtained, would seem to fulfil both these criteria.

Even if quantitative indexing from texture is not practical, qualitatively, it can be seen there is still a lot of information to be gained from the texture in Fig. 6.2a. For example, the two lowest angle peaks exhibit very similar intensity variations so their reciprocal lattice vectors might be expected to lie almost parallel to each other in the unit cell and thus have similar indexings.

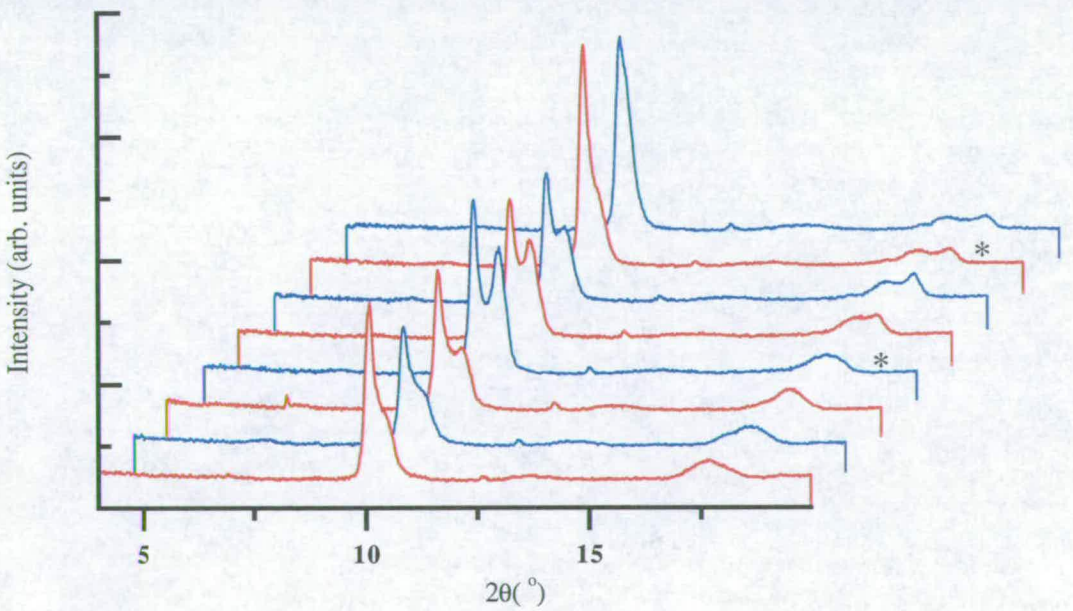
6.3 Anisotropic Stress and Strain

Figure 6.3a shows 2θ variations around the powder rings of a sample of CsBr at 52.5 GPa. The splitting of the lowest angle powder rings clearly varies as a function of azimuth around the powder rings. Figure 6.3b shows the 1-d plots from various sectors around the image. The asterisks mark the sectors along the direction of the arrows in Fig. 6.3a. Depending on the sector, the first peak can be observed as a singlet or a doublet. The collection of the nearly complete powder ring by the image-plate shows immediately the variable splitting. Interestingly, it is the ring at higher 2θ that 'wanders' as a function of azimuth while the ring a lower 2θ is close to circular. Similar changes in splitting can be seen in the higher angle rings.

The origin of such splittings is not completely understood. If the sample was under anisotropic stress then the strain induced in the lattice will depend on the orientation of the crystallites within the diffracting volume. This case is most analogous to preferred orientation and could possibly be tackled using a model similar to the symmetrised harmonics model presented in Chapter 4 to fit the changes in position around the powder rings. For anisotropic stress, the strain induced depends on the orientation of the crystallite with respect to the stress field and does not depend on the indexing of the powder rings; all powder rings would exhibit the same 2θ wander. This is *not* what is observed in Fig. 6.3a where some rings wander more than others; there is obviously some (hkl)-dependent effect at work in addition to the anistropic stress.



(a)



(b)

Figure 6.3. (a) CsBr at 52.5 GPa. The arrows highlight the variable splitting of the lowest angle peaks cause by strongly anisotropic strain in the sample. (b) 1-d plots at various angles around the 2-d image. The asterisks mark those along the arrowed directions in the 2-d image.

Two possible candidates for explaining the (hkl)-dependent aspect of the 2θ variations seen in Fig. 6.3a, are: (i) anisotropic elastic properties of the sample material, and (ii) defects in the crystallites, such as stacking faults. If a material with anisotropic elastic properties is put under isotropic stress it will exhibit anisotropic strain. This situation poses no problem for structure solution and refinement since the strain satisfies the symmetry of the crystal. However, under anisotropic stress the strain of a crystallite depends on its orientation. In powder diffraction the data collected will be an average over many different crystallite orientations and the symmetry of the strain will not be readily apparent without knowledge of the orientation of all the crystallites contributing to the powder pattern.

Peak displacements can also be caused by defects in the crystallites such as stacking faults. Stacking faults affect the reflections from the faulted planes but have little effect on the reflections from planes perpendicular to the fault plane. In this respect, stacking faults cause (hkl)-dependent effects on the powder pattern but, as for anisotropic strain, the orientational effects must come from the sample stress conditions. Whatever combination of effects cause 2θ wander in 2-d powder patterns collected from samples under pressure, it is expected that 2θ wander of the type shown in Fig. 6.3a will be amenable to similar analysis as presented in Chapter 4 for modelling preferred orientation.

There is an experimental possibility for relieving the anisotropic nature of the stress in the sample—annealing. Anisotropic stresses in the sample exist only if the material is strong enough to withstand the shear stress involved. Heating the sample will tend to weaken the material, lowering its yield strength, and thus relieve the shear stress. Care has to be taken when heating the beryllium-backed pressure cells described in Chapter 2 when the sample is at high pressure. Heating will soften the beryllium as well as the sample and the backing discs might fail at high temperatures. It may not be possible to achieve temperatures where the sample becomes sufficiently weak to relieve the anisotropic stresses before the

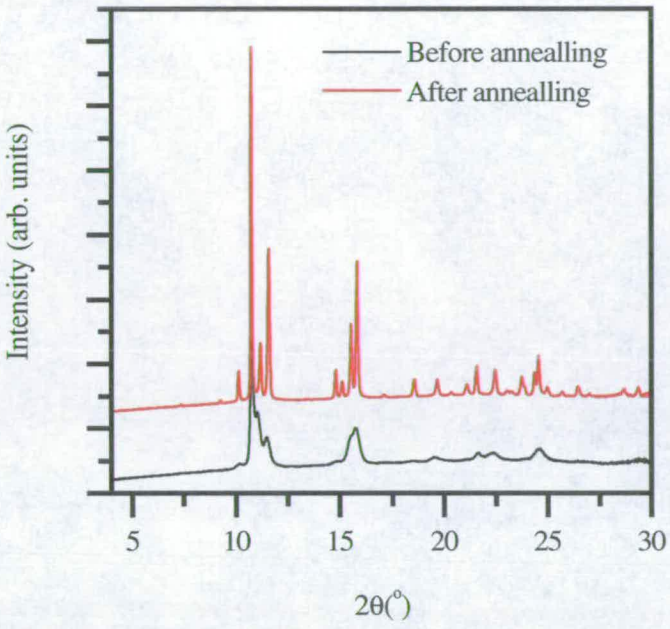


Figure 6.4. (a) GaAs at 22 GPa before (black) and after (red) annealling at 200°C.

beryllium-backed pressure cells fail.

Figure 6.4 shows the powder pattern of a sample of GaAs at 22 GPa and room temperature before and after annealing at 200°C. As can be seen, the powder pattern is considerably sharper after annealling than before, leading to a corresponding increase in resolution and data quality. This is quite encouraging, but 200°C is a modest temperature and similar attempts to anneal CsI at 35 GPa by heating the sample to 200°C had no effect on the pattern. Higher temperatures seem to be required to anneal CsI (which exhibits the same problems as CsBr) but it is not clear how safe it is to heat Be-backed cell to temperatures greater than 200°C and no attempts have been made to heat the cells to temperatures above 200°C. Using cells which support the diamond on different backing materials (e.g. open cone tungsten carbide backed cells) will help to overcome this problem, enabling materials to be heated to higher temperatures without risking cell failure.

Chapter 7

Conclusions

Microstuctural effects in powder samples at high-pressure can be severe and can greatly reduce the accuracy of structural studies or even prevent structural analysis from being carried out. If accurate structural studies of materials at high pressure are to be successful, it is crucial that microstructure in samples is detected and if possible modelled and taken into account fully at all stages of structure solution and refinement.

The 2-d nature of the image-plate detector has made it possible to detect the presence of microstructure—such as preferred orientation or texture, or anisotropic stress—in the sample. As these effects are anisotropic, their effect on the powder diffraction pattern depends on the orientation of the sample with respect to the incident beam and the azimuthal angle around the beam at which the diffraction is detected. Microstructural effects can cause variations of intensity (preferred orientation and texture) and variations in radial distance (anisotropic stress) around the powder rings, and these variations differ depending on the orientation of the sample with respect to the incident beam. The possibility of modelling these effects by the use of the full 2-d data available from the image-plate combined with the ability to observe the diffraction from a sample in a variety of orientations with respect to the incident beam has been explored in

this thesis.

The experimental techniques of angle-dispersive high-pressure powder diffraction have been developed to include the ability to carry out routine sample inclinations to allow data about the microstructure in the sample to be collected with little contamination from the gasket. By incorporating a high-precision rotation stage in the sample stage combined with digital position encoding of the micrometers and new pressure cell holders that ensure kinematic location on the sample stage, it is now possible to incline samples routinely without the need to carry out a full alignment every time the sample is removed and replaced on the sample stage. Data quality has been enhanced by the installation of new shielding that completely encloses the experimental set-up and the use of a beamstop to capture the part of the incident beam that passes through the sample has greatly reduced the background recorded by the image-plate. In anticipation of future microstructural studies—in particular, the study of peak position variation around the powder rings—the image-plate holder has been upgraded to permit the accurate alignment of the image-plates perpendicular to the incident beam so the effects plate tilt can confidently be removed from any analysis of peak position wander around the rings. The image-plate data analysis software has been upgraded to include facilities for outputting azimuthal sectors from the image from which intensity and position variations of the powder rings are extracted. A new analytic absorption correction for sample in diamond-anvil pressure cells inclined to the beam has been presented.

A demonstration has been given of the qualitative information available from the combination of 2-d data and sample inclinations about the preferred orientation present in samples at high pressure. New least-squares refinement software has been written that can fit the previously developed simple analytic function model of preferred orientation to the intensity variations around many powder rings simultaneously. It has been found that this model has trouble fitting the extreme variations caused by strong but well behaved preferred orientation. A

new model, based on the symmetrised spherical harmonics model of texture commonly used by the texture analysis community, has been developed and applied to the analysis of preferred orientation using 2-d data with considerable success. This model is also sufficiently general to describe more complex textures than the simple, smooth, axially symmetric textures that the simple analytic function model describes, and thus provides a path toward the full solution of the texture problem at high pressure. The first quasi-2-d Rietveld refinement has been carried out in the form of simultaneous refinement of 24 sectors of a 2-d image exhibiting the effects of PO. For 2-d images collected from non-inclined samples that show peak intensity and position changes around the powder rings, 2-d Rietveld refinement will play a necessary part in the future of accurate structural studies of materials at high pressure.

The structural pressure dependence of the cinnabar phase of HgS has been followed with and without the presence of severe preferred orientation in the sample. By modelling the preferred orientation with the symmetrised harmonics model is has been shown that the refined atomic coordinates can be de-correlated from preferred orientation in the sample.

A brief overview has been given of other texture effects and anisotropic stress effects in powder samples at high pressure. There is an interesting possibility that texture in a sample might actually be advantageous when the sample's structure is unknown. The (hkl)-dependent nature of texture could help to index or provide a relative indexing of a powder pattern. Anisotropic stress in the sample is a major hurdle for structure solution. Although, no quantitative model has been developed, there is certainly a great deal of information about this effect revealed in the 2-d image-plate data and it is expected that the anisotropic stress effect will be amenable to modelling similar to the texture modelling presented in this thesis.

Much effort has gone into developing experimental equipment and procedures to enable samples to be inclined routinely without contamination from the gasket

surrounding the sample. Unfortunately, contamination from the beryllium backing disc of the diamond-anvil cell used to carry out the experiments presented in this thesis causes quite significant contamination of the powder pattern with Be powder rings. Open cone cells exist where the diffraction pattern only passes through diamond but these cells necessarily have small a opening angle in order to provide sufficient support to the diamond to allow the cells to reach high pressure. Since the accuracy of microstructure modelling often depends on inclining the sample at the highest possible angle to the beam in order to bring about the largest possible variations around the powder rings, the small opening cone angle of these cells restricts the modelling of sample microstructure by the methods presented in this thesis. Future development of pressure cells to improve the angular access to the sample is expected.

High temperature will also play an increasingly important part in high-pressure structural studies. The primary purpose of combined high-pressure high-temperature experiments will be to study the vast array of new physics and structures that occur in this regime. Such studies are of particular interest for their applicability to planetary interiors where materials are under extreme pressure and temperature. The development of this combined technique will likely have a secondary advantage in the form of sample annealing where non-hydrostatic stresses are relieved because the application of temperature softens the stressed materials such that they cannot support large anisotropic stresses.

The ever increasing power of computers has now made it practical to carry out Rietveld analysis of 2-d powder patterns. It has been shown that the current version of GSAS (Larson and Von Dreele (1985)) can perform such a refinement. However, no current Rietveld refinement package is fully applicable to modelling data collected by image-plates from samples at high pressure in diamond-anvil cells. There is particular need for a new peak profile description, especially one that includes a model of anisotropic peak displacements. As stated, at present,

anisotropic displacements are the cause of severe problems for high-pressure structural studies even when the general structure is known. It is expected that new Rietveld software applicable to high-pressure structural studies will be developed in future.

The advent of area detectors such as the image-plate has permitted an unparalleled increase in the accuracy of high-pressure structural studies. The data collected by the image-plate are now of sufficiently high quality that the accuracy of such studies is more limited by sample quality (i.e the presence of sample microstructure) than data quality. However, the 2-d nature of the image-plate combined with suitable experimental techniques (sample inclination) has allowed both qualitative and quantitative information about sample microstructure to be extracted without reference to a full structural model. It is clear that 2-d data analysis will play an increasingly important role in the future of accurate high-pressure structural studies using powder diffraction techniques.

References

Adams, D. M., Private communication (1992).

Allan, D. R., Ph. D. thesis, The University of Edinburgh (1993).

Aurivillius K. L., Acta Chem. Scand. **4**, 1413 (1950).

Aurivillius, K. L. and Carlsson, I., Acta Chem. Scand., **12**, 1297 (1958).

Barrett, C., Massalski, T. B., in 'Structure of Metals' International Series of Materials Science and Technology, Vol. 35, Pergamon Press (1992).

Birch, F., J. Geophys. Res., **57**, 227 (1952).

Block, S., Weir, C. E. and Piermarini, G. J., Science, **148**, 947 (1965).

Boultif, A. and Louer, D., J. Appl. Cryst., **24**, 987 (1991).

Bunge, H. J., Texture Analysis in Materials Science. London:Butterworth (1982).

Buras, B., Staun, J., Olsen, S., Gerward, L., Will, G. and Hinze, E., J. Appl. Cryst., **10**, 431 (1977).

Čapkova, P., Peschar R. and Schenk, H., J. Appl. Cryst., **26**, 449 (1993).

Čapkova, P. and Valvoda, V., Czech. J. Phys. B, **24**, 891 (1974).

Decker, D. L., Bassett, W. A., Merrill, L., Hall, H. T. and Barnett, J. D., J. Phys. Chem. Ref. Data, **1**, 773 (1972).

Dollase, W. A., J. Appl. Cryst., **19**, 267 (1986).

Forman, R. A., Piermarini, G. J., Barnett, J. D. and Block, S., Science, **176**, 284 (1972).

Huang, T. and Ruoff, A. L., Phys. Rev. B, **27** 7811 (1983).

Huang, T. and Ruoff, A. L., Phys. Rev. B, **31**, 5976 (1985).

Imhof, J., Textures Micostruct., **5**, 73 (1982).

Jamieson, J. C., Lawson, A. W. and Nachtrieb, N. D., Rev. Sci. Inst., **30**, 1016 (1959).

Jayaraman, A., Phys. Rev. Lett., **29**, 1674 (1972).

Jayaraman, A., Rev. Mod. Phys., **55**, 65 (1983).

Kusaba, K. and Weidner, D. J., Bull. Am. Phys. Soc., **38**, 1516 (1993).

Larson, A. C. and Von Dreele, R. B., General Structure Analysis System (GSAS), Los Alamos National Laboratory Report LAUR 86-748 (1985).

Liebenberg, D. H., Phys. Lett. A, **73**, 4 (1979).

Mao, H. K., Bell, P. M., Shaner, J. W. and Steinberg D. J., J. Appl. Phys., **49**, 3279 (1978).

Mao, H. K., Mao, A. and Bell, P. M., Abstracts of the 8th AIRAPT Conference, Uppsala, Edited by C. M. Backman, T. Johannisson, L. Tegner, Vol. II, 453 (1982).

Mao, H. K., Wu, Y., Hemley, R. J., Chen, L. C., Shu, J. F., Finger, L. W. and Cox, D. E., Phys. Rev. Lett., **64**, 1749 (1990).

Mao, H. K. and Bell, P. M., Carnegie Inst. Washington Yearbook, **79**, 409 (1980).

March, A., Z. Kristallogr., **81**, 285 (1932).

Marino, A. N. and Warekois, E. P., Science, **142**, 672 (1963).

Matthies S., Wenk, H.-R. and Vinel, G. W., J. Appl. Cryst., **21**, 285 (1988).

Matthies, S. and Vinel, G. W., Phys. Status Soldi B, **112**, K111 (1982).

McMahon, M. I., Nelmes, R. J., Wright, N. G. and Allan, D. R., Phys. Rev. B, **48**, 16246 (1993).

McMahon, M. I. and Nelmes, R. J., J. Phys. Chem. Solids., **56** 485 (1995).

McMahon, M. I. and Nelmes, R. J., Phys. Rev. Lett., **78**, 3697 (1997).

Merrill L. and Bassett, W. A., Rev. Sci. Inst., **45**, 290 (1974).

Nelmes, R. J., Hatton, P. D., McMahon, M. I., Piltz, R. O., Crain, J., Cernik, R. J. and Bushnell-Wye, G., Rev. Sci. Inst., **63**, 1039 (1992).

Nelmes, R. J., McMahon, M. I., Wright, N. G., Allan, D. R. and Loveday, J. S., J. Phys. Chem. Solids., **56**, 539 (1995a).

Nelmes, R. J., McMahon, M. I., Wright, N. G. and Allan, D. R., J. Phys. Chem. Solids., **56**, 545 (1995b).

Nelmes, R. J., McMahon, M. I., Wright, N. G. and Allan, D. R., Phys. Rev. B, **48**, 1314 (1993).

Nelmes, R. J. and McMahon, M. I., J. Synch. Rad., **1**, 69 (1994).

Peschar, R., Schenk, H. and Čapkova, P., J. Appl. Cryst., **28**, 127 (1995).

Piermarini, G. J., Block, S. and Barnett, J. S., J. Appl. Phys., **44**, 5377 (1973).

Piermarini, G. J. and Block, S., Rev. Sci. Inst., **46**, 973 (1975).

Piermarini, G. J. and Weir, C. E., J. Res. Natl. Bur. Stand., Sec. A **66**, 325 (1962).

Piltz, R. O., McMahon, M. I., Crain, J., Hatton, P. D., Nelmes, R. J., Cernik, R. J. and Bushnell-Wye, G., Rev. Sci. Inst., **63**, 700 (1992).

Popa, N. C., J. Appl. Cryst., **25**, 611 (1992).

Qadri, S. B., Skelton, E. F. and Webb A. W., Bull. Am. Phys. Soc., **38**, 1545 (1993).

Rietveld, H. M., J. Appl. Cryst., **2**, 65 (1969).

Rietveld, H. M., J. Appl. Cryst., **2**, 65 (1969).

Ruer, D. and Baro, R., J. Appl. Cryst., **10**, 458 (1977).

San-Miguel, A., Polian, A., Gauthier, M. andItié, J. P., Phys. Rev. B, **48**, 8683 (1993).

San-Miguel, A., Wright, N. G., McMahon, M. I. and Nelmes, R. J., Phys. Rev. B, **51**, 8731 (1995).

Sasa Y. and Uda, M., J. Solid State Chem., **18**, 63 (1976).

Shimomura, O., Takemura, K., Fujihisa, H., Fujii, Y., Ohishi, Y., Kikegawa, T., Amemiya, Y. and Matsushita, T., Rev. Sci. Inst., **63**, 967 (1992).

Spain, I. L. and Dunstan, D. J., J. Phys. E, **22**, 923 (1989).

Stanton, M., Phillips, W. C., Li, Y. and Kalata, K., J. Appl. Cryst., **25**, 549 (1992).

Svensson, S. O., Hammersley, A. P., Thompson, A., Gonzalez, A. and Ursby, T., CCP4/EPS-EACBM Newsletter **29** (1993).

Toraya, H. and Marumo, F., Mineral. J., **10**, 211 (1981).

Uda M., Z. Anorg. Allg. Chem., **350**, 105 (1967).

Van Valkenburg, A., Conference Internationale Sur-les-Hautes Pressions, LeCreusot, Saone-et-Loire, France (1965).

Weir, C. E., Lippincott, E. R., Van Valkenburg, A. and Bunting, E. N., J. Res. Natl. Bur. Stand., Sec. A **63**, 55 (1959).

Weir, C. E., Block, S. and Piermarini, G. J., J. Res. Natl. Bur. Stand., Sec. C **69**, 275 (1965).

Werner, A., Hochheimer, H. D., Strössner, K. and Jayaraman, A., Phys. Rev. B, **28**, 3330 (1983).

Werner, P. E., Eriksson, L. and Westdahl, M., J. Appl. Cryst., **18**, 367 (1985).

Will, G., Parrish, W. and Huang, T. C., J. Appl. Cryst., **16**, 611 (1983).

Williams, R. D., J. Appl. Phys., **39**, 4329 (1968).

Wright, N. G., McMahon, M. I., Nelmes, R. J. and San-Miguel, A., Phys. Rev. B, **48**, 13111 (1993).

Wright, N. G., Ph. D. thesis, The University of Edinburgh (1994).

Young, R. A., Mackie, P. E. and Von Dreele, R. B., J. Appl. Cryst., **10**, 262 (1977).

Published Work

High Pressure Research, 1996, Vol. 14, pp. 277–286
Reprints available directly from the publisher
Photocopying permitted by license only

© 1996 OPA (Overseas Publishers Association)
Amsterdam B.V. Published in The Netherlands under
license by Gordon and Breach Science Publishers SA
Printed in Malaysia

2-d DATA COLLECTION IN HIGH PRESSURE POWDER DIFFRACTION STUDIES – APPLICATIONS TO SEMICONDUCTORS

M. I. McMAHON, R. J. NELMES, H. LIU and S. A. BELMONTE

Department of Physics and Astronomy, The University of Edinburgh, Edinburgh, U.K.

(Received June 5 1995)

Using angle-dispersive diffraction techniques and synchrotron radiation, we have made a detailed re-examination of the high-pressure behaviour of a number of core II–VI, III–V and group IV semiconductors. Despite much previous work on these materials, the good resolution afforded by angle-dispersive techniques, and the high-sensitivity of the image-plate area detector have yielded many new results which reveal that the accepted structural systematics have to be modified quite substantially. In this paper, we summarise the newly emerging structural systematics, and use the results to show how access to full 2-d powder patterns has proved essential in determining correct crystal structures.

KEY WORDS: High-pressure crystallography, angle-dispersive powder diffraction, image plate area detector, Rietveld refinement, semiconductors.

INTRODUCTION

Structural studies of II–VI, III–V and group IV semiconductors have remained at the forefront of high-pressure crystallography since the development of high-pressure diffraction techniques in the early 1960's. Very broadly, the picture that has been built up over these last 30 years is that the ambient-pressure 4-fold coordinated diamond/zincblende structure (wurtzite in a few cases) transforms first to a 6-fold coordinated tetragonal β-tin structure, and then to an 8- or 12-fold coordinated hexagonal structure, with an NaCl phase between the zincblende and β-tin phases in many of the III–V and II–VI systems[1]. There are some exceptions, but this is the accepted general trend: a progression through a sequence of increasingly coordinated, high-symmetry structures, with no variable atomic coordinates in most cases.

During the past 4 years, we have made a systematic re-examination of the core II–VI, III–V and group IV semiconductors at SRS Daresbury, using angle-dispersive techniques and an image-plate detector. The superior resolution afforded by angle-dispersive techniques, and the unrivalled sensitivity of image-plate data have enabled us to show that the carefully-constructed picture of structural systematics in these materials is substantially incomplete and incorrect[1–3]. Studies of Si and Ge, AlX, GaX and InX (X = P, As, Sb), and ZnX, CdX and HgX (X = S, Se, Te) have *all*

yielded unexpected new results that reveal a quite different picture. The principal features of the newly emerging structural systematics are:

1) The fact that between the cubic ambient-pressure phase and the cubic or hexagonal very high-pressure phases, there is a wide range of pressure in which all the systems so far examined have orthorhombic structures with *variable* atomic coordinates.
2) The emergence of key structure types completely new to these systems–such as those with Cmcm symmetry (first found in ZnTe) and Imma symmetry (first found in Si).
3) The apparent rarity or absence of tetragonal symmetry in general and the β-tin structure in particular (except in the group IV elements).

The solution and refinement of new low-symmetry structures has required a whole new level of data-collection and structural-analysis techniques[4]. Although it has proved trivial in many cases to show that a particular structure is not, for example, β-tin, it has often proved somewhat more difficult to determine what the *true* crystal structure is. For example, a consequence of low-symmetry structures is many overlapped reflections, which can lead to ambiguous indexing schemes or spacegroup determinations; the presence of variable atomic coordinates creates a degree of structural ambiguity – very different structures can have similar diffraction patterns; and preferred orientation and effects like deviatoric stress can make definitive structure solution difficult.

It has become clear that the key to reducing and eventually overcoming these problems is the collection of full 2-dimensional Debye-Scherrer (DS) patterns on an appropriate area detector – in our case, an image-plate detector. We have found that high-quality 2-d images provide two substantial, and often crucial, benefits over the restricted images obtainable with slot-aperture pressure cells: firstly, the signal:noise ratio of the integrated profile and the accuracy of the peak intensities are greatly enhanced by the much increased number of data points in the full 2-d image, and, secondly, important information on preferred orientation and effects like deviatoric stress can be obtained from the full 2-d image *prior* to integration. In this paper, we consider these two types of benefits in turn, and give examples from our recent studies of cases where 2-d data have been crucial. We also consider recent advances in diamond anvil cell technology which have extended the upper pressure limit at which full 2-d images can be obtained, and discuss the future availability of 2-d images at pressures above 100 GPa.

EXPERIMENTAL TECHNIQUES

All diffraction data have been collected on station 9.1 at SRS Daresbury. The incident wavelength is chosen to eliminate $\lambda/3$ contamination, and is typically either 0.4447Å (near to the In K-edge) or 0.4654 Å (near to the Cd K-edge). The 2-dimensional Debye-Scherrer patterns are collected on Kodak image plates and are read on a Molecular Dynamics 400 A PhosphorImager, using a pixel size of $88 \times 86\,\mu m^2$. Details of our experimental set up, alignment procedure, and pattern integration

software have been reported previously[4]. Details of the conical-aperture pressure cells used in our studies are given below. Structural results have been obtained through full Rietveld refinement of the integrated profiles using the programs MPROF and GSAS.

DISCUSSION

2-d Images: The Benefits of Improved Signal: Noise and Accuracy

The first step in determining an unknown structure is to index the diffraction pattern. For correct indexing, observation of the lowest-angle reflection is often critical. As these reflections are often very weak in low symmetry structures, the increased signal: noise obtained from the full-pattern integration can be crucial to observing them. The diffraction pattern in Figure 1 was obtained from a 6-hour exposure of ZnTe-III at 15.7 GPa. The inset shows a very weak reflection [indexed as (110) in the final Cmcm unit cell], which was detected only in the integration of this multi-hour exposure of a full 2-d pattern. This reflection proved to be the key to solving the long-standing problem of the ZnTe-III structure[5].

After indexing the integrated profile, the next step in structure solution is to determine the spacegroup – a process which often depends on determining which reflections are *absent*. The extent to which one can be confident that a reflection is, or is not, absent is greatly improved by achieving the greatest possible signal: noise. For example, in the ZnTe-III profile shown in Figure 1, one can be confident that the (100), (010), (001), (101), and (011) reflections are absent at low angles, while the very weak (110) reflection is present. Analysis reveals that this barely visible reflection is the only feature in the whole diffraction profile that distinguishes between the

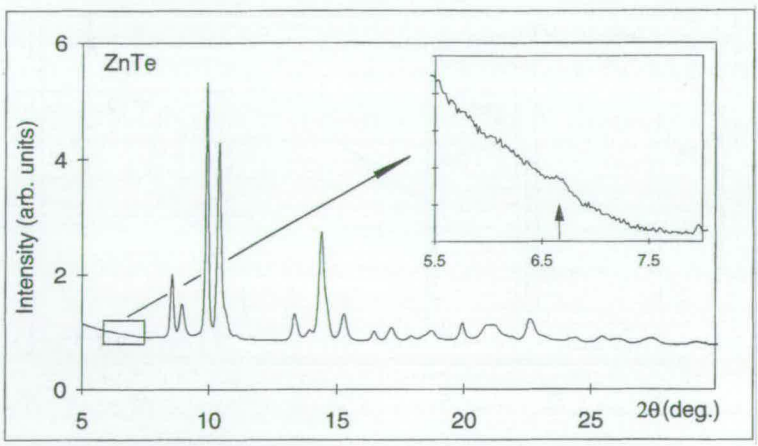


Figure 1 Integrated profile of a pattern recorded from a sample of ZnTe-III at 15.7 GPa. The inset shows an enlarged view of the weak (110) reflection.

true spacegroup, Cmcm, and two others, Cmca and C2cb[5]. A still more extreme example is given by InSb-IV, the complex structure of which was readily solved once the spacegroup had been determined[6]. The inset to Figure 2 shows a low-angle region of the InSb-lV profile, collected both near to (*n*) and far from (*f*) the In K-edge. As with ZnTe-III, it was only the presence of the (110) reflection that decided between Cmcm and Cmca/C2cb. This reflection has an intensity $< 0.1\%$ of the strongest reflection, and (as the inset shows) was observable only in an 8-hour exposure near the In K-edge – using anomalous dispersion techniques to enhance the difference in scattering power between In and Sb.

The ability to observe very small intensity changes has enabled us to use anomalous-dispersion techniques routinely in this way to help distinguish similarly scattering atoms in systems like InSb[7] and CdTe[8], and determine whether or not their high-pressure structures are site ordered. The use of anomalous dispersion has also proved essential in our studies of the Cmcm structures of ZnTe[5] and HgTe[9], where two subtly (but significantly) different, ordered atomic arrangements give rise to similar diffraction profiles, despite the very different scattering powers of the two atomic species. In such cases, distinguishing between the different possible arrangements can depend on detecting very small changes in reflection intensities. For HgTe, we had to collect data at both the Te K-edge, and the Hg L-edges to try to make the distinction.

Accuracy in reflection intensities is particularly important in determining the pressure dependence of crystal structures; and this is of vital interest for the many high-pressure structures of the core semiconductors now shown to have variable atomic coordinates. Figure 3 shows the complex behaviour of the nearest-, next-nearest-, and second-nearest-neighbour bondlengths in CdTe through the NaCl → Cmcm phase transition at 10 GPa[10]. This complexity arises mainly from the

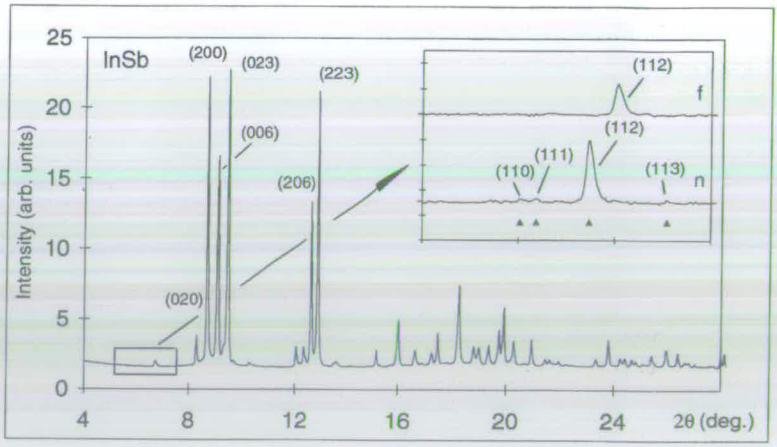


Figure 2 Integrated profile from a pattern recorded from a sample of InSb-IV at 5.1 GPa. The inset shows, on a common intensity scale, an enlarged view of the low-angle region of the profile recorded at 0.4635 Å, far (f) from the In K-edge, and at 0.4445 Å, near (n) the In K-edge (0.4439 Å).

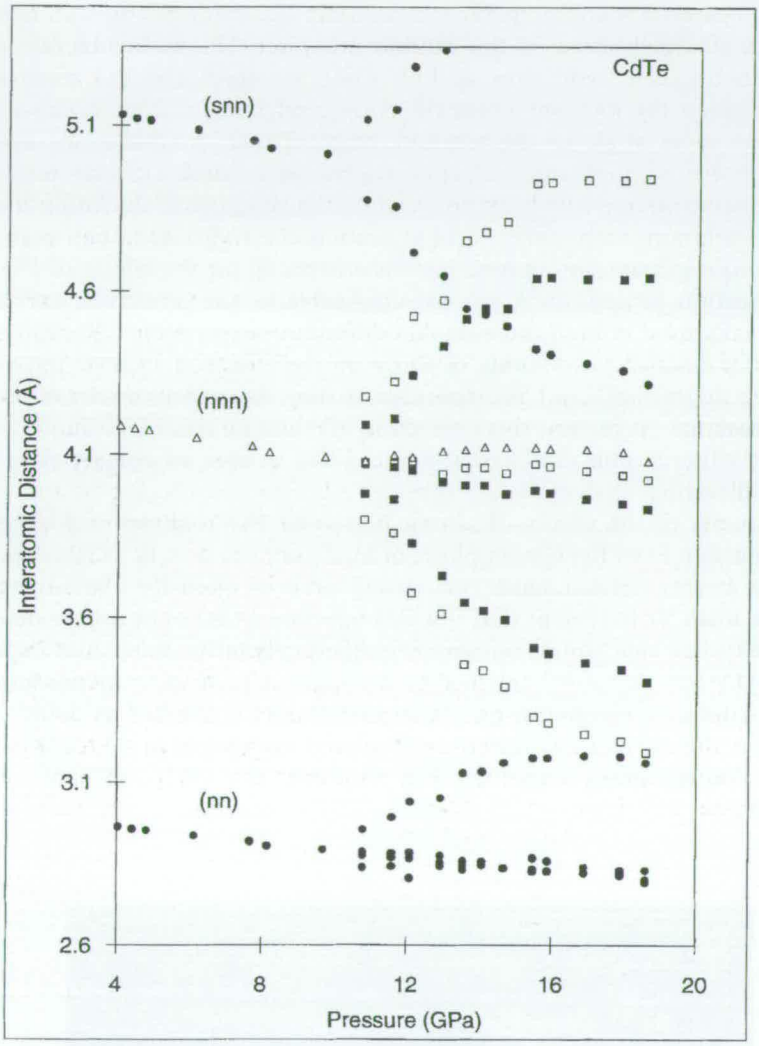


Figure 3 The pressure dependence of the nearest- (nn), next-nearest- (nnn), and second-nearest-neighbour (snn) distances in CdTe through the NaCl → Cmcm phase transition at 10 GPa. Cd-Te distances are denoted •, Cd-Cd distances are denoted □, Te-Te distances are denoted ■, and Δ denotes equal Cd-Cd and Te-Te distances.

difference in the pressure dependence of the two variable atomic coordinates in the Cmcm structure, which varies by only 6% over a pressure range of 8 GPa[10].

2-d Images: Information Available Prior to Integrating

We have found that important, and often vital, information can also be obtained from the 2-d images *prior* to integration. The most apparent information available is

that on preferred orientation (PO), a commonly occurring problem in high-pressure diffraction studies because of the extreme sample environment. In our studies, we distinguish between two forms of PO: axial, in which the PO distribution axis (POA) is along the incident beam direction; and non-axial, in which the POA is inclined at some angle to the incident beam. These two cases are distinguished experimentally by the former affecting the whole of each DS ring uniformly, and thus producing no intensity variation around the rings, while the latter does produce intensity variations (sometimes strong) around the rings. Although many Rietveld refinement programs contain methods for correcting for the effects of PO, the standard correction procedures[11] are not applicable to the particular diffraction geometry normally used in high-pressure AD diffraction experiments. Recently, however, as part of a detailed programme of study on the effects of PO, we have developed the correct algorithm[9] and incorporated it into the widely-used GSAS crystallographic package. At present this correction assumes an axial distribution – while we frequently observe non-axial distributions – and is used to correct only the integrated profile rather than the 2-d image.

An example of the effects of strong non-axial PO is given in Figure 4, which shows a pattern from the Cmcm phase of HgTe collected at 12.3 GPa. The principal DS rings in this pattern have two strong arcs of intensity 180° apart, and are otherwise weak. It is evident that if a slot-aperture DAC or scanning detector were being used, then one would obtain very different relative intensities depending on how the DAC or detector happened to be oriented relative to the variations in the powder pattern. Although this particular uncertainty is avoided by collecting the full DS pattern, the use of a 2-d detector still proved insufficient in this case to determine the true relative peak intensities. For example, the (002) reflection, which was

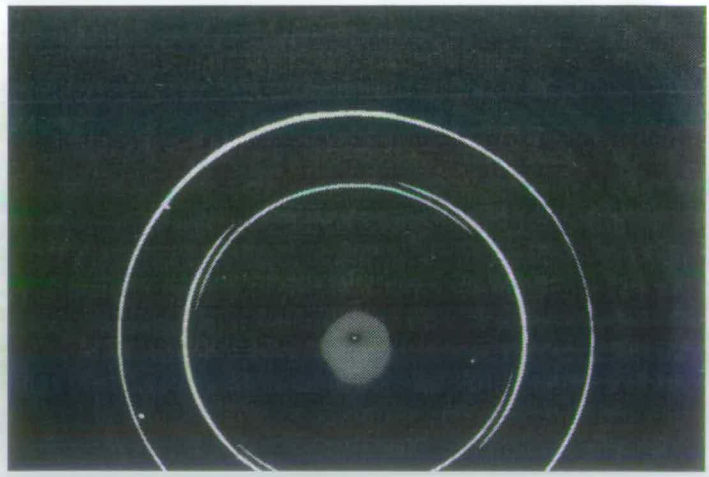


Figure 4 2-d diffraction pattern recorded from a sample of HgTe-IV at 12.3 GPa. The contrast of the image has been adjusted so as to enhance the intensity variation around the strongest Debye-Scherrer rings.

calculated to be quite strong, was completely absent in both the integrated profile and full 2-d image. However, as the axis of the DAC was inclined relative to the incident beam, the (002) reflection grew steadily in intensity, as illustrated in Figure 5. (Large changes in relative intensity are also apparent in the other reflections shown in this Figure.) As with the principal reflections, the (002) ring comprised two high-intensity arcs and might *still* have remained unobserved with a scanning detector or slot-aperture DAC. The successful detection of the (002) reflection removed uncertainty about the correctness of the structure solution, and this qualitative approach has proved valuable in several other cases. The next objective is to use the 2-d data to make accurate *quantitative* corrections for PO effects. Substantial progress has been made in this, as shown in the inset to Figure 6, which shows the dramatic intensity variation around the (003) powder ring – arrowed in the main Figure – of an HgS cinnabar sample inclined at 50° to the incident beam, and the (good) fit to these observations given by the present PO model.

The second type of information available from the 2-d images is that on deviatoric stress (due to stresses within the sample), and other effects which give rise to relative displacement of diffraction peaks. These are serious problems in high-pressure crystallography – more basic than that posed by PO which, although hindering space-group determination and structure refinement, does not prevent unit-cell indexing, the first step in structure analysis. In a sample with strong deviatoric stress, for example, the reflection positions do not fit any crystal lattice and definitive indexing

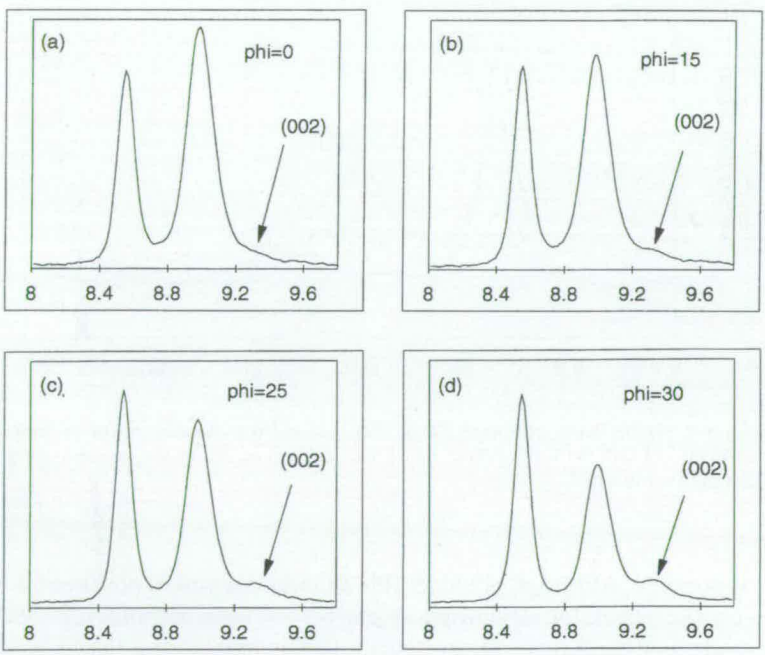


Figure 5 Integrated profiles of HgTe-IV collected with the DAC axis inclined at (a) 0°, (b) 15°, (c) 25° and (d) 30° to the incident x-ray beam. The position of the (002) reflection is indicated in each profile.

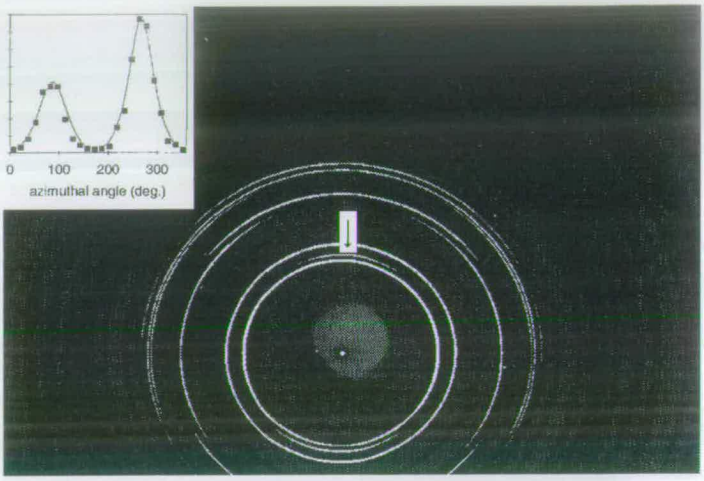


Figure 6 2-d diffraction pattern recorded from a highly-oriented HgS cinnabar sample inclined at 50° to the incident beam. The contrast of the image has been adjusted so as to enhance the intensity variation around the strongest Debye-Scherrer rings. The inset shows the dramatic intensity variation around the (003) powder ring – arrowed in the main Figure – and the fit to these observations given by the present preferred orientation model.

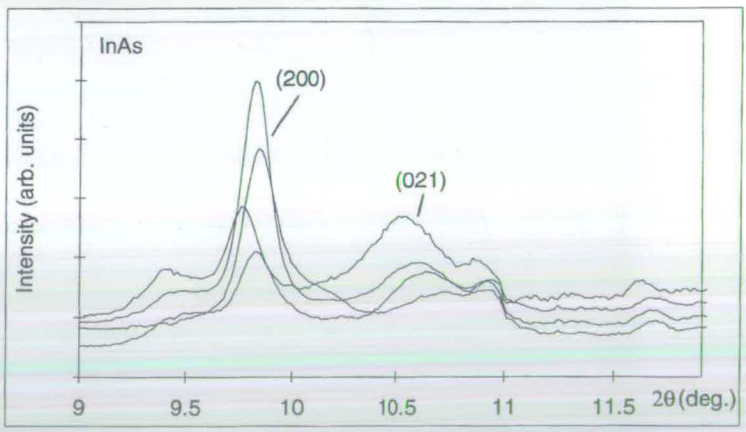


Figure 7 Integrated profiles from alternate 30° sectors, around the incident beam, from a pattern recorded from InAs at 23.5 GPa with the pressure cell axis inclined at 30° to the incident beam. The (200) and (021) reflections are indicated.

can prove impossible. Although considerable theoretical and experimental work has been done on the effects of deviatoric stress[12,13], several simplifying assumptions have been made; firstly, that the stress distribution is axial along the DAC axis, and, secondly, that the distribution is symmetric about that axis. Under these conditions, the DS rings from a sample affected by deviatoric stress will remain circular but will

have altered radii, and it is then not possible to decide whether a unit cell cannot be obtained because of deviatoric stress or because all possible unit cell options have not been exhausted. However, analysis of 2-d images shows that these assumptions are often not valid, and rings can be seen *not* to be circular. In any case, this manifestation of deviatoric stress in the sample can be obtained by inclining the pressure cell axis to the incident beam, as for studies of PO. It is thereby possible to decide whether a sample has deviatoric stress or not, even when nothing is known about the structure.

This technique has proved immensely useful in our studies of the III–V semiconductors, where both the diffraction profiles of the high-pressure phases, and the nature of the transitions from the lower-pressure NaCl phases, lead us to believe they probably have the orthorhombic Cmcm structure, despite misfits to orthorhombic unit cells. Figure 7 shows profiles obtained by integrating alternate 30° sectors, around the incident beam, from a pattern recorded from InAs at 23.5 GPa with the pressure cell axis inclined at 30° to the incident beam. The radius (2θ angle) of reflections can be seen to vary significantly, particularly for the (021) reflection where the variation is as much as $\sim 0.07°$. These displacements are large enough to account for the misfits to the Cmcm unit cell, and are tentatively ascribed to deviatoric stress. However, considerably more work is required before such effects can be corrected for prior to indexing.

2-d Images: Pressure Cells

In this paper we have described the greatly improved data quality and information about the sample's microstructure that is obtained from collecting full 2-d images. The diamond anvil cells (DACs) we have used in such studies have beryllium backing plates on the diamonds permitting full 2-d patterns to be collected to a maximum 2θ angle of either 40° (Merrill-Bassett type) or 50° (Diacell DXR4 and DXR5 type)[14]. While such cells provide wide angular access to the sample, the upper pressure limits obtainable using such cells have traditionally been severely limited by the relative softness of the beryllium plates. Recently, however, the availability of much harder beryllium has enabled us to use Be-backed cells at considerably higher pressures. For example, Merrill-Bassett DACs can now be routinely operated to 15 or 20 GPa (with 600 μm or 400 μm culets respectively), while we routinely operate to 65–70 GPa with a Diacell DXR5 DAC (with 300 μm culets). Recent studies using a gas-membrane driven pressure cell (Diacell DXR-GM) allowed diffraction studies of Cu to 75 GPa, before diamond failure. Using even harder beryllium, it should be possible to extend the upper pressure limit of such cells to beyond 100 GPa in the near future. Since PO and effects like deviatoric stress will generally become more pronounced with increasing pressure, this further development is essential.

CONCLUSIONS

The ability to collect full 2-d Debye-Scherrer patterns using the image plate system has been crucial in our diffraction studies of the core II–VI, III–V and group IV

semiconductors. The emerging dominance, in these materials, of low-symmetry structures, with refineable atomic coordinates and complex site ordering, have meant that high-quality data with high signal:noise are essential. The integrated profiles obtained using image-plate techniques provide such data, and allow the routine use of Rietveld refinement methods and anomalous dispersion techniques. Also of increasing importance is the information contained in the 2-d image itself, especially that concerned with preferred orientation and deviatoric stress (and other sources of peak displacement). As these effects are more pronounced at higher pressures, and can prevent even the most basic analysis of the diffraction profiles, 2-d image analysis can be expected to play an increasingly vital role in the detailed study of materials at high pressures.

Acknowledgements

We gratefully acknowledge the assistance of N. G. Wright, D. R. Allan, J. S. Loveday, A. A. Nield and G. Bushnell-Wye in various aspects of the experimental work, and the support of research grants from EPSRC and facilities made available by Daresbury Laboratory. Valued assistance with the maintenance and development of pressure cells has been given by D. M. Adams of Diacell Products.

References

1. See M. I. McMahon and R. J. Nelmes, Structural Studies of Tetrahedrally-Coordinated Semiconductors at High Pressure – New Systematics, *J. Phys. Chem. Solids.*, **56**, 485 (1995), and references cited therein.
2. R. J. Nelmes, M. I. McMahon, N. G. Wright and D. R. Allan, Structural Studies of II–VI Semiconductors at High Pressure, *J. Phys. Chem. Solids.*, **56**, 545 (1995).
3. R. J. Nelmes, M. I. McMahon, N. G. Wright, D. R. Allan, H. Liu and J. S. Loveday, Structural Studies of III–V and Group IV Semiconductors at High Pressure, *J. Phys. Chem. Solids.*, **56**, 539 (1995).
4. R. J. Nelmes and M. I. McMahon, High-Pressure Powder Diffraction on Synchrotron Sources, *J. Synchr. Rad.*, **1**, 69 (1994), and references cited therein.
5. R. J. Nelmes, M. I. McMahon, N. G. Wright and D. R. Allan, Crystal Structure of ZnTe-III, *Phys. Rev. Lett.*, **73**, 1805 (1994).
6. R. J. Nelmes and M. I. McMahon, Ordered Superstructure of InSb-IV, *Phys. Rev. Lett.*, **74**, 106 (1995).
7. R. J. Nelmes, M. I. McMahon, P. D. Hatton, J. Crain and R.O. Piltz, The Phase Transitions in InSb to 5GPa, *Phys. Rev.*, **B 47**, 35 (1993).
8. M. I. McMahon, R. J. Nelmes, N. G. Wright and D. R. Allan, Phase Transitions in CdTe to 5GPa, *Phys. Rev.*, **B 48**, 16246 (1993).
9. N. G. Wright, Preferred Orientaion Modelling in High-pressure Powder Diffraction Applied to Structural Studies of Semiconductors, PhD thesis, University of Edinburgh (1994).
10. R. J. Nelmes, M. I. McMahon, N. G. Wright and D. R. Allan, Phase Transitions in CdTe to 28 GPa, *Phys. Rev.*, **B 51**, 15723 (1995).
11. W. A. Dollase, Correction of Intensities for Preferred Orientation in Powder Diffractometry: Application of the March Model, *J. Appl. Cryst.*, **19**, 267 (1986).
12. A. J. Singh, The Lattice Strains in a Specimen (Cubic System) Compressed Nonhydrostatically in an Opposed Anvil Device, *J. Appl. Phys.*, **73**, 4278 (1993).
13. N. Funamori, T. Yagi and T. Uchida, Deviatoric Stress Measurement under Uniaxial Compression by a Powder X-ray Diffraction Method, *J. Appl. Phys.*, **75**, 4327 (1994).
14. D. M. Adams, Diacell Products, 54 Ash Tree Road, Leicester, UK.

Imma phase of germanium at ~80 GPa

R. J. Nelmes, H. Liu, S. A. Belmonte, J. S. Loveday, and M. I. McMahon
Department of Physics and Astronomy, The University of Edinburgh, Mayfield Road, Edinburgh, EH9 3JZ, United Kingdom

D. R. Allan
Bayerishes Geoinstitut, Universität Bayreuth, D-95440 Bayreuth, Germany

D. Häusermann and M. Hanfland
European Synchrotron Radiation Facility, Boîte Postale 200, F-38043, Grenoble, France

(Received 27 July 1995)

Ge has been studied to 81 GPa with angle-dispersive diffraction techniques, using an image-plate area detector and high-brilliance synchrotron radiation from the European Synchrotron Radiation Facility. A previously unknown phase of Ge, with orthorhombic symmetry *Imma*, is found to exist above ~75 GPa—between the well established β-tin and simple hexagonal phases. This phase is the same as that found recently between the β-tin and simple hexagonal phases of Si.

Until recently, silicon and germanium were both believed to transform from the ambient-pressure diamond phase first to a β-tin phase, and then to a simple hexagonal (SH) phase under increasing pressure.[1,2] These two transitions were reported at 10 GPa and 13–16 GPa in Si (Ref. 1) and 11 and 75 GPa in Ge.[2] However, it has now been discovered that there is an intermediate phase, with orthorhombic symmetry *Imma*, between the β-tin and SH phases in Si.[3] The *Imma* structure is shown in Fig. 1. It becomes the β-tin structure when $a=b$ and $\Delta=0.25$, and the SH structure when $b/c=\sqrt{3}$ and $\Delta=0.50$. A continuous structural change from β-tin-to-SH through *Imma* is thus possible. However, the β-tin-to-*Imma* transition at 13.2(3) GPa and the *Imma* to SH transition at 15.6(3) GPa were both found to be first order, with volume changes ($\Delta V/V_0$) of 0.2(1)% and 0.5(1)%, respectively.[4] There also appear to be discontinuous changes in Δ at the transitions; it was found to vary from ~0.3 to 0.4 over the stability range of the *Imma* phase.[4] The existence of an intermediate *Imma* phase from ~13 to ~16 GPa explains the quite wide variation of transition pressures previously reported for the supposed β-tin-to-SH transition.[1] And the apparently discontinuous nature of the two new transitions may account for previously unexplained changes in the superconducting transition temperature reported in the 12–16 GPa range.[5–8]

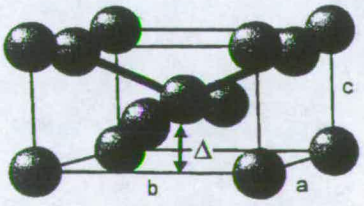


FIG. 1. The *Imma* structure of germanium, with atoms in the 4(*e*) positions at $(0,\frac{1}{4},\Delta/2)$, or $(0,\frac{1}{2},\Delta)$ relative to the origin chosen here. The origin has been moved from its standard position to facilitate comparison with the β-tin and simple hexagonal (SH) structures: when $a=b$ and $\Delta=0.25$, the *Imma* structure is equivalent to the β-tin structure, while if $b/c=\sqrt{3}$ and $\Delta=0.50$, the *Imma* structure is equivalent to the SH structure.

Ab initio calculations on the *Imma* phase have been performed by Lewis and Cohen.[9] They find that its energy is lower than, or equal to, that of the β-tin and SH phases over a wide range of V/V_0 from ~0.80 to 0.63, and they predict continuous β-tin-to-*Imma* and *Imma*-to-SH transitions. The observed range of existence is much smaller, from V/V_0~0.69 to 0.68, and the transitions appear to be discontinuous as said. However, there are several possible reasons for these discrepancies, one of which is the effect of finite temperature.[9] The calculations do agree well with the structural results in predicting only a small variation in Δ, from ~0.34 to ~0.37, over the observed range of stability of the phase.

In subsequent similar work on germanium, Lewis and Cohen[10] predict that it, too, should have an intermediate *Imma* phase between the β-tin and SH phases. The predicted behavior is very similar to that calculated for Si,[9] except that they find a much larger range over which the *Imma* phase is expected to be β-tin-like ($a\approx b$, $\Delta\approx 0.25$). Vohra *et al.* found a transition from β-tin direct to SH in Ge at 75(3) GPa.[2] We now report a reexamination of this transition, using angle-dispersive powder-diffraction techniques with an image-plate area detector. We find an *Imma* phase existing over the range from ~75 up to at least 81 GPa, the highest pressure reached in this study.

Diffraction data were collected on beamline 3 at the European Synchrotron Radiation Facility (ESRF), Grenoble, using an image-plate area detector. A Si(111) Laue-Bragg monochromator was used to select a wavelength of $\lambda=0.4592$ Å from the white beam produced by a hybrid wiggler, and a Si mirror was used to focus the beam vertically and to remove higher order harmonics. Although the mirror is able to focus a 600 μm white beam to less than 20 μm, the optical combination of the Laue-Bragg monochromator with the mirror focuses such a beam only to approximately 120 μm full width at half maximum. Attenuators

0163-1829/96/53(6)/2907(3)/$06.00

© 1996 The American Physical Society

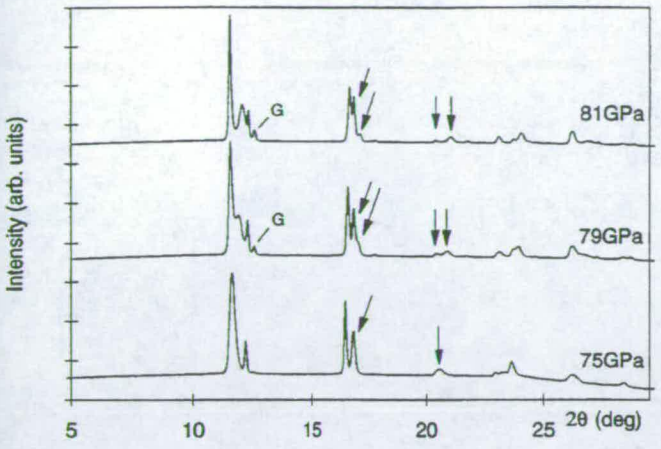


FIG. 2. Integrated profiles of powder-diffraction patterns recorded from germanium at 75, 79, and 81 GPa. The vertical and inclined arrows in the 75 GPa profile mark two single peaks of the β-tin phase which each split into two separate peaks in the 79 and 81 GPa profiles, as indicated. The peak marked "G" in the 79 and 81 GPa profiles is a weak tungsten gasket line.

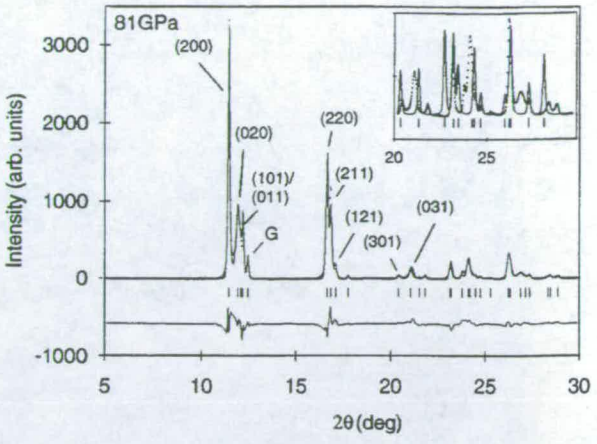


FIG. 3. Fit to the profile of Ge at 81 GPa with the *Imma* structure, and also a component of bcc tungsten to model the gasket lines. The tick marks show the positions of all the reflections allowed by symmetry. The difference between the observed and calculated profiles is displayed below the tick marks. Some principal reflections are indexed. The peak marked "G" is the strongest tungsten gasket line. The inset shows the higher angle part of the best fit obtained to the 81 GPa profile with a mixed-phase β-tin/SH model (plus, again, tungsten for the gasket lines): the calculated peak positions are shown by the tick marks.

were used to remove the unwanted long wavelength part of the wiggler spectrum in order to preserve the optical quality of the first monochromator crystal, and 20×20 μm^2 slits were used to define the beam for the very high pressure measurements. The sample to image-plate distance was ~370 mm, and was calibrated using a standard Si sample. Image plates were read on a Molecular Dynamics scanner using a pixel size of 176×176 μm^2, and were then integrated around the powder rings to produce 1-d profiles. Details of the experimental set up and pattern integration software are reported in Refs. 11 and 12.

The sample material was a finely ground powder prepared from 99.9999% pure Ge purchased from the Aldrich Chemical Company. Samples were loaded into Diacell DXR-5 and DXR-GMW diamond-anvil pressure cells,[13] with a 4:1 methanol:ethanol mixture as a pressure-transmitting medium. Flat 200-μm-culet diamonds were used, with tungsten gaskets. In these pressure cells, the diamond anvils are supported on Be discs, and so complete 2-d powder patterns are obtained. The pressure was measured using the ruby fluorescence technique.[14] The structural results were obtained from full Rietveld refinement of the integrated profiles using the program MPROF.[15]

As the sample pressure was increased, the transition to the β-tin phase was observed and then no further changes other than compression occurred until ~70 GPa. At this pressure, the first strong line in the powder pattern started to become discernibly broadened and asymmetric. Figure 2 shows three profiles then collected at 75, 79, and 81 GPa. The broadening and asymmetry of the first line is evident in the 75 GPa profile. At 79 GPa, it has clearly split into two peaks and the separation increases at 81 GPa. This is very similar to the sequence of changes shown in Fig. 2 of Ref. 4 for the *Imma* phase of Si. As in Si, the first reflection can be seen to move to *lower* 2θ as the pressure increases. Other key features are the splitting of the single peaks marked by an inclined and a vertical arrow in the 75 GPa profile, into two separate peaks in the 79 GPa profile, and (further apart still) in the 81 GPa profile.

Figure 3 shows the fit obtained in a Rietveld refinement of the *Imma* structure for the 81 GPa profile. The refined unit-cell dimensions at this pressure are $a=4.572(1)$ Å, $b=4.386(1)$ Å, and $c=2.461(1)$ Å, and Δ refines to 0.390(4). As for Si, we also tested a mixed β-tin/SH model. This can fit the low-angle group of reflections quite well, but the very poor fit at higher angles—illustrated in the inset to Fig. 3—clearly allows this interpretation to be rejected. Ge evidently has the same *Imma* phase as Si, as predicted by the recent calculations.[10] The fact that this phase was not detected in the previous study (Ref. 2) can be attributed to the lower resolution of energy-dispersive data. Figure 1 of Ref. 2 shows a diffraction pattern of the β-tin phase at 72 GPa. The first two β-tin reflections (200 and 101) are only just resolved, and the second doublet (220 and 211) is not resolved at all. Clearly, the reflections shown in our Fig. 2 appearing between 200 and 101 of β-tin (at $2\theta\sim12°$), and as a shoulder on the high-angle side of 211 of β-tin (at $2\theta\sim17°$), would not have been detectable. However, Vohra *et al.*[2] do indicate that their diffraction pattern at 77.7 GPa could not be completely indexed as SH.

The distortion of the *Imma* unit cell from the tetragonal symmetry of β-tin can be characterized by $(a-b)/(a+b)\neq0$ and $\Delta\neq0.25$; and the distortion from SH by $b/c\neq\sqrt{3}$ and $\Delta\neq0.5$. At 81 GPa, $(a-b)/(a+b)=0.0208(2)$ and $b/c=1.782(6)$. These values are the same as in Si at 14.4(2) GPa,[4] while the value of Δ appears to correspond to that in Si at a slightly higher pressure of ~15 GPa. However, this (small) difference may not be significant as there was quite a large variation in the Δ values obtained for Si on pressure increase and pressure decrease.[4]

As discussed above, the evidence from this study indicates that the transition from the β-tin phase to *Imma* occurs at approximately 75 GPa. However, the maximum pressure we were able to reach (81 GPa) was not sufficient to locate the transition from *Imma* to the SH phase. If the transition has a small discontinuity as in Si,[4] an estimate of ~85 GPa can be obtained for the transition pressure from the rate of change between 79 GPa and 81 GPa in Fig. 2. This would accord with the report of a single-phase SH diffraction pattern at 90 GPa by Vohra *et al.*[2] Hence the best present estimate of the stability range of the *Imma* phase is ~75 to ~85 GPa.

We conclude that Ge behaves the same way as Si in transforming from its β-tin phase to an intermediate orthorhombic *Imma* phase on increasing pressure. The two systems exhibit very similar orthorhombic distortions in terms of the unit-cell dimensions and also the variable atomic coordinate, Δ. Further work is now planned to determine the β-tin-to-*Imma* and *Imma*-to-SH transition pressures, and to follow the structural pressure dependence of this phase in Ge—where the greater range of stability will allow the relationship between the cell dimensions and Δ to be explored in more detail. It is of particular interest to relate the distortion of the pseudohexagonal *bc* layers to the range of structural stability, with reference both to the calculations of Lewis and Cohen,[10] and our recent study of an *Imma* phase stable over at least 40 GPa in (site-disordered) GaSb.[16]

This work is supported by a grant from the U.K. Engineering and Physical Sciences Research Council. Valued assistance with the maintenance and development of pressure cells has been given by D. M. Adams of Diacell Products.

[1] J. Z. Hu, L. D. Merkle, C. S. Menoni, and I. L. Spain, Phys. Rev. B **34**, 4679 (1986), and references therein.
[2] Y. K. Vohra, K. E. Brister, S. Desgreniers, A. L. Ruoff, K. J. Chang, and M. L. Cohen, Phys. Rev. Lett. **56**, 1944 (1986).
[3] M. I. McMahon and R. J. Nelmes, Phys. Rev. B **47**, 8337 (1993).
[4] M. I. McMahon, R. J. Nelmes, N. G. Wright, and D. R. Allan, Phys. Rev. B **50**, 739 (1994).
[5] M. A. Il'ina and E. S. Itskevich, Fiz. Tverd. Tela (Leningrad) **22**, 3139 (1980) [Sov. Phys. Solid State **22**, 1833 (1980)].
[6] K. J. Chang, M. M. Dacorogna, M. L. Cohen, J. M. Mignot, G. Chouteau, and G. Martinez, Phys. Rev. Lett. **54**, 2375 (1985).
[7] T. H. Lin, W. Y. Dong, K. J. Dunn, C. N. J. Wagner, and F. P. Bundy, Phys. Rev. B **33**, 7820 (1986).
[8] J. M. Mignot, G. Chouteau, and G. Martinez, Phys. Rev. B **34**, 3150 (1986).
[9] S. P. Lewis and M. L. Cohen, Phys. Rev. B **48**, 16 144 (1993).
[10] S. P. Lewis and M. L. Cohen, Solid State Commun. **89**, 483 (1994).
[11] D. Häusermann and M. Hanfland, High Pressure Res. (to be published).
[12] A. P. Hammersley and S. O. Svensson, High Pressure Res. (to be published); A. P. Hammersley (unpublished).
[13] D. M. Adams, Diacell Products, 54 Ash Tree Road, Leicester, UK.
[14] H. K. Mao, J. Xu, and P. M. Bell, J. Geophys. Res. **91**, 4673 (1986).
[15] A. N. Fitch and A. D. Murray (unpublished).
[16] M. I. McMahon, R. J. Nelmes, N. G. Wright, and D. R. Allan, Phys. Rev. B **50**, 13 047 (1994).

J. Synchrotron Rad. (1996). **3**, 112–119

Observation and Modelling of Preferred Orientation in Two-Dimensional Powder Patterns

N. G. Wright,† R. J. Nelmes, S. A. Belmonte and M. I. McMahon

Department of Physics and Astronomy, The University of Edinburgh, Edinburgh EH9 3JZ, UK

(*Received 27 January 1996; accepted 12 March 1996*)

A novel approach to the detection and modelling of preferred orientation is presented, based on the interpretation of two-dimensional powder patterns. A simple graphical construction is introduced to aid interpretation, and the application of this construction to some standard diffraction geometries is discussed. It is also shown in outline how a standard preferred-orientation model can be adapted to describe two-dimensional data.

Keywords: preferred orientation; powder diffraction; area detectors; two-dimensional data.

1. Introduction

Preferred orientation of sample crystallites has long been one of the most studied aspects of powder diffraction. In some fields, notably metallurgy (Barrett & Massalski, 1992), the emphasis has been on studying samples of known structure and extensive techniques have been developed to determine the crystallite orientation distribution from the observed diffraction patterns, collected from many sample orientations (Järvinen, Merisalo, Pesonen & Inkinen, 1970; Bunge, Dahms & Brokmeier, 1989; Dahms & Bunge, 1989). In powder diffraction studies performed to determine crystal structures (normally from data obtained using one sample orientation), preferred orientation is often modelled during structure refinement by using a simple analytic function (Rietveld, 1969; Capkova & Valvoda, 1974; Dollase, 1986). However, such a method presupposes that an approximate trial structure is known and this is clearly not the case during structure solution. Strong preferred orientation can be a serious stumbling block in structure solution from powder diffraction data because of large differences between observed and true reflection intensities. Even if the general arrangement of the structure is known, structural variables can be strongly biased by correlations with a preferred-orientation model selected simply on the basis that it appears to improve the fit to the data.

If the proportion of crystallites contributing to each reflection can be determined experimentally, however, then the reflection intensities can be corrected reliably and structure solution and refinement can proceed without uncertainties. Recent developments in texture analysis have highlighted the importance of this direct approach and outlined possible techniques using conventional one-dimensional data-collection methods (Järvinen, 1993; Cerny, Valvoda & Chladek, 1995; Peschar & Schenk, 1995). Unfortunately, the collection of the large amount of data required in such an approach is difficult and time-consuming with a conventional scanning detector, and this is a significant impediment. However, the problem can be overcome with the large-area two-dimensional X-ray detectors, such as image plates, that have been developed over the past few years for high-pressure powder diffraction (see Nelmes & McMahon, 1994). By collecting a whole diffraction pattern of complete powder rings in parallel, a large amount of additional information is recorded in a remarkably short time. It so happens that high-pressure conditions often cause rather pronounced preferred orientation in samples, and it is this convergence of a well adapted detector with strong effects that has stimulated our texture studies (Wright, 1995). However, the results are in no way limited to high-pressure applications, and can be expected to be of wide use in all powder diffraction work.

In this paper we illustrate the nature of two-dimensional data and introduce a simple graphical construction that gives a straightforward interpretation of the relationship between the data and the underlying preferred-orientation distribution. We show how a standard preferred-orientation model can be adapted to describe the two-dimensional data and we outline the application and possible benefits of this approach for some standard diffraction geometries.

2. Preferred-orientation effects in two dimensions

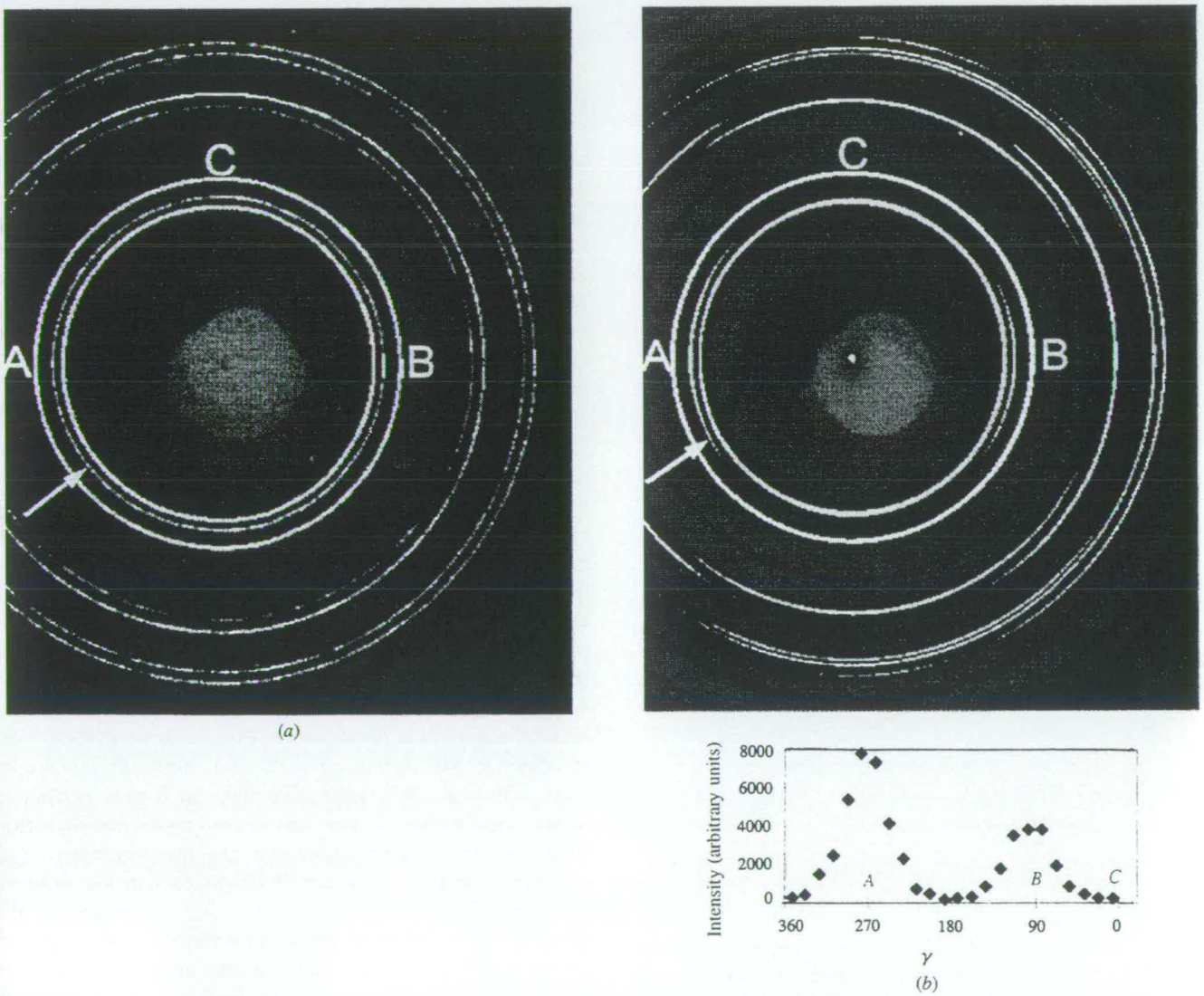
Fig. 1 shows two-dimensional diffraction patterns obtained from the same sample of precompressed HgS in two different orientations with respect to the incident X-ray beam. These patterns were collected on station 9.1 at SRS, Daresbury, using an image-plate detector and an X-ray wavelength of ~0.45 Å. The diffraction pattern of Fig. 1(*a*) was collected with the incident beam striking the sample along the axis of symmetry of the crystallite distribution, and the recorded intensities are uniform around the powder

† Now at Department of Electrical and Electronic Engineering, Merz Court, The University of Newcastle upon Tyne, Newcastle NE1 7RU, UK.

© 1996 International Union of Crystallography
Printed in Great Britain – all rights reserved

rings. In this case, the effects of preferred orientation manifest themselves only in departures of the relative reflection intensities from the ideal values corresponding to the crystal structure of the sample. Fig. 1(*b*) was collected with the distribution axis inclined at 50° to the incident beam, and clear variations in intensity can be seen around the powder rings. It is these intensity variations that contain the information required to define the preferred-orientation distribution in the sample without any knowledge of the crystal structure other than the unit cell. We will first show this qualitatively and then, in the next section, develop a quantitative model.

For simplicity, the distribution of crystallite orientations can be taken to be uniaxial and axially symmetric. Indeed, many samples have such a distribution, as shown by the axial symmetry of Fig. 1(*a*). (More complex distributions can, in principle, be treated by extensions of the same procedures as apply to this simple case.) A symmetric uniaxial distribution can be represented by contours on a spherical surface, as drawn schematically in Fig. 2, where values of the contours are shown decreasing from 4 at the poles to 1 at the equator. In a sample that exhibits preferred orientation, a particular crystallographic direction in each crystallite (the preferred-orientation *direction*, POD) tends to align along the axis of the distribution (the preferred-orientation *axis*, POA). [For example, for a sample with hexagonal symmetry and the unique axis taken along **c**, pressed into a flat-plate container, the POD is likely to be [001] with the POA normal to the flat plate.] Consider a particular crystallite, typical of the sample, as shown in



(*a*) (*b*)

Figure 1
Two-dimensional diffraction patterns collected from the same HgS sample with (*a*) the axis of the crystallite distribution coincident with the incident X-ray beam, and (*b*) the axis of the crystallite distribution inclined at 50° to the incident beam. Note the intensity variations around the powder rings in (*b*). The ring of the (003) reflection is marked by an arrow in both patterns, and the plot of intensity *versus* γ (°) shows the variation of intensity for this reflection in pattern (*b*). γ is the angle around the powder ring (see Fig. 4). [The sense of the γ axis has been chosen to remain consistent with Fig. 4 while keeping the larger maximum (at *A*) to the left of the smaller, as in pattern (*b*).] The letters *A*, *B* and *C* mark the same positions around γ as illustrated in Fig. 3.

Fig. 2(*a*). Suppose that it is approximately shaped like a disc – viewed edge-on in the Figure – and that the POD is perpendicular to the plane of the disc. Such a crystallite in a general orientation has its POD at an angle α to the POA (see Fig. 2*a*), and the contours quantify how the relative probability of the POD being inclined at a given angle decreases as α increases.

Consider an incident beam direction labelled IB in Fig. 2(*a*), and the diffracted beam direction, DB, for reflection *hkl*. Suppose that the crystallite shown in Fig. 2(*a*) contributes to DB. The scattering vector $\mathbf{K}_{hkl}$ then bisects the angle between IB and DB, and $\mathbf{K}_{hkl}$ is at an angle ψ to the POD, where ψ is determined by the lattice parameters of the sample. However, *all* crystallites with their scattering vectors along the $\mathbf{K}_{hkl}$ direction will contribute to DB, and this family of crystallites is defined as all those with PODs lying on the cone shown in Fig. 2(*a*), with half-angle ψ around the $\mathbf{K}_{hkl}$. Thus, the probability of crystallites being oriented such as to contribute to the *hkl* reflection in direction DB is obtained as an integration of the distribution function around the circle where the POD cone intersects the surface of the sphere.

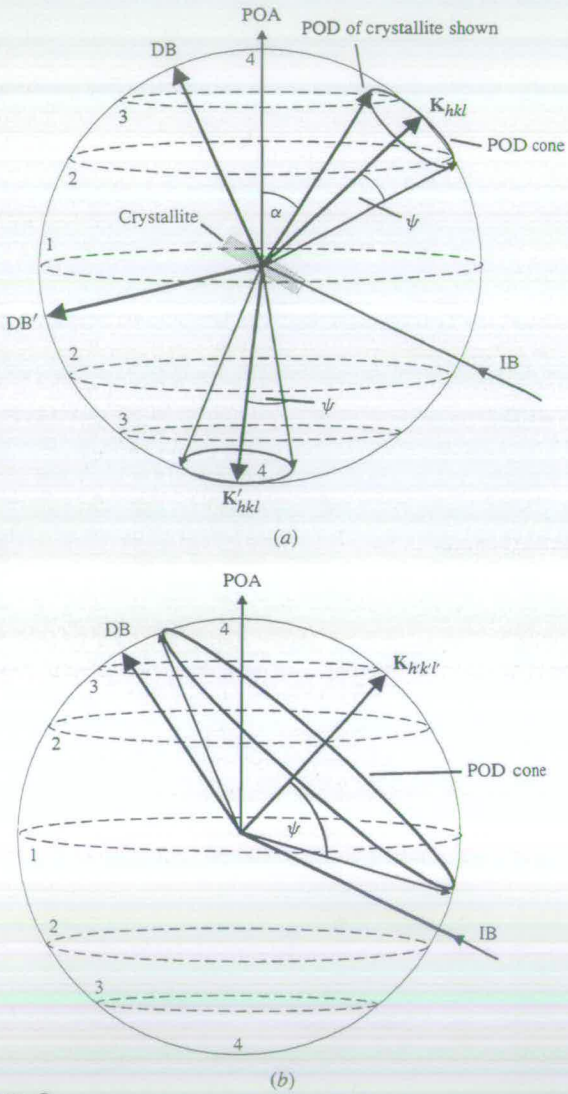


Figure 2
A uniaxial probability distribution function for crystallite orientations (ODF) can be represented as a series of contours on a unit sphere; the numbers 1 to 4 represent the value of the contours. (*a*) The POD cones for two points, DB and DB′, on the powder ring for reflection *hkl* when the incident beam (IB) strikes the crystallite distribution at an angle to the POA. A typical crystallite is shown, with its POD inclined at an angle α to the POA. (*b*) The POD cone for one point on a powder ring for a reflection, $h'k'l'$, with a large ψ angle.

Consider now another point on the *hkl* powder ring, given by DB′. The particular crystallite drawn in Fig. 2(*a*) will not contribute to this diffracted beam; DB′ is made up from reflections from another family of crystallites with PODs lying on the POD cone shown around $\mathbf{K}'_{hkl}$. It is immediately evident that the integrated probability is higher for this POD cone: more crystallites will contribute to DB′ than to DB and so the intensity of DB′ will be greater than that of DB. This difference is the source of the intensity variations around the powder rings in Fig. 1(*b*).

In the particular case drawn in Fig. 2(*a*), where ψ is small, the average of the integrated probability around the POD cone will be similar to the probability at the point where $\mathbf{K}_{hkl}$ passes through the surface of the sphere. Then the variation of intensity around the powder ring approximately gives a direct measure of the variation in the orientation distribution function (ODF) around the locus explored by all the *hkl* scattering vectors from $\mathbf{K}_{hkl}$ to $\mathbf{K}'_{hkl}$. However, it is important to note that the relationship between the ODF and the intensity variations is not so simple in general. Fig. 2(*b*) shows a POD cone for a different reflection, $h'k'l'$, with a large value of ψ. It is clear that the average of the integrated probability will differ from that for the single direction $\mathbf{K}_{h'k'l'}$ by an amount that depends on the form of the ODF.

The above discussion has illustrated some of the main two-dimensional effects of preferred orientation. In subsequent sections, we wish to analyse the effects of preferred orientation in more detail for a general diffraction geometry and for particular geometries in common use. In order to represent adequately the two-dimensional effects involved, it is helpful to consider three points (at least) in the diffraction pattern. A convenient form of construction for general use is then as shown in Fig. 3: three POD cones, separated by 90° in γ (see Fig. 1), and with a small ψ angle.

Fig. 3(*a*) shows a three-cone diagram for the setting in which the incident beam strikes the crystallite direction such that the POA coincides with the incident beam. The contours intersected by the POD cones can be seen to be identical in all three positions and consequently the intensity is the same at these three (and all other) points on the powder ring – *i.e.* the intensity around any powder ring is uniform – ignoring other possible effects such as polarization of the incident beam. This is the case illustrated by the two-dimensional image of Fig. 1(*a*), in which the positions around γ labelled *A* (270°), *B* (90°) and *C* (0°) correspond to the directions of DB(*A*), DB(*B*) and DB(*C*), respectively.

Fig. 3(*b*) is the diagram for a setting in which the incident beam strikes the sample at an angle β to the POA. The contours intersected by the three POD cones can be seen to represent different probabilities, and it is this effect that creates the pattern of intensity variation seen in Fig. 1(*b*). The angle β in Fig. 3(*b*) is 50°, as used in recording this image, and the arrowed powder ring in Fig. 1(*b*) has a small POD cone angle, as here. The POD cones for points *A* and *B* intersect contours of higher value than those for point *C* which will thus be an intensity minimum, as seen in Fig. 1(*b*). It is evident that the contours of the POD cone for point *A* are of higher value than those for point *B*, with the result that the maxima do not have the same intensity, which accounts for the variation seen in the plot of intensity *versus* γ in Fig. 1(*b*). This asymmetry arises because the POD cone axes ($\mathbf{K}_{hkl}$) are not perpendicular to the incident beam, but are rotated away from perpendicular through the diffraction angle, θ. Thus, the asymmetry between the two maxima will increase with diffraction angle for a given angle β between the incident beam and the POA – until the cone axis of the larger maximum [$\mathbf{K}_{hkl}(A)$ in this case] reaches the maximum of the ODF.

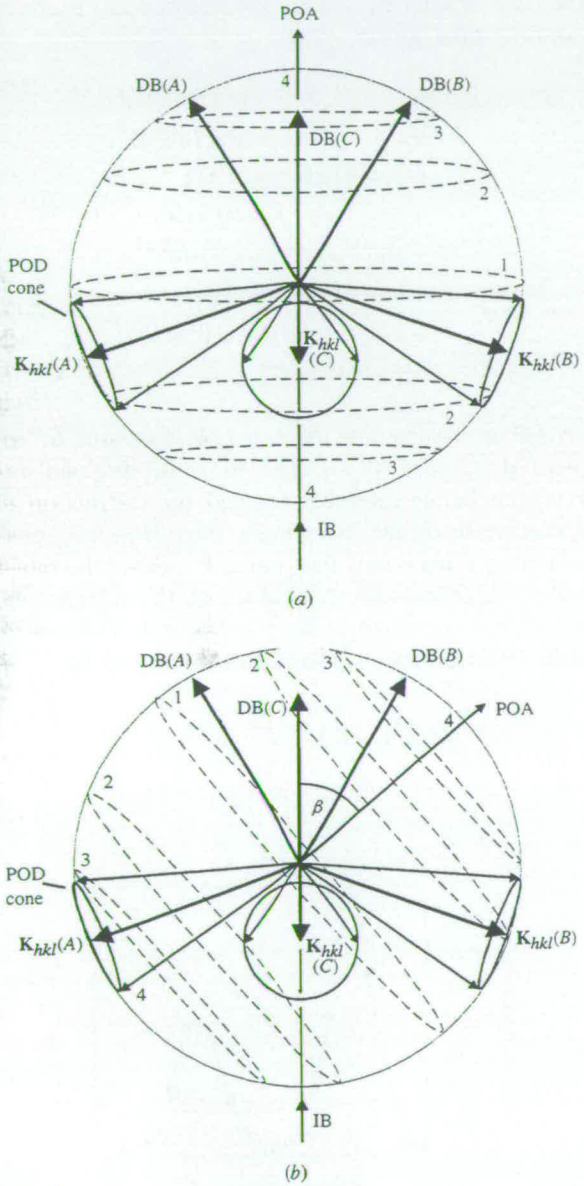


Figure 3
POD cone diagrams for diffraction at the three marked positions in γ (*A*, *B* and *C*) around the arrowed ring in (*a*) Fig. 1(*a*), and (*b*) Fig. 1(*b*). The angle between the POA and IB in (*b*) is labelled β. $\mathbf{K}_{hkl}(C)$ and DB(*C*) are directed upwards out of the plane of the diagram.

It must be noted that another reflection, at similar θ but with a much larger POD-cone angle (ψ), would have its maxima and minima at different γ values from those of the particular reflection examined in Figs. 3(*b*) and 1(*b*). For example, if the POD-cone angle were increased greatly in Fig. 3(*b*), it can be seen that the average contour levels explored around a scattering vector near $\mathbf{K}_{hkl}(A)$ would decrease, while those explored around a vector near $\mathbf{K}_{hkl}(C)$ would (on average) increase. The variation in the γ angles at which different powder rings have their maxima and minima is evident in Fig. 1(*b*).

It is also important to stress that the foregoing analysis of intensity variations applies to single unoverlapped reflections – *e.g.* the (001) reflection of a tetragonal sample in which the *c* lattice parameter is sufficiently different from *a* (= *b*) to separate the (001) peak from the (100)/(010) peak. For a compound peak, like the latter one, the nature of the intensity variations will depend on the direction of the POD. If in this tetragonal example the POD is along [001], then ψ will be 90° for both (100) and (010) and so they will have identical variations as a function of γ. But, if the POD is along *e.g.* [100], then ψ will be 0° for (100) and 90° for (010), and their intensity variations will be 90° out of phase in γ; the maxima of the variations for (100) will coincide with the minima for (010), and so the observed variations around the (100)/(010) ring may be small even if the preferred-orientation effects are large. The intensity will not be uniform, however, and information about the ODF can still be extracted from such compound rings; but analysis of non-compound rings is considerably more straightforward. The overlap of symmetry-related reflections in preferred-orientation analysis has been discussed recently by Capkova, Peschar & Schenk (1993). In practice, there will also be similar problems for non-symmetry-related reflections if they are close enough in *d* spacing to overlap in the observed powder pattern. The HgS ring selected for analysis in Figs. 1 and 3 is the (003) reflection from a sample with hexagonal symmetry, and is not overlapped by symmetry-related or any other reflections, other than trivially by $(00\bar{3})$.

3. Preferred-orientation model

The qualitative discussion above provides a basis for understanding the effects of preferred orientation on a two-dimensional diffraction pattern. This section develops a mathematical model which can be used to extract the degree of sample texture quantitatively and thus correct the

reflection intensities for the effects of preferred orientation. Fig. 4(*a*) shows the orientation of the incident beam (IB), diffracted beam (DB) and scattering vector ($\mathbf{K}_{hkl}$) for diffraction at a given point on a diffraction pattern collected in a general scattering geometry. The z axis is set along the incident beam, which is usually horizontal, with x and y then vertical and horizontal, respectively, in the experimental set-up. Let θ be the scattering angle as defined by Bragg's Law, and γ be the angle between the x axis and the projection of both DB and $\mathbf{K}_{hkl}$ onto the xy plane [shown shaded in Fig. 4(*a*)]. If the two-dimensional detector is placed in the xy plane, γ corresponds to the angle around the powder rings; when $\gamma = 0°$, the diffracted beam and the scattering vector are in the (vertical) xz plane. (Point C in Fig. 1 is at $\gamma = 0°$.) Fig. 4(*b*) shows the cone of POD vectors for all the crystallites in the sample that are contributing to the *hkl* reflection in the selected direction.

The orientation of the POA with respect to the incident beam can be described in terms of the spherical polar coordinates, β and φ, of Fig. 4(*c*) as

$$\mathbf{POA} = \mathbf{a}\sin(\beta)\cos(\varphi) + \mathbf{b}\sin(\beta)\sin(\varphi) + \mathbf{c}\cos(\beta), \quad (1)$$

where (**a**, **b**, **c**) are unit vectors in the (x, y, z) directions. Expressing the POD vectors in terms of the coordinate axes of Fig. 4 is not trivial. However, by transforming to other coordinate axes, it can be shown (Wright, 1995) that the POD vector of a given diffracting crystallite can be expressed in terms of the (x, y, z) axes of Fig. 4 as

$$\begin{aligned}\mathbf{POD} = \mathbf{a}[&-\sin(\gamma)\sin(\psi)\cos(\delta)\\ &+ \sin(\theta)\cos(\gamma)\sin(\psi)\sin(\delta)\\ &+ \cos(\theta)\cos(\gamma)\cos(\psi)]\\ &+ \mathbf{b}[\cos(\gamma)\sin(\psi)\cos(\delta)\\ &+ \sin(\theta)\sin(\gamma)\sin(\psi)\sin(\delta)\\ &+ \cos(\theta)\sin(\gamma)\cos(\psi)]\\ &+ \mathbf{c}[\cos(\theta)\sin(\psi)\sin(\delta)\\ &- \sin(\theta)\cos(\psi)], \end{aligned} \quad (2)$$

where δ (defined in terms of the transformed axes) takes the values 0–2π to represent different orientations of the POD on the cone around $\mathbf{K}_{hkl}$. A simple vector (dot) product of (1) and (2) then gives

$$\begin{aligned}\cos(\alpha) = \sin(\beta)\cos(\varphi)&[-\sin(\gamma)\sin(\psi)\cos(\delta)\\ &+ \sin(\theta)\cos(\gamma)\sin(\psi)\sin(\delta)\\ &+ \cos(\theta)\cos(\gamma)\cos(\psi)]\\ &+ \sin(\beta)\sin(\varphi)[\cos(\gamma)\sin(\psi)\cos(\delta)\\ &+ \sin(\theta)\sin(\gamma)\sin(\psi)\sin(\delta)\\ &+ \cos(\theta)\sin(\gamma)\cos(\psi)]\\ &+ \cos(\beta)[\cos(\theta)\sin(\psi)\sin(\delta)\\ &- \sin(\theta)\cos(\psi)]. \end{aligned} \quad (3)$$

The ODF is assumed to be a simple function of angle α [here designated $P(\alpha)$], and thus the probability of a crystallite being correctly oriented for diffraction to a particular point on the *hkl* powder ring, $\langle P(\alpha)\rangle_{hkl}$, can be calculated by numerically integrating $P(\alpha)$ over the range of α angles which describe crystallites on the relevant cone. If the ODF is assumed to have the March–Dollase form (March, 1932; Dollase, 1986) then the integral is

$$\begin{aligned}\langle P(\alpha)\rangle_{hkl} = (1/2\pi)\int_0^{2\pi}&[R^{-1}\sin^2(\alpha)\\ &+ R^2\cos^2(\alpha)]^{-3/2}\mathrm{d}\delta, \end{aligned} \quad (4)$$

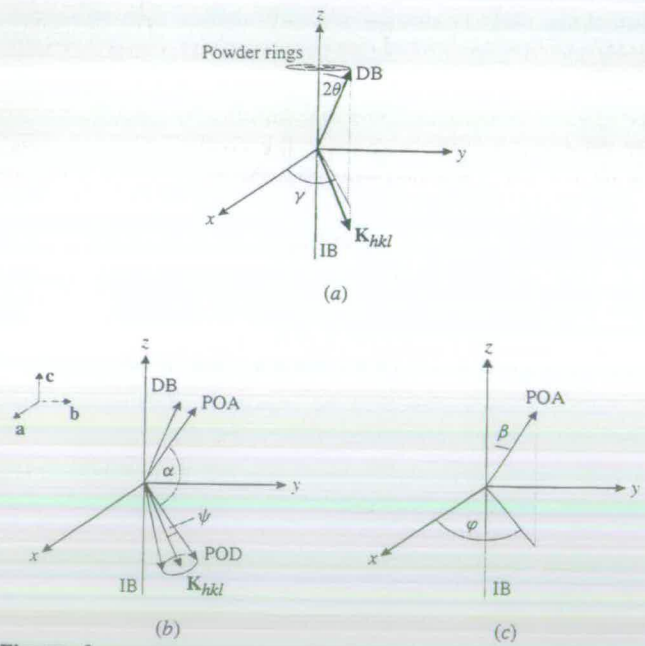


Figure 4
(*a*) The orientation of the incident beam (IB), diffracted beam (DB) and scattering vector ($\mathbf{K}_{hkl}$) with respect to the Cartesian axes. (*b*) The orientation of the PODs with respect to the POA. Angle α describes the orientation of the PODs relative to the POA and thus *varies* for different orientations of the POD on the POD cone around $\mathbf{K}_{hkl}$. ψ is the half-angle of the POD cone. (*c*) The orientation of the POA with respect to the Cartesian axes. Other angles and symbols are defined in the text.

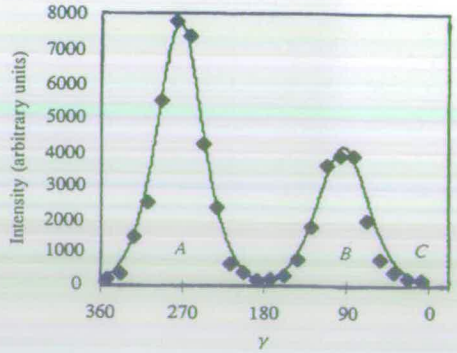


Figure 5
The observed (points) and calculated intensity variation around the powder ring shown in Fig. 1(*b*). The calculated line has been obtained by fitting the preferred-orientation model to the observed data. [The sense of the γ axis is as in Fig. 1.]

where R is the refinable parameter of the March–Dollase function and describes the degree of sample texture. The calculated intensity, $I_{calc}(hkl)$, predicted by the model for that point on the powder ring is then given by:

$$I_{calc}(hkl) = I_{ideal}(hkl) \sum_{M(hkl)} [\langle P(\alpha)\rangle_{hkl}/M(hkl)] \qquad (5)$$

where $I_{ideal}(hkl)$ is the intensity of the (hkl) powder ring from an ideal randomly oriented sample of the same volume, $M(hkl)$ is the multiplicity of the (hkl) reflection and $\langle P(\alpha)\rangle_{hkl}$ is the average value (integrated over the relevant POD cone) of the normalized distribution for that point on the powder ring [from (4)]. The parameters that $\langle P(\alpha)\rangle$ depends on are θ and ψ, which are determined from the lattice parameters and unit-cell indexing; β and φ, the direction of the POA with respect to the incident beam; R, the parameter of the ODF; and γ, the angle around the powder rings. For a given reflection from a given sample in a given orientation, all of these parameters apart from γ are fixed or known. Variation of γ for a given reflection corresponds to the POD cone exploring the ODF, as shown for three different diffracted-beam directions in Fig. 3. [As previously discussed, the variation of intensity with γ is most straightforwardly observed and understood for a single reflection, not overlapped by either symmetry-related reflections or other reflections with almost the same d spacing. However, (5) is summed over all symmetry-related hkl reflections: when applied to the tetragonal sample considered in §2 above, for example, the calculated intensity for the (100) ring as a function of γ will then be the sum of the (100) and (010) variations added together.]

Fig. 5 shows the fit given by the model to the observed intensity around the powder ring of the (non-overlapped) HgS (003) reflection plotted in Fig. 1(*b*). The agreement between the data and the calculated intensity predicted by the model is excellent and indicates that this approach can be used to understand the effects of very pronounced preferred orientation on the full two-dimensional diffraction pattern.

4. Two-dimensional aspects of preferred orientation in some standard geometries

This section discusses the implications of preferred orientation for data collection in the principal standard diffraction geometries used in synchrotron studies.

4.1. *Transmission geometry*

In this case, the incident beam strikes the sample along the axis of the crystallite distribution (the POA) and thus transmission geometry is identical to the simple case considered above in Fig. 3(*a*). This is the diffraction geometry commonly used in high-pressure X-ray studies – assuming the POA to be aligned with the pressure-cell axis as is often, although not always, true. The consequences of this scattering geometry can be seen mathematically in the simplification of (3) when $\beta = 0°$:

$$\cos(\alpha) = \cos(\theta)\sin(\psi)\sin(\delta) - \sin(\theta)\cos(\psi), \qquad (6)$$

i.e. there is no dependence of the value of $\cos(\alpha)$ [and hence $\langle P(\alpha)\rangle_{hkl}$] on the angle around the powder ring, γ. The effects of preferred orientation are seen only in changes to the relative intensities between reflections compared with those obtained from an ideal non-textured sample. The presence of preferred orientation is then not readily apparent and can be detected only if a structural model is available. However, this difficulty can be overcome by inclining the sample such that the X-ray beam strikes the sample at an angle [*i.e.* the general case of Fig. 3(*b*) considered above]. We have found this inclination technique to be of great value as it allows any preferred orientation to be explored prior to structural solution or refinement, and we now routinely apply it to most samples.

4.2. *Debye–Scherrer geometry*

In this geometry the incident beam enters the sample perpendicular to the sample capillary axis, with which the POA is assumed to be coincident (see Fig. 6). For a small ψ angle (as drawn), the POD cones for points A and B in the diffraction pattern are at higher probability than the cone for point C and so point C is a minimum. [As discussed in relation to Fig. 3(*b*), this would be reversed for a reflection with a sufficiently large ψ angle, and C would become a maximum.] As the contours on which the POD cones lie for points A and B are the same, the maxima at points A and B are of equal intensity. It is common during data collection

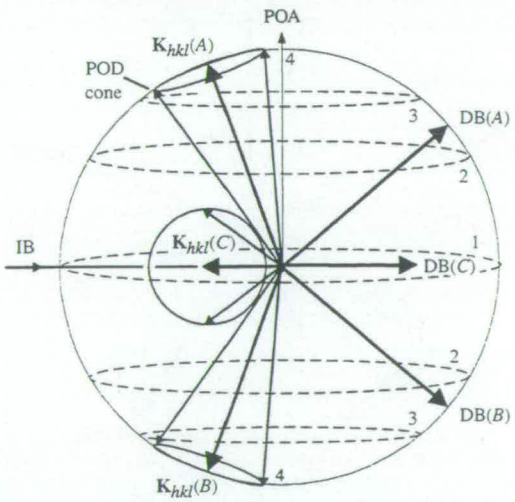


Figure 6
Debye–Scherrer geometry. The orientation of the POD cones for diffraction into three selected points on a powder ring for the incident beam (IB) striking the crystallite distribution perpendicular to the sample capillary axis, which is assumed to be coincident with the POA. By comparing the values of the contours intersected by the POD cones at the three selected points, it can be seen that points A and B are equal relative maxima and point C is a minimum. $\mathbf{K}_{hkl}(C)$ and DB(C) are directed upwards out of the plane of the diagram.

in this geometry to rotate the capillary about its own axis. This enforces the axial symmetry about the POA (which is otherwise only assumed). However, as can be seen from Fig. 6, the variation in intensity around the powder ring is unaffected by this rotation.

This geometry is commonly used with a high-resolution scanning detector, which records a thin strip of the diffraction pattern in the plane perpendicular to the POA. No information on intensity variation around the powder rings is recorded, and hence the presence of preferred orientation cannot be determined unless a structural model is available. However, the degree of preferred orientation could be readily assessed by placing an area detector, such as an image plate, perpendicular to the incident beam so as to record a substantial fraction of the powder rings. Simple averaging of the intensity around the powder rings would produce intensities closer to those expected from a ideal sample than those obtained by the one-dimensional detector, although for optimum accuracy the intensity variation around the powder rings should be modelled and the correct intensities obtained accordingly.

It is possible that the true POA of the sample may not coincide with the capillary axis (as assumed above), or not with the axis around which the capillary is rotated. The rotation will then produce a more complex, albeit still symmetric, effective ODF. In such cases, the maxima at points A and B would remain equal for a rotating sample but would be found to differ in intensity with the sample stationary.

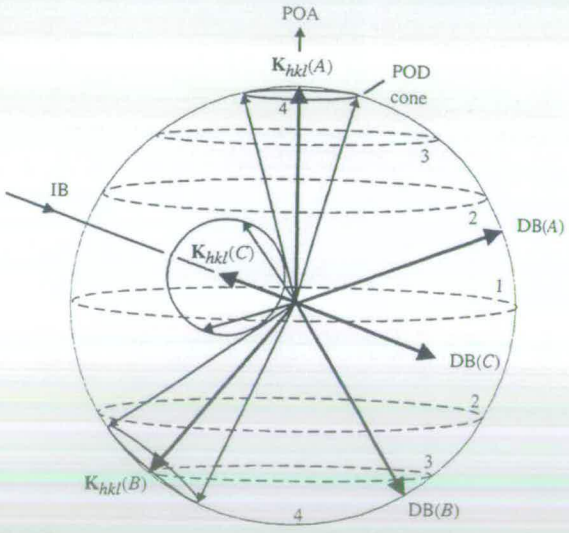


Figure 7
Bragg–Brentano geometry. The orientation of the POD cones for diffraction into three selected points on a powder ring for the incident beam (IB) striking the crystallite distribution such that, for DB(A), the scattering vector $\mathbf{K}_{hkl}$ is coincident with the flat-plate normal (assumed to be coincident with the POA). By comparing the values of the contours intersected by the POD cones at the three selected points, it can be seen that points A and B are unequal relative maxima and point C is a minimum. At point A, the contours intersected by the POD cone are of constant value. $\mathbf{K}_{hkl}(C)$ and DB(C) are directed upwards out of the plane of the diagram.

4.3. *Bragg–Brentano geometry*

In this geometry, the orientation of the sample relative to the incident beam is adjusted for each reflection such that the scattering vectors for the crystallites contributing to the measured intensity coincide with the normal to the flat-plate sample holder. One particular such setting is shown in Fig. 7, with the detector taken to be at point A on the powder ring and the POA assumed to coincide with the flat-plate normal (around which the sample is usually rotated). Points A and B are maxima in the diffraction pattern and point C is a minimum for a reflection with a small POD-cone angle, ψ, as previously discussed. And it can be seen that point A is at a stronger maximum than point B. This geometry is normally used with a small detector [at point A, *i.e.* set to collect DB(A)], and so the intensity variation around the powder rings is not observed. The Bragg–Brentano geometry represents a special case in which measurements are made with all positions on the POD cone lying on the same contour ($\alpha = \psi$), and thus $P(\alpha)$ is the same for all contributing crystallites.

As in the Debye–Scherrer case, the preferred orientation could be readily assessed by taking an exposure with the sample stationary and an image plate placed perpendicular to the incident beam – including, in a similar way, an assessment of the assumption that the POA coincides with the flat-plate normal.

5. Conclusions

We have shown how the detection and modelling of preferred orientation can be greatly aided and simplified by the collection of full two-dimensional powder patterns on a suitable area detector, and have presented a straightforward graphical interpretation of preferred-orientation effects in two-dimensional patterns for a number of standard diffraction geometries. We have also outlined the essential elements of a general quantitative model.

In closing, we remark that a simple *qualitative* assessment of the preferred orientation in a sample can be valuable, and is often sufficient for many purposes. For example, a two-dimensional pattern collected with the incident beam inclined to the expected preferred-orientation axis will reveal immediately whether the sample has any significant preferred orientation and, if so, approximately how strong the effects are. This is already useful information. Beyond that, a comparison of two-dimensional patterns collected at two different inclinations to the preferred-orientation axis will show directly which reflections are weakened and which are strengthened by preferred-orientation effects, and that is sufficient to place tight constraints on any preferred-orientation model included in structure refinement. With a little more effort, but still without quantitative modelling of the two-dimensional data, it is often even possible to identify the preferred-orientation direction using the simple graphical approach we have proposed.

We suggest that many powder diffraction studies would benefit from the routine collection of two-dimensional

patterns to assess sample preferred orientation in these ways – and better still, model it. This is particularly true for work at synchrotron sources where area-detector systems are now becoming widely available and good two-dimensional patterns can be collected very quickly.

This work is supported by the UK Engineering and Physical Sciences Research Council and by facilities made available by Daresbury Laboratory, UK. We are grateful for assistance with the experimental facilities from G. Bushnell-Wye and A. A. Neild.

References

Barrett, C. & Massalski, T. B. (1992). *Structure of Metals, International Series on Materials Science and Technology*, Vol. 35. Oxford: Pergamon Press.

Bunge, H. J., Dahms, M. & Brokmeier, H. G. (1989). *Crystallogr. Rev.* **2**, 67–86.

Capkova, P., Peschar, R. & Schenk, H. (1993). *J. Appl. Cryst.* **26**, 449–452.

Capkova, P. & Valvoda, V. (1974). *Czech. J. Phys.* B**24**, 891–894.

Cerny, R., Valvoda, V. & Chladek, M. (1995). *J. Appl. Cryst.* **28**, 247–253.

Dahms, M. & Bunge, H. J. (1989). *J. Appl. Cryst.* **22**, 439–447.

Dollase, W. A. (1986). *J. Appl. Cryst.* **19**, 267–272.

Järvinen, M. (1993). *J. Appl. Cryst.* **26**, 525–531.

Järvinen, M., Merisalo, M., Pesonen, A. & Inkinen, O. (1970). *J. Appl. Cryst.* **3**, 313–318.

March, A. (1932). *Z. Kristallogr.* **81**, 285–288.

Nelmes, R. J. & McMahon, M. I. (1994). *J. Synchrotron Rad.* **1**, 69–73.

Peschar, R. & Schenk, H. (1995). *J. Appl. Cryst.* **28**, 127–140.

Rietveld, J. (1969). *J. Appl. Cryst.* **2**, 1–8.

Wright, N. G. (1995). PhD thesis, The University of Edinburgh, Scotland.

"Hidden" High-to-Low Cristobalite Type Transition in HgSe and HgTe at High Pressure

M. I. McMahon, R. J. Nelmes, H. Liu, and S. A. Belmonte

Department of Physics and Astronomy, The University of Edinburgh, Mayfield Road, Edinburgh, EH9 3JZ, United Kingdom

(Received 22 April 1996)

A transition from the zinc blende (ZB) phase to a distorted-ZB structure has been found in both HgSe and HgTe. This is a structure type not previously reported in any of the II-VI or III-V systems. The transition occurs ~1 GPa above the pressure at which the ZB phase becomes unstable against the cinnabar phase, and is thus observable only because of the sluggishness of the ZB to cinnabar transformation. The atomic coordinates of the distorted-ZB structure are remarkably similar to those of the cations in the low-cristobalite phases of $AlPO_4$ and $GaPO_4$. [S0031-9007(96)00885-X]

PACS numbers: 61.50.Ks, 62.50.+p

HgSe and HgTe both have the tetrahedrally-coordinated zinc blende (ZB) structure at ambient pressure, and transform to the cinnabar structure under applied pressure [1,2]. This transformation involves a substantial structural rearrangement and a 9% increase in density, and is quite sluggish in both systems at room temperature [3]—requiring several hours at pressures some 0.5 GPa above the onset of the transition to reach apparent completion [1,3]. The pressures at which the transitions are reported to start have increased as more hydrostatic techniques have been used: from 0.75 [1,2] to ~1.0 GPa [4] in HgSe, and from 1.4 to ~1.9 GPa [5] in HgTe. This is probably another manifestation of the inherently sluggish and reconstructive nature of the transition. (A similar effect has been reported for the diamond to β-tin transition in Si [6].)

While making a more detailed study of the ZB to cinnabar transition in HgSe, we have found that good hydrostatic conditions also substantially increase the range of coexistence of the ZB and cinnabar phases, allowing the discovery of a previously unobserved phase that appears reproducibly in all mixed ZB/cinnabar samples at ~2.1 GPa, before the transformation to the cinnabar phase is complete. The same behavior has since been found in HgTe. The new phase has a distorted-tetrahedral, orthorhombic structure, with space group $C222_1$. No such structure has been reported previously for any of the II-VI or III-V systems. However, the atomic coordinates are remarkably similar to those of the cations in the low-cristobalite phase of $AlPO_4$ and $GaPO_4$ [7]. Since the cation coordinates in the (idealized) high-cristobalite phases are as in ZB [8], the ZB to $C222_1$ transition in HgSe and HgTe is of the high-to-low cristobalite type. This reveals an interesting and unexpected link to the structures of SiO_2 and its analogs. Another unusual aspect of the $C222_1$ phase is that it is observable only because of the sluggish nature of the lower-pressure transition from ZB to cinnabar: the ZB to $C222_1$ transition may thus be termed a "hidden" transition.

Diffraction data were collected at room temperature on station 9.1 at the Synchrotron Radiation Source, Daresbury, using angle-dispersive diffraction techniques and an image-plate area detector. The incident wavelength was 0.4654 Å. The sample of HgTe was the same as that used in Ref. [9], while the HgSe was a fine powder of 99.999% purity obtained from the Aldrich Chemical Company. Samples were loaded into Merrill-Bassett diamond-anvil pressure cells with 4:1 methanol:ethanol as a pressure transmitting medium and chips of ruby for pressure measurement [10]. After structure solution, the final structural parameters, including lattice parameters, were obtained from Rietveld refinement [11] of the full integrated profiles using the program MPROF [12]. Details of our beam-line setup, experimental procedures, and data analysis techniques have been reported previously [13].

The first and most detailed of the studies reported in this Letter have been carried out on HgSe. On pressure increase, the cinnabar phase of HgSe was first observed at 1.15(5) GPa. This is at the upper end of the range of previously reported pressures for the onset of the transition (see above), in accord with the hydrostatic conditions of the present study. On further compression, the proportion of the cinnabar phase increases only gradually. Figure 1(a) shows a pattern obtained at 2.00 GPa: The strongest reflections are still those of the ZB phase (as indexed)—as said, the sluggishness of the transition is much increased by the hydrostatic conditions. At the slightly higher pressure of 2.15 GPa [Fig. 1(b)], the cinnabar reflections have grown further at the expense of ZB and some extra reflections have appeared, as marked by arrows in the inset. These extra reflections become stronger with a further small increase in pressure to 2.25 GPa [Fig. 1(c)]—they are now visible in the full profile (as marked) as well as in the inset—and the ZB phase has almost all transformed. Above 2.25 GPa, the reflections from the new phase decrease in intensity, and above ~3.4 GPa the sample becomes single-phase cinnabar. On pressure decrease, the new phase is not observed at all; the cinnabar phase transforms directly back to the ZB phase at ~0.4 GPa. (This pressure of ~0.4 GPa is the same as was reported for the reverse transition in early studies [1], which would have been as "hydrostatic" on pressure decrease as the present study.)

It was found that the proportions of the ZB, new, and cinnabar phases could be varied by changing the rate of

 © 1996 The American Physical Society

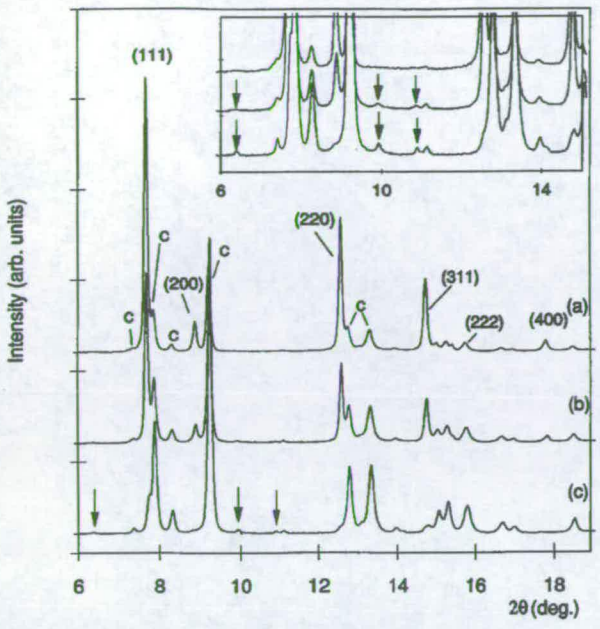


FIG. 1. Integrated powder-diffraction profiles from HgSe at (a) 2.00 GPa, (b) 2.15 GPa, and (c) 2.25 GPa. In profile (a), the reflections from the zinc blende phase are indexed, and those from the cinnabar phase are labeled "C" (up to $2\theta \sim 14°$). The inset shows the range up to ~15° on an expanded intensity scale for the same three profiles. Arrows in the inset and in profile (c) mark reflections from the new phase.

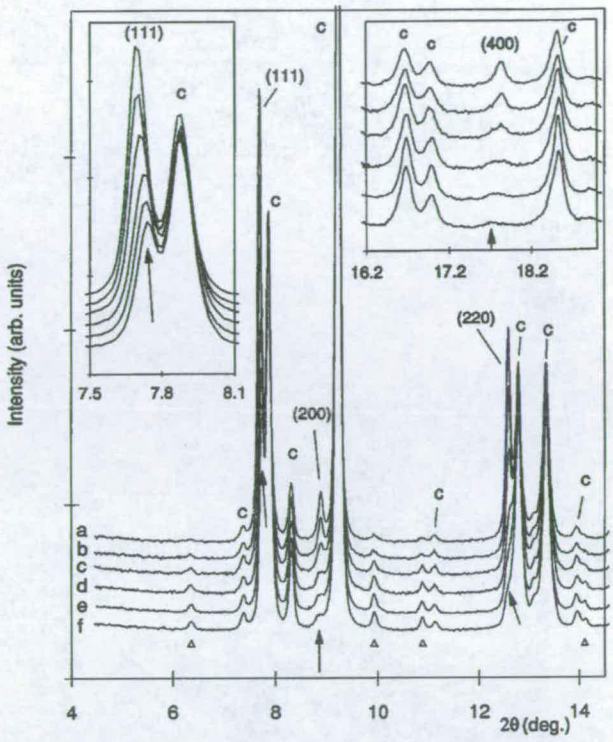


FIG. 2. Integrated powder-diffraction profiles from HgSe (a) on reaching a pressure of 2.25 GPa, and then 9, 20, 30, 42, and 76 h later in (b) to (f), respectively. The insets show the low-angle strong reflections on an expanded 2θ scale, and a higher-angle region around the zinc blende (400) reflection, for the same six profiles. The zinc blende reflections are indexed in profile (a), and the main cinnabar reflections are labeled "C." The Δ symbols mark the extra reflections of the new phase, and the arrows mark new-phase reflections derived from the zinc blende reflections.

increase of pressure. In particular, the amount of the new phase in the sample can be maximized by increasing pressure quite quickly to 2.25 GPa, and then maintaining this pressure for 2–3 days. This is illustrated in Fig. 2. Profile (a) was recorded soon after a sample reached 2.25 GPa. There is much more ZB than in Fig. 1(c), and the extra reflections of the new phase are just visible [their positions are marked by Δ below profile (f)]. Profiles (b) to (e) were recorded at intervals over the following 42 hours, and show the ZB reflections (indexed) decreasing in intensity, while the new-phase reflections grow and the cinnabar peaks (labeled "C") remain constant. Profile (f) was recorded 34 h after (e), and shows no further change. There is thus a transition directly from ZB to the new phase, starting at 2.10(5) GPa. This phase is stable indefinitely up to 2.25(5) GPa, above which it transforms (sluggishly) to the cinnabar phase.

Closer examination of the profiles in Fig. 2 reveals that it is not only the intensities of the ZB peaks that change as a function of time, but also their apparent *positions*. This is most evident for the ZB (111) and (400) reflections, which are enlarged in the insets; they appear to shift to higher and lower 2θ values, respectively, with time. However, it is only the ZB peaks that exhibit this behavior; neither the extra peaks that arise from the new phase (those marked Δ in Fig. 2) nor the peaks from the cinnabar phase show any change in position with time. It seems clear that the apparent shift in ZB peak positions arises as a result of intensity transfer to new-phase peaks that have slightly different 2θ values. These peaks are marked with arrows below profile (f)—some in the main figure and some in the insets. They will no longer index to the ZB structure, and we conclude that this sample is a mixture of the new and cinnabar phases only: The ZB phase has all transformed.

It can be seen that the arrowed reflections in Fig. 2(f) are very similar to the original ZB reflections in their relative intensities as well as their 2θ values. This suggests a close structural relationship between the two phases. Further support for this conclusion comes from the observation that a slight pressure reduction leads to a complete transformation of the new phase back to ZB. The lack of significant hysteresis is in marked contrast to the transition between ZB and the cinnabar phase, which involves a substantial structural rearrangement.

Ab initio indexing, using the program DICVOL [14], revealed that the positions of all 8 reflections marked in Fig. 2(f) could be accounted for by a C-face centered orthorhombic unit cell with approximate lattice parameters of $a = 5.98$ Å, $b = 5.89$ Å, and $c = 6.05$ Å. For a physically reasonable density, this unit cell must contain 8 atoms, the same as the ZB phase. From extrapolation, the lattice parameter of the ZB phase at 2.25 GPa is 5.997(5) Å. The volume decrease at the ZB to new-phase

transition is therefore only ~1.2%. This is considerably smaller than the volume change at the ZB to cinnabar transition [9.9(1)% at 1.80 GPa], and very much smaller than the volume change accompanying phase transitions on pressure increase from the ZB or diamond phases of other binary and elemental semiconductors, which are typically in the range ~20% [15].

Because the new phase can be observed only as a minority component in two-phase patterns, a definitive determination of the space group of the new structure is difficult. However, only $C222_1$ was found both to be consistent with the observed systematic absences *and* to allow an atomic arrangement at all similar to the ZB structure. With the Hg atoms on the 4(a) sites of $C222_1$ at $(x, 0, 0)$ and the Se atoms on the 4(b) sites at $(0, y, 1/4)$, the ZB structure is obtained when the lattice parameters are all equal ($a = b = c$), $x = 0.25$, and $y = 0.25$. A more detailed account of the derivation of the space group, the structure solution, and tests of the uniqueness of the solution will be published separately [16].

The best fit to the mixed-phase profile at 2.25 GPa is shown in Fig. 3, in which the 8 reflections identified in Fig. 2(f) are indexed on the $C222_1$ unit cell (some in the inset). The refined lattice parameters for the $C222_1$ phase are $a = 5.992(1)$ Å, $b = 5.879(1)$ Å, and $c = 6.045(2)$ Å, with atomic coordinates $x(\mathrm{Hg}) = 0.302(1)$ and $y(\mathrm{Se}) = 0.207(2)$, and, for the cinnabar phase, $a = 4.174(1)$ Å, $c = 9.626(1)$ Å, and atomic coordinates $u(\mathrm{Hg}) = 0.666(1)$ and $v(\mathrm{Se}) = 0.540(1)$. To check the site ordering of this structure, trial refinements were also made with

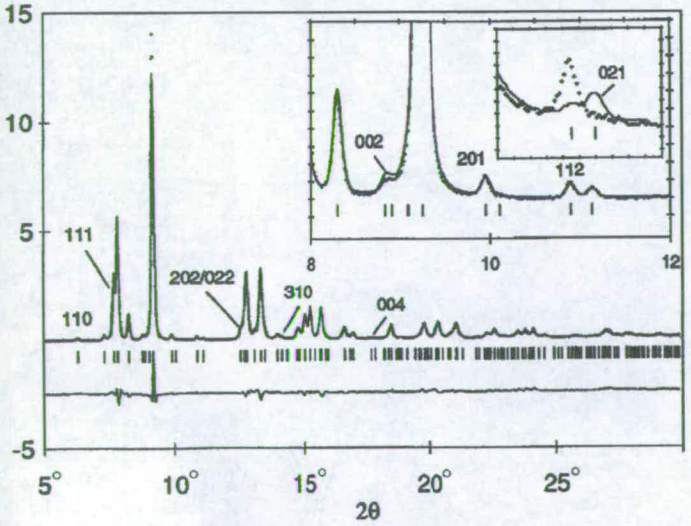


FIG. 3. Two-phase Rietveld fit to the HgSe profile in Fig. 2(f). The visible nonoverlapped $C222_1$ reflections are indexed; other reflections are from the cinnabar phase. The tick marks show the positions of all reflections allowed by symmetry in both phases. The difference between the observed (dots) and calculated (solid line) profiles is displayed below the tick marks. The region from $2\theta = 8°$ to $12°$ is enlarged in the inset; the second inset shows the best fit to the (201) and (021) reflections with the Hg and Se sites interchanged. Intensity scales are arbitrary.

(i) a site-disordered model, with each site 50:50 occupied by Hg and Se, and (ii) a model in which the positions of the Hg and Se atoms were interchanged. Both gave significantly poorer fits to the data. The (002) reflection would be absent in a site-disordered structure, and is plainly present in recorded profiles [see also Fig. 2(f)]. The fit to the (201) reflection shown in the inset of Fig. 3 is with the site assignment as refined above. If Hg and Se are interchanged, most of the intensity appears instead in the (021) reflection—as shown in the second inset—and this clearly does not fit the data. The lattice parameters and atomic coordinates quoted above for the cinnabar phase in the mixed-phase refinement are the same within error as those given by a single-phase cinnabar sample at the same pressure [0.666(1) and 0.539(1)]—obtained on pressure decrease. This indicates that the $C222_1$ structure accounts well for all the noncinnabar features in the mixed-phase profile, including any that are overlapped by the cinnabar reflections [16].

In the light of these results for HgSe, we reexamined the ZB to cinnabar transition in HgTe, and found very similar behavior, except that the $C222_1$ phase appears at a slightly higher pressure. $C222_1$ reflections are first detectable at 2.25 GPa, and the rate of transformation from ZB is greatest at 2.40 GPa. Above that pressure, $C222_1$ transforms to cinnabar and has not been detected in any sample above ~3.6 GPa. Refinements of a mixed-phase profile at 2.55 GPa give $a = 6.295(2)$ Å, $b = 6.241(2)$ Å, and $c = 6.364(2)$ Å for the $C222_1$ component, with $x(\mathrm{Hg}) = 0.315(1)$ and $y(\mathrm{Te}) = 0.205(2)$. The distortion of the unit cell (from cubic) is less than in HgSe; also, the difference in scattering between Hg and Te is less than between Hg and Se. For these reasons, it is difficult to detect the (002) reflection or discriminate between the two different fits to (201)/(021) discussed for HgSe, and the site assignment cannot be conclusively tested. However, there is no reason or evidence to expect it to differ from that of HgSe.

The $C222_1$ structure of HgSe is fourfold coordinated, but each atom has two nearest neighbors at 2.580(8) Å, and the other two at 2.653(7) Å; the Se-Hg-Se angles range from 94° to 125°; and the Hg-Se-Hg angles range from 96° to 125°. Thus, though the structural arrangement is very much like that of ZB, the distortions from perfect tetrahedral coordination are considerable. (The distortions are similar in HgTe.) This is the first report of a distorted tetrahedral structure in any of the II-VI or II-V systems. Some structures of this type *are* known in silicon and germanium, namely, the BC8, R8, and ST12 phases obtained on pressure release [17,18]. Though their structures are quite different from $C222_1$, it is interesting to compare the magnitudes of their distortions. In BC8 silicon, the nearest-neighbor (nn) bond lengths are 2.306 and 2.392 Å, with bond angles of 99.2° and 117.9°—and the distortions of R8 silicon are very similar. In ST12 germanium, the nn bond lengths are 2.479, 2.486, and 2.489 Å, and the bond angles vary from 88.1° to 135.0°. These distortions are close to those observed in the $C222_1$ phase

of HgSe (and HgTe), particularly for BC8 (and R8) silicon. However, as said, $C222_1$ is another quite different structure.

There is a closer and more remarkable structural relationship with the low-cristobalite phases of $AlPO_4$ and $GaPO_4$. These have the same space group as the $C222_1$ phases of HgSe and HgTe, and have similarly nearly cubic unit cells [7]. Moreover, the fractional coordinates $x(Al) = 0.306$ and $y(P) = 0.198$ in $AlPO_4$, and $x(Ga) = 0.327$ and $y(P) = 0.183$ in $GaPO_4$ [7] are strikingly similar to those found (above) for HgSe and HgTe. In the same way, the ambient-pressure ZB phase of HgSe and HgTe has the same spatial arrangement of atoms as the cations in the (idealized) high-cristobalite phase of $AlPO_4$ and $GaPO_4$ [8]. The ZB to $C222_1$ transition in HgSe and HgTe is thus analogous to a high-to-low cristobalite transition—a somewhat surprising and unexpected result. However, a relationship of this kind between a tetrahedrally coordinated semiconductor and a SiO_2 polymorph *has* been noted previously [19]. The spatial arrangement of the Si atoms in the keatite polymorph of SiO_2 [20] is almost identical to the ST12 polymorph of Ge [17]: both have the same space group, $P4_32_12$, with Si on the 4(a) and 8(b) sites at $(0.410, 0.410, 0)$ and $(0.326, 0.120, 0.248)$, respectively, in keatite [20], and the Ge atoms on the same sites at $(0.4088, 0.4088, 0)$ and $(0.3270, 0.1216, 0.2514)$ in ST12-Ge [17]. However, a relationship of this kind has never previously been reported for any of the II-VI or III-V systems. The new results for HgSe and HgTe suggest that the structures of SiO_2 and its polymorphs may provide a fruitful source of structural models for other high-pressure or metastable phase of the tetrahedrally coordinated semiconductors.

A crucial aspect of the ZB to $C222_1$ transitions in HgSe and HgTe is that they would not be observed but for the sluggishness of the ZB to cinnabar transitions. In this sense, we describe the ZB to $C222_1$ transitions as "hidden." We note that they have all the characteristics of equilibrium transitions: they occur at definite, reproducible pressures; they give rise to a phase that is stable indefinitely over a definable range of pressure; and the structural change is reversible, with very little hysteresis. It is probable that the true equilibrium phase is cinnabar, but this need *not* be the case. We know of no other example of such transitions on pressure increase in the II-VI, III-V, or group IV semiconductors. But the possibility opens up the prospect of an interesting new class of high-pressure structures and phase transitions, and it may well prove fruitful to conduct experiments at low temperature where the sluggishness of reconstructive transitions will generally be enhanced.

In conclusion, we have found that the ZB phase of HgSe and HgTe transforms to a distorted-tetrahedral structure with $C222_1$ symmetry—not previously known in any of the II-VI or III-V semiconductors—at a pressure ~1 GPa above that at which ZB becomes unstable against the cinnabar phase. The $C222_1$ phase can be observed only because of the sluggishness of the transition to cinnabar in these systems. The structural change is remarkably like that undergone by the cations at the high-to-low cristobalite transition in $AlPO_4$ and $GaPO_4$. This, and a similar relationship between ST12 germanium and the keatite polymorph of SiO_2, suggest that other SiO_2-type structures may be found in the elemental and binary semiconductors.

We would like to thank A. A. Neild and G. Bushnell-Wye of the Daresbury Laboratory for their help in preparing the beam-line equipment. This work is supported by a grant from the Engineering and Physical Sciences Research Council, funding from the Council for the Central Laboratory of the Research Councils, and by facilities made available by Daresbury Laboratory.

[1] J. A. Kafalas, H. C. Gatos, M. C. Lavine, and M. D. Banus, J. Phys. Chem. Solids **23**, 1541 (1962).
[2] A. N. Mariano and E. P. Warekois, Science **142**, 672 (1963).
[3] A. Jayaraman, W. Klement, and G. C. Kennedy, Phys. Rev. **130**, 2277 (1963).
[4] A. Onodera, A. Ohtani, M. Motobayashi, T. Seiko, O. Shimomura, and F. Fukunaga, in *Proceedings of the 8th AIRAPT Conference 1981,* edited by C-M. Blackman, T. Johannison, and L. Tengner (Arkitektkopia, Uppsala, 1982), Vol. 1, p. 321.
[5] T. M. Turusbekov and E. I. Estrin, Sov. Phys. Solid State **21**, 558 (1979).
[6] J. Z. Hu, L. D. Merkle, C. S. Menoni, and I. L. Spain, Phys. Rev. B **34**, 4679 (1986).
[7] R. C. L. Mooney, Acta Crystallogr. **9**, 728 (1956).
[8] H. D. Megaw, *Crystal Structures: A Working Approach* (Saunders, Philadelphia, 1973).
[9] M. I. McMahon, N. Wright, D. R. Allan, and R. J. Nelmes, Phys. Rev. B **53**, 2163 (1996).
[10] H. K. Mao, P. M. Bell, J. W. Shaner, and D. J. Steinberg, J. Appl. Phys. **49**, 3276 (1978).
[11] H. M. Rietveld, J. Appl. Crystallogr. **2**, 65 (1969).
[12] A. N. Fitch and A. D. Murray (unpublished).
[13] R. J. Nelmes and M. I. McMahon, J. Synchrotron Radiat. **1**, 69 (1994).
[14] D. Louër and R. Vargas, J. Appl. Crystallogr. **15**, 542 (1982).
[15] S. C. Yu, I. L. Spain, and E. F. Skelton, Solid State Commun. **25**, 49 (1978).
[16] H. Liu, M. I. McMahon, R. J. Nelmes, and S. A. Belmonte (to be published).
[17] J. Donohue, *The Structure of the Elements* (John Wiley and Sons, New York, 1974).
[18] J. Crain, G. J. Ackland, J. R. Maclean, R. O. Piltz, P. D. Hatton, and G. S. Pawley, Phys. Rev. B **50**, 13 043 (1994).
[19] A. F. Wells, *Structural Inorganic Chemistry* (Clarendon Press, Oxford, 1984), p. 131.
[20] J. Shropshire, P. P. Keat, and P. A. Vaughan, Z. Kristallogr. **112**, 409 (1959).

Nonexistence of the Diatomic β-Tin Structure

R. J. Nelmes, M. I. McMahon,* and S. A. Belmonte

Department of Physics and Astronomy, The University of Edinburgh, Edinburgh EH9 3JZ, United Kingdom

(Received 1 July 1997)

Many high-pressure phases of the III-V and II-VI semiconductors have been believed to have the diatomic equivalent of the (tetragonal) β-tin structure. Recent work has shown this to be incorrect in several cases. It is now shown that the same is true of all the remaining possibilities—AlSb, HgSe, InP, and GaP. The phases concerned all have orthorhombic structures of the *Cmcm* type. The apparent nonexistence of the β-tin structure has important implications for the structural systematics. [S0031-9007(97)04474-8]

PACS numbers: 61.50.Ks, 62.50.+p

The start of structural studies of group IV, III-V, and II-VI semiconductors under pressure was marked by Jamieson's discovery in 1963 [1] that the first transition in silicon and germanium is to the tetragonal β-tin structure previously known only in elemental tin. Very soon afterwards, he carried out the first diffraction studies of the high-pressure transitions in AlSb, GaSb, and InSb, which have the cubic zinc-blende structure at ambient pressure [2]. He concluded that they all transform to a β-tin-like structure in which the metal and Sb atoms are probably ordered onto different sites—that is to say, with the metal atoms at (0, 0, 0) and $(\frac{1}{2}, \frac{1}{2}, \frac{1}{2})$, and the Sb atoms at $(0, \frac{1}{2}, \Delta = \frac{1}{4})$ and $(\frac{1}{2}, 0, \Delta + \frac{1}{2} = \frac{3}{4})$. This is generally referred to as simply "β-tin," but where it is necessary to make the distinction we will call this the "diatomic β-tin" structure (henceforth d-β-tin) as against the true, monatomic β-tin structure (m-β-tin) of Si and Ge. Site-disordered binary systems can also be regarded as having the m-β-tin structure.

Subsequent work confirmed the β-tin phase in AlSb [3], GaSb [4], and InSb [5], and revealed the same zinc-blende (ZB) to β-tin transition also in GaP [6]. In his pioneering work, Jamieson [2] found different behavior in InP and InAs, with the ZB phase transforming to an NaCl structure. This was later shown to be true also of all the II-VI systems, except the Hg chalcogenides—where there is the NaCl phase but it is preceded by a cinnabar phase [7]—and ZnTe [8]. However, when the NaCl phase was taken through a further transition at higher pressures, it was found in nearly all cases to transform to β-tin—in InP [9], InAs [10], CdTe [11], and probably HgSe and HgTe [7]. The majority of III-V and II-VI systems thus appeared to exhibit a transition from fourfold coordinated ZB directly to quasisixfold coordinated β-tin, or first to NaCl and then to β-tin. This perception has steadily grown since Jamieson's early work, and β-tin has come to occupy a central role in the high-pressure structural systematics of the III-V and II-VI semiconductors.

However, recent results on GaSb [12], InAs [13], InSb [14], CdTe [15], and HgTe [16] have shown that their supposed β-tin phases do not, in fact, have that structure. This is very surprising, and suggests the whole nature of the systematics may be in question. We have therefore undertaken studies of all the remaining possibilities—in AlSb, HgSe, InP, and GaP—and can now show conclusively that their supposed β-tin phases are also incorrect interpretations. In this Letter, we present these results and discuss the remarkable conclusion that then follows: *there is, as yet, no evidence for the d-β-tin structure in* any *of the III-V or II-VI systems*—despite much theoretical work apparently establishing its stability.

First, we will rehearse the already established new results on GaSb, InSb, CdTe, HgTe, and InAs. They were all obtained following the introduction of angle-dispersive x-ray (ADX) powder diffraction using an image-plate detector [17], which yields data of considerably greater resolution and sensitivity than were previously available.

GaSb was long believed to transform from ZB to β-tin at ~7 GPa [4]. Image-plate data revealed several features not consistent with β-tin [12] that are well fitted by a site-disordered (and thus quasimonatomic) orthorhombic structure, with *Imma* symmetry, found also in Si and Ge [18]. This is a distorted β-tin structure, in which the z-coordinate, Δ (see above), differs significantly from $\frac{1}{4}$—rising from 0.31 at 7 GPa to 0.37 at 35 GPa [12]. The supposed β-tin InSb-II phase has been shown to have an orthorhombic *Immm* structure which differs significantly from β-tin in having an 8% difference between the a and b lattice parameters and a Δ value of 0.5 [14,19]. These give rise to peak splittings, other non-β-tin peaks, and d-spacing misfits to β-tin that were already evident—and sometimes remarked upon—in earlier studies [14].

CdTe was thought to transform from an NaCl phase to β-tin at 10 GPa, and then to orthorhombic *Pmm*2 at 12 GPa [11]. In fact, the 10 GPa transition is to the orthorhombically distorted NaCl structure, with *Cmcm* symmetry, first found in ZnTe [8], and this is stable to at least 28 GPa [15]; the proposed *Pmm*2 structure can be understood as a subcell. In their study of HgTe, Huang and Ruoff [7] identified a β-tin-like phase between 12 and 38 GPa; they suggested that $\Delta = 0$ gives the closest fit to their data, but it is not evidently different from the fit with the β-tin value of $\Delta = \frac{1}{4}$. In any case, there are various other misfits and discrepancies, and they are all

 0031-9007/97/79(19)/3668(4)$10.00 © 1997 The American Physical Society

accounted for very well by a strongly first-order transition from NaCl to the same *Cmcm* structure as in CdTe [16]. Vohra *et al.* [10] reported a transition from the NaCl phase of InAs to β-tin at 17 GPa. But non-NaCl peaks become clearly visible at pressures as low as 9 GPa in the image-plate ADX data, and grow in intensity with pressure increase [13]; these peaks are obscured by nonsample lines in the energy-dispersive x-ray (EDX) data [10]. Though there are some small unexplained features in the ADX patterns [13], the transition appears to be very similar to the continuous NaCl to *Cmcm* transition in CdTe. There is no transition at 17 GPa, and—again—no β-tin phase.

We now turn attention to the new studies of AlSb, HgSe, InP, and GaP. Diffraction data were collected on station 9.1 at the Synchrotron Radiation Source, Daresbury, using an image-plate area detector [17]. The incident wavelength was ~0.45 Å. Finely ground samples were made from starting material of 99.99+% purity, and—except GaP—loaded with 4:1 methanol:ethanol as a pressure medium and chips of ruby for pressure measurement; GaP was loaded without any medium because of its high sensitivity to water. (AlSb was tested with and without methanol:ethanol. There was no difference, except that sharper diffraction peaks were obtained *with* the medium.) Profile refinements were carried out with the program GSAS [20].

Jamieson's identification [2] of the first high-pressure phase of AlSb as β-tin at ~10 GPa was amended to NaCl by Yu *et al.* [4] and to orthorhombically distorted NaCl—with a transition pressure of 7.7(5) GPa—by Baublitz and Ruoff [21]. However, the most recent study by Greene *et al.* [3] returned to the β-tin interpretation. Figure 1 shows our diffraction pattern in this phase at 14.7 GPa, and it is plainly not β-tin which—among many other things—cannot account for two of the lowest-angle lines. These lines appear to have been beyond the range of the EDX data of Greene *et al.*; they detected only the three strongest lines (marked by asterisks) as visible features in patterns dominated by peaks from a gold pressure marker and Sb fluorescence [3]. The calculated profile in Fig. 1 is from a site-ordered *Cmcm* structure with $a = 5.353(1)$ Å, $b = 5.788(1)$ Å, $c = 5.086(1)$ Å, $y(\mathrm{Al}) = 0.599(1)$, and $y(\mathrm{Sb}) = 0.163(1)$. The main reflections are indexed on this cell, which is very similar to the cell proposed by Baublitz and Ruoff [21]. There are small misfits in a few (weak) peak positions, but these do not appear to fit *any* lattice. This is a problem we have encountered in several III-V and II-VI phases, and is likely to arise from nonhydrostatic (deviatoric) stress or stacking faults. Otherwise, the profile fits well to all the known features—and the relative intensities—of a *Cmcm* pattern. We thus conclude that *Cmcm*—or a very similar structure—is the most probable interpretation. Refinement of a mixed-phase ZB/*Cmcm* pattern at 8.1 GPa shows the *Cmcm* distortions to be already fully developed at the transition, with $a = 5.448(1)$ Å, $b = 5.847(9)$ Å, $c = 5.150(1)$ Å, $y(\mathrm{Al}) = 0.55(4)$, and $y(\mathrm{Sb}) = 0.15(1)$; and $a = 5.9344(2)$ Å for ZB, giving $\Delta V/V_0 = 19.5(2)\%$.

In their first study of the transition from the NaCl phase III of HgSe to phase IV, starting at 28 GPa, Huang and Ruoff reported the phase-IV structure as orthorhombic [22]. Later they reinterpreted the same data (with some differences in analysis) in terms of the same two β-tin-like structures as they considered for HgTe [7]. As in that case (above), the observed intensities fit equally well with the β-tin value of $\Delta = \frac{1}{4}$. However, neither of these structures accounts for five peaks—labeled A, B, C, D, and F by Huang and Ruoff [7]—which were attributed to a second, hexagonal phase (A and B) and various other uncertain causes (C, D, and F) [7]. (The previous, orthorhombic interpretation fitted all of these "extra" lines, except that "A" was not included [22].) Figure 2 shows a site-ordered *Cmcm* fit to our data collected at 35.6 GPa. The general similarity to the AlSb pattern in Fig. 1 is clear. There are also small misfits as in AlSb (in 020 and 220), and some additional ones.

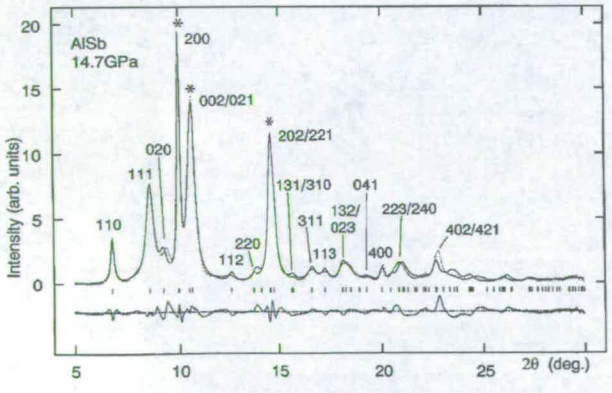


FIG. 1. Rietveld refinement fit of the *Cmcm* structure to a profile from AlSb at 14.7 GPa. Tick marks show the positions of all reflections allowed by symmetry. Reflections giving rise to visible peaks are indexed; overlapping ones are separated by an oblique line. The difference between the observed and calculated profiles is displayed below the tick marks. Asterisks mark reflections visible in the data of Ref. [3].

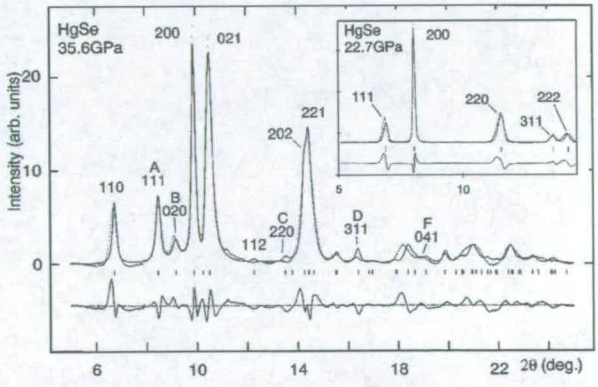


FIG. 2. As Fig. 1 for HgSe at 35.6 GPa. "A" to "D" and "F" label the same features as in Fig. 4 of Ref. [7]. The best fit to a profile from the NaCl phase at 22.7 GPa is shown in the inset.

We again attribute these to microstructural effects, for which there is direct evidence in the NaCl phase (of the same sample), as shown in the inset. A *Cmcm* (or *Cmcm*-like) structure is clearly the most probable interpretation, particularly since *Cmcm* fits so well (at a much lower pressure) to HgTe [16]. Features A, B, and D are well accounted for, and C and F probably are—as indexed. (There is also the lowest-angle reflection, 110, which would have been under the fluorescence peaks in the earlier studies.) The fit in Fig. 2 gives $a = 5.153(1)$ Å, $b = 5.559(1)$ Å, $c = 4.972(2)$ Å, $y(\mathrm{Hg}) = 0.644(1)$, and $y(\mathrm{Se}) = 0.141(2)$. The transition from the NaCl phase is first order, as in HgTe [16], with a (small) $\Delta V/V_0$ of 0.9(5)%.

The evidence for an NaCl to β-tin transition at 19 GPa in InP rests only on weak lines reported at the top pressure, just before gasket failure, in the study by Menoni and Spain [9]. We find that the NaCl phase remains stable until 28(1) GPa, above which pressure the continuous transition shown in the inset of Fig. 3 occurs. These changes have all the characteristics of the continuous NaCl to *Cmcm* transition first observed in CdTe [15]. The site-ordered *Cmcm* fit in Fig. 3 to data collected at 45.6 GPa gives $a = 4.879(1)$ Å, $b = 5.088(2)$ Å, $c = 4.923(3)$ Å, $y(\mathrm{In}) = 0.658(1)$, and $y(\mathrm{P}) = 0.143(2)$; unlike all other *Cmcm* phases found previously, the unit cell is close to tetragonal. Apart from some difficulty with the very broadened 111 reflection, the fit is very good.

Yu *et al.* reported that the transition from the ZB phase at 22 GPa in GaP was *not* to a β-tin structure [4]. But a more detailed study soon after by Baublitz and Ruoff [6] concluded that it was β-tin, and this was supported by Hu *et al.* [23] who also reinterpreted the data of Yu *et al.* as a mixture of ZB and β-tin. However, the data in Fig. 6 of Baublitz and Ruoff show a reflection not allowed in β-tin—as the authors recognized—and there are clear shoulders that are also not accounted for on the low-angle side of the "β-tin" 200 and 220 peaks. All these features are reproduced in our data, as shown in inset (ii) of Fig. 4 for a pattern collected at 37.3 GPa, well above a transition pressure of 26(1) GPa (see also Ref. [23]); in addition, we detect a very weak 110 reflection. The calculated profile in Fig. 4 is with a site-*dis*ordered *Cmcm* structure, which gives a good fit to all the features with $a = 4.707(2)$ Å, $b = 4.949(1)$ Å, $c = 4.701(3)$, $y(\mathrm{Ga/P}) = 0.647(3)$, and $y(\mathrm{Ga/P}) = 0.159(3)$. The lack of long-range site ordering is made evident by the weakness of 110 and the absence of 111—as shown by the site-ordered "fit" in inset (i). The pattern is otherwise very similar to that of InP in Fig. 3, and GaP is like InP in having a unit cell close to tetragonal. A mixed-phase ZB/*Cmcm* sample at 29.4 GPa gives $\Delta V/V_0 = 14.0(2)\%$.

So, it can be shown conclusively that none of the III-V or II-VI phases previously thought to have the β-tin structure in fact does so. All these phases have various lower-symmetry structures: site-disordered *Imma* in GaSb, site-ordered *Immm* in InSb (InSb-II), site-disordered *Cmcm* in GaP, and site-ordered *Cmcm* (or *Cmcm*-like) in AlSb, InP, InAs, CdTe, HgTe, and HgSe. The site-disordered *Imma* structure has since also been found in InSb (phase P5 [19]), and what may be the only known true β-tin structure has been discovered in the new, site-disordered P2 phase of InSb [14]. P2 has so far been obtained only in mixed-phase samples with InSb-II, which makes it difficult to be certain that there is no departure from tetragonal symmetry. However, there is known to be a true β-tin phase in InSb when it is brought down to ambient pressure from above 2 GPa at low temperature (77 K) [14], and it seems likely that this is the same phase as P2. Other recent work has shown GaAs-II to have the *Cmcm* structure [18]—probably site-disordered as in GaP; as noted, there is a (site-ordered) *Cmcm* phase in ZnTe [8]; and NaCl to (site-ordered) *Cmcm* transitions have also been found in CdSe and ZnSe [18]. The corrected interpretations of the supposed β-tin phases are thus in accord with the new systematics emerging from several other III-V and II-VI systems.

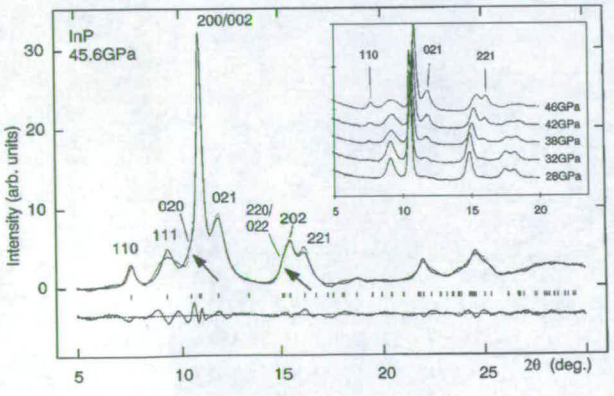


FIG. 3. As Fig. 1 for InP at 45.6 GPa. Arrows mark weak shoulders that indicate the orthorhombic splitting. The continuous growth of the *Cmcm* 110, 021, and 221 reflections above 28 GPa is shown in the inset.

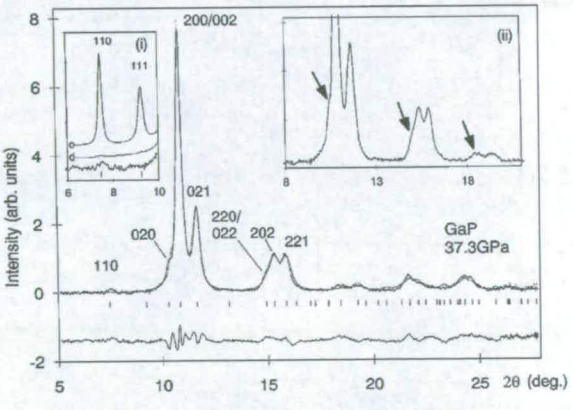


FIG. 4. As Fig. 1 for GaP at 37.3 GPa, except that the fit is with a site-disordered *Cmcm* structure. The best fit with a site-ordered *Cmcm* structure, "o", is compared with the site-disordered fit, "d", for the low-angle region in inset (i). Part of the pattern is enlarged in inset (ii), and arrows mark the non-β-tin features also visible in Fig. 6 of Ref. [6].

Except in the site-disordered *Imma* phases of GaSb and InSb, and the P2 phase of InSb, the structural differences from β-tin are not small; only in the three quasimonatomic cases do the structures come close to β-tin. It is to be noted that even truly monatomic β-tin is an unusual structure; apart from tin itself, it exists over just 2 GPa in Si and is found over a large pressure range only in Ge [18]. It is otherwise unknown. And the (site-ordered) diatomic β-tin structure does not appear to exist at all; not only have we shown its nonexistence (so far) in the III-V and II-VI systems under pressure, but a search of databases [24] reveals no known examples in *any* binary system under any conditions.

Yet theoretical and computational work has long appeared to show that the d-β-tin phase *should* exist [4], with a calculated energy significantly less than the NaCl structure in many cases [25]. Even in the most recent work, d-β-tin has still emerged as a possible equilibrium phase in some cases in which the *Cmcm* and *Immm* structures have now been included in new calculations: for example, in GaAs—where the d-β-tin energy is marginally less than that of the *Cmcm* structure at very high pressures [26], and in GaP—where the d-β-tin energy is clearly less than that of *Cmcm* above 20 GaP and a transition from *Cmcm* to d-β-tin is predicted [27]. But there is no evidence of the phase in GaAs [18], and Fig. 4 shows GaP still in the *Cmcm* phase at 37 GPa. The nonexistence of d-β-tin thus appears to be significant, suggesting some impediment to its formation. Its structure is quite different from *Cmcm*, and there may be kinetic hindrance to a transformation between them. A possibly more significant factor is that the known site-ordered high-pressure phases—NaCl, *Cmcm*, and *Immm*—have a structural feature in common; they are all made up of flat NaCl-like layers, differing only in the stacking. The d-β-tin structure is a strong departure from that. In their calculations of a *Cmcm*-like structure for GaAs, Zhang *et al.* [28] concluded that the Fermi surface is anisotropic, with a corresponding difference between more metallic bonding in the NaCl planes and more covalent bonding linking the planes. An interesting sidelight comes from the fact that β-tin-like structures are formed only in the quasimonatomic site-disordered phases—*Imma* GaSb and InSb, and P2 InSb—in which truly NaCl-like planes cannot be defined.

We thus conclude that diatomic β-tin, one of the apparently key structures in the high-pressure systematics of the III-V and II-VI semiconductors, has, in fact, never yet been found to exist; that calculations show it may nonetheless be an equilibrium structure in some cases; and that why it has not yet been observed is likely to prove an interesting and significant question.

We thank H. Liu for assistance with some of the experimental work, and A. A. Neild and G. Bushnell-Wye for technical support. This work is supported by a grant from the Engineering and Physical Sciences Research Council, by funding from the Council for the Central Laboratory of the Research Councils, and by facilities made available by Daresbury Laboratory. M. I. M. acknowledges a fellowship from the Royal Society.

*Now at Department of Physics, University of Liverpool, Liverpool, U.K.

[1] J. C. Jamieson, Science **139**, 762 (1963).
[2] J. C. Jamieson, Science **139**, 845 (1963).
[3] R. G. Greene, H. Luo, K. Ghandehari, and A. L. Ruoff, J. Phys. Chem. Solids **56**, 517 (1995).
[4] S. C. Yu, I. L. Spain, and E. F. Skelton, Solid State Commun. **25**, 49 (1978), and references therein.
[5] R. E. Hanneman, M. D. Banus, and H. C. Gatos, Phys. Chem. Solids **25**, 293 (1964).
[6] M. Baublitz and A. L. Ruoff, J. Appl. Phys. **53**, 6179 (1982).
[7] T. Huang and A. L. Ruoff, Phys. Rev. B **31**, 5976 (1985).
[8] R. J. Nelmes, M. I. McMahon, N. G. Wright, and D. R. Allen, Phys. Rev. Lett. **73**, 1805 (1994), and references therein.
[9] C. S. Menoni and I. L. Spain, Phys. Rev. B **35**, 7520 (1987).
[10] Y. K. Vohra, S. T. Weir, and A. L. Ruoff, Phys. Rev. B **31**, 7344 (1985).
[11] J. Z. Hu, Solid State Commun. **63**, 471 (1987).
[12] M. I. McMahon, R. J. Nelmes, N. G. Wright, and D. R. Allan, Phys. Rev. B **50**, 13 047 (1994).
[13] R. J. Nelmes, M. I. McMahon, N. G. Wright, D. R. Allan, H. Liu, and J. S. Loveday, J. Phys. Chem. Solids **56**, 539 (1995).
[14] R. J. Nelmes, M. I. McMahon, P. D. Hatton, J. Crain, and R. O. Piltz, Phys. Rev. B **47**, 35 (1993), and references therein.
[15] R. J. Nelmes, M. I. McMahon, N. G. Wright, and D. R. Allan, Phys. Rev. B **51**, 15 723 (1995).
[16] M. I. McMahon, N. G. Wright, D. R. Allan, and R. J. Nelmes, Phys. Rev. B **53**, 2163 (1996).
[17] R. J. Nelmes and M. I. McMahon, J. Synchrotron Radiat. **1**, 69 (1994).
[18] M. I. McMahon and R. J. Nelmes, Phys. Status Solidi (b) **198**, 389 (1996).
[19] R. J. Nelmes and M. I. McMahon, Phys. Rev. Lett. **77**, 663 (1996).
[20] R. B. Von Dreele and A. C. Larson (unpublished).
[21] M. Baublitz and A. L. Ruoff, J. Appl. Phys. **54**, 2109 (1983).
[22] T. Huang and A. L. Ruoff, Phys. Rev. B **27**, 7811 (1983).
[23] J. Z. Hu, D. R. Black, and I. L. Spain, Solid State Commun. **51**, 285 (1984).
[24] Search on space groups $I4_1/amd$ and $I4md$ in the U.K. Chemical Database Service, D. A. Fletcher, R. F. McMeeking, and D. J. Parkin, Chem. Inf. Comput. Sci. **36**, 746 (1996).
[25] S. B. Zhang and M. L. Cohen, Phys. Rev. B **35**, 7604 (1987).
[26] A. Mujica, R. J. Needs, and A. Munoz, Phys. Rev. B **52**, 8881 (1995).
[27] A. Mujica and R. J. Needs, Phys. Rev. B **55**, 9659 (1997).
[28] S. B. Zhang, D. Erskine, M. L. Cohen, and P. Y. Yu, Solid State Commun. **71**, 369 (1989).